Chair of Physical Chemistry

Doctoral Thesis

Fundamental structure-property relations of triple-conducting $Ba(Ce,Fe,Acc)O_{3-\delta}$ ceramics

Dipl.-Ing. Christina Nader, BSc

July 2024

MONTANUNIVERSITÄT LEOBEN
www.unileoben.ac.at

EIDESSTATTLICHE ERKLÄRUNG

Ich erkläre an Eides statt, dass ich diese Arbeit selbstständig verfasst, andere als die angegebenen Quellen und Hilfsmittel nicht benutzt, den Einsatz von generativen Methoden und Modellen der künstlichen Intelligenz vollständig und wahrheitsgetreu ausgewiesen habe, und mich auch sonst keiner unerlaubten Hilfsmittel bedient habe.

Ich erkläre, dass ich den Satzungsteil „Gute wissenschaftliche Praxis" der Montanuniversität Leoben gelesen, verstanden und befolgt habe.

Weiters erkläre ich, dass die elektronische und gedruckte Version der eingereichten wissenschaftlichen Abschlussarbeit formal und inhaltlich identisch sind.

Datum 29.07.2024

Unterschrift Verfasser/in
Christina Nader

Acknowledgement

Just as many individuals (oxygen ions) are involved in the conduction of protons, so too have many people contributed their part to complete this project, my dissertation.

My special thanks go to my supervisors Edith Bucher, Andreas Egger and Rotraut Merkle, and my Mentor Raul Bermejo Moratinos – thank you for your time, your guidance and advice, your encouragement and your excellent expertise. I consider myself very lucky to have had the opportunity to work with you.

Besides these three, I would like to thank all my colleagues at the Chair of Physical Chemistry and the „PROTEC“ project team at the Centre for Electron Microscopy, Graz and Max Planck Institute for Solid State Research, Stuttgart. Thank you for your support, collaborative spirit, insightful discussions and positive team atmosphere.

The research presented in this work has received funding from the Austrian Research Promotion Agency FFG (grant no. 871659).

Image taken from: K.D. Kreuer, A. Rabenau, W. Weppner, Vehicle Mechanism, A New Model for the Interpretation of the Conductivity of Fast Proton Conductors, *Angewandte Chemie International Edition in English* **21** (1982) (3) 208, https://doi.org/10.1002/anie.198202082.

Kurzfassung

Infolge der voranschreitenden Klimakrise und der daraus resultierenden Intensivierung der Nutzung umweltfreundlicher, jedoch volatiler Energieträger, erlangen Technologien zur Energieumwandlung und -speicherung eine zunehmende Relevanz. Eine vielversprechende Möglichkeit stellen Brennstoff- und Elektrolysezellen dar, die zur Umwandlung von chemischer in elektrische Energie und umgekehrt verwendet werden können. Protonenleitende Brennstoffzellen (PCFC), welche momentan noch einen geringen Technologiereifegrad besitzen, bieten zahlreiche Vorteile hinsichtlich Effizienz, Kosten und Langlebigkeit. Gegenwärtig wird intensiv an neuen Materialien für die Luftelektrode geforscht, da diese den limitierenden Faktor hinsichtlich der Performance darstellt.

Die vorliegende Arbeit untersucht grundlegende Materialeigenschaften von Akzeptor-substituierten selbstgenerierten Kompositen, im Hinblick auf eine zukünftige Anwendung in PCFC-Luftelektroden. Die beiden Perowskit-Phasen der Komposite sollen gemeinsam die gewünschten Eigenschaften erfüllen. Diese setzen sich aus einer ausreichenden Protonenaufnahme und -leitfähigkeit, einer guten elektronischen Leitfähigkeit sowie einer guten katalytischen Aktivität für die Sauerstoffreduktion zusammen. Zahlreiche Proben mit unterschiedlichen Zusammensetzungen und substituiert mit verschiedenen Akzeptoren werden synthetisiert und hinsichtlich der für den gedachten Einsatz relevanten Eigenschaften charakterisiert. Dazu wird eine Vielzahl von komplementären Methoden eingesetzt, darunter neue und innovative Ansätze. Die Kristallstruktur, die Gitterparameter sowie die relativen Phasenanteile werden mittels Röntgendiffraktometrie bestimmt. Durch Auslagerungsexperimente wird die Mischungslücke in Abhängigkeit der Zusammensetzung des kristallographischen B-Platzes der Perowskitstruktur (ABO_3) untersucht, welche mit ICP-OES sowie STEM analysiert wird. Thermogravimetrie wird zur Bestimmung der Sauerstoff-Nichtstöchiometrie und der effektiven Protonenaufnahme genutzt. Aufgrund der fehlenden Möglichkeit zur Bestimmung der Verteilung der Protonenaufnahme zwischen den beiden Phasen der Komposite können thermodynamische Parameter lediglich für Reinphasen ermittelt werden. Die Mobilität der Protonen wird mit einem neuartigen Ansatz bestimmt, wobei Isotopenaustauschexperimente durchgeführt und die resultierenden Diffusionsprofile analysiert werden. Mittels Leitfähigkeits- und Leitfähigkeitsrelaxationsmessungen werden die elektrische Leitfähigkeit und die Sauerstoffaustausch-kinetik untersucht.

Die Ergebnisse der vorliegenden Arbeit zeigen Struktur-Eigenschaftsbeziehungen auf und liefern damit Designrichtlinien für die Optimierung der Materialien hinsichtlich gewünschter Eigenschaften. Weiters wird anhand fundamentaler Zusammenhänge aufgezeigt, dass innerhalb des gewählten Materialsystems gewisse Grenzen hinsichtlich der optimalen Verteilung der Akzeptoren bestehen. Abschließend werden Vorschläge für zukünftige alternative Materialsysteme gemacht.

Abstract

As a consequence of the ongoing climate crisis and the resulting intensification of the use of environmentally friendly but volatile energy sources, technologies for energy conversion and storage are becoming increasingly relevant. Fuel and electrolysis cells, which convert chemical energy into electrical energy and vice versa, represent a promising option. Proton conducting fuel cells (PCFC), which currently still exhibit a relatively low technology readiness level, offer several advantages in terms of efficiency, costs and longevity. Current research is focused on developing new materials for the air electrode, as this is the primary factor limiting performance.

The present work examines the fundamental material characteristics of acceptor-substituted self-generated composites with the objective of future utilisation in PCFC air electrodes. It is expected that the two perovskite phases of the composite will together fulfil the desired properties. These include sufficient proton uptake and conductivity, good electronic conductivity, and good catalytic activity for oxygen reduction. A substantial number of samples with varying compositions and substituted with different acceptors are synthesised and characterised in order to evaluate their suitability for the intended application. For this purpose, a variety of complementary methods are employed, including novel and innovative approaches. The crystal structure, lattice parameters and relative phase fractions are determined by X-ray diffraction. By annealing experiments, the miscibility gap is investigated as a function of the composition of the crystallographic B-site of the perovskite (ABO_3), which is analysed employing ICP-OES and STEM. Thermogravimetry is used to determine the oxygen nonstoichiometry and the effective proton uptake capacity. As it is not possible to quantify the distribution of the proton uptake between the two phases of the composite, thermodynamic parameters can only be calculated for single phases. The mobility of the protons is determined using a novel approach, based on isotope exchange experiments and subsequent analysis of the resulting diffusion profiles. Conductivity and conductivity relaxation measurements are employed to analyse the electrical conductivity and oxygen exchange kinetics.

The results of the present work demonstrate the existence of structure-property relationships, thereby providing design guidelines for optimising the materials with regard to the desired properties. Moreover, the fundamental relationships indicate the existence of limitations to the optimal distribution of acceptors within the selected material system. Based on these observations, suggestions are made regarding potential alternative material systems that could be considered in future research.

Table of contents

List of abbreviations

CR	Conductivity relaxation
DFT	Density functional theory
EC	Electrical conductivity
EDTA	Ethylenediaminetetraacetic acid
EDX	Energy-dispersive X-ray spectroscopy
EELS	Electron energy loss spectroscopy
FFT	Fast Fourier transformation
FIB	Focused ion beam
HAADF	High-angle annular dark-field
HR-TEM	High-resolution transmission electron microscopy
ICP-OES	Inductively coupled plasma – optical emission spectroscopy
IEDP	Isotope exchange diffusion profile
MIEC	Mixed (oxygen) ionic electronic conductor
OCV	Open-circuit voltage
ORR	Oxygen reduction reaction
PCEC	Protonic ceramic electrolysis cell
PCFC	Protonic ceramic fuel cell
SE	Secondary electrons
SEM	Scanning electron microscopy
SOFC	Solid oxide fuel cell
SPS	Spark plasma sintering
STEM	Scanning transmission electron microscopy
TG	Thermogravimetry
ToF-SIMS	Time-of-flight secondary ion mass spectrometry
TPB	Triple phase boundary
XRD	X-ray powder diffraction

1. Introduction

The changing global climate due to increased greenhouse gas emissions has led to a rethinking of energy consumption and sources, and intensified the search for clean, environmentally friendly and sustainable alternatives. Renewable energy sources include solar and wind power, geothermal heat and hydroelectricity. However, the availability of these sources is subject to fluctuations that are beyond our control, ranging from the scale of minute to seasonal variations [1]. The increasing share of renewable energy in the electrical energy mix poses the challenge of balancing the shortage or excess of available energy to ensure grid stability and secure power supply. Energy conversion and storage technologies, such as fuel cells, are an interesting option for balancing overproduction and underproduction over time. Fuel cells convert chemical energy into electrical energy and vice versa. There are various types of fuel cells, with solid oxide fuel cells (SOFC) being particularly promising for stationary applications due to their high efficiency, relatively low costs and flexibility regarding the utilised fuel [2]. State-of-the-art SOFCs contain an oxygen ion conducting electrolyte and are operated at high temperatures (800-1000 °C), which are necessary to ensure sufficiently fast ionic transport and reaction kinetics. However, the high temperatures also lead to stress in the components, challenges concerning the durability, and the necessity for expensive and complex thermal management systems. To increase efficiency, reduce costs and improve durability, the reduction of the operating temperature to 300-500 °C is a promising approach. One option to decrease the operating temperature, while retaining the performance of the cell, is the use of proton conducting ceramic electrolytes, which have a lower activation energy for diffusion than oxygen ions [3]. Iwahara et al. were the first to report protonic conductivity in ceramic solid electrolytes [4-6]. Today, perovskite-type cerates and zirconates $Ba(Ce,Zr,Y)O_{3-\delta}$ are well-studied state-of-the-art materials [7-9], which exhibit significant proton conductivity at temperatures as high as 300-700°C due to their low activation energy for protonic transport [5, 8]. The potential for use at reduced temperatures makes proton conductors interesting for applications in the field of electrochemical conversion and storage, including protonic ceramic fuel cells (PCFC), hydrogen production, hydrogen separation membranes, and the synthesis of ammonia, for example [10-13]. The reported results of PCFCs have been promising in recent years [10, 14-16]. However, the expected performance has not yet been achieved, likely due to the reduced catalytic activity of the air electrode resulting from kinetic limitations due to the reduced temperature [17]. Consequently, the development of novel air electrode materials with improved performance at lower temperatures has become a key focus of research to enhance the performance. The development of air electrodes for PCFCs started with the utilisation of mixed oxygen ion and electron conducting oxides, as used in state-of-the-art SOFCs designed for elevated operating temperatures. As a consequence of improved electrolyte materials, the air electrode, optimised for SOFCs, became increasingly the limiting factor for the performance in PCFCs. Therefore, it is necessary to develop air electrodes with a specific focus on their use in PCFCs [18]. Due to the mixed oxygen ionic and electronic conductivity of typical SOFC air electrode materials, the active zone for the oxygen reduction reaction (ORR) in PCFCs is limited to the triple phase boundary (TPB), as shown in Figure 1.1a. In order to expand

the active zone for ORR to the entire surface of the air electrode, it is necessary to introduce additional protonic defects into the material. This led to the concept of triple conducting oxides, which are ceramics that conduct protons, oxygen ions and electrons. The presence of protonic charge carriers in the bulk of the electrode, leads to the availability of protons at the surface of the electrode, thus enabling ORR at the two-phase boundary between the electrode and the gas phase, as shown in Figure 1.1b. Triple conducting oxides represent a relatively young but highly topical field of research, of great interest for both fundamental and applied purposes [16, 19-26].

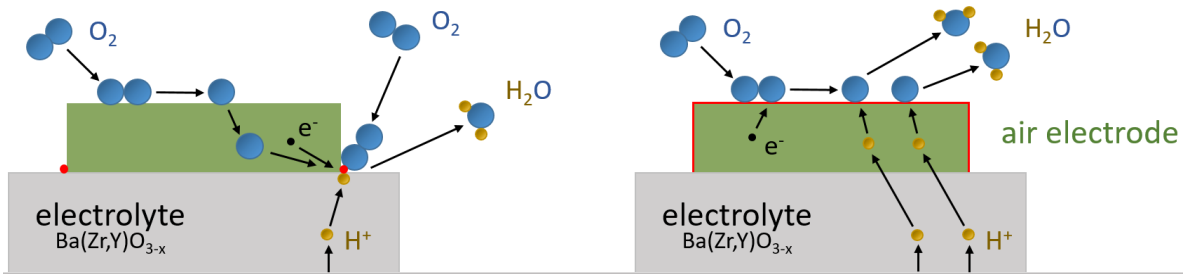

(a) Mixed ionic and electronic conducting oxide

(b) Triple conducting oxide

Fig. 1.1 Reaction and transport pathways at the air electrode consisting of a **(a)** mixed oxygen ion and electron conducting oxide and **(b)** triple (proton, oxygen ion and electron) conducting oxide. Active zones for the ORR are marked in red. Adapted from [27].

The aim of this thesis is to develop a fundamental understanding of the complex structure-property relationships in two-phase composites and single phases from the $Ba(Ce,Fe,Acc)O_{3-\delta}$ system. Inspired by the self-generated composites first published for the model system $BaCe_{0.5}Fe_{0.5}O_{3-\delta}$ by Cheng et al. [28], this work investigates the influence of a variety of acceptor substituents on crystal structure, phase composition, and mass and charge transport properties. The two-phase composite approach aims at the formation of a mainly proton conducting and a mainly electron conducting phase, which together fulfil the requirement of triple conductivity. The two phases separate in-situ during the synthesis process, which also represents a novel approach to the production of composites.

In relation to these objectives, four research questions are defined:

I. **Which properties of the acceptor substituent govern its distribution between the two phases of the composite?**
II. **How can the protonic conductivity in materials with three charge carriers be meaningfully determined?**
III. **What are the effects of acceptor substitution on the fundamental material properties?**
IV. **Which optimisation guidelines can be derived from the obtained comprehensive results?**

In order to optimise the model system in terms of its proton uptake capacity, the method of acceptor substitution is utilised, which is explained in more detail in section 2.3. Acceptor substitution. Consequently, several different composites and single phases with varying substituents and compositions will be synthesised. A comprehensive characterisation of the properties is conducted in order to investigate the dependence of structure, composition and properties. One specific property, which is especially challenging to investigate, is the protonic conductivity in materials with three different charge carriers. In this context, a new measurement method will be implemented. By analysing the obtained data and identifying relations, optimisation guidelines will be derived.

2. Theoretical background

The potential and relevance of protonic ceramic fuel cells is reflected in the development of the number of related publications. Bello et al. have investigated the annual research output on the topic of PCFCs and found a continuously increasing trend, as shown in Figure 2.1. This signals an increasing interest and intensified activities in this relatively new but highly topical research area.

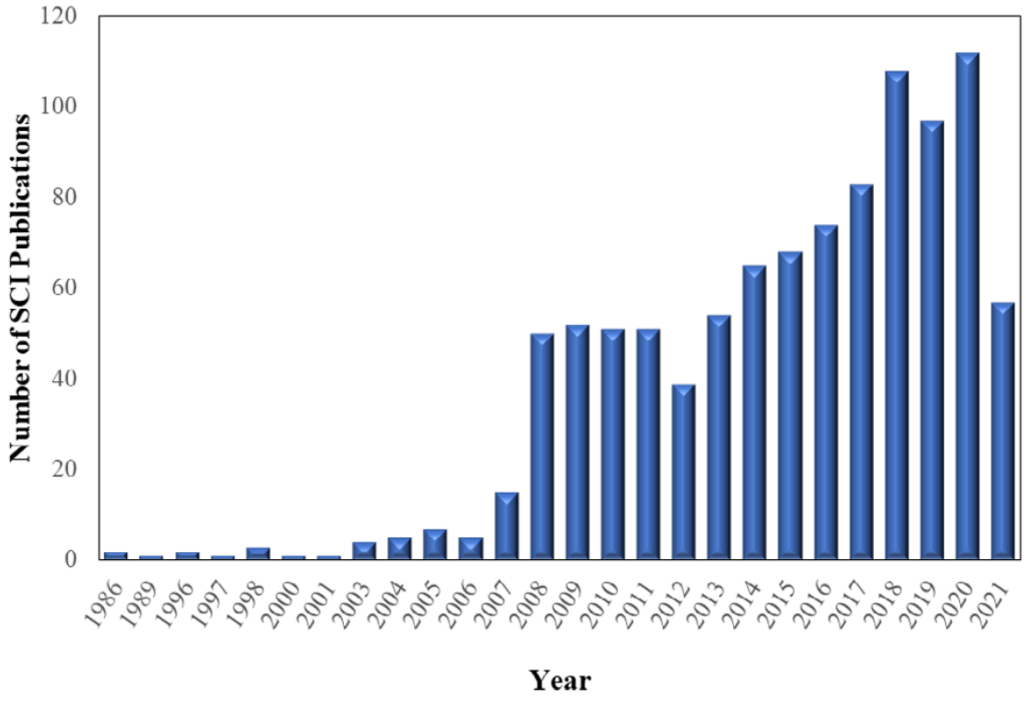

Fig. 2.1 Number of publications related to PCFC research from 1986 until 2021. Taken from [2].

2.1. Protonic ceramic fuel cells

Protonic ceramic fuel cells (PCFC) are highly efficient devices used for the direct conversion of chemical energy derived from various fuels into electrical energy [10, 14, 15, 17, 29]. Conversely, the same principle can be applied to convert electrical energy into chemical energy with a protonic ceramic electrolysis cell (PCEC) [11, 30-33]. The PCFC is a ceramic based technology. Reactants, such as hydrogen and oxygen, are separated by a gas-tight, electronically isolating but ionically conducting electrolyte ceramic. In contrast to solid oxide fuel cells (SOFC) [34-36], which are based on an oxygen ion conducting electrolyte, the electrolyte of PCFCs conducts protons. Therefore, in a PCFC, the product water (Equation 2.1) is produced only at the air electrode, which has the benefit of preventing dilution of the fuel stream at the fuel electrode. This potential for higher fuel utilisation results in an increased theoretical performance, which is even higher for PCFCs, operated at reduced temperature, as the theoretical efficiency increases with decreasing operating temperature. An additional advantage

towards SOFCs is an expected cost reduction for the stack production of PCFCs [37]. The reduced operating temperature results in a less demanding environment for the structural and functional materials, which leads to less degradation and therefore to lower requirements and a larger selection of materials. Nevertheless, there are several requirements on the components, including thermomechanical and chemical compatibility with the directly adjacent material. Furthermore, the materials must be suitable for the prevailing atmospheric conditions in order to ensure a safe and reliable long-lasting operation. Current state-of-the-art materials are discussed in more detail in the following sections. Figure 2.2 illustrates the reaction and transport pathways within a protonic ceramic fuel cell and a protonic ceramic electrolysis cell that is operated with hydrogen and water vapour, respectively.

$$2\,H_2 + O_2 \rightleftharpoons 2\,H_2O$$

Eq. 2.1 Reaction of hydrogen and oxygen in fuel cell mode

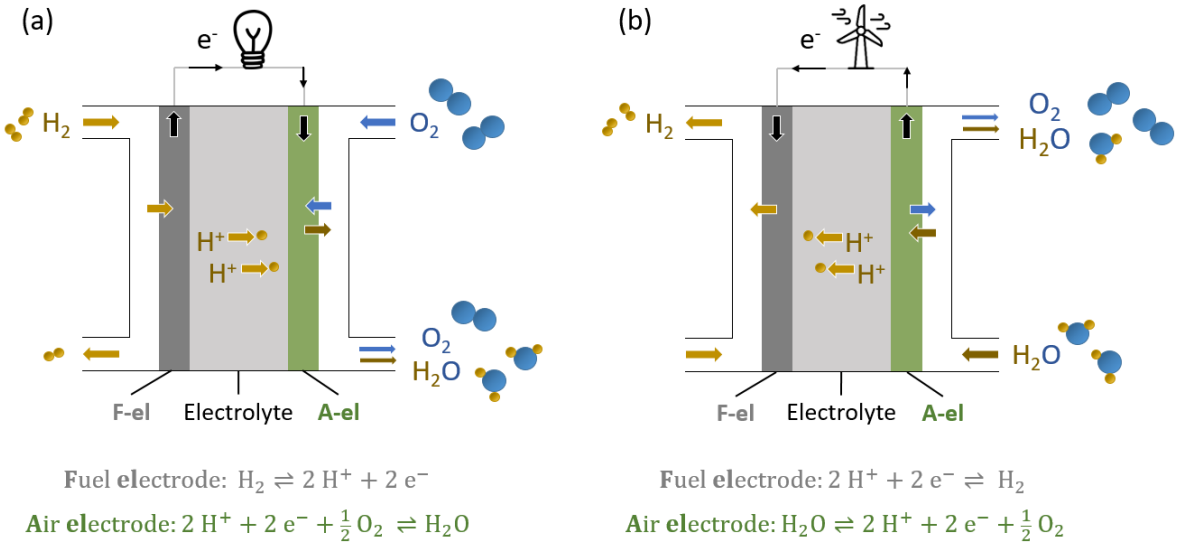

Fuel electrode: $H_2 \rightleftharpoons 2\,H^+ + 2\,e^-$

Air electrode: $2\,H^+ + 2\,e^- + \frac{1}{2}O_2 \rightleftharpoons H_2O$

Fuel electrode: $2\,H^+ + 2\,e^- \rightleftharpoons H_2$

Air electrode: $H_2O \rightleftharpoons 2\,H^+ + 2\,e^- + \frac{1}{2}O_2$

Fig. 2.2 Reaction and transport pathways of a **(a)** protonic ceramic fuel cell and **(b)** protonic ceramic electrolysis cell operated with hydrogen and water vapour, respectively.

In fuel cell mode, protons (H^+), which are formed by hydrogen molecules releasing electrons (Equation 2.2), pass from the fuel electrode through the electrolyte to the air electrode. The electrons, which are transferred to the fuel electrode via an external circuit, reduce oxygen, resulting in the formation of oxygen ions. These ions then react with the protons, releasing water vapour (Equation 2.4). This process generates an open-circuit voltage (OCV) of approximately 1 V. The construction of stacks, which connect numerous cells in a series, allows for the summation of the voltage of all cells and generates thereby higher voltages at useful currents.

2.1.1. Electrolyte

In terms of structural properties, the electrolyte must have a sufficiently high density and be gas-tight in order to prevent direct crossover of reactants, and to create continuous transport paths for protons. Typical electrolyte materials are perovskites with a general formula ABO_3 (Figure 2.3). The A-site is occupied by divalent alkaline earth metals with a larger ionic radius, such as Ca, Sr, La or Ba. Among these, Ba shows the most promising results in terms of protonic conductivity [8]. The B-site is typically occupied by smaller tetravalent lanthanide and transition metal ions like Ce and Zr. Cerium is the more promising B-site ion in terms of protonic conductivity [7, 38, 39], however, it has a poor chemical stability in the presence of water and acidic gases [40-42]. Zirconium, on the other hand, exhibits excellent chemical stability in operating conditions [7, 43, 44]. However, it has a poor sinterability, which results in lower protonic conductivity due to an increase in grain boundary volume [7, 8, 43].

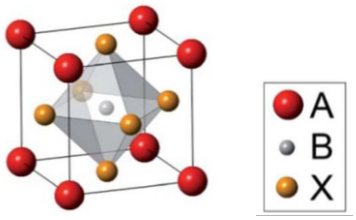

Fig. 2.3 Ideal structure of a cubic ABO_3 perovskite, which is characterised by the B-site being located in the centre of oxygen octahedron (X = O) and the A-site being situated at the corners of the cubic unit cell. Image taken from [45].

As described in detail in section 2.4. Proton uptake in triple conducting oxides, oxygen vacancies are required for proton uptake. These oxygen vacancies are created by substituting the B-site with trivalent ions, such as Y and Yb among others (refer to section 2.3. Acceptor substitution). State-of-the-art electrolyte materials for protonic ceramic fuel cells are acceptor substituted $Ba(Ce,Zr,Y,Yb)O_{3-\delta}$ perovskites (BCZYYb), as used in [10, 14, 15, 31, 32].

2.1.2. Fuel electrode

At the fuel electrode, hydrogen molecules release two electrons and become protons, as described by Equation 2.2. The gas phase is responsible for the transport of hydrogen to the surface where this reaction takes place. To be able to transport the released electrons to the current collector and protons to the electrolyte, respectively, the electrode should conduct both electrons and protons. In addition, the fuel electrode should be stable under reducing conditions and compatible with a variety of fuels (e.g. CO_2 atmosphere tolerance) to enable flexible use of the fuel cell. Typical fuel electrode materials are ceramic-metallic composites (“cermets”), consisting of Ni and a proton conducting oxide. Depending on the electrolyte material, Ni-BCZYYb is a typical fuel electrode composite for fuel cells with a BCZYYb electrolyte [2, 32, 46, 47].

$$2\,H_2 \rightleftharpoons 4\,H^+ + 4\,e^-$$

Eq. 2.2 Reaction of hydrogen oxidation

In contrast to the electrolyte, the electrode should have a porosity of 20-40 % in order to increase the number of electrochemically active sites for the anode reaction and to enable sufficient gas transport [2]. This porosity is achieved by reducing NiO to Ni, or by the use of pore formers like starch or graphite [18, 48].

2.1.3. Air electrode

Similar to the fuel electrode, the air electrode needs a sufficient degree of porosity in order to facilitate the transport of educts (oxygen) and products (water vapour) to and from the surface of the air electrode, respectively. Furthermore, the material must be stable against water vapour under operating conditions, compatible with other cell components, and exhibit a good performance. On the surface, adsorbed oxygen reacts with electrons, and is thereby reduced to oxygen ions (Equation 2.3). These ions then react with protons, forming water vapour (Equation 2.4).

$$O_2 + 4\,e^- \rightleftharpoons 2\,O^{2-}$$

Eq. 2.3 Reaction of oxygen reduction

$$2\,O^{2-} + 4\,H^+ \rightleftharpoons 2\,H_2O$$

Eq. 2.4 Reaction of water formation

High catalytic activity for the oxygen reduction reaction is of great importance for the performance. Depending on the properties of the air electrode material, there are different transport and reaction pathways. At the beginning of technical development, mixed ionic and electronic conducting oxides (MIEC), such as $Ba_{0.5}Sr_{0.5}Co_{0.8}Fe_{0.2}O_{3-\delta}$ [15, 49] and $La_{0.6}Sr_{0.4}Co_{0.2}Fe_{0.8}O_{3-\delta}$ [50, 51], were employed as air electrodes in PCFCs. These materials were initially developed for oxygen ion conducting SOFCs and conduct mainly electrons and oxygen ions. Due to the oxygen ion conductivity, there are more transport paths available for oxygen ions than in pure electronic conductors such as platinum. However, the active zone for water formation (Equation 2.4) is still limited to the triple phase boundary of the air electrode, electrolyte and gas phase (Figure 1.1a). To expand the electrochemically active zone to the entire surface of the air electrode, which increases the performance significantly, triple conducting oxides with protonic defects as additional charge carriers are a promising alternative (Figure 1.1b). The requirements for triple conducting air electrodes are high catalytic activity for ORR and electronic, protonic and oxygen ion conductivity. To ensure fast charge transfer and efficient current collection, the electronic conductivity should be higher than 10 S cm^{-1}. For the expansion of the active zone, it is estimated that a protonic conductivity of at least 10^{-5} S cm^{-1} should be sufficient [22, 27]. In principle, there are two different approaches to meet these requirements. One approach is to use a suitable single phase material that conducts electrons, protons and oxygen ions [19, 22-25]. This can be achieved for example by substituting the B-site of proton conducting electrolyte materials

with transition metals, such as Fe, Ni or Co. An alternative approach is to utilise composites in which two phases take over part of the requirements cooperatively. Composites with one predominantly electron conducting phase and a second, mainly proton conducting phase, have been reported [21, 52-57]. This work addresses the approach of composites.

2.2. Self-generated composites

A special manufacturing approach for the preparation of composites is the in-situ phase separation during "one-pot" synthesis. This method allows for the preparation of homogenously distributed, self-generated nanocomposites, which are rich in two-phase boundaries. Figure 2.4 shows the transport pathways and reaction sites of traditional composites, prepared by mechanical mixing, in comparison to self-generated composites prepared by "one-pot" synthesis.

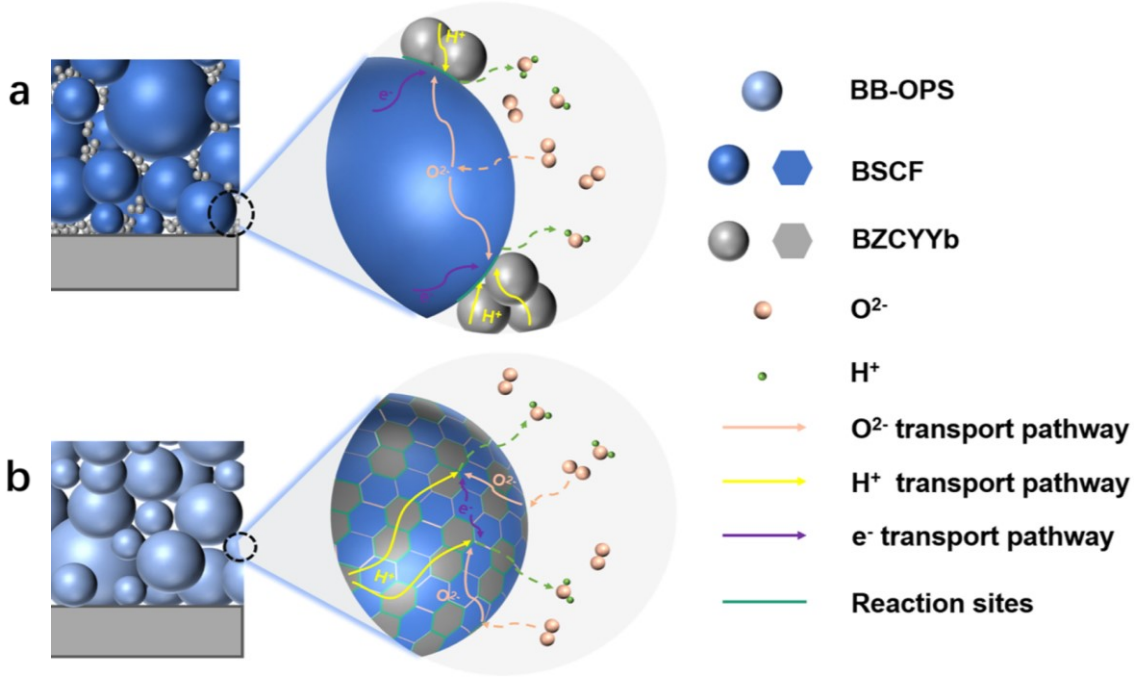

Fig. 2.4 Comparison of the transport pathways and reaction sites of **(a)** conventionally prepared composites and **(b)** composites prepared by "one-pot" synthesis. Image taken from [26].

Conventional composites are prepared by mixing two separately synthesised materials. The mechanical mixing frequently results in an inhomogeneous distribution of the two phases, which, in combination with larger particle sizes, leads to poor phase percolation and extends the length of the transport pathways. This results in a limited number of active reaction sites [26]. Furthermore, the two phases can form undesirable additional phases during operation at elevated temperatures, which results in a reduction in performance. Self-generated composites have the advantage of well mixed and tightly connected phases in sub-micrometer range, leading to a highly active material. In contrast

to traditional composites, self-generated composites separate in-situ into two phases resulting in a stable, durable composite. Cheng et al. investigated the model system $BaCe_{0.5}Fe_{0.5}O_{3-\delta}$, which is prepared by "one-pot" synthesis [28]. During the calcination process, the precursor separates into two phases. One phase is rich in Ce and predominantly protonic conducting, while the other is rich in Fe and mainly oxygen ion and electron conducting. However, due to the mutual solubility of Ce and Fe in the respective other phase, both phases also have a limited conductivity for the charge carriers of the other phase. Figure 2.5 illustrates the miscibility gap of $BaCe_{1-x}Fe_xO_{3-\delta}$, which is dependent on the composition of the precursor. In the range of $0.15 \leq [Fe] \leq 0.80$, the precursor forms a composite. Compositions with higher or lower amounts of Fe are single phase. In all compositions, the Ce-rich and Fe-rich phases are oxides with a perovskite structure (Figure 2.3). The A-site, which is typically occupied by larger 12-coordinate cations, is occupied by barium ions (Ba^{2+}). The B-site cations, typically 6-coordinate smaller cations, are cerium (Ce^{4+}) and iron (with mixed valence Fe^{3+}/Fe^{4+}) in amounts depending on the precursor composition.

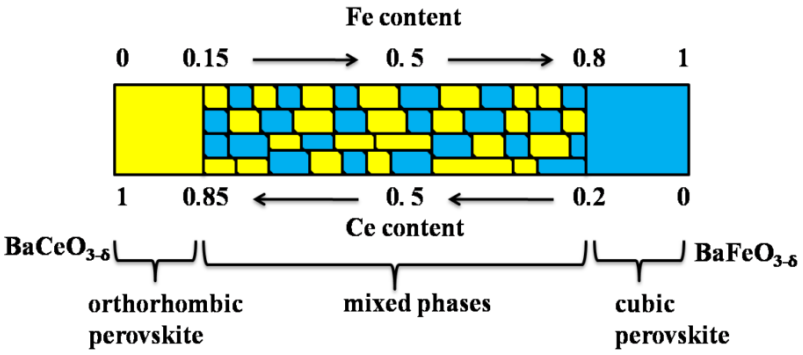

Fig. 2.5 Schematics illustrating the single phase and composite regions of the $BaCe_{1-x}Fe_xO_{3-\delta}$ model system depending on the precursor composition. Yellow areas illustrate the Ce-rich phase and blue areas the Fe-rich phase. In the range of $0.15 \leq [Fe] \leq 0.80$ the material forms both phases, resulting in composites. Image taken from [28].

2.3. Acceptor substitution

To optimise the model system $BaCe_{1-x}Fe_xO_{3-\delta}$ in terms of its proton uptake capacity, the B-site can be substituted with trivalent ions (acceptor substituents, Acc), which is also called acceptor substitution. By replacing tetravalent Ce with trivalent substituents, the oxygen vacancy concentration $[V_O^{\bullet\bullet}]$ increases according to Equation 2.5.

$$Acc_2O_3 \rightleftharpoons 2\,Acc'_B + 3\,O_O^{\times} + V_O^{\bullet\bullet}$$

Eq. 2.5 Defect formation by acceptor substitution in Kröger-Vink notation

This is essential for the uptake of protons, as water is incorporated into oxygen vacancies (Equation 2.6). The substitution with different acceptors has already been investigated for $BaCeO_3$ [6, 7, 39, 43, 58, 59]. In terms of protonic conductivity, Y is the most promising substituent for $BaCeO_3$ and $BaZrO_3$ [8]. The solubility limit of Y is approximately 20% of the available B-sites. In contrast, In has complete solubility in $BaCeO_3$, making it an interesting alternative [58]. However, not only the type and amount of the acceptor substituent is crucial, also the distribution of the substituent between the two phases determines the properties. For instance, the proton uptake capacity is sensitive to the presence of acceptor substituents and also to the presence of Fe. The Ce-rich phase is the phase with the higher degree of hydration. As the amount of acceptor substituent incorporated into the Ce-rich phase increases, the relative increase in proton uptake capacity also gets higher.

2.4. Proton uptake in triple conducting oxides

The determination of the proton uptake in triple conducting oxides is not straightforward, as the incorporation of protons can occur via two different routes. The predominating mechanism is determined by the defect chemical regime, which means by the concentrations of charge carriers present. In electrolytes with oxygen vacancies as ionic charge carriers, water incorporation occurs exclusively through an acid-base reaction (hydration reaction, Equation 2.6).

$$H_2O + V_O^{\bullet\bullet} + O_O^{\times} \rightleftharpoons 2\,OH_O^{\bullet}$$

Eq. 2.6 Proton uptake via hydration reaction in Kröger-Vink notation

In this process, a covalent bond is formed between a proton (H^+) and a lattice oxygen (O_O^x), and an oxygen vacancy is filled with a hydroxide ion (OH^-), which in total results in two protonic defects ($OH_O^{\bullet}$) for one water molecule. Electrolytes, such as $Ba(Ce,Zr,Y,Yb)O_{3-\delta}$ perovskites, become fully hydrated in humid atmosphere. In the case of typical air electrode materials with redox-active transition metals (e.g. Fe, Ni, Co) on the B-site, the oxygen vacancies become hydrated only to a small degree. The preferred mechanism of proton uptake in air electrode materials depends on the experimental conditions. Due to the presence of additional charge carriers, namely electron holes ($h^{\bullet}$), the oxygen exchange equilibrium (Equation 2.8) must be considered. In the case of $Ba(Ce,Fe,Acc)O_{3-\delta}$ composites, the electron holes, which are p-type charge carriers, are localised at the Fe-ions, which can also be written as $Fe_{Fe}^{\bullet}$. By combining Equations 2.6 and 2.8, the proton uptake in mixed conducting oxides can be formulated as a redox reaction (hydrogenation, Equation 2.7), which describes the proton uptake at the expense of holes [22]. In order to determine the proton uptake capacity in mixed conducting oxides, the atmospheric conditions must be carefully adjusted to guarantee that the proton uptake occurs exclusively via one of these mechanisms. When the condition $2\,[V_O^{\bullet\bullet}] > [h^{\bullet}]$ is fulfilled, protonation through the hydration reaction (Equation 2.6) dominates [22].

$$H_2O + 2\,O_O^{\times} + 2\,h^{\bullet} \rightleftharpoons 2\,OH_O^{\bullet} + \frac{1}{2}\,O_2$$

Eq. 2.7 Proton uptake via hydrogenation in Kröger-Vink notation

$$\frac{1}{2}O_2 + V_O^{\bullet\bullet} \rightleftharpoons O_O^{\times} + 2\,h^{\bullet}$$

Eq. 2.8 Oxygen exchange reaction in Kröger-Vink notation

Details on the experimental settings can be found in section 3.5. Thermogravimetry. Further calculations are performed with the oxygen vacancy concentration from the electroneutrality condition according to Equation 2.9.

$$[Acc'] = 2\,[V_O^{\bullet\bullet}] + [h^{\bullet}] + [OH_O^{\bullet}]$$

Eq. 2.9 Electroneutrality condition in Kröger-Vink notation

2.5. Proton transport mechanisms

The dominant proton transport mechanism for perovskites is the Grotthuss mechanism [60, 61]. Proton transport between two oxygen ions in a perovskite structure by Grotthuss mechanism involves two steps. The proton performs (i) rotational motions around the actual oxygen ion and is then (ii) transferred to the neighbouring oxygen ion. Via the breaking and formation of O–H bonds the proton is hopping from one oxygen ion to another. Figure 2.6 visualises the movement of a proton during the transfer process. The proton transfer actually comprises two parts [62]: (i) Approach of the initial and final O from the equilibrium distance on the crystal (almost 3 Å) to ~2.5 Å, without much changes of the O–H bond length. (ii) This O...O approach allows the hydrogen bond to the final O to become strengthened, and this then enables the actual proton transfer with a low barrier. Proton conduction in substituted perovskites is additionally influenced by the presence of substituents. This is the case for both redox-active transition metals and acceptor substituents. In the case of acceptors the phenomenon “trapping” due to attractive interactions between protons and acceptor substituents has been reported [61]. The binding energy of protons in the vicinity of substituents is higher, which makes the migration from one oxygen ion to another more difficult, thus reducing the diffusion coefficient of protons.

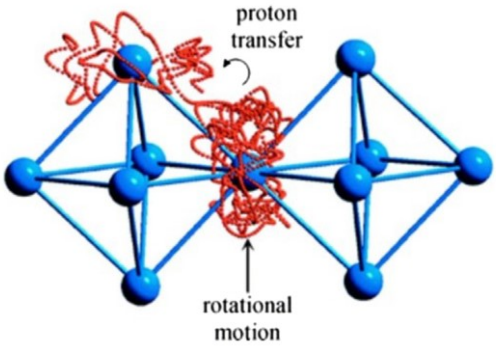

Fig. 2.6 Proton transport via Grotthuss mechanism. The motion of a single proton is illustrated by the red spheres. The transport includes two steps, which are (i) rotational motion and (ii) proton transfer to a neighbouring oxygen ion (blue spheres). Trajectory from a molecular dynamics simulation, taken from [60, 63].

3. Materials and methods

3.1. Acceptor-substituted Ba(Ce,Fe)$O_{3-\delta}$ composites and single phases

This thesis deals with various materials within the Ba(Ce,Fe,Acc)$O_{3-\delta}$ system. All materials, grouped by type and composition, can be found in the appendix (Tables A1 – A15). Based on the type of phase formation, they can be divided into three groups:

i. Self-generated Ba(**Ce**,Fe,Acc)O_3 - Ba(Ce,**Fe**,Acc)O_3 composites, consisting of a Ce-rich and an Fe-rich phase. The material separates in-situ during the calcination process, forming two phases. In addition to different compositions of unsubstituted Ba(Ce,Fe)$O_{3-\delta}$ (Table A7), materials with a variety of acceptor substituents (Acc = Y, In, Gd, Nd, Sc, Sm, Yb) were synthesised to investigate the influence of the nature of the substituent on proton uptake. As Y and In showed promising results in this respect, these were selected for more profound investigations. For Y-substituted self-generated composites, $BaCe_{1-(x+y)}Fe_xY_yO_{3-\delta}$ solid solutions were investigated as a function of Fe:Y ratio (Table A1), Ce:Y ratio (Table A2) and Ce:Fe ratio (Table A3). For In-substituted self-generated composites the influence of the Ce:In ratio (Table A4) and the Ce:Fe ratio (Table A5) was investigated.

ii. Single phases based on the phase compositions of self-generated composites to investigate the properties of the individual phases. Solid solutions outside the miscibility gap were studied for both Y- and In-substituted $BaCe_{0.8-x}Fe_xAcc_{0.2}O_{3-\delta}$. Thus, a series of Fe-rich compositions, ranging from those with extremely low Ce content to the limits of miscibility was prepared. Additionally, Ce-rich compositions near the miscibility gap and containing very high levels of Ce were analysed. The chosen compositions aim to investigate the miscibility gap in more detail and the influence of Ce and Fe on proton uptake. For Ce-rich single phases with variable amounts of Y and In, and a fixed Fe content, the proton uptake was investigated as a function of acceptor substituent concentration. In addition, Fe-rich single phases with various quantities of Ce, Y and In were analysed.

iii. Artificial composites with compositions closely matching those of self-generated composites. These were investigated for comparison in order to understand the impact of the type of phase formation on the material properties.

3.2. Nomenclature and abbreviations

In this thesis, abbreviations for the different materials are used for better readability. The abbreviations for self-generated composites and single phase materials are based on their precursor compositions. These follow two essential rules: (i) The typical elements of the A- and B-site such as Ba, Ce and Fe are abbreviated with their initial letters B, C, F respectively. The acceptor substituents are indicated with their element symbols, except In, which is given as I. (ii) Following the elements, the

stoichiometric amounts of the respective B-site elements are listed. For Ba, which completely occupies the A-site, there is no reported information. According to this, $BaCe_{0.87}Fe_{0.08}Y_{0.05}O_{3-\delta}$ is specified as BCFY870805 and BCFI343 is referring to $BaCe_{0.30}Fe_{0.40}In_{0.30}O_{3-\delta}$. For single phase materials with only two different elements on the B-site, the stoichiometric amount is only given for the last element, thus $BaFe_{0.95}Y_{0.05}O_{3-\delta}$ is given as BFY05. There is a separate regulation for artificial composites, which consist of varying proportions of a Ce-rich and an Fe-rich phase. The proportions of the respective phase are given as volume percentage. These follow the abbreviation BcBf where Bc stands for the Ce-rich phase and Bf for the Fe-rich phase. According to this, BcBf8020 is referring to an artificial composite consisting of 80 vol.% Ce-rich phase and 20 vol.% Fe-rich phase.

3.3. Sample preparation

According to the three different groups of materials, there are three different types of sample preparation. The process for synthesising the calcined powder, as described in the next chapter, always remains unchanged. Depending on the type of material, there may exist an intermediate step between calcination and sintering, i.e. mixing of the phases for an artificial composite, and the densification process can occur via two distinct methods, i.e. spark plasma sintering and conventional sintering. These different methods are described in the following chapters.

3.3.1. Sol-gel synthesis

All samples were prepared via sol-gel synthesis using the ethylenediaminetetraacetic acid (EDTA)-citric acid method. Stoichiometric amounts of the metals, in the form of metal-nitrates, were dissolved together with anhydrous citric acid and EDTA in distilled water, using the molar ratio 1(metals):2(citric acid):1(EDTA). By adding 25% aqueous ammonia, the pH was adjusted to approximately 8. All reagents for the synthesis were obtained in analytical grade quality from Sigma Aldrich. The temperature was then continuously increased to remove water and form a gel, which self-ignites and combusts around 500 °C. The resulting raw ash was milled in a porcelain mortar and subsequently calcined in an alumina crucible at 1000 °C for 10 h in air (heating and cooling rates of 5 K min^{-1}). Depending on the composition of the precursor, the calcined powders could be single phase or composite, which was checked by XRD measurements. For certain samples, the overall stoichiometry was also examined via ICP-OES. All samples were ground in dry state in a zirconia ball mill for one hour, regardless of any subsequent mixing or compaction procedures.

3.3.2. Spark plasma sintering

In addition to conventional solid-state sintering, there are several other sintering technologies [64]. Self-generated composites were densified using spark plasma sintering (SPS) (FCT Systeme GmbH, Germany). This technique utilises uniaxial pressure and heating by pulsed high DC current in a graphite die. The electrical current flowing through the die and the sample (if it is conducting) enables fast heating rates and − combined with pressure − a fast sintering and densification process [65]. This allows

high densities for nanomaterials, as the grain growth is reduced, and it avoids phase changes that would occur at high sintering temperatures. Due to these advantages SPS was used for densification of self-generated composites. To achieve high densities during conventional sintering, it would be necessary to maintain the samples at temperatures above the miscibility gap for an extended time, which would result in formation of a single phase material. To prevent single phase formation, SPS was used for self-generated composites to achieve very dense pellets while retaining the composite. Depending on the theoretical density of the composition, about 3 g of ground calcined powder were filled into a graphite die and compressed via two graphite rods. To prevent reduction of the sample by graphite, an yttria-stabilised zirconia (YSZ) felt was used to separate the sample from the graphite dies. Table 3.1 shows parameters used for SPS and achieved densities for selected samples. The heating and cooling rates ranged between 50 and 150 K min^{-1}, and the dwell time was 5 min. After sintering, the pellets were roughly ground to eliminate the YSZ, and their geometric density was determined.

Tab. 3.1 Example parameters for self-generated $BaCe_{0.8-x}Fe_xIn_{0.2}O_{3-\delta}$ ($0.20 \leq x \leq 0.60$) composites compacted via SPS and densities achieved for the respective sample.

Precursor	Mold diameter / mm	Temperature / °C	Force / kN	Geom. density / g cm^{-3}	Theor. density / g cm^{-3}	Rel. density / %
$BaCe_{0.30}Fe_{0.50}In_{0.20}O_{3-\delta}$	14	1000	12	5.769	6.079	95
$BaCe_{0.40}Fe_{0.40}In_{0.20}O_{3-\delta}$	10	1000	6	5.941	6.315	94
$BaCe_{0.50}Fe_{0.30}In_{0.20}O_{3-\delta}$	14	1000	12	5.832	6.260	93
$BaCe_{0.60}Fe_{0.20}In_{0.20}O_{3-\delta}$	10	1100	6	5.923	6.332	94

3.3.3. Conventional sintering

Single phase materials were densified using conventional sintering. In this process the ground calcined powders were compacted inside a rubber mold (Ø 15 mm) using an isostatic press by applying a force of 200 kN for approximately 1 min. The resulting green body was then sintered in a magnesia crucible in either air or N_2, at a temperature between 1300 and 1500 °C for 4 or 8 hours – depending on the composition.

3.3.4. Artificial composites

In addition to the characterisation of self-generated composites and single phases, artificial composites were also investigated. Thermogravimetry showed that self-generated composites have a lower proton concentration than would be expected for a composite mixed from a Ce-rich and an Fe-rich phase with the same overall stoichiometry (refer to section 4.6. Proton uptake capacity, Figure 4.25). It was assumed that the unwanted accumulation of the acceptor substituent in the Fe-rich phase (refer to section 4.4. Microstructure and elemental distribution, Figure 4.11) is responsible for a decrease in proton uptake capacity in the Ce-rich phase (refer to section 4.6. Proton uptake capacity, Figure 4.24),

resulting in a significantly lower level of proton uptake in general. To obtain better control over the acceptor distribution between the two phases and prevent the enrichment of the acceptor substituent in the Fe-rich phase, artificial composites were prepared. For this purpose, a Ce-rich ($BaCe_{0.76}Fe_{0.04}Y_{0.20}O_{3-\delta}$) and an Fe-rich phase ($BaCe_{0.04}Fe_{0.76}Y_{0.20}O_{3-\delta}$) were synthesised separately and then mixed in varying proportions. The partial dissolution of Fe in the cerate phase and Ce in the ferrate phase makes both phases triple conducting. Artificial composites were prepared in three different compositions, as shown in Table 3.2.

Tab. 3.2 Prepared artificial composites with their respective proportions of Ce- and Fe-rich phase.

Abbreviation	Overall composition	vol.% of Ce-rich phase	vol.% of Fe-rich phase
BcBf8020	$BaCe_{0.60}Fe_{0.20}Y_{0.20}O_{3-\delta}$	80	20
BcBf6535	$BaCe_{0.48}Fe_{0.32}Y_{0.20}O_{3-\delta}$	65	35
BcBf5050	$BaCe_{0.37}Fe_{0.43}Y_{0.20}O_{3-\delta}$	50	50

Initial attempts to prepare artificial composites were made by mixing the Fe-rich and Ce-rich phases in dry state using a zirconia ball mill for one hour. The mixed powder was then annealed for 6 hours at 700 °C in a magnesia crucible under N_2 atmosphere followed by SPS – the parameters are listed in Table 3.3. Heating and cooling rates were between 50 and 150 K min^{-1}, and the dwell time was 5 min. After this, the pellets were roughly ground to eliminate the YSZ. Although the proton uptake of the artificial composites was notably higher than that of equivalent self-generated composites, especially for Ce-rich samples (refer to section 4.6. Proton uptake capacity, Figure 4.25), it did not reach the expected levels. The local cation composition and distribution within the individual phases, investigated by scanning transmission electron microscopy and energy-dispersive X-ray spectroscopy (STEM-EDX) indicate that the composition of the two phases deviates from the original composition. EDX maps showed inhomogeneities in Ce-rich grains, revealing a decrease in Y and increase in Ce content towards the edges (refer to section 4.4. Microstructure and elemental distribution, Figures 4.12 and 4.13). Cation interdiffusion, particularly for Y, occurs during the preparation process and results in an enrichment of Y in the Fe-rich phase. In an attempt to improve the preparation of artificial composites, another approach was used with BcBf5050. To minimise cation interdiffusion during sintering, the calcined powders of the pure phases were annealed separately before sintering. $BaCe_{0.76}Fe_{0.04}Y_{0.20}O_{3-\delta}$ was annealed at 1380 °C for 16 h and $BaCe_{0.04}Fe_{0.76}Y_{0.20}O_{3-\delta}$ at 1230 °C for 16 h. SEM images of annealed powders are shown in the appendix (Figures A1 and A2). To ensure a gentler mixing process, the powders were mixed manually in an agate mortar, annealed and then compacted using SPS. As there was no significant increase in proton uptake achieved with this method, no additional samples were prepared.

Tab. 3.3 SPS parameters for artificial composites and densities achieved for the respective sample.

Abbreviation	Mold diameter / mm	Temperature / °C	Force / kN	Geom. density / g cm^{-3}	Theor. density / g cm^{-3}	Rel. density / %
BcBf8020	10	1150	6	5.828	6.089	96
BcBf6535	10	1100	6	5.674	6.044	94
BcBf5050	10	1150	6	5.594	5.999	93

3.4. Fundamental characterisation

3.4.1. X-ray powder diffraction

X-ray powder diffraction (XRD) analyses were carried out at room temperature after calcination and once again after sintering. The calcined powders were analysed with a BRUKER-AXS D8 Advance ECO X-ray diffractometer (MUL, Leoben). The diffractometer was operated at 40 kV and 25 mA using a Cu Kα radiation source (λ = 1.5406 Å). The acquisition time was set to 2 s per step with a scanning rate of 0.01° s^{-1}. Measurements on particles from crushed sintered pellets were done with a PANalytical Empyrean X-ray diffractometer (MPI, Stuttgart) using a Cu Kα radiation source (λ = 1.5406 Å) operated at 40 kV and 40 mA. The acquisition time was set to 2 s per step, while the scan rate was 0.02° s^{-1}. The measurements at Max Planck Institute for Solid State Research (MPI, Stuttgart) were carried out by Helga Hoier. The relative phase amounts of the composites and lattice parameters of the phases were acquired via whole pattern profile fitting by the LeBail method carried out with TOPAS [66, 67]. For the Fe-rich phase the peak positions were fitted to a cubic unit cell (space group $Pm\bar{3}m$). The structure of the Ce-rich phase is influenced by substitution. When unsubstituted, the peak positions of the Ce-rich phase were fitted to an orthorhombic unit cell (space group *Pmcn*), while the peak positions of acceptor-substituted Ce-rich phases were fitted to a trigonal unit cell (space group $R\bar{3}c$).

3.4.2. Powder annealing

To determine the temperature of single phase formation and obtain information on the miscibility gap, annealing experiments were performed on self-generated composites. Particles from crushed SPS pellets with a grain size < 100 µm were annealed for 4 h at each selected temperature in an alumina crucible. After each annealing stage, the particles were cooled to room temperature and analysed using XRD before being heated to the subsequent temperature. The investigation of the acquired XRD patterns was focused on the development of phase fraction and lattice parameters.

3.4.3. Inductively coupled plasma optical emission spectrometry

Inductively coupled plasma optical emission spectrometry (ICP-OES) is a method to acquire the average cation composition of a sample. The measurements were conducted in the chemistry laboratory of Max Planck Institute for Intelligent Systems (MPI, Stuttgart) by Samir Hammoud. Selected samples in the Ba(Ce,Fe,Y/In)O_3 system were sintered by SPS, dissolved in hydrochloric acid and analysed with a SPECTRO CIROS (SPECTRO Analytical Instruments GmbH).

3.4.4. Analytical scanning transmission electron microscopy

Scanning transmission electron microscopy and energy-dispersive X-ray spectroscopy (STEM-EDX) were utilised to evaluate the local cation composition and distribution within the individual phases, surface damage due to preparation, and material alterations after conductivity relaxation measurements. Fresh SPS sintered samples underwent a re-oxidation via annealing in static air for 4 h at 1000 °C in a conventional furnace prior to analysis. The lamellae chosen for analysis were extracted from within the pellet through fragmentation (except in the case of surface analysis) and prepared using a focused ion beam (FIB) microscope FEI NOVA 200 NanoLab. The FIB preparation was carried out by Martina Dienstleder (Graz Centre for Electron Microscopy). Measurements were conducted using an FEI TITAN^3 G2 60-300 microscope equipped with a C_s-probe corrector and a Super-X detector system. The microscope was operated at an accelerating voltage of 300 kV, and the images were captured using a high-angle annular dark-field (HAADF) detector. The software packages GMS 3 (Gatan) and Velox 2 (Thermo Fisher Scientific) were used to acquire HAADF images and EDX spectrum images. All STEM measurements were carried out by Judith Lammer (Graz Centre for Electron Microscopy). For each sample, a minimum of one EDX map and several EDX point spectra were recorded on grains of both phases. To determine the crystal structure of the two phases, high-resolution transmission electron microscopy (HR-TEM) and fast Fourier transformation (FFT) were carried out for selected samples. In order to prevent channelling effects, quantification by EDX was only performed on grains that were not aligned with the low-index zone axis in relation to the electron beam. For further evaluation, the results of EDX spectroscopy were classified into Fe-rich and Ce-rich phases. The classification criteria were based on the Ce:Fe ratio in the grain – a higher concentration of Fe classified the grain as Fe-rich, while a higher concentration of Ce classified it as Ce-rich.

3.5. Thermogravimetry

Thermogravimetry (TG) was carried out to study the proton uptake capacity and oxygen nonstoichiometry of composites and single phase materials. Particles of a specific size obtained from sintered pellets were used in the experiments. The pellets underwent sintering, crushing, grinding, and were subsequently sieved into two distinct sizes. For the TG experiments, a particle size range of 100-250 µm was selected. This range was found to be optimal as it was large enough to prevent surface-controlled oxygen incorporation and water adsorption and small enough to ensure short equilibration times [22]. Typically, an amount of 0.5 to 1.5 g was analysed in an alumina crucible. TG experiments

were conducted using a thermogravimetry analyser STA449C Jupiter (Netzsch, Germany) at MPI, Stuttgart. The setup is gas-tight and permanently flushed with 60 ml min^{-1} N_2 divided between two gas flows. 10 ml min^{-1} of inert gas flows through the balance compartment (protective gas) and 50 ml min^{-1} flows through the sample compartment. The latter comes from a gas mixing system which enables adjustment of the water partial pressure pH_2O by bubbling part of the carrier gas flow through a thermostated water evaporator (Figure 3.1). A quadrupole mass spectrometer (QMS 200 F1, Balzers Prisma, Germany) was used to analyse the exhaust gas flow.

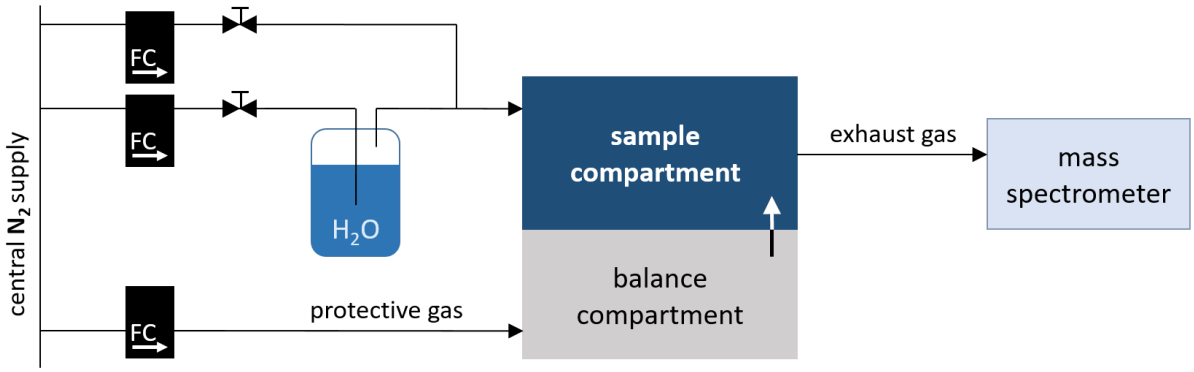

Fig. 3.1 Sketch of the TG measurement setup used. FC denotes flow controllers.

3.5.1. Oxygen nonstoichiometry measurements

Oxygen nonstoichiometry measurements were conducted by Rotraut Merkle (MPI, Stuttgart) for two selected single phases from the BCFY system using the same setup. An additional gas flow of O_2 was used to adjust the oxygen partial pressure pO_2 in the range of $0.00083 \leq pO_2/bar \leq 0.83$. The measurements were carried out as functions of temperature ($300 \leq T / °C \leq 800$) and pO_2.

3.5.2. Isothermal proton uptake measurements

Isothermal proton uptake measurements were conducted in a temperature range of 300-700 °C in 50 to 100 °C steps. Before the actual measurement, the sample was equilibrated in dry N_2 at 700 °C and then rapidly cooled to the desired temperature at a rate of 20 K min^{-1}. This ensures that all Fe ions are present as Fe^{3+} and the oxygen exchange reaction should be "frozen-in" (refer to section 4.5. Oxygen stoichiometry). With this procedure the condition $2\,[V_O^{\bullet\bullet}] > [h^{\bullet}]$ should be fulfilled, protonation through the hydration reaction (refer to section 2.4. Proton uptake in triple conducting oxides, Equation 2.6) is preferred, and complications from hole-proton defect interactions are avoided [22, 68]. Thereby, the change in sample mass can be used to determine the proton concentration at a certain temperature. Figure 3.2 shows the variation in sample mass during an experiment conducted at 400 °C with the self-generated composite $BaCe_{0.3}Fe_{0.5}In_{0.2}O_{3-\delta}$.

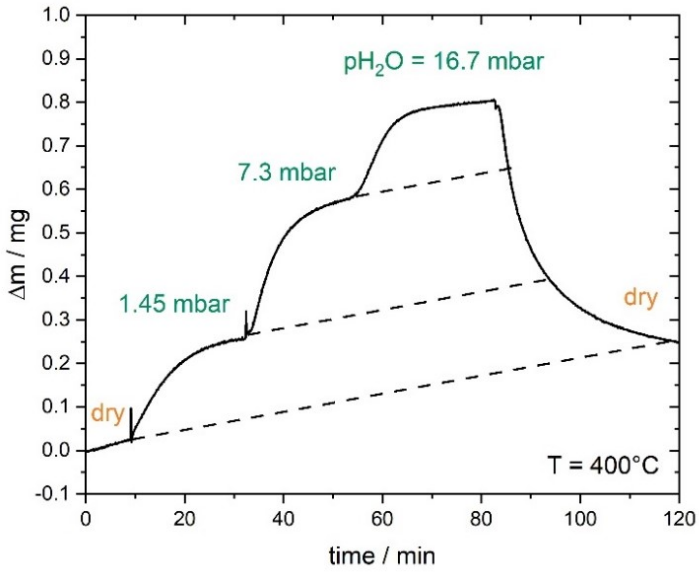

Fig. 3.2 Change in sample mass of $BaCe_{0.3}Fe_{0.5}In_{0.2}O_{3-\delta}$ (1423 mg; composite) caused by the change of water partial pressure. The baselines are illustrated by dashed lines, which are not horizontal due to drift in sample mass [69].

The measurement starts by equilibrating at the chosen measurement temperature. Subsequently, the water partial pressure is gradually increased in stages from dry to three different pH_2O levels (1.45, 7.3 and 16.7 mbar) and then back to dry. During this process, the sample incorporates water, which is detected as an increase in sample mass. In addition, oxygen is also incorporated, but at a much slower rate, resulting in a drift in the baseline, illustrated by dashed lines in Figure 3.2. This drift was subtracted from the data during the evaluation process. The settings for the flow controllers and thermostat at different pH_2O levels can be found in the appendix (Table A16). For single phase materials, the standard enthalpy $\Delta H^{\circ}_{hydrat}$ and entropy $\Delta S^{\circ}_{hydrat}$ of hydration can be determined from the van't Hoff plot ($\ln(K_{hydrat})$ versus T^{-1}) [22], where K_{hydrat} is determined with the oxygen vacancy concentration from the electroneutrality condition (Equation 2.9). Since the distribution of the proton uptake between the individual phases in a composite is not known, the mass action constants of the hydration reaction (refer to section 2.4. Proton uptake in triple conducting oxides, Equation 2.6) K_{hydrat} as well as $\Delta H^{\circ}_{hydrat}$ and $\Delta S^{\circ}_{hydrat}$, can only be calculated for single phase materials.

$$K_{hydrat} = \frac{[OH^{\bullet}_{O}]^2}{pH_2O\,[V^{\bullet\bullet}_{O}]\,[O^{x}_{O}]}$$

Eq. 3.1 Formula for the calculation of K_{hydrat} from the proton concentration

$$\Delta G^{\circ}_{hydrat} = \Delta H^{\circ}_{hydrat} - T\,\Delta S^{\circ}_{hydrat} = -R\,T\,\ln(K_{hydrat})$$

Eq. 3.2 Formula for the determination of $\Delta H^{\circ}_{hydrat}$ and $\Delta S^{\circ}_{hydrat}$

3.6. Isotope exchange diffusion profiling and secondary ion mass spectrometry

3.6.1. Isotope exchange

The investigated materials are predominantly electronically conductive, but they also exhibit ionic conductivity, including proton and significant oxygen ion conductivity. It is difficult to separate the proton conductivity from the total electrical conductivity, which makes the direct measurement of the protonic conductivity and mobility challenging [19]. Therefore, the proton mobility was investigated by isotope exchange diffusion profile (IEDP) method employing time-of-flight secondary ion mass spectrometry (ToF-SIMS). The experiments were conducted using dense sintered samples that had been dried beforehand. These samples were then humidified with D_2O. Humidification with D_2O is preferred over H_2O due to the high concentration of H and H-containing compounds in the vacuum of the SIMS setup (residual gas). This uncertainty would affect the reliability of the result, which also makes H-D exchange problematic. Therefore, the chemical diffusion of deuterium oxide (D_2O) was analysed. The chemical diffusion coefficient characterises the kinetics of diffusion resulting from a gradient in chemical potential, corresponding in the present case to a concentration gradient.

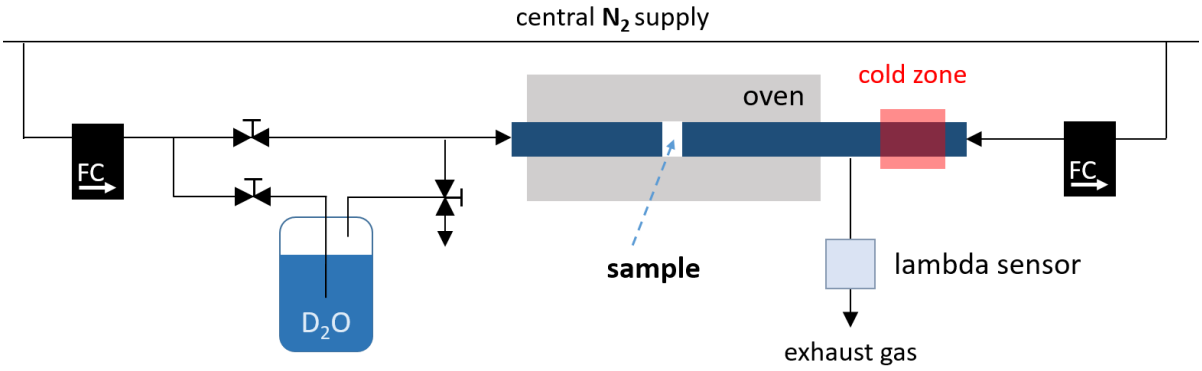

Fig. 3.3 Sketch of the setup for the isotope exchange experiment. FC denotes flow controllers.

Figure 3.3 shows a sketch of the setup used for the isotope exchange experiments. There are two sample placement areas in the setup: the oven zone and the cold zone. The oven zone is supplied with 30 ml min^{-1} N_2, which is fed to the sample either dry or humidified by a bubbler containing heavy water D_2O (99.9 atom% D) at room temperature. The bubbler delivers a humidification of approximately 20 mbar water partial pressure. To quench the sample, it can be removed from the oven zone by pulling the sample holder to the cold zone. The area designated as the cold zone (highlighted in red in Figure 3.3) is located outside the oven and maintained at room temperature. It is supplied with dry N_2. The experiments were carried out using densely sintered SPS pellets with a relative density of at least 95% [70]. Before being placed in a gold tray and inserted into the quartz glass sample holder, the pellet was

polished and quartered. The sample was dried for at least 10 hours by heating to 700 °C in a stream of dry N_2. At a cooling rate of 10 K min^{-1}, the nominally dry sample was then cooled to the selected measurement temperature at which the exchange is to take place. Prior to the exchange, the pipe of the D_2O stream was flushed for approximately 5 minutes, then the gas supply to the sample was switched from dry to humidified and the time was recorded. To ensure meaningful analysis with SIMS, it is important to select an appropriate exchange time that results in a diffusion profile depth similar to the area that can be analysed (refer to section 3.6.2. Secondary ion mass spectrometry). If the diffusion takes too long, the profile cannot be recorded completely and therefore cannot be analysed correctly. Conversely, if it is too short, too few data points are available to obtain a reliable result. The initial exchange times were estimated using conductivity approximations. Since diffusion coefficients are temperature-dependent and vary between materials, we calculated or estimated the exchange times for subsequent experiments based on existing results. After the chosen exposure time, the sample was quenched to stop the diffusion of deuterium and preserve the established diffusion profile. Details on the exchange parameters are summarised in Tables A17 and A18 in the appendix.

The sample should be processed with great care to avoid any distortion of the existing D_2O diffusion profile. It should not be heated excessively or exposed to water vapour. During critical processing steps, the temperature was monitored and did not exceed 40 °C. If there were extended waiting periods between processing steps, the sample was deep-frozen. To prevent uncertainties caused by time-related changes in the diffusion profile, we produced samples just-in-time and did not store them for an extended time between exchange experiment and taking measurements. Directly after the exchange annealing, the sample was embedded with a 2-component embedding agent from “Technovit 5000”, and the temperature development during curing was monitored. To uncover the diffusion profile, the upper part of the sample was lapped until a sufficiently large area was exposed. Figure 3.4 shows a sketch of the sample within the embedding material, with an arrow indicating the direction of lapping. The resulting geometry of the sample for the SIMS measurement is shown on the right.

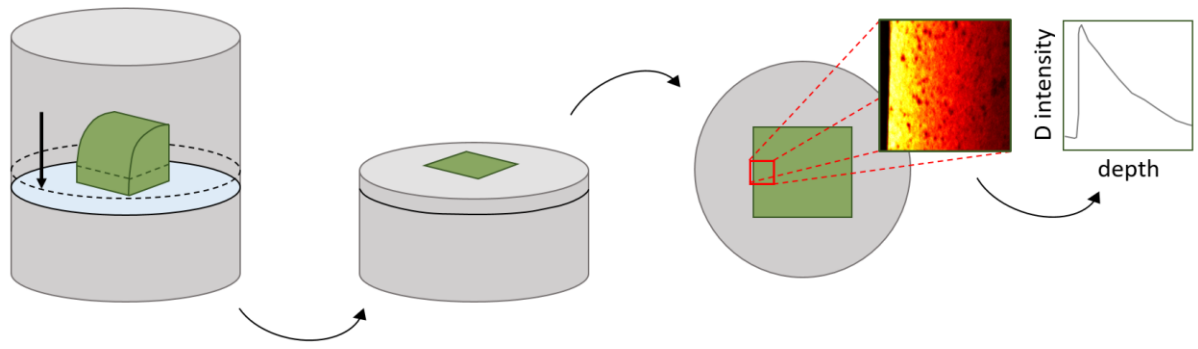

Fig. 3.4 Schematic diagram of the sample (green) and measurement position within the embedding material (grey).

3.6.2. Secondary ion mass spectrometry

Secondary ion mass spectrometry (SIMS) provides spatially resolved concentrations of species and can distinguish between isotopes. This technique has previously been employed to investigate proton conductors [71-74]. There are two distinct methods of measurement [75]. Depth profiling is employed for short diffusion profiles, with depths of up to 10 µm. For larger penetration depths, the diffusion profile is uncovered by cutting or lapping perpendicular to the surface as described in the previous section and the surface is imaged using a line scan technique. This work employed the latter technique, where the surface area is analysed. The measurements were performed with a ToF-SIMS V NCS (IONTOF, Germany) using the software Surfacelab 7.1. The sample was introduced into the vacuum chamber. First, the top layer, covering an area of 800 x 800 µm², was sputtered using a primary ion beam with low energy (Cs^+ source with 1 keV ion energy and 93 – 106 nA current). The interaction of primary ions with the sample removes material, effectively eliminating impurities and ensuring accurate measurements later on. For the measurement, an area of 500 x 500 µm² was bombarded with a primary ion beam (Bi^+ source with 30 keV ion energy and 1.8 – 2.4 pA current). Again, particles such as atoms and molecules are removed from the sample, and some of these are ionised. The charged particles with a certain polarity (in this work negatively charged secondary ions were analysed) are collected by accelerating them into a reflection type time-of-flight mass spectrometer. Figure 3.5 shows a schematic representation of a ToF-SIMS instrument.

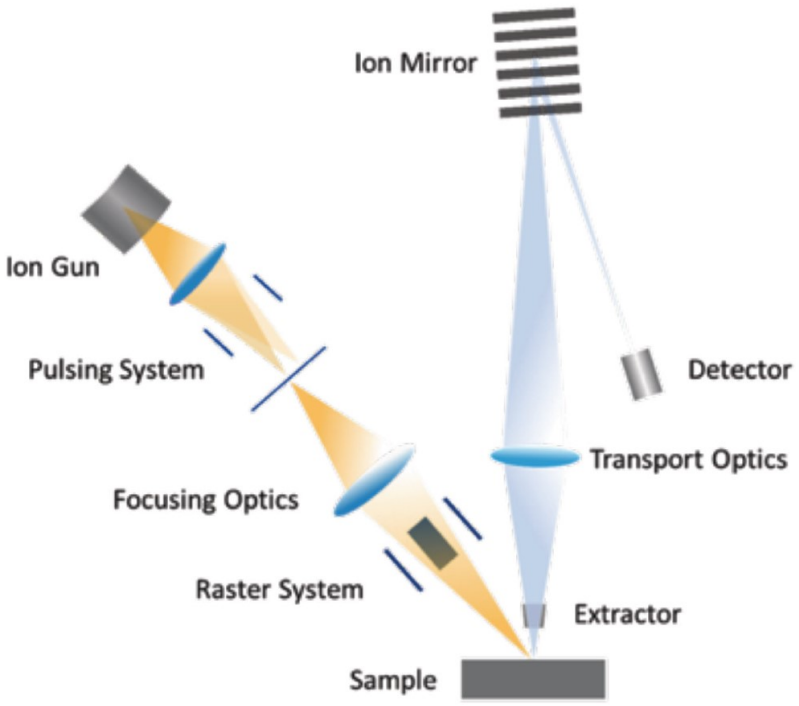

Fig. 3.5 Sketch of a ToF-SIMS instrument, showing the primary ions in orange and the secondary ions in blue. Image taken from [76].

The ions are identified and counted by the ion detector, which can differentiate between lighter and heavier ions based on their relative time of arrival. Since all ions experience the same accelerating voltage and travel the same distance, lighter ions reach the detector earlier than heavier ions. As a result, the ions can be assigned to specific elements and isotopes based on their mass. By scanning the focussed ion beam over the surface and recording the detected ions and their location, a mass resolved secondary ion image is obtained (Figure 3.6 left). The SIMS measurements were conducted in the scientific facility "Interface Analysis" of Max Planck Institute for Solid State Research (MPI, Stuttgart) by Tolga Acartürk.

3.6.3. Isotope profile fitting

For further data processing, a direction was specified in which the two-dimensional spatially resolved concentrations were summed to obtain a one-dimensional diffusion profile (Figure 3.6 middle). Care was taken to ensure that any holes or uneven edges that may distort the result are excluded. This data was exported for $^2H^-$ and $^2HO^-$ to carry out further analysis with both profiles for comparison. The chemical diffusion coefficient for D_2O ($D^{\delta}_{D_2O}$) was determined by non-linear fitting of an appropriate diffusion model to the normalised data C'(x). An error function describing diffusion with a constant surface concentration was used, assuming that the surface reaction is infinitely fast [77].

$$C'(x) = \frac{c(x,t) - c_1}{c_2 - c_1} = \mathrm{erfc}\left(\frac{x}{2\sqrt{D\,t}}\right)$$

Eq. 3.3 Error function used for non-linear fitting

The assumption of fast surface reaction is reasonable for the hydration reaction, given that it requires only proton transfer and the uptake of OH^- into a $V_O^{\bullet\bullet}$. This is kinetically less limited than e.g. the incorporation of O_2, which requires the splitting of the strong O=O double bond. Assuming fast surface reaction, the surface concentration c_2 (x = 0) is considered to be constant. The profile is in a semi-infinite condition, which means that the concentration decreases to the baseline, which may be either inside or outside the measurement area. If the baseline is inside, then the baseline concentration c_1 corresponds to its value, if it is outside, an approximation is used. The variable t represents the duration of the exchange annealing process. For each sample, the $^2H^-$ and $^2HO^-$ concentration profiles were analysed, which typically agreed well. In most cases, concentration profiles at each of the two D_2O-exposed sample edges were measured. For the evaluation process the analysis function in Origin was employed. The program receives t and a starting value for D^{δ}. Under the condition of low hydration and in the absence of trapping effects, the chemical diffusion coefficient of D_2O approximately corresponds to the diffusion coefficient for protonic defects $D_{OH_O^{\bullet}}$ [78]. Additional measurements were conducted with reduced *p*D_2O to verify this condition. Instead of 30 ml min^{-1} N_2, this time only 3 ml min^{-1} passed through the bubbler, while the remaining gas flow was fed directly to the oven in dry state. As this variation did not affect the values for $D^{\delta}_{D_2O}$, we considered this condition as fulfilled.

From $D_{OH_O^\bullet}$ and the concentration of protonic defects $c_{OH_O^\bullet}$, the ionic conductivity of protons $\sigma_{OH_O^\bullet}$ was estimated using the Nernst-Einstein equation. The variables F and R represent the Faraday constant and the universal gas constant, respectively. The charge number, z, is set to 1.

$$\sigma_{OH_O^\bullet} = \frac{z^2 F^2 c_{OH_O^\bullet} D_{OH_O^\bullet}}{R T}$$

Eq. 3.4 Nernst-Einstein equation

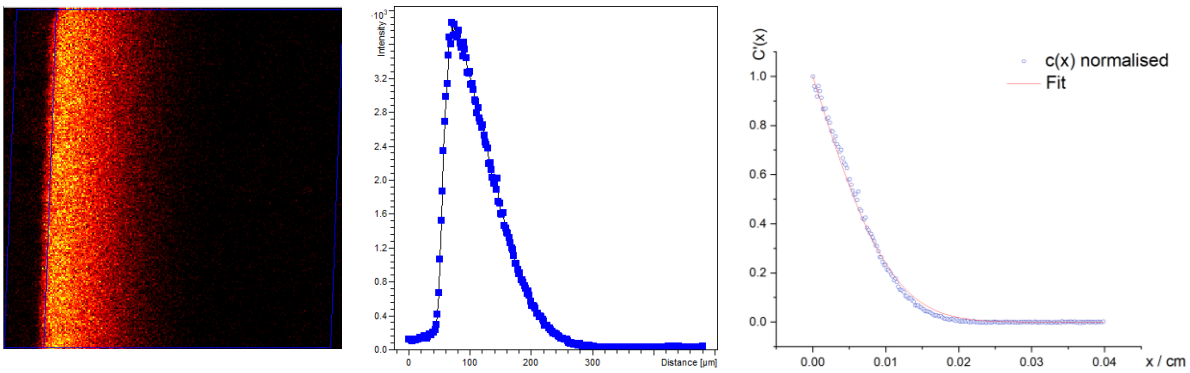

Fig 3.6 Secondary ion mapping (left) and one-dimensional concentration profile of $^2H^-$ (middle) for $BaCe_{0.04}Fe_{0.76}Y_{0.20}O_{3-\delta}$ annealed for 90 min in D_2O at 350 °C. The right figure shows the normalised diffusion profile C'(x) and the fitting curve.

3.7. Electrical dc-conductivity and conductivity relaxation measurements

3.7.1. Sample preparation

Electronic dc-conductivity and conductivity relaxation measurements were carried out with dense ceramic samples. The composites were densified using spark plasma sintering (SPS) and mechanically processed in non-reoxidised state as reoxidising the pellet can lead to stress and triggers cracks as a result. The pellet was cut to an area of about 5x5 mm² and a thickness of about 1 mm with a diamond wire saw. Using a manual water-cooled polishing machine, the surface of the sample was polished to a fineness of 1 µm. The prepared sample was then reoxidised in a thermobalance starting in pure Ar at 700 °C. After complete equilibration the oxygen partial pressure was gradually increased to 10% O_2, followed by cooling at 1 K/min. The reoxidised sample was then contacted with gold wire and gold paste as shown in Figure 3.7. Then the sample was connected to a sample holder and placed in a quartz glass reactor. After every contacting step the gold paste was burned in with a conventional oven in air. The temperature program is summarised in Table A19 in the appendix.

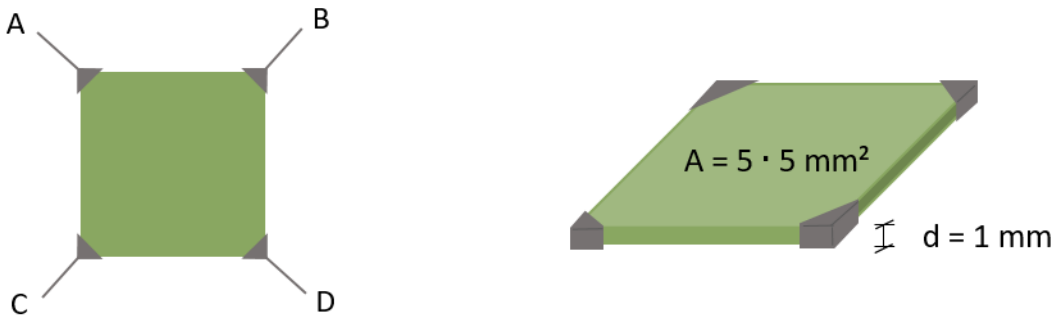

Fig 3.7 Arrangement of the contacts in four-point van der Pauw geometry.

3.7.2. Four-point dc-conductivity measurements

The electrical conductivity was investigated by four-point dc-conductivity measurements according to van der Pauw [79, 80]. This is a method to determine the specific resistance of flat samples of arbitrary shape with a uniform thickness. The contacts must be sufficiently small and arranged around the circumference of the sample. The resistance $R_{AB,CD}$ is calculated from the current between the contacts A and B and the measured potential difference between the contacts C and D. Similarly, to determine the resistance $R_{BC,DA}$ a current is passed between the contacts B and C and the potential difference is measured between the contacts D and A. The values of the current and voltage are mean values from two consecutive measurements. With the relationship between $R_{AB,CD}$ and $R_{BC,DA}$ and the sample thickness d the specific resistance ϱ can be calculated with Equation 3.5. The reciprocal of the specific resistance is the specific conductivity σ. The measurement evaluation for the electrical conductivity was performed with a Python program which automatically reads and processes the data and calculates the result.

$$\exp\left(-\pi\, R_{AB,CD}\,\frac{d}{\varrho}\right) + \exp\left(-\pi\, R_{BC,DA}\,\frac{d}{\varrho}\right) = 1$$

Eq. 3.5 Calculation of the specific resistance ϱ

Figure 3.8 shows a schematic representation of the setup for dc-conductivity and dc-conductivity relaxation measurements. The contacted sample was placed in a quartz glass reactor inside an oven to control the temperature. The gas flow was set to 3 litres per hour and could be delivered in dry or humidified state to the sample compartment. Measurements were carried out in a temperature range of 400 ≤ T / °C ≤ 800 in steps of 50 °C. A gas flow with 10 or 15 % O_2, rest Ar was applied to the sample, first in dry state and then in a humidified state. Additional measurements were carried out in dry state at the end to check for reversibility. The humidification was achieved by bubbling the carrier gas through ultrapure water at a temperature of 20 °C. To avoid cracks due to rapid humidification, the thermostated water should initially be kept at a lower temperature (T ~ 5 °C) to maintain a low pH_2O in the beginning. Once a new equilibrium is reached, the temperature of the thermostat and thereby

the pH_2O can be gradually increased to the chosen level. Furthermore, it is crucial to carry out the process at a sample temperature where the material does not absorb much water (T ≥ 500 °C; refer to section 4.6. Proton uptake capacity). However, measurements in a humid atmosphere inside a quartz glass reactor must not exceed a certain temperature to avoid Si-poisoning [81]. Therefore, measurements in humid atmosphere were only performed at temperatures of 400 ≤ T / °C ≤ 600.

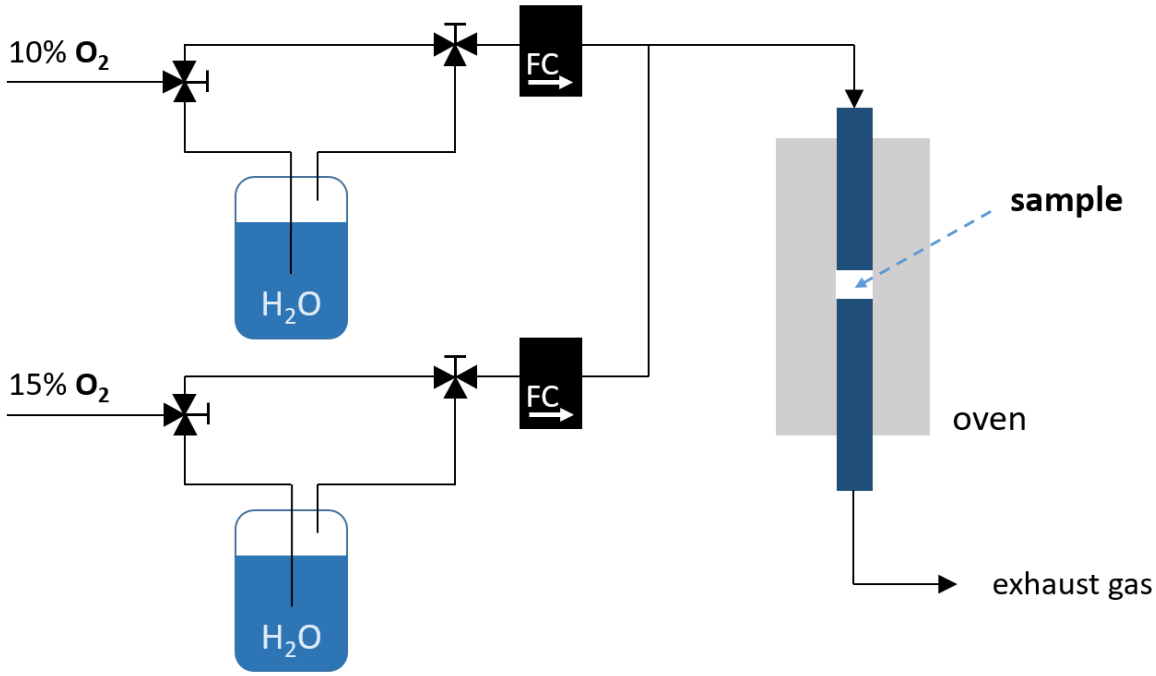

Fig 3.8 Sketch of the setup used for four-point dc-conductivity and dc-conductivity relaxation measurements under dry and humidified conditions. FC denotes flow controllers.

3.7.3. Dc-conductivity relaxation measurements

The bulk diffusion kinetics of O^{2-} ions were determined by dc-conductivity relaxation measurements [82, 83]. The relaxation measurements were made in parallel with the dc-conductivity measurements on the same samples in the same setup. Changes in pO_2 were performed between gas flows with 10 or 15 % O_2, rest Ar. This type of measurement is only applicable to materials that are predominantly electronic conducting. In such cases, the time required to reach the new equilibrium is solely controlled by the movement of ionic species. A change in the partial pressure of oxygen pO_2 results in release or incorporation of oxygen in the sample. This oxygen exchange reaction (refer to section 2.4. Proton uptake in triple conducting oxides, Equation 2.8) is a redox reaction in which the concentrations of charge carriers, i.e. electron holes $h^{\bullet}$ and oxygen vacancies $V_O^{\bullet\bullet}$, vary. In materials with redox-active transition metals (i.e. Fe), as in the materials studied, an increase or decrease in the concentration of electron holes originates from a change in the valence of Fe^{3+}/Fe^{4+}. A stepwise change in pO_2 therefore

causes a change in electrical conductivity, which can be calculated from the applied current and the resulting voltage. The time dependent values of the electrical conductivity σ_t (Figure 3.9 on the right side) were normalised using Equation 3.6 and yield − plotted as a function of time − the relaxation curve for the fitting procedure. In this equation, σ_0 is the conductivity in equilibrium state before the change in pO_2 and σ_∞ is the equilibrium value at the end of the relaxation.

$$\sigma_{norm} = \frac{\sigma_t - \sigma_0}{\sigma_\infty - \sigma_0}$$

Eq. 3.6 Calculation of the normalised specific conductivity

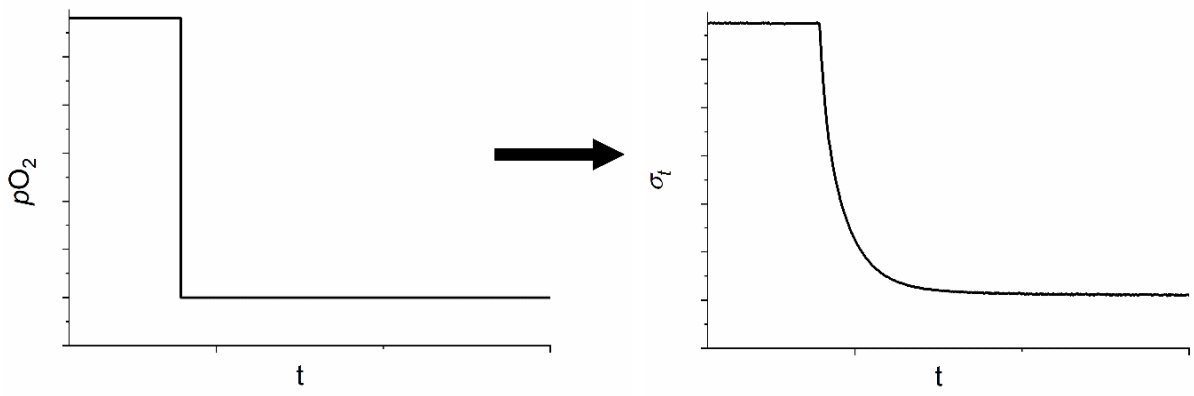

Fig 3.9 Ideal change in pO_2 and resulting relaxation curve of the electrical conductivity σ_t of a $Ba(Ce,Fe,Acc)O_{3-\delta}$ two-phase composite.

The oxygen exchange kinetics is described by the chemical bulk diffusion coefficient D_{chem} and the chemical surface exchange coefficient k_{chem}. By non-linear fitting of an appropriate diffusion model, D_{chem} and k_{chem} can be obtained from the normalised data from Equation 3.6. The recorded relaxation curve can be described with one of the following fitting functions, depending on the kinetic regime [84, 85]. Equation 3.7 assumes the overall kinetics is limited by bulk diffusion. If this is the case, the intersection of the $\ln(1-\sigma_{norm})$ vs. t plot with the ordinate is close to -0.21 and Equation 3.7 can be used to obtain the chemical bulk diffusion coefficient D_{chem}.

$$\ln(1-\sigma_{norm}) = \ln\left(\frac{8}{\pi^2}\right) - \frac{D_{chem}\,\pi^2}{L^2}\,t$$

Eq. 3.7 Diffusion model describing diffusion controlled kinetics

Equation 3.8 assumes a limitation of the overall kinetics by surface exchange. If this is the case, the intersection of the $\ln(1-\sigma_{norm})$ vs. t plot with the ordinate is close to 0 and this fitting function is used to obtain the chemical surface exchange coefficient k_{chem}.

$$\ln(1-\sigma_{norm}) = -\frac{2\,k_{chem}}{L}\,t$$

Eq. 3.8 Diffusion model describing surface exchange controlled kinetics

If both diffusion and surface exchange contribute to limiting the overall kinetics, the intersection with the ordinate falls between -0.21 and 0. In this case Equation 3.9 is used for fitting. This diffusion model includes both processes and the respective fit provides values for D_{chem} and k_{chem}. However, this diffusion model is only applied if the relaxation curve cannot be described by either Equation 3.7 or Equation 3.8.

$$\ln(1-\sigma_{norm}) = \ln\left(\frac{2\,k_{chem}^2}{\frac{D_{chem}^2\,\gamma^2\left(\frac{k_{chem}\,L}{D_{chem}}\right)^2}{4}+\frac{\gamma^2\,L^2}{4}+\frac{k_{chem}\,L}{2\,D_{chem}}}\right) - D_{chem}\,\gamma^2\,t$$

Eq. 3.9 Diffusion model describing mixed controlled kinetics

During the evaluation process, two assumptions are made: (i) For the surface exchange reaction of oxygen, a first order kinetics is assumed. (ii) The kinetic parameters D_{chem} and k_{chem} are assumed to remain constant during the change in pO_2, which is fulfilled if the change is sufficiently small. The fitting procedure was performed with the analysis function in the software Origin. As input parameters σ_{norm} as a function of the time t and the thickness of the sample L were provided to the program.

4. Results and discussion

4.1. Phase formation

The unsubstituted $BaCe_{1-x}Fe_xO_{3-\delta}$ system investigated by Cheng et al. [28] separates in-situ during calcination into an Fe-rich ($BaCe_{0.15}Fe_{0.85}O_{3-\delta}$) and a Ce-rich phase ($BaCe_{0.85}Fe_{0.15}O_{3-\delta}$). Both phases are perovskites with different crystallographic symmetries. The driving force behind the decomposition is the difference in the radii of the B-site ions ($r(Ce^{4+})$ = 0.870 Å, $r(Fe^{3+})$ = 0.645 Å and $r(Fe^{4+})$ = 0.585 Å for a coordination number of VI [86]). In the unsubstituted system, the precursor decomposes within a range of $0.20 \leq [Ce] \leq 0.85$. Higher ($[Ce] \geq 0.85$) and lower ($[Ce] \leq 0.20$) amounts of cerium lead to single phase compounds. The equimolar composition $BaCe_{0.5}Fe_{0.5}O_{3-\delta}$ remains in the two-phase region up to high temperatures – at 1400 °C the system is still two-phase and at 1450°C the material starts to melt [28]. This behavior was confirmed for two additional compositions, $BaCe_{0.3}Fe_{0.7}O_{3-\delta}$ and $BaCe_{0.7}Fe_{0.3}O_{3-\delta}$. The addition of acceptor substituents has an influence on the miscibility gap. The effect of acceptor substitution was investigated for Y and In by XRD analysis of a wide range of compositions. Figure 4.1 gives an overview of selected diffraction patterns of $BaCe_{0.8-x}Fe_xIn_{0.2}O_{3-\delta}$ (x = 0.2, 0.4, 0.6) and unsubstituted $BaCe_{0.5}Fe_{0.5}O_{3-\delta}$. As expected, all diffractograms show reflections of two phases. The reflections are assigned to a Ce-rich and an Fe-rich perovskite phase. The Fe-rich phase has a cubic structure ($Pm\bar{3}m$, SG#221), while the Ce-rich phase has a trigonal structure ($R\bar{3}c$, SG#167) for the acceptor-substituted materials and an orthorhombic structure (*Pmcn*, SG#62) for unsubstituted compositions.

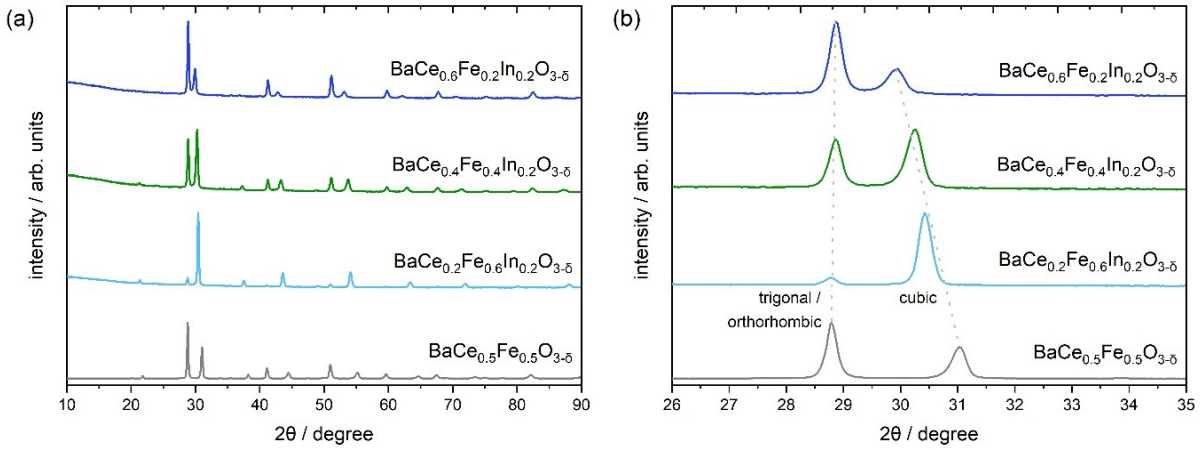

Fig. 4.1 (a) XRD-patterns of self-generated $BaCe_{0.8-x}Fe_xIn_{0.2}O_{3-\delta}$ (x = 0.2, 0.4, 0.6) composites compared to unsubstituted $BaCe_{0.5}Fe_{0.5}O_{3-\delta}$ [87]. The analyses were performed with particles of crushed SPS sintered pellets at room temperature. **(b)** Detailed image of a selected diffraction angle range of the XRD plots showing the peak shift [69].

The intensities of the peaks of the respective phase depend on the composition. As the Ce content increases, the intensity of the peaks of the Ce-rich trigonal phase becomes stronger while that of the Fe-rich cubic phase decreases. Figure 4.1b shows a detailed image of the reflections. Those of the cubic structure shift to lower diffraction angles with an increasing amount of Ce in the precursor, which was also observed for Y-containing samples [87]. The trigonal structure shows a similar but less pronounced behavior with peaks shifting slightly to higher angles with an increasing amount of Ce in the precursor. This also has an effect on the lattice parameters of the two phases (refer to section 4.3. Lattice parameters).

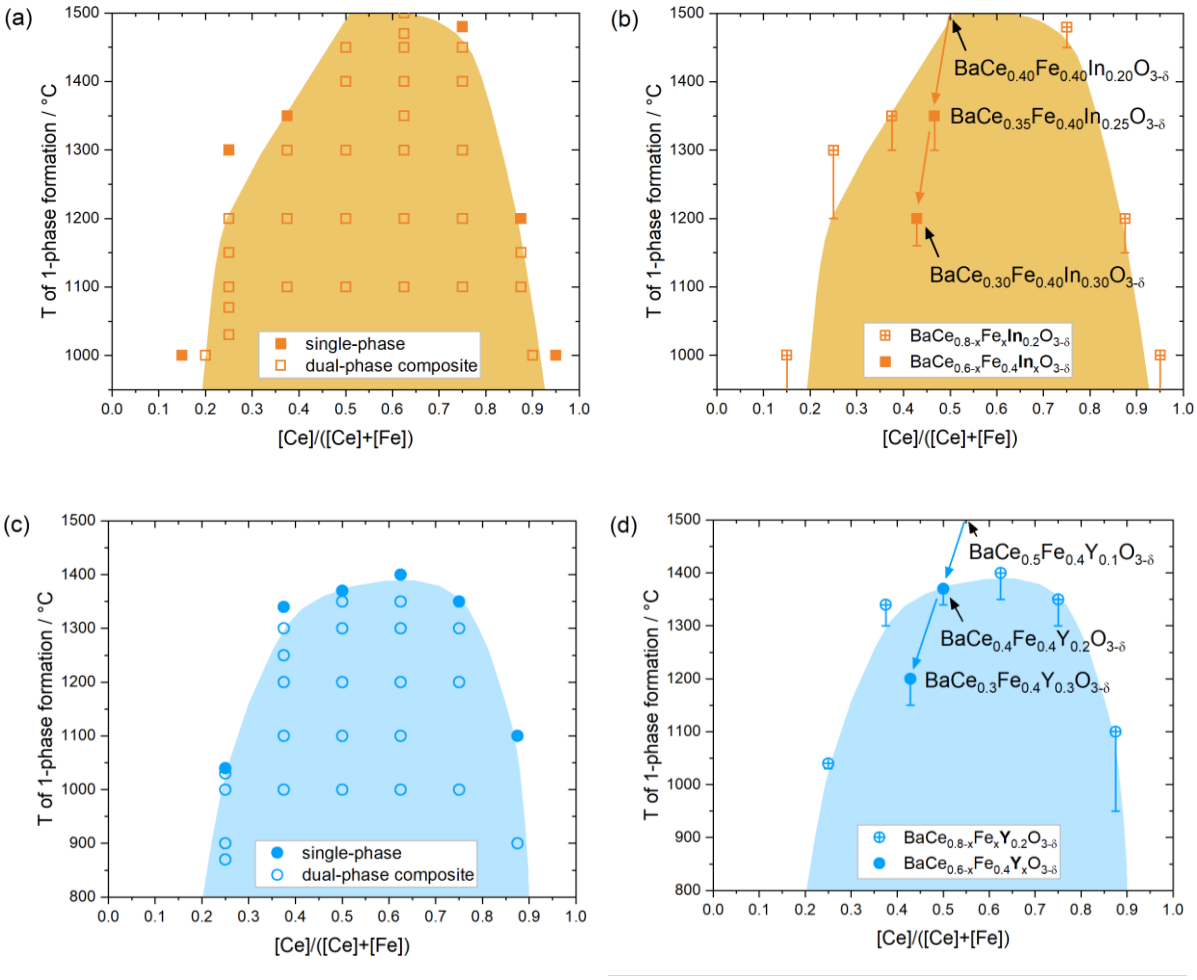

Fig. 4.2 Phase compositions in $BaCe_{0.8-x}Fe_xIn_{0.2}O_{3-\delta}$ and $BaCe_{0.8-x}Fe_xY_{0.2}O_{3-\delta}$ composites and additional composites with higher contents of acceptor substituents as a function of [Ce]/([Ce]+[Fe]) determined by annealing experiments [69] . In **(a)** and **(c)** the closed symbols show the temperatures of single phase formation for the respective composition and the open symbols represent the individual measurement points. The temperatures of single phase formation are shown **(b)** as open symbols for $BaCe_{0.8-x}Fe_xIn_{0.2}O_{3-\delta}$ composites and as closed symbols for $BaCe_{0.6-x}Fe_{0.4}In_xO_{3-\delta}$ composites and **(d)** as open symbols for $BaCe_{0.8-x}Fe_xY_{0.2}O_{3-\delta}$ composites and as closed symbols for $BaCe_{0.6-x}Fe_{0.4}Y_xO_{3-\delta}$ composites. The filled areas outline the miscibility gap.

Measurement points from the annealing experiments conducted on $BaCe_{0.8-x}Fe_xIn_{0.2}O_{3-\delta}$ and $BaCe_{0.8-x}Fe_xY_{0.2}O_{3-\delta}$ are shown in Figures 4.2a and 4.2c, respectively. The open symbols represent temperatures at which a composite is maintained, while the closed symbols indicate the temperatures of single phase formation for the respective ratio of [Ce]/([Ce]+[Fe]). Some compositions of $BaCe_{0.8-x}Fe_xIn_{0.2}O_{3-\delta}$ stay biphasic until temperatures at which partial melting occurs, whereas composition closer to the limit of miscibility become single phase at temperatures between 1000 and 1500 °C. The temperature of single phase formation decreases as the composition of the system approaches the limits. Substitution with Y further narrows the miscibility gap. All compositions become single phase below 1500 °C and compared to In-substituted samples, this occurs at lower temperatures. Additionally, the influence of the degree of substitution on the miscibility gap was investigated. Figures 4.2b and 4.2d show the temperatures of single phase formation of compositions with different amounts of acceptor substituent. For both systems, the temperature at which the material becomes single phase decreases with increasing acceptor concentration and vice versa. Therefore, $BaCe_{0.5}Fe_{0.4}Y_{0.1}O_{3-\delta}$ remains biphasic at temperatures up to 1500 °C, whereas $BaCe_{0.3}Fe_{0.4}In_{0.3}O_{3-\delta}$ becomes single phase already at 1200 °C. The likely cause is the incorporation of the acceptor substituents into the Fe-rich phase. Compared to the unsubstituted system, the larger ions ($r(Y^{3+})$ = 0.900 Å and $r(In^{3+})$ = 0.800 Å – compared to $r(Fe^{3+})$ = 0.645 Å and $r(Fe^{4+})$ = 0.585 Å [86]) expand the lattice of the Fe-rich phase. This potentially allows for the incorporation of more Ce into the Fe-rich phase, leading to the lattice parameters approaching each other (refer to section 4.3. Lattice parameters, Figure 4.6a). The result is increased miscibility and a smaller miscibility gap with increasing acceptor concentration.

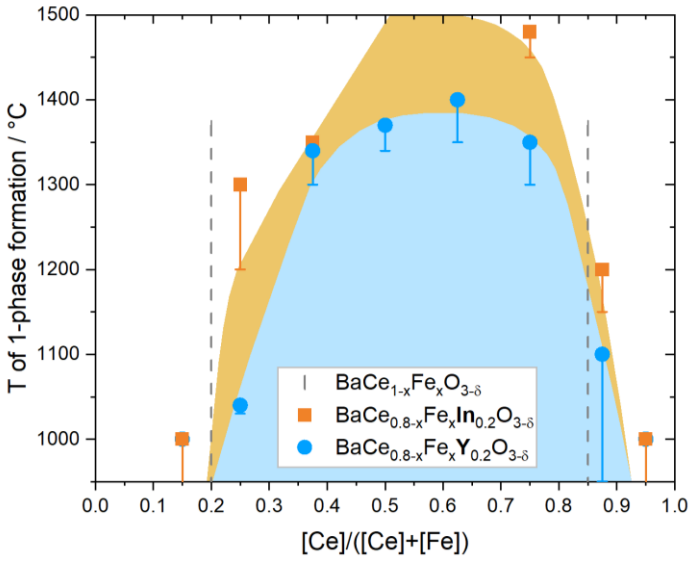

Fig. 4.3 Comparison of the temperatures of single phase formation as a function of [Ce]/([Ce]+[Fe]) for the unsubstituted $BaCe_{0.5}Fe_{0.5}O_{3-\delta}$ system (dashed lines) [28], the Y-substituted system (blue) [87] and the In-substituted system (orange) [69].

Figure 4.3 compares the miscibility limits of unsubstituted $BaCe_{0.5}Fe_{0.5}O_{3-\delta}$ [28] with two acceptor-substituted systems (Acc = In [69] and Y [87]). At temperatures below 1000 °C the range of the miscibility gaps is similar for all three systems. The limit of miscibility for low Ce-concentrations is [Ce]/([Ce]+[Fe]) = 0.2, which forms a composite for substituted and unsubstituted precursors at 1000 °C. For higher amounts of Ce, the miscibility limit of acceptor-substituted precursors shifts towards compositions with a higher Ce-concentration. The unsubstituted composite with the highest amount of Ce is $BaCe_{0.85}Fe_{0.15}O_{3-\delta}$, whereas acceptor-substituted precursors with [Ce]/([Ce]+[Fe]) = 0.875 also form a composite. To examine the behaviour of phase formation, the Goldschmidt tolerance factor [88] was calculated for $BaCe_{0.8-x}Fe_xIn_{0.2}O_{3-\delta}$ (Equation 4.1). This parameter is an indicator for the stability of the crystal lattice of perovskite structures with the general formula ABO_3. It is calculated from the ionic radius of the A-site ion r_A, the B-site ion r_B and oxygen r_O.

$$t = \frac{r_A + r_O}{\sqrt{2}\,(r_B + r_O)}$$

Eq. 4.1 Goldschmidt tolerance factor

Tables 4.1 and 4.2 show the tolerance factors for the precursor phases (assuming the composition stays single phase) and two separate phases (assuming a composite is formed). The separate phases are similar to those found in real composites. One phase is rich in Fe, while the other is rich in Ce. The B-site occupation used for the calculation corresponds to the actual measured local concentrations in analysed samples and is taken from Table 4.6. For the calculation the ionic radii of oxygen, the A-site and the B-site ion with the coordination number VI, XII and VI, respectively, were taken from Shannon et al. [86]. The mean values were calculated using the relative phase amounts (molar fractions) obtained from LeBail fitting of XRD patterns (Tables 4.3 and 4.4). For Fe, an oxidation state of 4+ was assumed. However, depending on the chemical composition of the B-site, at least a part of Fe would be present as Fe^{3+}. As a result, the Goldschmidt tolerance factor is overestimated, whereby the deviation should not exceed 0.025.

Tab. 4.1 Goldschmidt tolerance factors of $BaCe_{0.8-x}Fe_xIn_{0.2}O_{3-\delta}$, calculated for Ce- and Fe-rich phases in the composites, their mean values, as well as the precursor compositions.

	Goldschmidt tolerance factor t			
Precursor	Ce-rich phase	Fe-rich phase	Mean value	Precursor
$BaCe_{0.2}Fe_{0.6}In_{0.2}O_{3-\delta}$	0.9699	1.0156	1.0122	1.0208
$BaCe_{0.3}Fe_{0.5}In_{0.2}O_{3-\delta}$	0.9673	1.0247	1.0130	1.0070
$BaCe_{0.4}Fe_{0.4}In_{0.2}O_{3-\delta}$	0.9509	1.0033	0.9827	0.9936
$BaCe_{0.5}Fe_{0.3}In_{0.2}O_{3-\delta}$	0.9711	1.0202	0.9921	0.9806
$BaCe_{0.6}Fe_{0.2}In_{0.2}O_{3-\delta}$	0.9480	0.9906	0.9639	0.9679

Tab. 4.2 Goldschmidt tolerance factors of $BaCe_{0.6-x}Fe_{0.4}In_xO_{3-\delta}$, calculated for Ce- and Fe-rich phases in the composites, their mean values, as well as the precursor compositions.

	Goldschmidt tolerance factor t			
Precursor	Ce-rich phase	Fe-rich phase	Mean value	Precursor
$BaCe_{0.3}Fe_{0.4}In_{0.3}O_{3-\delta}$	1.0019	1.0050	1.0047	0.9969
$BaCe_{0.35}Fe_{0.40}In_{0.25}O_{3-\delta}$	-	-	-	0.9953
$BaCe_{0.4}Fe_{0.4}In_{0.2}O_{3-\delta}$	0.9509	1.0033	0.9827	0.9936

Compounds with a cubic crystal structure or perovskite structures with small distortions typically have a tolerance factor ranging from 0.8 to 1. In Tables 4.1 and 4.2, the precursor phases marked in green do not become single phase even at high temperatures. For those marked in blue, the temperature of single phase formation lies below the melting temperature. No correlations were found between the Goldschmidt tolerance factor and the behaviour of single phase formation. This suggests that additional parameters have to be taken into account. The Goldschmidt tolerance factors of $BaCe_{0.8-x}Fe_xY_{0.2}O_{3-\delta}$ and $BaCe_{0.6-x}Fe_{0.4}Y_xO_{3-\delta}$ are summarised in Tables A20 and A21 in the appendix. With the results from XRD measurements quantitative phase analyses were carried out for all samples investigated. The obtained relative phase amounts (weight fractions) are summarised in Tables 4.3 and 4.4 for In-containing composites. For the whole pattern profile fitting by the LeBail method, the actual B-site occupancies of the Ce- and Fe-rich phases from Table 4.6 were used if available. The amount of the species determines the increase or decrease of the relative amount of the respective phases. Compositions with a higher amount of Ce have a higher weight fraction of the Ce-rich phase, and vice versa. This is similar to the intensities of the peaks in the diffractogram, which are proportional to the weight fraction.

Tab. 4.3 Weight fractions, molar mass and molar fractions of the Ce-rich phases of self-generated composites. The data is obtained from quantitative phase analyses of XRD patterns measured at room temperature on crushed sintered pellets.

	Ce-rich phase		
Precursor	Amount / wt.-%	M / g mol^{-1}	Amount / mol.-%
$BaCe_{0.2}Fe_{0.6}In_{0.2}O_{3-\delta}$	8.3	304.8	7.5
$BaCe_{0.3}Fe_{0.5}In_{0.2}O_{3-\delta}$	22.6	304.2	20.4
$BaCe_{0.4}Fe_{0.4}In_{0.2}O_{3-\delta}$	41.9	313.3	39.3
$BaCe_{0.5}Fe_{0.3}In_{0.2}O_{3-\delta}$	59.8	301.6	57.2
$BaCe_{0.6}Fe_{0.2}In_{0.2}O_{3-\delta}$	65.0	317.6	62.7
$BaCe_{0.3}Fe_{0.4}In_{0.3}O_{3-\delta}$	10.9	309.1	10.0
$BaCe_{0.35}Fe_{0.40}In_{0.25}O_{3-\delta}$	35.8	-	-

Tab. 4.4 Weight fractions, molar mass and molar fractions of the Fe-rich phases of self-generated composites. The data is obtained from quantitative phase analyses of XRD patterns measured at room temperature on crushed sintered pellets.

	Fe-rich phase		
Precursor	Amount / wt.-%	M / g mol^{-1}	Amount / mol.-%
$BaCe_{0.2}Fe_{0.6}In_{0.2}O_{3-\delta}$	91.7	273.1	92.5
$BaCe_{0.3}Fe_{0.5}In_{0.2}O_{3-\delta}$	77.4	267.7	79.6
$BaCe_{0.4}Fe_{0.4}In_{0.2}O_{3-\delta}$	58.1	280.4	60.7
$BaCe_{0.5}Fe_{0.3}In_{0.2}O_{3-\delta}$	40.2	271.0	42.8
$BaCe_{0.6}Fe_{0.2}In_{0.2}O_{3-\delta}$	35.0	288.1	37.3
$BaCe_{0.3}Fe_{0.4}In_{0.3}O_{3-\delta}$	89.1	279.4	90.0
$BaCe_{0.35}Fe_{0.40}In_{0.25}O_{3-\delta}$	64.2	-	-

The molar mass of the individual phases, which was used to estimate the molar fractions, was also calculated from the B-site occupancies. The results for this are also shown in Tables 4.3 and 4.4. Data on mass fractions, molar masses and molar fractions of composites with different acceptor substituents are given in Tables A22 – A25 in the appendix.

4.2. Cation composition

Table 4.5 shows the experimentally determined cation stoichiometry of selected composites compacted by SPS. The results of ICP-OES indicate a good agreement with the nominal precursor compositions, suggesting that no significant loss of specific elements occurred during processing. The analysis was also performed with Y-containing samples, which led to the same conclusion that there is a good match with the nominal composition (Tables A26 and A27).

Tab. 4.5 Nominal composition of the precursors compared to the cation composition of SPS sintered composites determined by ICP-OES [69].

Nominal composition	Compositions from ICP-OES
$BaCe_{0.2}Fe_{0.6}In_{0.2}O_{3-\delta}$	$BaCe_{0.197}Fe_{0.595}In_{0.196}O_{3-\delta}$
$BaCe_{0.4}Fe_{0.4}In_{0.2}O_{3-\delta}$	$BaCe_{0.399}Fe_{0.399}In_{0.200}O_{3-\delta}$
$BaCe_{0.5}Fe_{0.3}In_{0.2}O_{3-\delta}$	$BaCe_{0.504}Fe_{0.306}In_{0.200}O_{3-\delta}$
$BaCe_{0.6}Fe_{0.2}In_{0.2}O_{3-\delta}$	$BaCe_{0.592}Fe_{0.196}In_{0.196}O_{3-\delta}$
$BaCe_{0.3}Fe_{0.4}In_{0.3}O_{3-\delta}$	$BaCe_{0.294}Fe_{0.397}In_{0.295}O_{3-\delta}$

4.3. Lattice parameters

The lattice parameters of composites and single phases were obtained from profile fitting by LeBail method. Particles of crushed SPS sintered pellets were used for the measurements. The lattice parameters of the cubic Fe-rich phase are shown directly as obtained from profile fitting, while those of the trigonal Ce-rich phase are converted into pseudo-cubic lattice parameters with the following equation to enable comparison.

$$a_{pseudo} = \sqrt[3]{\frac{\text{cell volume}}{Z}}$$

Eq. 4.2 Pseudo-cubic lattice parameter

The number of formula units is Z = 6 for the space group $R\bar{3}c$ of acceptor-substituted compositions and Z = 4 for the space group *Pnma* of $BaCeO_3$. The results for the lattice parameters, as shown in the following figures, as well as additional data for artificial composites and single phases are summarised in Tables A28 – A36 in the appendix. Figure 4.4 shows the lattice parameters of self-generated $BaCe_{0.8-x}Fe_xIn_{0.2}O_{3-\delta}$ and $BaCe_{0.8-x}Fe_xY_{0.2}O_{3-\delta}$ composites as a function of Ce and Fe content. The pseudo-cubic lattice parameters of the Ce-rich phase in Figure 4.4a decrease slightly with an increasing amount of Ce in the precursor.

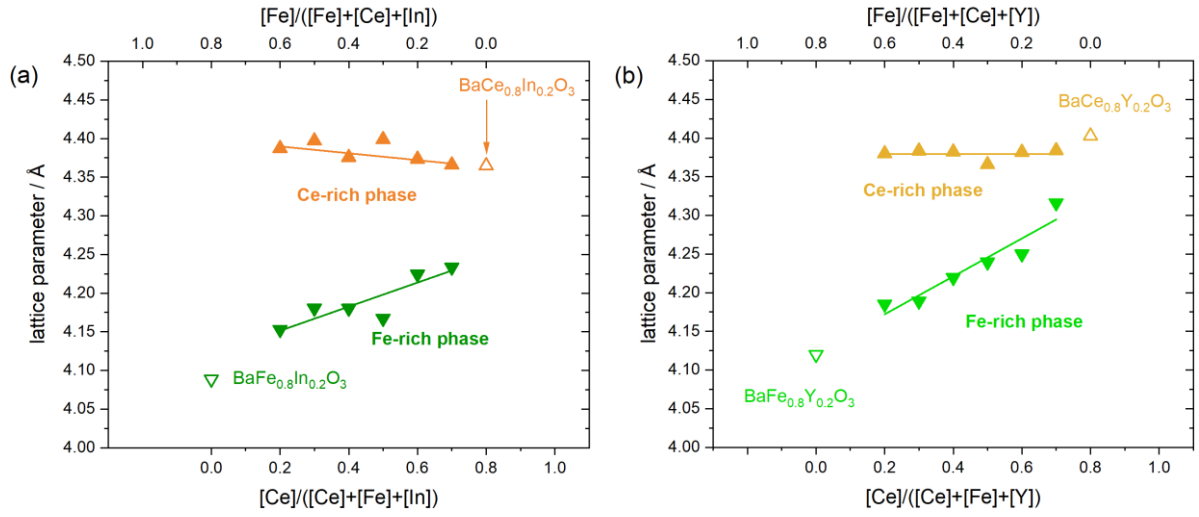

Fig. 4.4 Pseudo-cubic lattice parameters of the Ce-rich trigonal phase and lattice parameters of the Fe-rich cubic phase as a function of Ce and Fe content in the precursor of **(a)** $BaCe_{0.8-x}Fe_xIn_{0.2}O_{3-\delta}$ [69] and **(b)** $BaCe_{0.8-x}Fe_xY_{0.2}O_{3-\delta}$ [87] composites. The lattice parameter of acceptor-free $BaFeO_3$ is 4.02 Å [89] and $BaCeO_3$ has a pseudo-cubic lattice parameter of 4.40 Å [90]. The lines are a guide to the eye.

However, this contradicts the expected trend as the ionic radius of iron ($r(Fe^{3+})$ = 0.645 Å and $r(Fe^{4+})$ = 0.585 Å [86]) is smaller than that of cerium ($r(Ce^{4+})$ = 0.870 Å) and it can be observed in Figure 4.9 that with increasing Ce content, the amount of Ce in the Ce-rich phase increases and that of Fe decreases. The lattice parameters of the Fe-rich phase in $BaCe_{0.8-x}Fe_xIn_{0.2}O_{3-\delta}$ increase linearly with increasing Ce content, following Vegard's rule. As the Ce content in the Fe-rich phase increases (as shown in Figure 4.9), the larger Ce ions widen the lattice of the Fe-rich phase. The direction and strength of the change in the lattice parameters corresponds to those of the peak shift in the diffractograms (Figure 4.1b). The additional compositions $BaCe_{0.8}In_{0.2}O_{3-\delta}$ and $BaFe_{0.8}In_{0.2}O_3$ align with the observed trends. Figure 4.4b shows the lattice parameters of the $BaCe_{0.8-x}Fe_xY_{0.2}O_{3-\delta}$ system. The linear increase of the lattice parameters of the Fe-rich phase with increasing Ce content is similar to the In-substituted system and agrees well with $BaFe_{0.8}Y_{0.2}O_3$ [22]. In the Ce-rich phase, the pseudo-cubic lattice parameters remain constant, and the lattice parameter of $BaCe_{0.8}Y_{0.2}O_{3-\delta}$ [90] is slightly larger. The acceptor-free $BaFeO_3$ corresponds well to the trend in both systems. However, the pseudo-cubic lattice parameter of $BaCeO_3$ (*Pnma*, SG#62) aligns with the trend in the Y-system but is larger than $BaCe_{0.8-x}Fe_xIn_{0.2}O_{3-\delta}$.

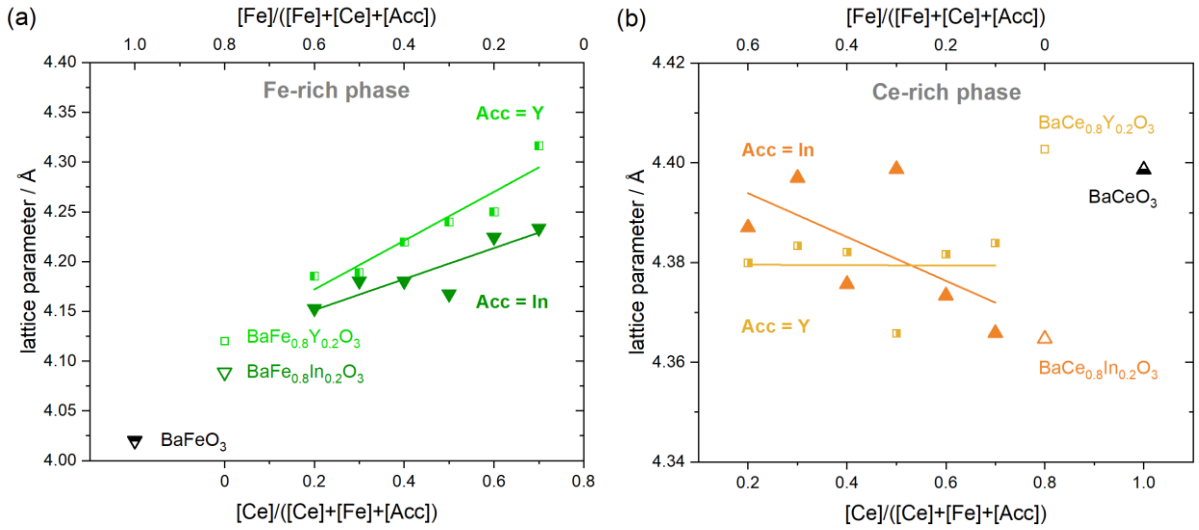

Fig. 4.5 Comparison of **(a)** the lattice parameters of the Fe-rich phase and **(b)** the pseudo-cubic lattice parameters of the Ce-rich phase of $BaCe_{0.8-x}Fe_xIn_{0.2}O_{3-\delta}$ [69] and $BaCe_{0.8-x}Fe_xY_{0.2}O_{3-\delta}$ [87] composites. The lines are a guide to the eye.

Figure 4.5 compares the lattice parameters of In- and Y-substituted composites. The pseudo-cubic lattice parameters of the Ce-rich phase, as shown in Figure 4.5b, have different tendencies, but are scattered. However, there are clear trends for the Fe-rich phase in Figure 4.5a. The lattice parameters of Fe-rich phases substituted with Y are larger than those substituted with indium. Presumably, the reason is the larger ionic radius of yttrium ($r(Y^{3+})$ = 0.900 Å [86]) compared to indium ($r(In^{3+})$ = 0.800 Å [86]), and the average amount of acceptor substituent in the Fe-rich phase is higher for Y than for In, resulting in a stronger distortion of the lattice. In addition, the lattice parameters of $BaCe_{0.8-x}Fe_xY_{0.2}O_{3-\delta}$

increase stronger with increasing Ce content than those of $BaCe_{0.8-x}Fe_xIn_{0.2}O_{3-\delta}$. The reason could be the Ce content in the Fe-rich phase, which increases more strongly with an increasing Ce-concentration in the Y-substituted system than in the In-substituted system. Figure 4.6a shows the lattice parameters of the Fe- and Ce-rich phases in $BaCe_{0.6-x}Fe_{0.4}Acc_xO_{3-\delta}$ composites as a function of acceptor concentration. Especially in the Fe-rich phase, the lattice parameters increase with an increase in the amount of acceptor substituents. This may be related to the narrowing of the miscibility gap with increasing acceptor content. The further expansion of the lattice of the Fe-rich phase provides more space for Ce, which could result in increased mutual solubility and miscibility, leading to a reduced miscibility gap with an increased acceptor concentration. It is evident from Figure 4.6b that the lattice parameters of the Ce- and Fe-rich phase of $BaCe_{0.4}Fe_{0.4}Acc_{0.2}O_{3-\delta}$ (Acc = Sc, In, Yb, Y, Gd, Sm) composites increase with an increasing ionic radius of the acceptor substituent. This effect may cause the stronger narrowing of the miscibility gap in the Y-substituted system. The lattice parameter of the Fe-rich phase in the Y-substituted system is larger due to the higher proportion (Figure 4.11) and the larger ionic radius of Y.

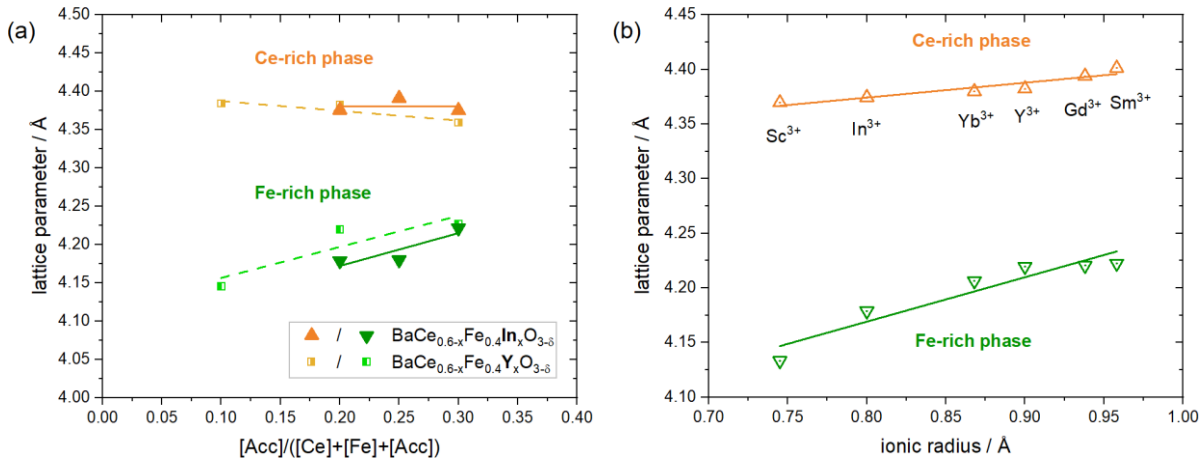

Fig. 4.6 Lattice parameters of the Fe- and Ce-rich phases in **(a)** $BaCe_{0.6-x}Fe_{0.4}Acc_xO_{3-\delta}$ composites as a function of acceptor concentration and **(b)** $BaCe_{0.4}Fe_{0.4}Acc_{0.2}O_{3-\delta}$ composites as a function of ionic radius of the acceptor substituent taken from Shannon et al. [86]. The lines are a guide to the eye.

Annealing experiments showed that $BaCe_{0.4}Fe_{0.4}Acc_{0.2}O_{3-\delta}$ composites with Acc = Sc, In, Yb stay two-phase up to the melting point, while composites with Acc = Y, Gd, Sm become single phase around 1400 °C. Figure 4.7 shows the results of the annealing experiments performed with In-substituted self-generated composites. As the annealing temperature increases, the lattice parameters of the two phases approach each other. The compositions shown in Figures 4.7a and 4.7b form trigonal Ce-rich single phases. Conversely, those in Figures 4.7c and 4.7d remain two-phase until they melt, while the composites in Figures 4.7e and 4.7f form cubic Fe-rich single phases.

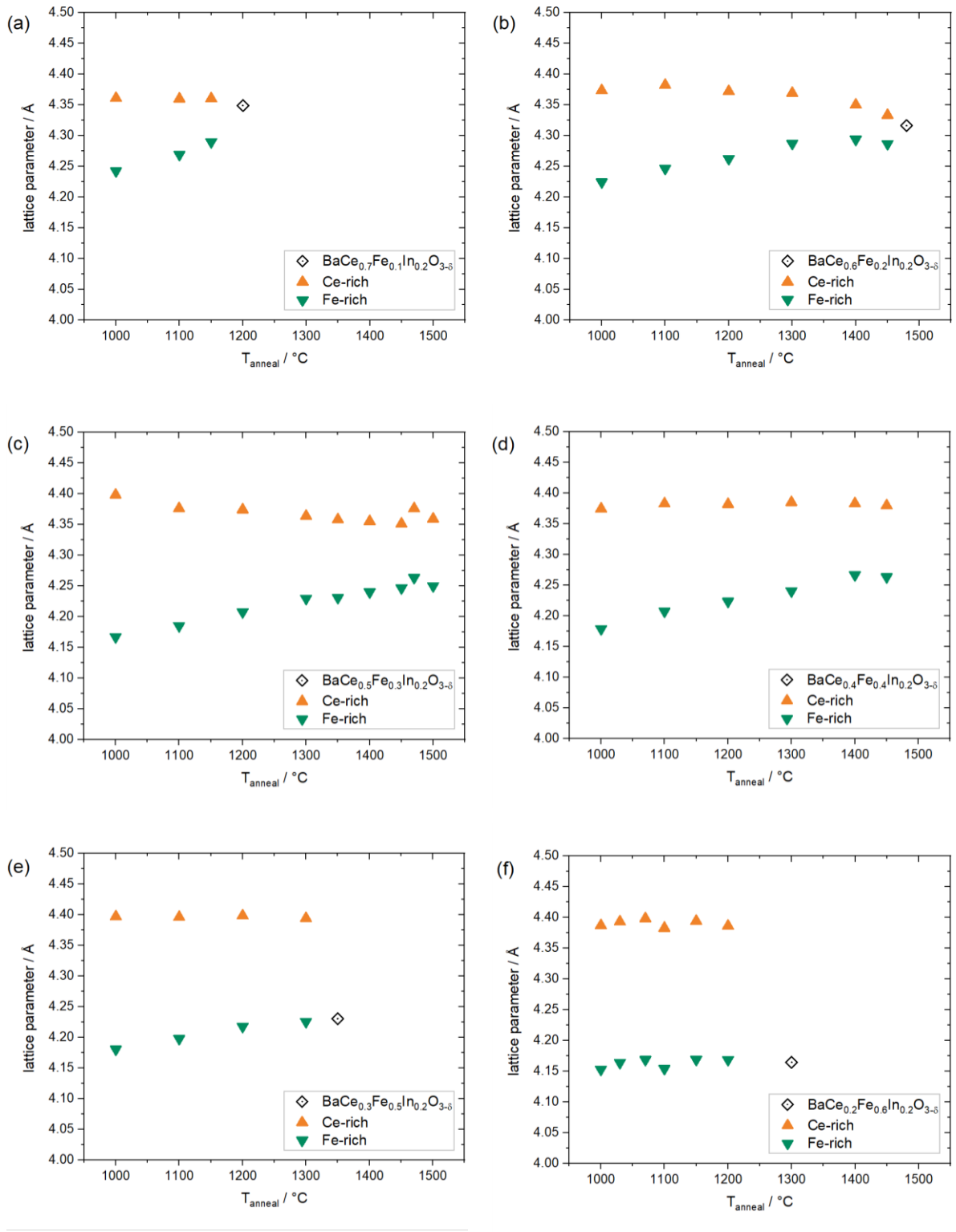

Fig. 4.7 (a) – (f) Lattice parameters of the cubic Fe-rich phase (green) and pseudo-cubic lattice parameters of the trigonal Ce-rich phase (orange) of $BaCe_{0.8-x}Fe_xIn_{0.2}O_{3-\delta}$ composites as a function of annealing temperature. The open symbols represent the temperature of single phase formation and the lattice parameter of the resulting Ce- or Fe-rich single phase [69].

The results of the annealing experiments with In-containing composites with other acceptor concentrations, as well as different compositions of Y-substituted composites and $BaCe_{0.4}Fe_{0.4}Acc_{0.2}O_{3-\delta}$ composites (Acc = Gd, Sc, Sm, Yb) are summarised in Figures A3 – A6 in the appendix.

4.4. Microstructure and elemental distribution

4.4.1. Composites

The fundamental concept of acceptor substitution aims to increase the concentration of oxygen vacancies (refer to section 2.3. Acceptor substitution, Equation 2.5), which can incorporate water and thus increase the proton uptake capacity. However, not only the presence of acceptor substituents is relevant, but also the distribution of substituents between the two phases. The Ce-rich phase is the phase with the higher degree of hydration, which is why acceptor substitution has a greater positive effect on the proton uptake capacity in this phase compared to the Fe-rich phase (refer to section 4.6. Proton uptake capacity, Figure 4.24). Therefore, the incorporation of substituents on the B-site of the Ce-rich phase is particularly desirable. However, results of transmission electron microscopy have shown that the acceptor substituents are not evenly distributed between the two phases. STEM-HAADF images and EDX elemental maps of selected cations (Ce, Fe, In) of different self-generated $BaCe_{0.8-x}Fe_xIn_{0.2}O_{3-\delta}$ composites sintered by SPS are shown in Figure 4.8. Apart from some holes caused by the sample processing, the materials are dense and have a small grain size in the sub-micrometre range. Sintering using SPS results in reduced grain growth, leading to smaller grain sizes due to the short time at moderate temperatures involved in this process. The variation in grain size among samples of different compositions arises not only from differences in composition, but also from the adapted conditions during sintering of the respective sample. The HAADF images and elemental maps in Figure 4.8 show two distinct phases. One is rich in Fe and the other is rich in Ce, as indicated by their respective signals. The elemental maps of indium show a more pronounced signal in areas of the Fe-rich phase. This suggests that indium is preferentially incorporated into the Fe-rich phase in all samples, which is confirmed by the local cation stoichiometry from STEM-EDX single spectra on individual grains (Table 4.6 and Figure 4.11). Up to 60 single spectra were recorded per phase. For certain samples, more than one composition for the Ce- or Fe-rich phase was found. Therefore, data points with similar compositions were categorised into groups and an average value was calculated for each group. As a result, some samples have multiple compositions, which are summarised in Table A41. For further evaluation, averaged local cation compositions were calculated. Table 4.6 shows the mean values of the local B-site composition in the two phases of $BaCe_{1-(x+y)}Fe_xIn_yO_{3-\delta}$ composites calculated from the results summarised in Table A41.

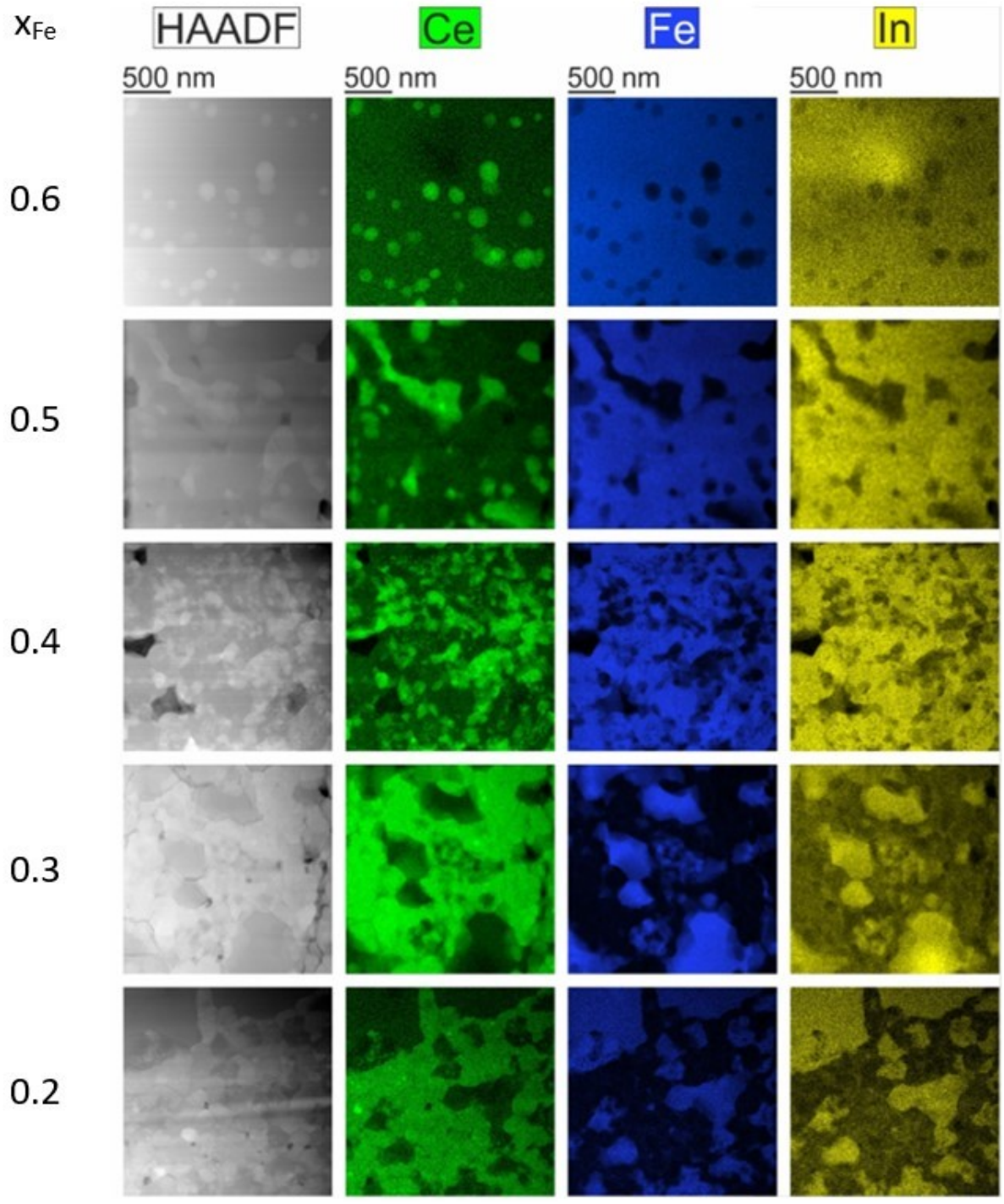

Fig. 4.8 STEM-HAADF images and EDX elemental maps for selected cations of SPS sintered self-generated $BaCe_{0.8-x}Fe_xIn_{0.2}O_{3-\delta}$ composites. The EDX point spectra used for quantification (see results in Table A41) are obtained from this areas [69].

Tab. 4.6 Averaged local cation composition (with standard deviation) of the B-site of Ce- and Fe-rich phases of self-generated SPS sintered $BaCe_{0.8-x}Fe_xIn_{0.2}O_{3-\delta}$ composites and $BaCe_{0.3}Fe_{0.4}In_{0.3}O_{3-\delta}$ calculated from Table A41 [69].

Precursor	Ce-rich phase	Fe-rich phase
$BaCe_{0.2}Fe_{0.6}In_{0.2}O_{3-\delta}$	$BaCe_{0.68}Fe_{0.21}In_{0.10}O_{3-\delta}$	$BaCe_{0.26}Fe_{0.57}In_{0.17}O_{3-\delta}$
$BaCe_{0.3}Fe_{0.5}In_{0.2}O_{3-\delta}$	$BaCe_{0.68}Fe_{0.22}In_{0.10}O_{3-\delta}$	$BaCe_{0.21}Fe_{0.64}In_{0.15}O_{3-\delta}$
$BaCe_{0.4}Fe_{0.4}In_{0.2}O_{3-\delta}$	$BaCe_{0.77}Fe_{0.11}In_{0.13}O_{3-\delta}$	$BaCe_{0.29}Fe_{0.46}In_{0.25}O_{3-\delta}$
$BaCe_{0.5}Fe_{0.3}In_{0.2}O_{3-\delta}$	$BaCe_{0.68}Fe_{0.27}In_{0.06}O_{3-\delta}$	$BaCe_{0.28}Fe_{0.62}In_{0.11}O_{3-\delta}$
$BaCe_{0.6}Fe_{0.2}In_{0.2}O_{3-\delta}$	$BaCe_{0.83}Fe_{0.06}In_{0.11}O_{3-\delta}$	$BaCe_{0.34}Fe_{0.35}In_{0.31}O_{3-\delta}$
$BaCe_{0.3}Fe_{0.4}In_{0.3}O_{3-\delta}$	$BaCe_{0.73}Fe_{0.16}In_{0.10}O_{3-\delta}$	$BaCe_{0.30}Fe_{0.48}In_{0.22}O_{3-\delta}$

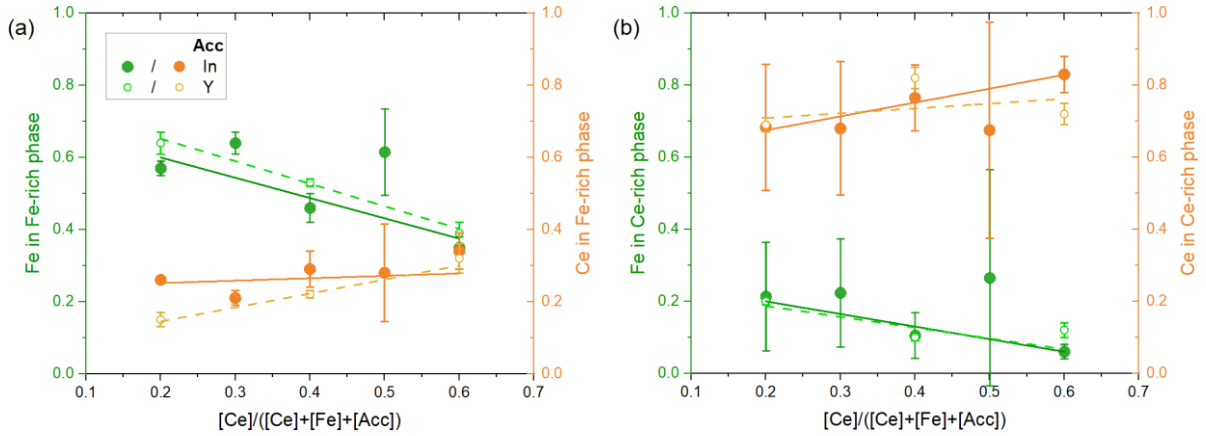

Fig. 4.9 Local concentrations of Ce and Fe in **(a)** the Fe-rich phase and **(b)** the Ce-rich phase of $BaCe_{0.8-x}Fe_xIn_{0.2}O_{3-\delta}$ and $BaCe_{0.8-x}Fe_xY_{0.2}O_{3-\delta}$ composites as a function of Ce content [69, 87]. The lines are a guide to the eye.

Figure 4.9 illustrates the data from Table 4.6 and shows the local concentrations of Ce and Fe in the two phases of In- and Y-substituted self-generated composites as a function of Ce content. Not only the relative amounts of the phases change with the Ce:Fe ratio in the precursor (Tables 4.3 and 4.4) but also the composition of the phases. As the amount of Ce in the precursor increases, the relative amount of Ce increases in the Ce- and Fe-rich phase, while the relative amount of Fe decreases in both phases. The variation in the Fe-rich phase of In-substituted composites could be explained by the distribution of indium between the two phases. With increasing amount of Ce in the precursor, the indium enrichment in the Fe-rich phase becomes stronger (Figure 4.11a). This results in a more distorted lattice of the Fe-rich phase due to the larger ionic radius of indium ($r(In^{3+})$ = 0.800 Å, $r(Fe^{3+})$ = 0.645 Å and $r(Fe^{4+})$ = 0.585 Å [86]). The increased space allows more Ce to be incorporated, leading

to a decrease in the relative amount of Fe. However, the enrichment of Y in the Fe-rich phase decreases as the amount of Ce in the precursor increases, indicating a subordinate role of the distribution of the acceptor substituent in this process. To develop a strategy for influencing the distribution of the acceptor substituents, two basic ideas were considered. The initial approach aimed to match the ionic radii of the acceptor substituents to the preferred phase by using a trivalent ion with a similar radius to Ce. The concept was further developed by considering the basicity of the oxides. This approach is based on the idea of substituting the B-site of the more or less basic $BaCeO_3$ or $BaFeO_3$, respectively, in the sense of an acid-base reaction. Indium, which is comparatively less basic and has a similar ionic radius to Ce (Figure 4.10), should have a higher affinity for the more basic Ce-rich phase. However, no clear correlations could be recognised between the ionic radius, the basicity and acceptor distribution. This suggests that the affinity for acceptor substituent incorporation into a certain phase does not only depend on the ionic radius and/or the basicity, but rather on a combination of different factors. The acceptor and defect distribution are being investigated in more detail by R. Merkle et al. using DFT calculations [91].

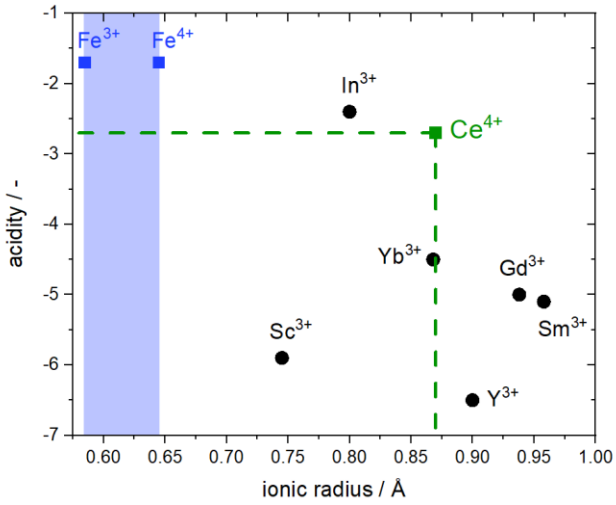

Fig. 4.10 Comparison of investigated acceptor substituents and the B-site ions Ce and Fe with regard to the acidity according to the Smith scale [92] and the ionic radii [86]. The acidity of Sc^{3+} (not given in [92]) is estimated from the acidities of Ti^{4+}, Zr^{4+} and Y^{3+} [69].

Figure 4.11 shows the distribution of different acceptor substituents between the Ce- and Fe-rich phase. The ratios (Acc in Fe-rich phase:Acc in Ce-rich phase) are calculated with the data from Tables 4.6 and A43 – A45. The green line represents an equal distribution of the acceptor substituent between the Ce- and Fe-rich phases. All data points above the line indicate an enrichment in the Fe-rich phase. The distribution of In, Y and Sc as a function of Ce content in the precursor are shown in Figure 4.11a. It can be observed that the unfavourable enrichment of indium in the Fe-rich phase increases with

increasing Ce content. In contrast, Y shows an opposite tendency and is less strongly enriched with increasing Ce content. Figure 4.11b gives an overview of the ratios of the local acceptor concentrations of $BaCe_{0.4}Fe_{0.4}Acc_{0.2}O_{3-\delta}$ composites (Acc = Y, Sc, In). The data indicates that Sc exhibits the strongest enrichment in the Fe-rich phase, while indium exhibits the lowest. Apart from $BaCe_{0.6}Fe_{0.2}Acc_{0.2}O_{3-\delta}$, the lowest enrichment in the Fe-rich phase is also observed for indium in other compositions (Figure 4.11a). As indium is the least basic ion of the three substituents, these results appear to support the considerations that the basicity of the substituent ion influences its distribution. However, indium is still enriched in the Fe-rich phase, which indicates that the basicity is not the only factor responsible for the distribution between the two phases.

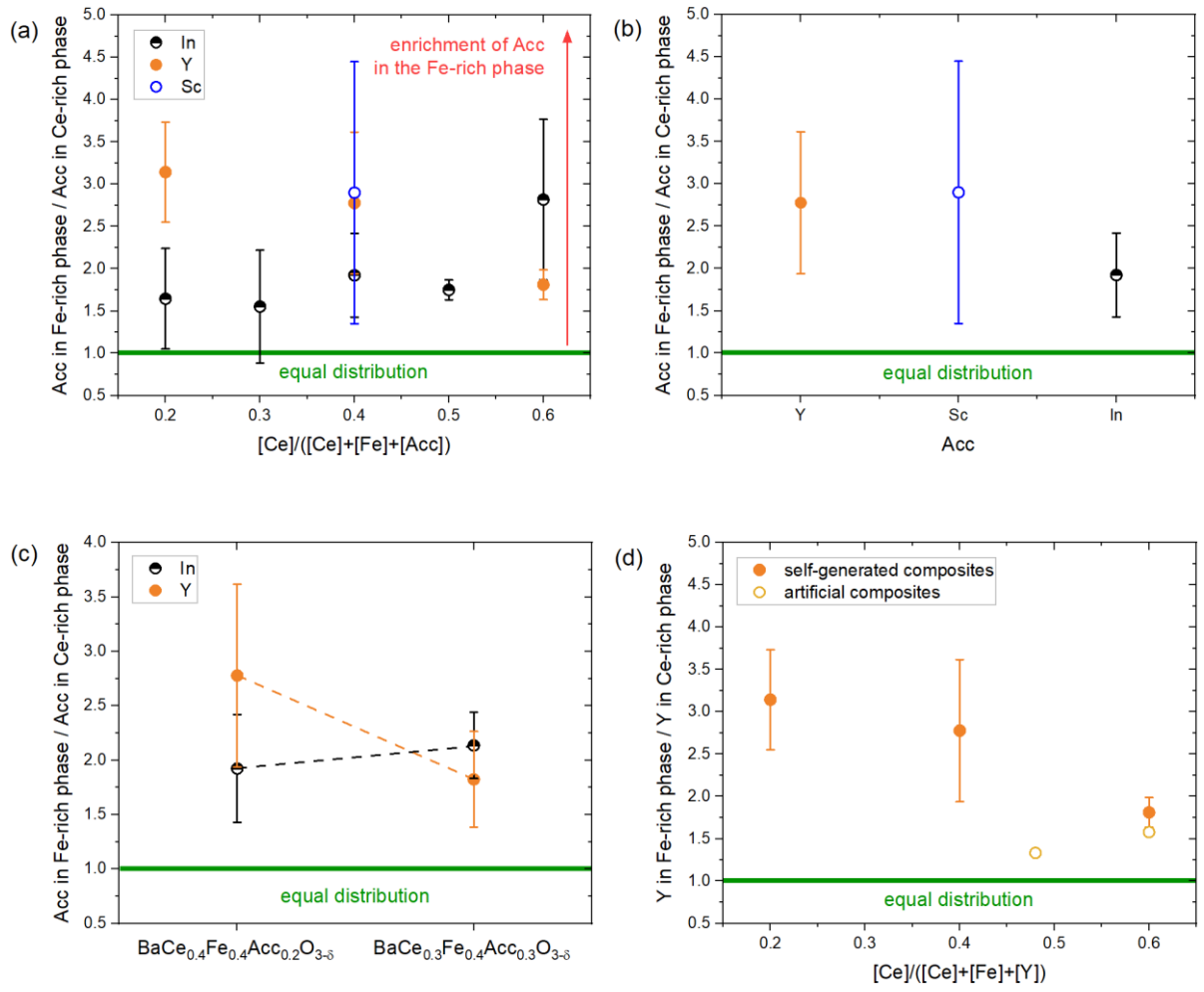

Fig. 4.11 Ratios of the local acceptor concentrations (Fe-rich phase:Ce-rich phase) in **(a)** different $BaCe_{0.8-x}Fe_xAcc_{0.2}O_{3-\delta}$ composites (Acc = In, Y [87], Sc) as a function of Ce content, **(b)** differently substituted composites with the same precursor composition ($BaCe_{0.4}Fe_{0.4}Acc_{0.2}O_{3-\delta}$) and **(c)** Y- and In-substituted composites with two different precursor compositions [69]. The lines are a guide to the eye. **(d)** Ratios of the local acceptor concentrations (Fe-rich phase:Ce-rich phase) in self-generated $BaCe_{0.8-x}Fe_xY_{0.2}O_{3-\delta}$ composites compared to artificial composites.

The distribution of acceptor substituents was also investigated with additional compositions containing a higher concentration of acceptor substituents. Figure 4.11c shows the distribution of indium and Y in $BaCe_{0.4}Fe_{0.4}Acc_{0.2}O_{3-\delta}$ and $BaCe_{0.3}Fe_{0.4}Acc_{0.3}O_{3-\delta}$. In this case, the trends for indium and Y also differ. While the enrichment of indium increases with an increased acceptor substituent concentration in the precursor, that of Y is lower and even less pronounced than that of the same composition with indium. Nevertheless, this behaviour should be verified by further samples with varying degrees of substitution. In order to influence the distribution of the acceptor between the Ce- and Fe-rich phase, artificial composites (refer to section 3.3.4. Artificial composites) were also investigated. The distribution of Y as a function of Ce content for self-generated and artificial composites is shown in Figure 4.11d. While the enrichment of Y in the Fe-rich phase is less pronounced in artificial composites, which represents an improvement in the acceptor distribution compared to self-generated composites, there is still a clear enrichment of the acceptor in the Fe-rich phase. Upon initial observation, the HAADF image and elemental maps of Ce and Fe in Figure 4.12 appear to be unremarkable. The sample is dense and consists of two distinct phases, one rich in Ce and the other rich in Fe. Examining the Y map reveals two key observations. As described in section 3.3.4. Artificial composites, the Ce- and Fe-rich phase are prepared separately and then mixed to obtain a composite. Both initial phases are substituted with the same amount of Y, so it can be expected that the phases in the sintered composite will also have the same amount of Y. However, this is not the case (Figure 4.12 and Table A45). Furthermore, upon closer examination of the Ce-rich grain marked in red, it can be observed that the grain has a lighter edge in the Ce map and a darker edge in the Y map. This indicates that the outside of the grain is enriched in Ce and depleted in Y.

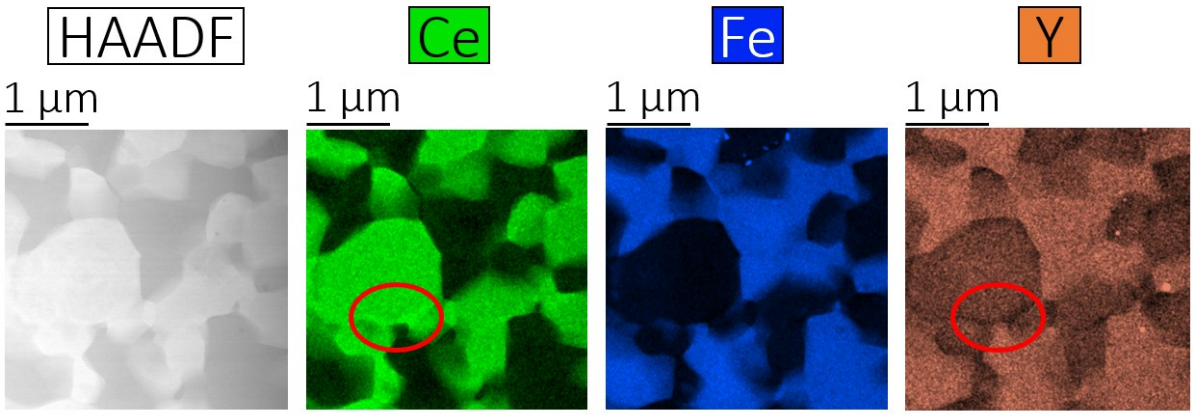

Fig. 4.12 STEM-HAADF image and EDX elemental maps for selected cations of a SPS sintered artificial BcBf6535 composite. The EDX point spectra used for quantification (see results in Table A45) are obtained from this area.

This is confirmed by a line profile through the Ce-rich grain in Figure 4.13. In particular, at the transition from the Ce-rich grain to the Fe-rich grain on the left side, there is a slight increase in the concentration of Ce, while a decrease is observed in the concentration of Y before entering the Fe-rich grain. It appears that cation interdiffusion occurs during the processing. Yttrium diffuses from the Ce-rich phase to the Fe-rich phase, and in return, Ce diffuses from the Fe-rich phase to the Ce-rich phase. Due to the pre-treatment prior to sintering, the interdiffusion could occur during one or more of the following steps: during the mixing process in the ball mill due to the mechanically introduced energy, during annealing for 6 hours at 700 °C, or during sintering. However, as an adapted preparation method did not result in an increased proton uptake capacity, this question was not pursued further.

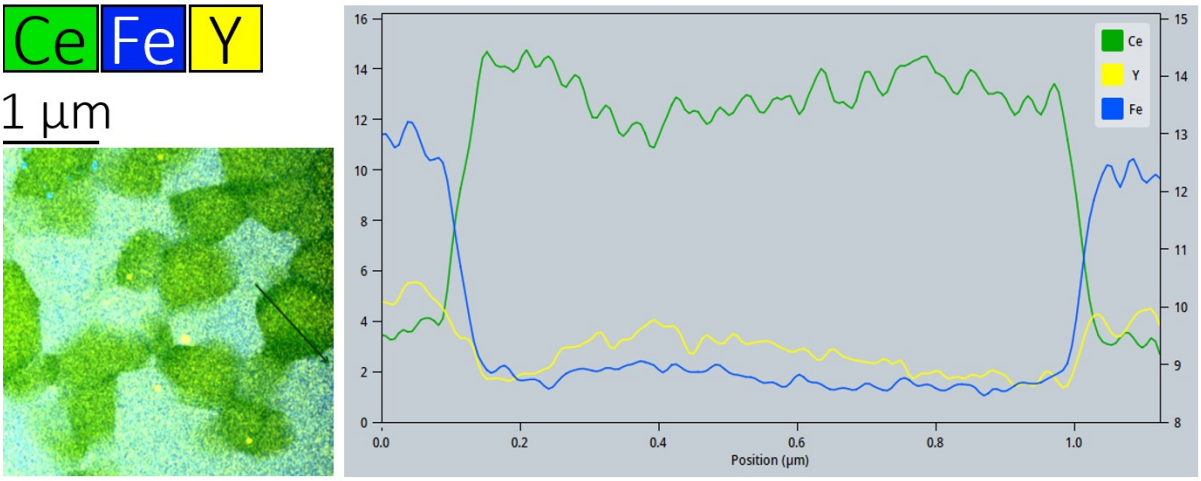

Fig. 4.13 EDX elemental map for selected cations (Ce, Fe, Y) and line profile of a Ce-rich grain in a SPS sintered artificial BcBf6535 composite.

4.4.2. Single phase materials

Two selected single phase materials were also analysed by STEM. Figure 4.14 shows HAADF images and elemental maps of the Ce-rich single phase $BaCe_{0.76}Fe_{0.04}Y_{0.20}O_{3-\delta}$ and the Fe-rich single phase $BaCe_{0.04}Fe_{0.76}Y_{0.20}O_{3-\delta}$. The HAADF image of $BaCe_{0.76}Fe_{0.04}Y_{0.20}O_{3-\delta}$ (top) shows a dense sintered sample with four adjacent grains. An examination of the elemental maps reveals a homogeneous distribution of the elements, as the individual grains cannot be distinguished from one another. The sintered sample of $BaCe_{0.04}Fe_{0.76}Y_{0.20}O_{3-\delta}$ (bottom) is generally also dense, although it has some breakouts from processing. Apart from the presence of minor Ce precipitations inside the breakouts, a homogeneous distribution of elements is observed across the grains.

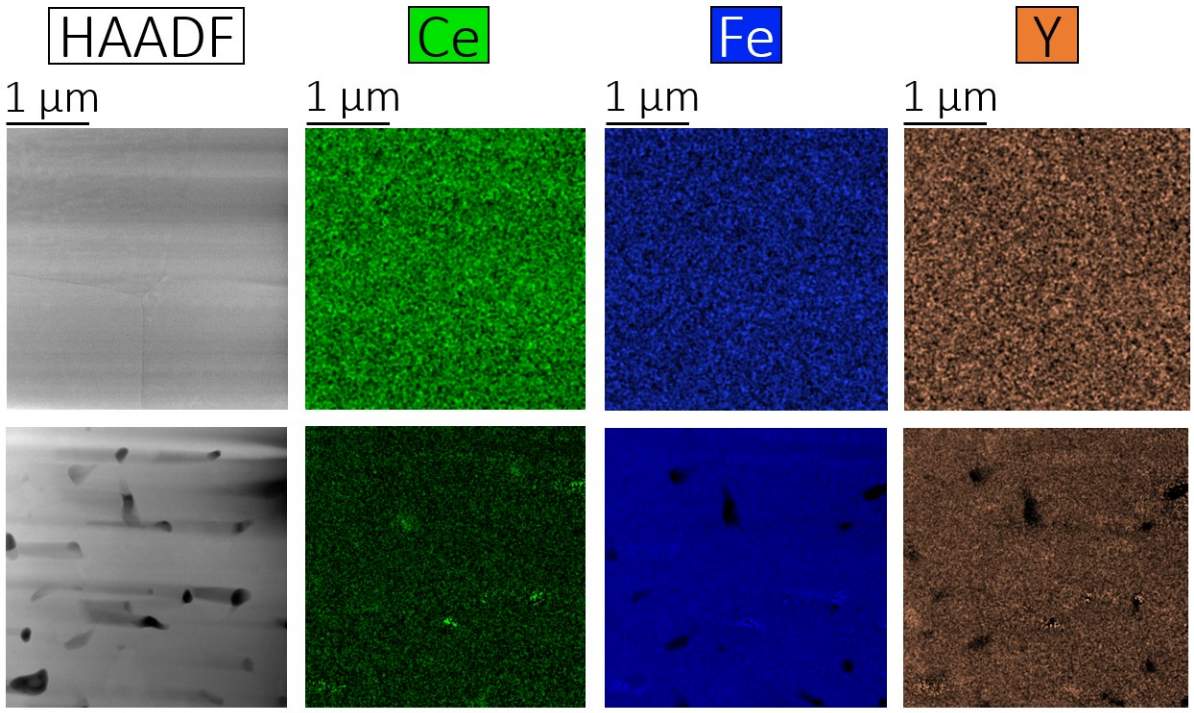

Fig. 4.14 STEM-HAADF images and EDX elemental maps for selected cations of SPS sintered single phases $BaCe_{0.76}Fe_{0.04}Y_{0.20}O_{3-\delta}$ (top) and $BaCe_{0.04}Fe_{0.76}Y_{0.20}O_{3-\delta}$ (bottom).

4.4.3. High-resolution STEM-HAADF and STEM-EDX images

To identify the crystal structure of the Ce- and Fe-rich phase in composites, high-resolution transmission electron microscopy (HR-TEM) and Fast Fourier transformation (FFT) was carried out with selected samples (Figure 4.15 and Figures A11 and A12).

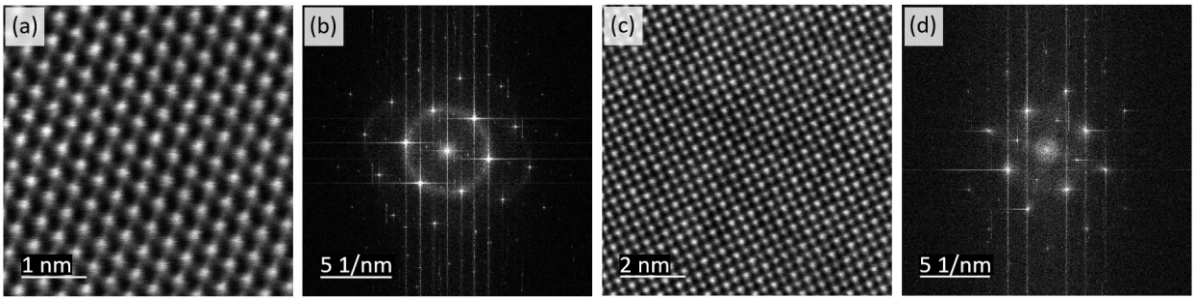

Fig. 4.15 (a) High resolution STEM-HAADF image with **(b)** the corresponding FFT image in [001] zone axis of the Ce-rich phase and **(c)** high resolution STEM-HAADF image with **(d)** the corresponding FFT image in [100] zone axis of the Fe-rich phase of the self-generated $BaCe_{0.6}Fe_{0.2}In_{0.2}O_{3-\delta}$ composite [69].

In $BaCe_{0.6}Fe_{0.2}In_{0.2}O_{3-\delta}$, as well as in all other examined composites, the Ce-rich phase (Figures 4.15a and 4.15b) has a trigonal structure, while the Fe-rich phase (Figures 4.15c and 4.15d) has a cubic structure. The elemental maps in Figure 4.16 show a homogeneous distribution of the elements within the Fe-rich phase. For a smaller area, additional electron energy loss spectroscopy (EELS) elemental maps were recorded. Figure 4.17 shows a homogeneous signal for the A-site (Ba) and a variation in the signal of the B-site (Ce, Fe), indicating the presence of atomic columns with different compositions.

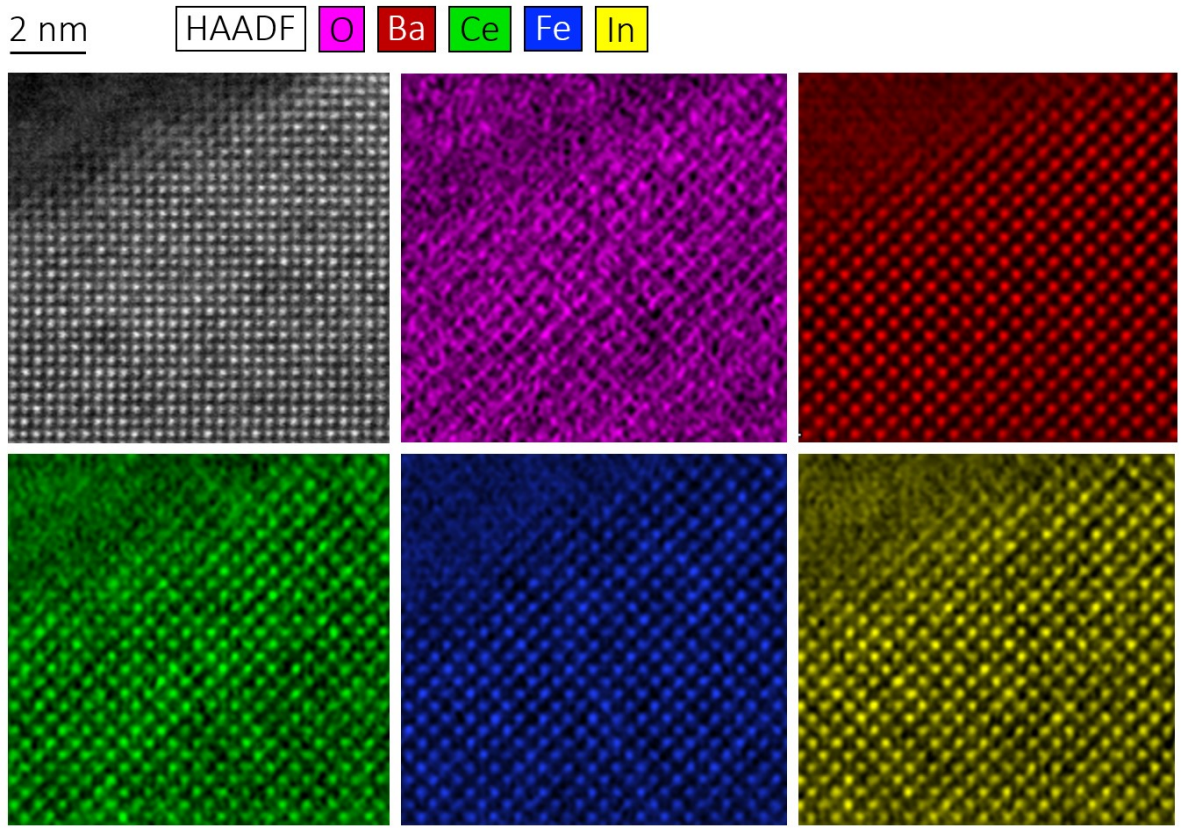

Fig. 4.16 High resolution STEM-HAADF image and EDX elemental maps for selected cations of the Fe-rich phase of the self-generated $BaCe_{0.6}Fe_{0.2}In_{0.2}O_{3-\delta}$ composite [69].

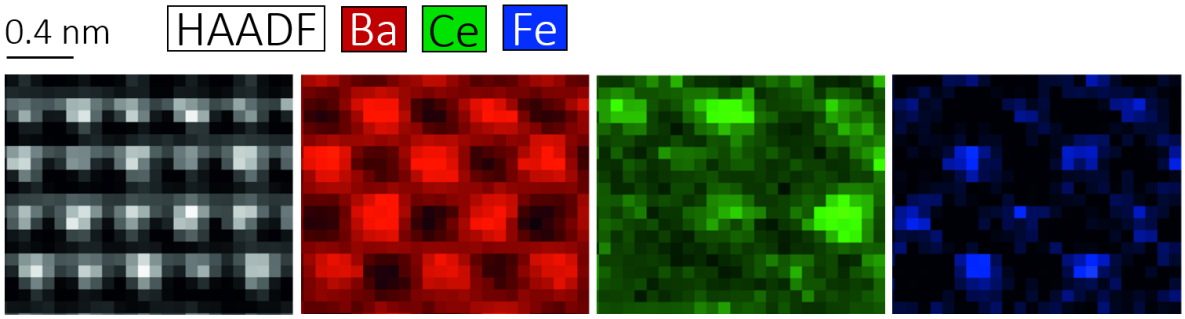

Fig. 4.17 High resolution STEM-HAADF image and EELS elemental maps for selected cations of the Fe-rich phase of the self-generated $BaCe_{0.6}Fe_{0.2}In_{0.2}O_{3-\delta}$ composite [69].

4.5. Oxygen nonstoichiometry

For the determination of the proton uptake capacity by thermogravimetry (refer to section 3.5. Thermogravimetry), the condition $2\,[V_O^{\bullet\bullet}] > [h^{\bullet}]$ must be verified to ensure that the proton uptake occurs preferentially via the hydration reaction (refer to section 2.4. Proton uptake in triple conducting oxides, Equation 2.6). The oxygen nonstoichiometry of two single phase samples is shown in Figure 4.18. These compositions were selected because the condition may not be fulfilled especially in samples with a considerable amount of Fe. The substitution of Ce^{4+} with trivalent ions, such as Y^{3+}, results in a certain concentration of oxygen vacancies $[V_O^{\bullet\bullet}]$ per formula unit. This amount of oxygen vacancies marks the state where all iron is present as Fe^{4+}. In the case of $BaCe_{0.4}Fe_{0.4}Y_{0.2}O_{3-\delta}$, if all Fe is tetravalent, then $[h^{\bullet}] = [Fe^{4+}] = [Fe] = 0.4$ and the concentration of oxygen vacancies per formula unit is determined by the concentration of Y. According to Equation 2.5 (refer to section 2.3. Acceptor substitution), this concentration of oxygen vacancies is given by $[V_O^{\bullet\bullet}] = \frac{1}{2}\,[Acc_B'] = \frac{1}{2}\,[Y_B'] = 0.1$. In atmospheres with different oxygen partial pressures, the distribution between Fe^{3+} and Fe^{4+} varies, which means oxygen is incorporated or released (refer to section 2.4. Proton uptake in triple conducting oxides, Equation 2.8). Consequently, when $[V_O^{\bullet\bullet}]$ increases, $[h^{\bullet}]$ will decrease and vice versa. At high temperatures and/or low pO_2, $[Fe^{4+}]$ approaches zero and all Fe is present as Fe^{3+}. The oxygen nonstoichiometry ($\delta = [V_O^{\bullet\bullet}]$) was determined from the weight changes observed in thermogravimetry in atmospheres with varying oxygen partial pressures [93]. The results in Figure 4.18, demonstrate that the condition $2\,[V_O^{\bullet\bullet}] > [h^{\bullet}]$ is fulfilled in the temperature and pO_2 regions investigated.

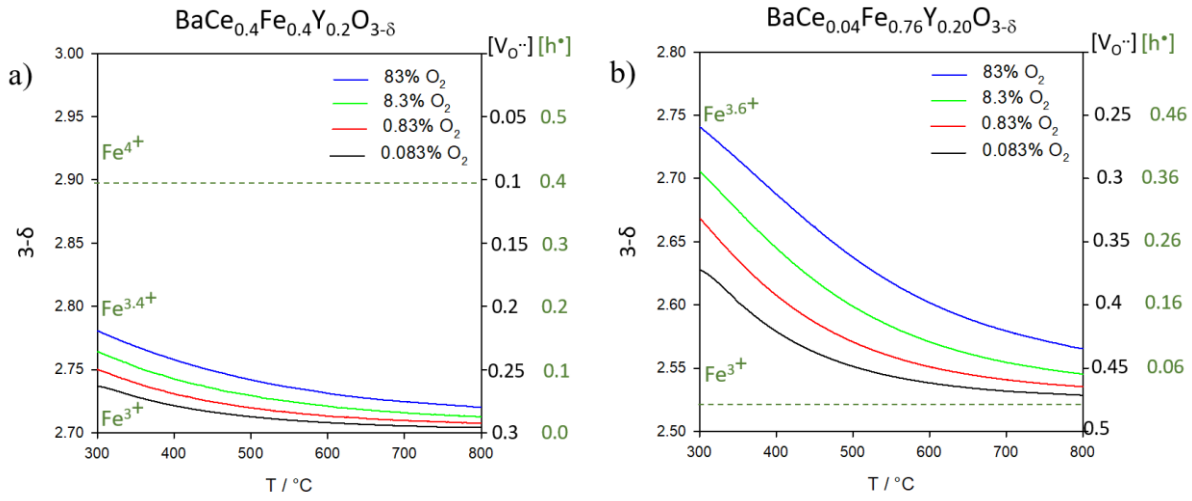

Fig. 4.18 Oxygen nonstoichiometry of **(a)** $BaCe_{0.4}Fe_{0.4}Y_{0.2}O_{3-\delta}$ and **(b)** $BaCe_{0.04}Fe_{0.76}Y_{0.20}O_{3-\delta}$ single phases as a function of temperature for oxygen partial pressures of $0.00083 \leq pO_2/\text{bar} \leq 0.83$.

4.6. Proton uptake capacity

The proton uptake capacity was investigated with single phase materials and composites, substituted with a variation of trivalent ions (acceptor substituents), as a function of the degree of substitution and Ce:Fe ratio. This was carried out in order to examine the impact of the B-site composition on the proton uptake capacity. Figure 4.19a gives an overview of the proton concentration as a function of temperature of $BaCe_{0.4}Fe_{0.4}Acc_{0.2}O_{3-\delta}$ composites with different acceptor substituents (Acc = In, Y, Yb, Gd, Sm, Sc). The proton concentration increases with decreasing temperature, which reflects the exothermic character of the hydration reaction (refer to section 2.4. Proton uptake in triple conducting oxides, Equation 2.6).

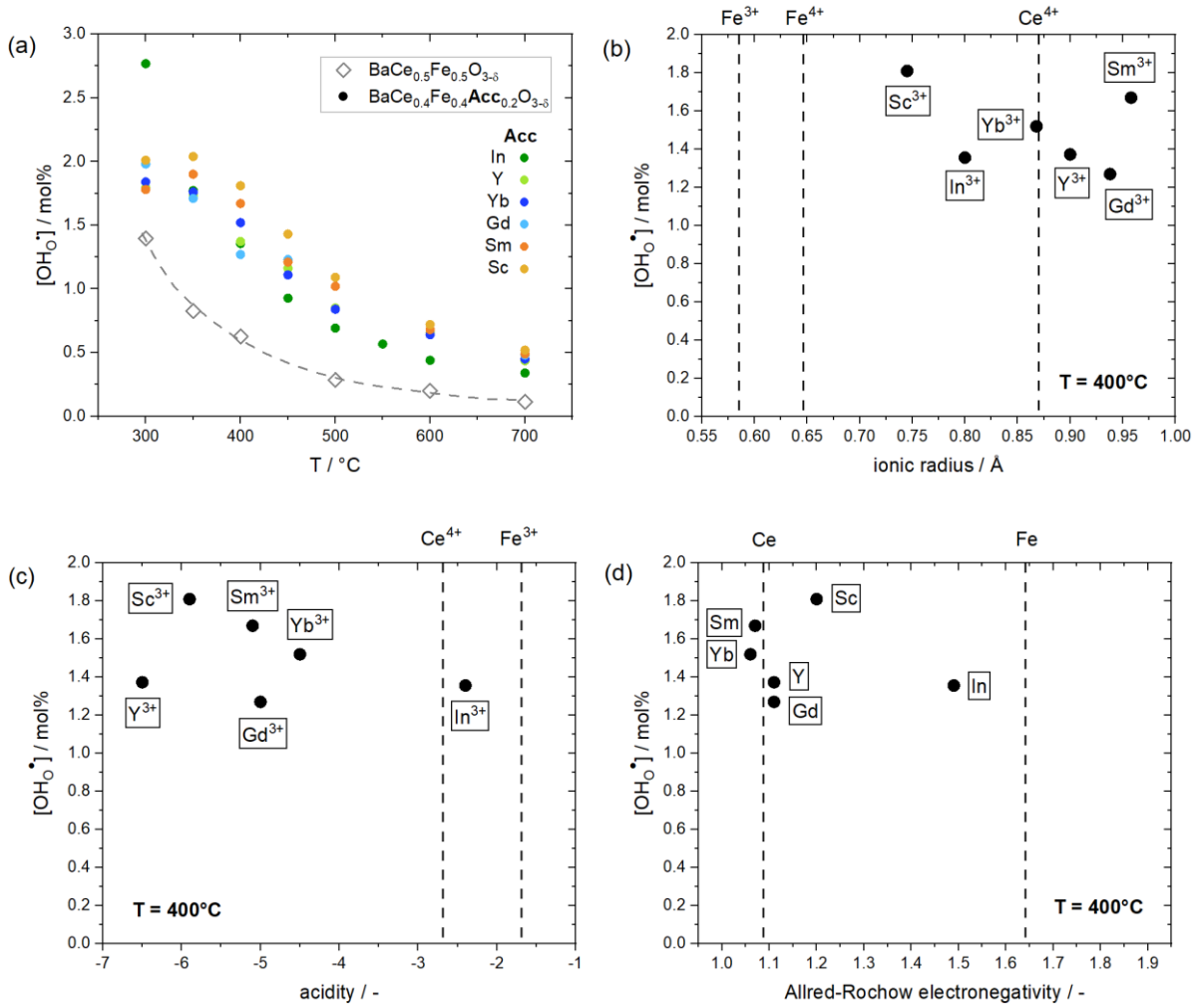

Fig. 4.19 Proton concentrations of $BaCe_{0.4}Fe_{0.4}Acc_{0.2}O_{3-\delta}$ (Acc = In, Y, Yb, Gd, Sm, Sc) composites in 17 mbar pH_2O with frozen-in oxygen stoichiometry **(a)** as a function of temperature compared to the unsubstituted composite $BaCe_{0.5}Fe_{0.5}O_{3-\delta}$ [87] (open symbols) and as a function of the substituent's **(b)** ionic radius according to Shannon et al. [86], **(c)** acidity according to Smith et al. [92] and **(d)** Allred-Rochow electronegativity according to Little et al. [94]. Figures 4.19a – 4.19c are taken from [69].

In composites, the proton concentrations obtained are effective parameters, i.e. it is not possible to distinguish which phase takes up which proportion of the protons. Therefore, it is not possible to derive thermodynamic parameters such as hydration enthalpy and entropy for composites. In comparison to the unsubstituted $BaCe_{0.5}Fe_{0.5}O_{3-\delta}$, the substitution with acceptors increases the proton uptake capacity, as expected. However, no significant differences in the magnitude of the observed increase have been identified between the substituents. Furthermore, no empirical correlations have been found, indicating that there is no clear trend in relation to the substituent's ionic radius (Figure 4.19b), acidity (Figure 4.19c) or electronegativity (Figure 4.19d). In $BaCe_{1-x}Acc_xO_{3-\delta}$ single phases, correlations between the hydration enthalpy and the electronegativity have been reported [8, 95]. The hydration enthalpy becomes more exothermic with a decreasing difference in electronegativity between the A- and B-site cations. As the Allred-Rochow electronegativity of the A-site ion, which is Ba in the case of this work, is 0.97 [94], all investigated cations have a higher electronegativity (see Figure 4.19d). Consequently, an increasing exothermic hydration enthalpy with decreasing electronegativity of the B-site ion is expected. Furthermore, there have been reports of correlations between the hydration enthalpy and the ionic radius in $BaCe_{1-x}Acc_xO_{3-\delta}$ single phases [95, 96]. In $BaCe_{0.9}Acc_{0.1}O_{3-\delta}$ (Acc = Nd, Y, Yb), the tolerance factor becomes smaller with a decreasing ionic radius of the substituent. The results identify a more exothermic hydration enthalpy with decreasing ionic radius. However, correlations like these already encounter limitations when utilising single phase cerates [95], and it is therefore obvious that the situation becomes even more complex when composite materials with redox-active transition metals are considered.

The introduction of Fe on the B-site results in an increased oxygen vacancy concentration, but also has a significant impact on the basicity of the oxygen ions, which represents a deviation from the ideal approximation of non-interacting defects. The increased covalence of the Fe–O bond in comparison to the Ce–O bond results in a reduced basicity of the oxygen ions, which makes their protonation less favourable. As shown in Figure 4.20a, even small amounts of Fe result in a significant decrease in proton concentration, reaching a plateau at an Fe content of approximately 0.2. In combination with Figure 4.20b, showing an increasing oxygen vacancy concentration with increasing Fe content, this indicates a reduced tendency for protonation, which is related to the reduced basicity of oxygen ions in the vicinity of Fe. A single Fe ion is in contact with six oxygen ions. The trend in Figure 4.20a indicates that the most significant effect is expected when the oxygen ion begins to interact with a single Fe ion. In the case of an additional Fe ion establishing contact with this oxygen, it is possible that the basicity of this oxygen ion is affected only to a limited extent. As the content of Fe increases, the majority of oxygen ions will have contact with more than one Fe ion, which has no significant impact on their tendency for protonation. This implies, as the greatest difference in basicity occurs upon contact with the first Fe ion, materials containing the smallest amounts of Fe are affected the most.In general, the Ce-rich phase is the phase with the higher degree of hydration, as reported in [97]. Typical electrolyte materials, such as $Ba(Ce,Acc)O_3$, become fully hydrated at temperatures below 300 °C, while electrode materials, such as $Ba(Fe,Acc)O_{3-\delta}$, exhibit lower degrees of hydration.

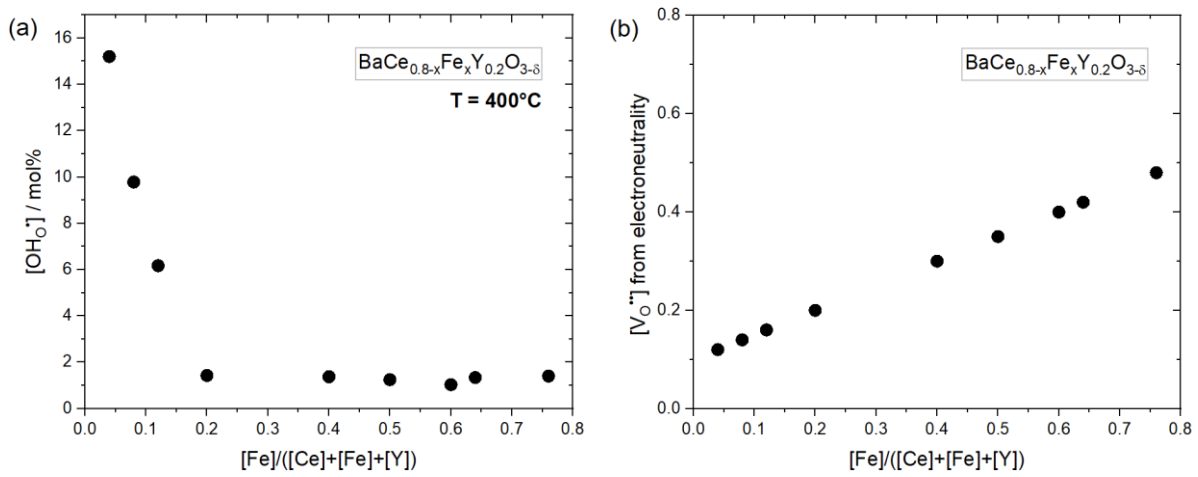

Fig. 4.20 (a) Proton concentration of $BaCe_{0.8-x}Fe_xY_{0.2}O_{3-\delta}$ single phases ($x < 0.2$ and $x > 0.6$) and composites ($0.2 \leq x \leq 0.6$) in 17 mbar pH_2O with frozen-in oxygen stoichiometry as a function of Fe content at 400 °C. **(b)** Oxygen vacancy concentration of $BaCe_{0.8-x}Fe_xY_{0.2}O_{3-\delta}$ derived from electroneutrality condition.

Figure 4.21a and 4.21b show the proton concentrations of Y- and In-substituted ferrates in comparison with Ce-rich $Ba(Ce,Fe,Acc)O_{3-\delta}$ single phases. The Y-substituted Ce-rich phase has a significantly higher proton concentration than the Y-substituted ferrate. The degree of hydration can be calculated according to Equation 4.2, with the oxygen vacancy concentration derived from the electroneutrality condition (Equation 2.9). It is evident from Figure 4.21c that the degree of hydration is also significantly higher for the Ce-rich phase. However, only part of the existing oxygen vacancies are hydrated. This can be attributed to the presence of redox-active Fe on the B-site, which influences the hydration thermodynamics and the proton concentrations significantly, as shown in Figure 4.20. In the case of the In-substituted system (Figures 4.21b and 4.21d), the Ce-rich phase also exhibits a higher proton concentration and degree of hydration. However, the difference between the substituted ferrate and Ce-rich phase is not as pronounced as it is for Y-substituted materials. This phenomenon can be attributed to the higher Fe content compared to the Y-substituted materials, which is especially crucial at low Fe contents, as it is the case here.

$$\alpha = \frac{[OH_O^{\bullet}]}{2\,[V_O^{\bullet\bullet}]_{max}}$$

Eq. 4.2 Degree of hydration [97]

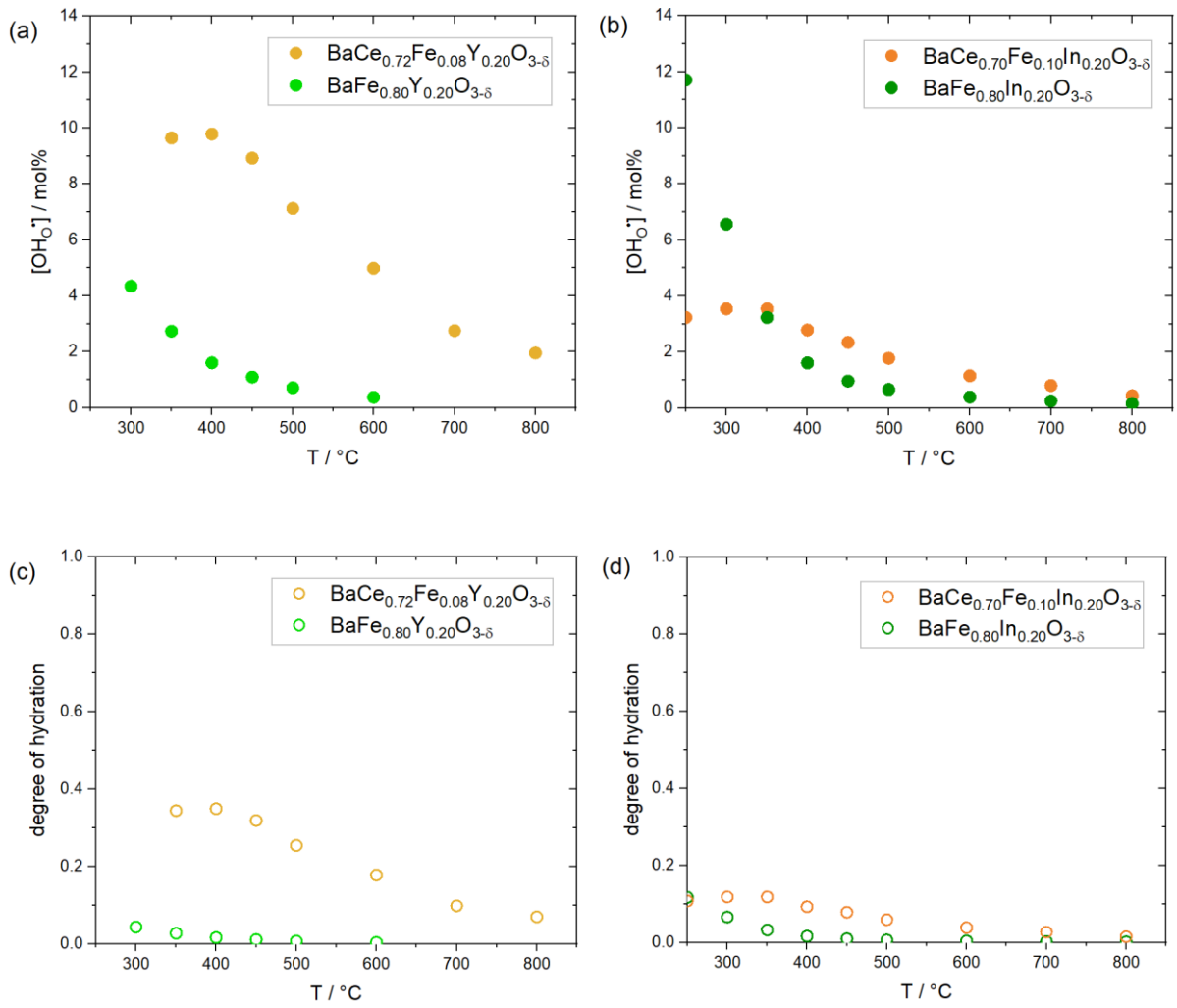

Fig. 4.21 (a)-(b) Proton concentration in 17 mbar pH_2O with frozen-in oxygen stoichiometry and **(c)-(d)** degree of hydration of ferrates and Ce-rich Ba(Ce,Fe,Acc)$O_{3-\delta}$ single phases substituted with Y compared to In as a function of temperature.

In accordance with the observed stronger tendency for hydration in the Ce-rich phase, the difference between electrolyte and electrode materials should also be reflected in the thermodynamic parameters. Figure 4.22 shows a more negative $\Delta H^{\circ}_{hydrat}$ for typical electrolyte materials, such as BCYs or BZYs, in comparison to typical electrode materials, such as BFZns or BSFs. As $\Delta S^{\circ}_{hydrat}$ is within the same range, this leads to a more negative $\Delta G^{\circ}_{hydrat}$ for electrolyte materials than for electrode materials, which is as expected. The data points in blue represent the thermodynamic parameters of Ba(Zr,Fe,Y)$O_{3-\delta}$ with varying amounts of Fe on the B-site (indicated by the numbers in the plot). As previously noted, the presence of Fe has an impact on the thermodynamic parameters. At very small amounts of Fe, $\Delta H^{\circ}_{hydrat}$ becomes less negative and reaches a plateau between $0.1 \leq [Fe] \leq 0.2$. As the Fe content increases further, $\Delta H^{\circ}_{hydrat}$ becomes more negative, but $\Delta S^{\circ}_{hydrat}$ also becomes more negative. In conclusion, the overall effect is a reduction in $\Delta G^{\circ}_{hydrat}$ with increasing Fe content.

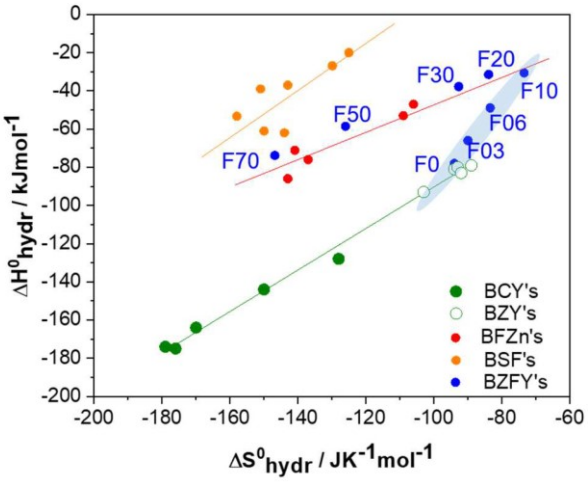

Fig. 4.22 $\Delta H^{\circ}_{hydrat}$ vs. $\Delta S^{\circ}_{hydrat}$ of typical electrolyte (BCYs and BZYs) and electrode materials (BFZns and BSFs) compared to BZFYs with different amounts of Fe on the B-site. Image taken from [97] with BCY and BZY data from [8].

The observed behaviour of the thermodynamic parameters as a function of Fe content in Figure 4.22 can be employed to interpret the observations made in this thesis. Figure 4.23a shows $\Delta H^{\circ}_{hydrat}$, $\Delta S^{\circ}_{hydrat}$ and $\Delta G^{\circ}_{hydrat}$ at 400 °C of $BaCe_{0.92-x}Fe_{0.08}Y_xO_{3-\delta}$ single phases. In comparison to Y-substituted ferrates, as shown in Figure 4.23b, $\Delta H^{\circ}_{hydrat}$ in Ce-rich materials is less negative. This phenomenon can be explained by the amount of Fe present on the B-site of the materials. The Ce-rich $Ba(Ce,Fe,Y)O_{3-\delta}$ single phases with an Fe content of 0.08 are located in the region [Fe] ≤ 0.1, where $\Delta H^{\circ}_{hydrat}$ in Figure 4.22 is already less negative. In contrast, the ferrates with an Fe content of 0.80 ≤ [Fe] ≤ 0.95, are in the region where $\Delta H^{\circ}_{hydrat}$ becomes more negative once more.

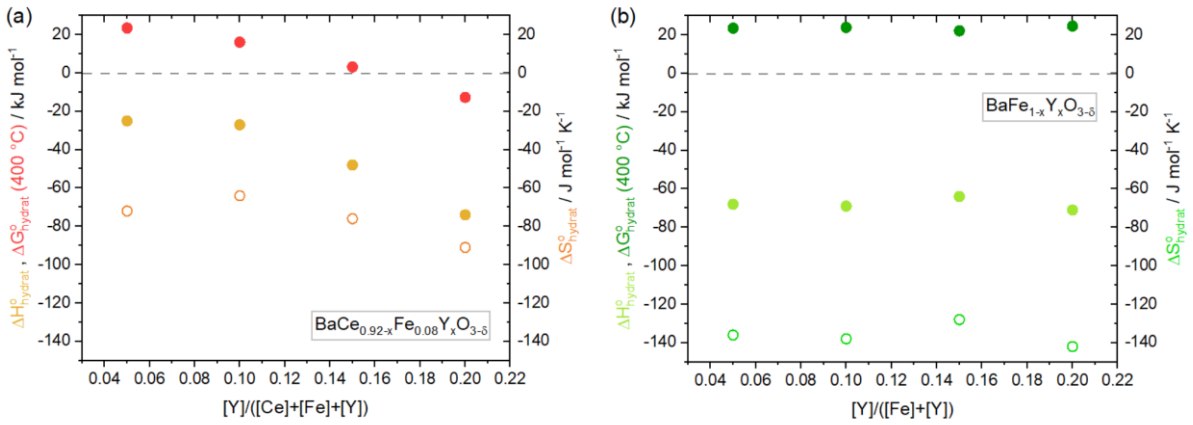

Fig. 4.23 $\Delta H^{\circ}_{hydrat}$, $\Delta S^{\circ}_{hydrat}$ and $\Delta G^{\circ}_{hydrat}$ as a function of Y content of **(a)** $BaCe_{0.92-x}Fe_{0.08}Y_xO_{3-\delta}$ single phases and **(b)** Y-substituted ferrates at 400 °C.

However, $\Delta S^{\circ}_{hydrat}$ in the ferrates is more negative than in Ce-rich Ba(Ce,Fe,Y)$O_{3-\delta}$ single phases, which in the end results in a positive $\Delta G^{\circ}_{hydrat}$ of approximately +20 kJ mol^{-1} in the ferrates and a negative $\Delta G^{\circ}_{hydrat}$ of approximately –10 kJ mol^{-1} for $BaCe_{0.72}Fe_{0.08}Y_{0.20}O_{3-\delta}$ at 400 °C. Thermodynamic parameters of In-substituted materials are summarised in Figure A13. In principle, they show the same characteristics. Indium substituted ferrates have a more negative $\Delta H^{\circ}_{hydrat}$, but also a more negative $\Delta S^{\circ}_{hydrat}$. Consequently, $\Delta G^{\circ}_{hydrat}$ at 400 °C of In substituted ferrates is also approximately +20 kJ mol^{-1}. Due to the higher Fe content, $\Delta G^{\circ}_{hydrat}$ of $BaCe_{0.70}Fe_{0.10}In_{0.20}O_{3-\delta}$ (+10 kJ mol^{-1} at 400 °C) is higher than that of $BaCe_{0.72}Fe_{0.08}Y_{0.20}O_{3-\delta}$, but remains less positive than that of In substituted ferrates.

Regarding substitution with different acceptors, the influence of the substituents on the bond properties and lattice distortions is also not trivial. Consequently, it is understandable that no clear trends were found with regard to only one property of the acceptor ion, as a combination of different factors influences the amount of oxygen vacancies, the tendency to hydrate them, trapping effects and the stability of defects. The system is further complicated by the varying compositions of the two phases in the composite. This makes it additionally difficult to compare different materials or substituents in detail. Another possible explanation for the lack of significant differences in the increase in proton uptake between the substituents is the predominant incorporation of the acceptor substituents into the Fe-rich phase (refer to section 4.4. Microstructure and elemental distribution, Figure 4.8). As already explained, the Ce-rich phase is the phase with the higher degree of hydration. Therefore, the acceptor substituents are required in the Ce-rich phase, where the potential for an increase in proton uptake is greater. Figure 4.23a shows a positive impact of increasing Y content in Ce-rich Ba(Ce,Fe,Y)$O_{3-\delta}$ single phases on $\Delta G^{\circ}_{hydrat}$, whereas there appears to be no influence in Y-substituted ferrates (Figure 4.23b). The same characteristics are observed for In-substituted materials (Figure A13). The same applies with regard to the proton uptake capacity, as shown in Figure 4.24. In the Fe-rich phase (Figure 4.24b) it appears that an increasing content of acceptor substituents has no influence on the proton concentration. However, in Ce-rich acceptor-substituted single phases (Figure 4.24a), there is a significant increase in proton uptake with increasing acceptor content. A lower amount of Fe in the Y-substituted material results in a more pronounced increase in proton concentration than in the In-substituted material with a higher Fe content. Consequently, the Ce-rich phase appears to have greater potential for improvement through acceptor substitution, which is why the substituents should be incorporated specifically in the Ce-rich phase. However, as observed in the composites, the substituents are enriched in the Fe-rich phase, regardless of their ionic radius or basicity (refer to section 4.4. Microstructure and elemental distribution, Figure 4.11). Therefore, only a small part of the potential is utilised. Furthermore, the presence of Fe also decreases the potential for improvement significantly, which may explain why there is no significant difference in the results obtained with the different acceptors. The original plots of the proton concentration as a function of temperature, as well as the van't Hoff plots, are summarised for all single phases in the appendix (Figures A14–A21).

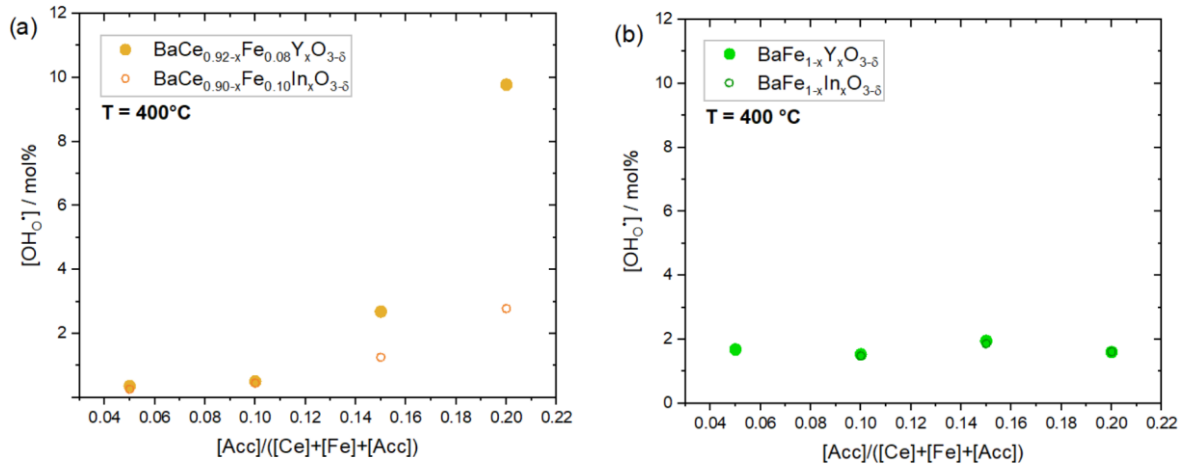

Fig. 4.24 Proton concentration as a function of acceptor content at 400 °C in 17 mbar pH_2O with frozen-in oxygen stoichiometry of **(a)** $BaCe_{0.92-x}Fe_{0.08}Y_xO_{3-\delta}$ and $BaCe_{0.90-x}Fe_{0.10}In_xO_{3-\delta}$ single phases and **(b)** Y- and In-substituted ferrates.

4.6.1. Single phases vs. composites

As previously discussed, in absolute terms the increase in proton uptake due to acceptor substitution in the Fe-rich phase is relatively modest and cannot compensate for the decrease in proton concentration in the Ce-rich phase resulting from the enrichment of acceptors in the Fe-rich phase. Consequently, the proton uptake in self-generated composites is reduced in comparison with a mixture of $BaCe_{0.8}Y_{0.2}O_{2.9}$ and $BaFe_{0.8}Y_{0.2}O_{3-\delta}$ or comparable single phases with mutual solubility of Ce and Fe in the respective other phase. Figure 4.25a compares the proton concentration of a Ce- and an Fe-rich single phase with the calculated expected weighted average of the two, which corresponds to a composite consisting of 50 vol.% Ce-rich phase and 50 vol.% Fe-rich phase. In comparison with a self-generated composite with the same average composition of the B-site, the expected level of proton concentration is considerably higher than the experimentally measured one (Figure 4.25b). Consequently, artificial composites prepared by mixing a Ce- and Fe-rich phase were also investigated with the objective of controlling the distribution of the acceptor between the two phases and avoiding the enrichment of acceptor substituents in the Fe-rich phase. Figure 4.25c shows the proton concentration of the self-generated composite BCFY442, the calculated weighted average of the two single phases $BaCe_{0.04}Fe_{0.76}Y_{0.20}O_{3-\delta}$ and $BaCe_{0.76}Fe_{0.04}Y_{0.20}O_{3-\delta}$, with a volume ratio of 50:50, and two artificial composites prepared with the same stoichiometry as used for the calculation of the expected average (the index “s” indicates an advanced manufacturing process). The results show that the reduction in proton uptake resulting from the enrichment of the acceptor substituents in the Fe-rich phase can be avoided to a limited extent. The artificial composites have a higher proton concentration than the self-generated composite, yet remain below the expected values. This limitation may be

attributed to cation interdiffusion during the preparation process (refer to section 4.4. Microstructure and elemental distribution, Figure 4.12). Furthermore, additional comparisons of self-generated and artificial composites with varying compositions were conducted, and the results are summarised in the appendix (Figure A22). As the amount of the Ce-rich phase increases, the difference between the measured and expected proton uptake becomes smaller.

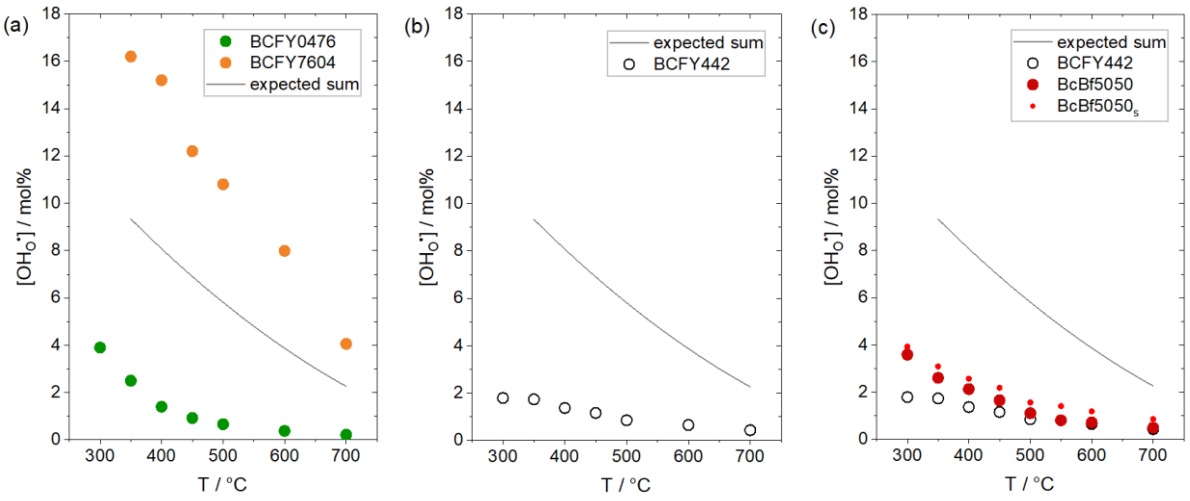

Fig. 4.25 Proton concentration as a function of temperature in 17 mbar pH_2O with frozen-in oxygen stoichiometry of **(a)** $BaCe_{0.04}Fe_{0.76}Y_{0.20}O_{3-\delta}$ and $BaCe_{0.76}Fe_{0.04}Y_{0.20}O_{3-\delta}$ single phases and the expected values of a composite with 50 vol.% of the first and 50 vol.% of the second phase, calculated by forming the average of the two, **(b)** the self-generated composite $BaCe_{0.4}Fe_{0.4}Y_{0.2}O_{3-\delta}$ compared to the expected average and **(c)** the artificial composite BcBf5050, consisting of 50 vol.%. $BaCe_{0.04}Fe_{0.76}Y_{0.20}O_{3-\delta}$ and 50 vol.% $BaCe_{0.76}Fe_{0.04}Y_{0.20}O_{3-\delta}$.

4.6.2. Influence of Ce:Fe ratio

The composition of the B-site is crucial for the proton uptake capacity. As previously discussed, Fe has a significant impact on the properties of the oxygen ions and, as a consequence, on the proton uptake capacity. Therefore, the proton concentration was investigated as a function of the Ce:Fe ratio for self-generated $BaCe_{0.8-x}Fe_xAcc_{0.2}O_{3-\delta}$ composites, with an Y or In content of 20% of the B-site. As shown in Figure 4.26a, the proton concentration in Y-substituted self-generated composites significantly increases with an increasing amount of Ce in the precursor. With regard to In-substituted composites, the same applies, as shown in Figure 4.26c. The increase in proton concentration with increasing Ce content is even more evident in Figures 4.26b and 4.26d, which show the proton uptake capacity as a function of Ce content at 500 °C. In composites, the observed decrease in proton uptake with increasing Fe content can be attributed to a combination of two factors. The increased concentration of redox-active Fe results in a less favourable incorporation of protons, and the decreased relative amount of the Ce-rich phase, which is the phase with the higher degree of hydration. These results are

consistent with expectations based on the results of single phases and the reported results of other mixed conducting materials, such as $BaZr_{0.88-x}Fe_xY_{0.12}O_{3-\delta}$ or $(Ba,Sr)FeO_{3-\delta}$ perovskites [22, 97-100]. The proton concentrations of additional Y- and In-substituted composites as a function of temperature are summarised in the appendix (Figure A23).

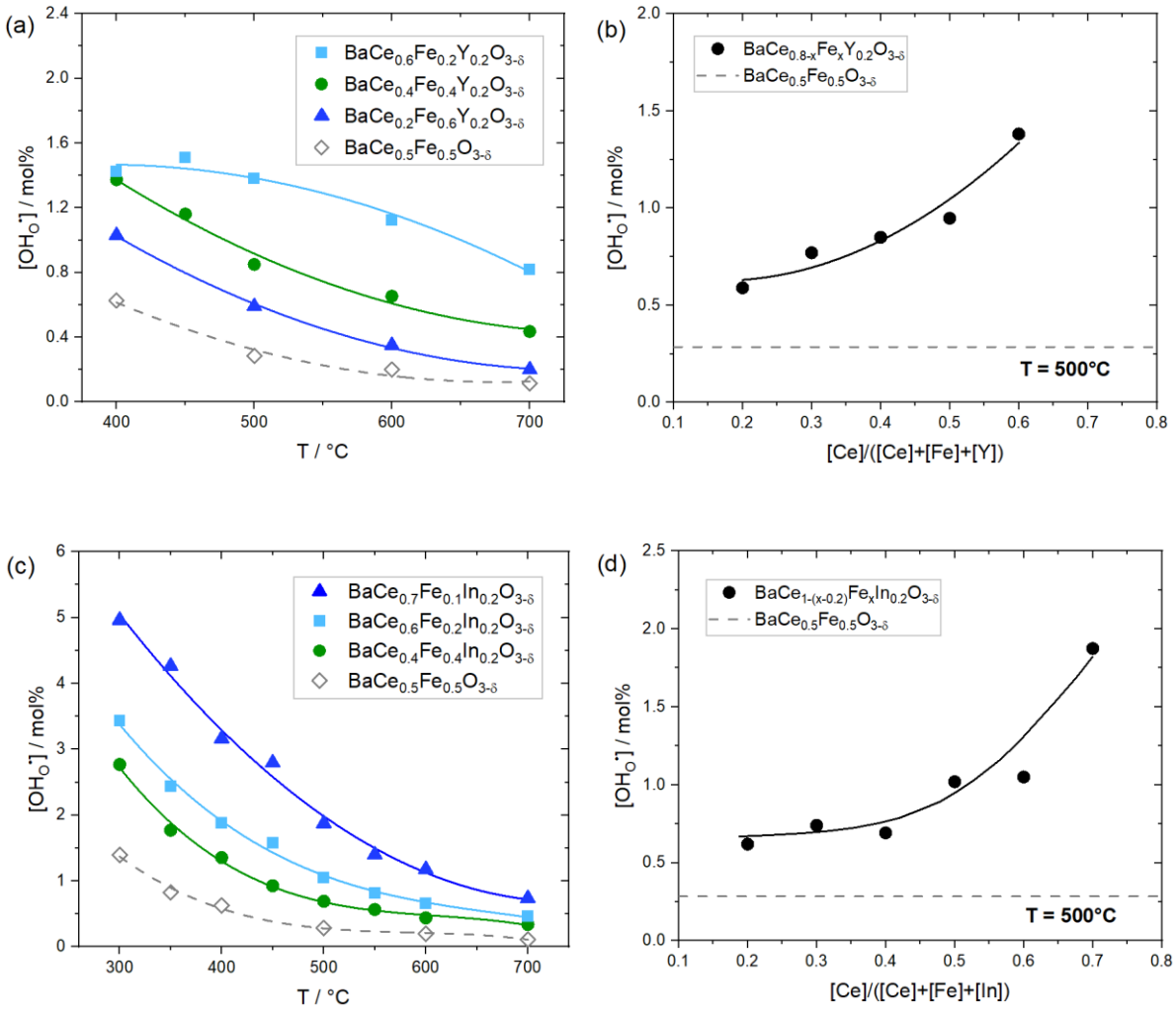

Fig. 4.26 Proton concentration as a function of temperature and Ce content in 17 mbar pH_2O with frozen-in oxygen stoichiometry of self-generated **(a)–(b)** $BaCe_{0.8-x}Fe_xY_{0.2}O_{3-\delta}$ composites and **(c)–(d)** $BaCe_{0.8-x}Fe_xIn_{0.2}O_{3-\delta}$ composites compared to the unsubstituted composite $BaCe_{0.5}Fe_{0.5}O_{3-\delta}$ [87]. Taken from [69, 87]. The lines are a guide to the eye.

4.6.3. Influence of Ce:Acc ratio

The presence of acceptor substituents also significantly influences the proton uptake capacity, as previously discussed. Consequently, the proton concentration was investigated as a function of the Ce:Acc ratio for self-generated $BaCe_{0.6-x}Fe_{0.4}Acc_xO_{3-\delta}$ composites substituted with Y or In, with an Fe

content of 40% of the B-site. Figures 4.27a and 4.27c show the proton concentration of selected self-generated composites with varying amounts of acceptor substituents as a function of temperature. As expected, based on the results of single phases, the proton concentration increases with increasing amount of acceptor in the precursor, which is even more evident in Figures 4.27b and 4.27d. The incorporation of acceptors results in a larger amount of oxygen vacancies (refer to section 2.3. Acceptor substitution, Equation 2.5) and increased basicity, both of which have a beneficial effect on the proton uptake. This positive effect increases with an increasing amount of acceptor, particularly in the Ce-rich phase, whereas the Fe-rich phase remains largely unaffected (Figure 4.24). However, as an elevated acceptor concentration in the precursor does not necessarily result in an increased amount of acceptor in the Ce-rich phase (Figure 4.11c), these results are not completely straightforward to interpret.

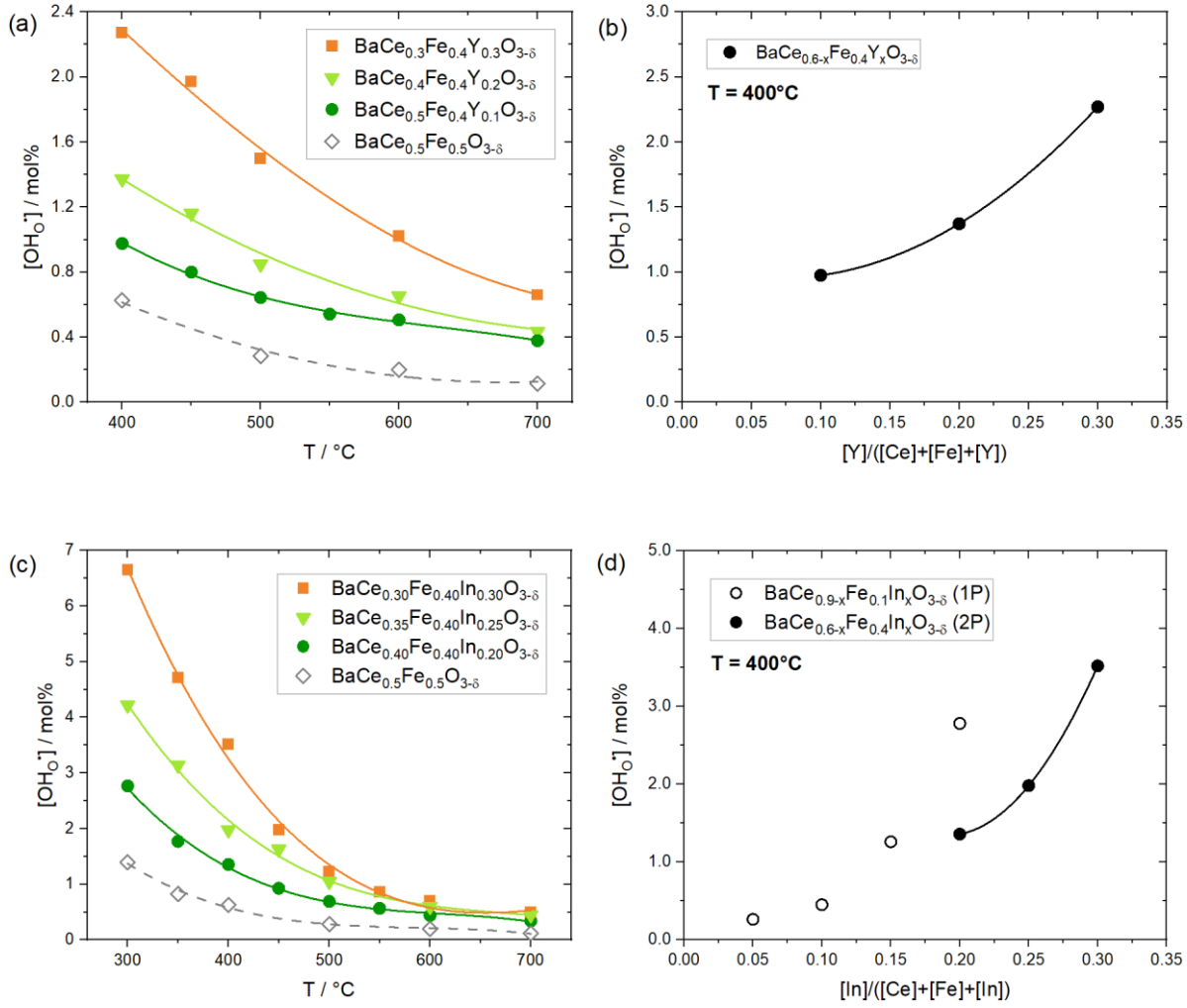

Fig. 4.27 Proton concentration as a function of temperature and Acc content in 17 mbar pH_2O with frozen-in oxygen stoichiometry of self-generated **(a)–(b)** $BaCe_{0.6-x}Fe_{0.4}Y_xO_{3-\delta}$ composites and **(c)–(d)** $BaCe_{0.6-x}Fe_{0.4}In_xO_{3-\delta}$ composites compared to the unsubstituted composite $BaCe_{0.5}Fe_{0.5}O_{3-\delta}$ [87]. Taken from [69]. The lines are a guide to the eye.

Nevertheless, the increase in proton concentration is a consequence of the increase in acceptor concentration. Consequently, composites with higher amounts of acceptor substituents are beneficial for proton uptake. However, it is also important to consider that the miscibility gap narrows and the electrical conductivity decreases with increasing acceptor concentration.

4.7. Chemical diffusion coefficient of D_2O

In the previous section, the concentration of protonic defects in equilibrium state in single phases and composites was discussed in relation to the composition of the B-site. The current section will examine the proton mobility in selected single phase and composite samples with different Ce:Fe ratios. The chemical diffusion coefficient of deuterium oxide $D^{\delta}_{D_2O}$ was determined for Ce- and Fe-rich Y-substituted single phases and composites.

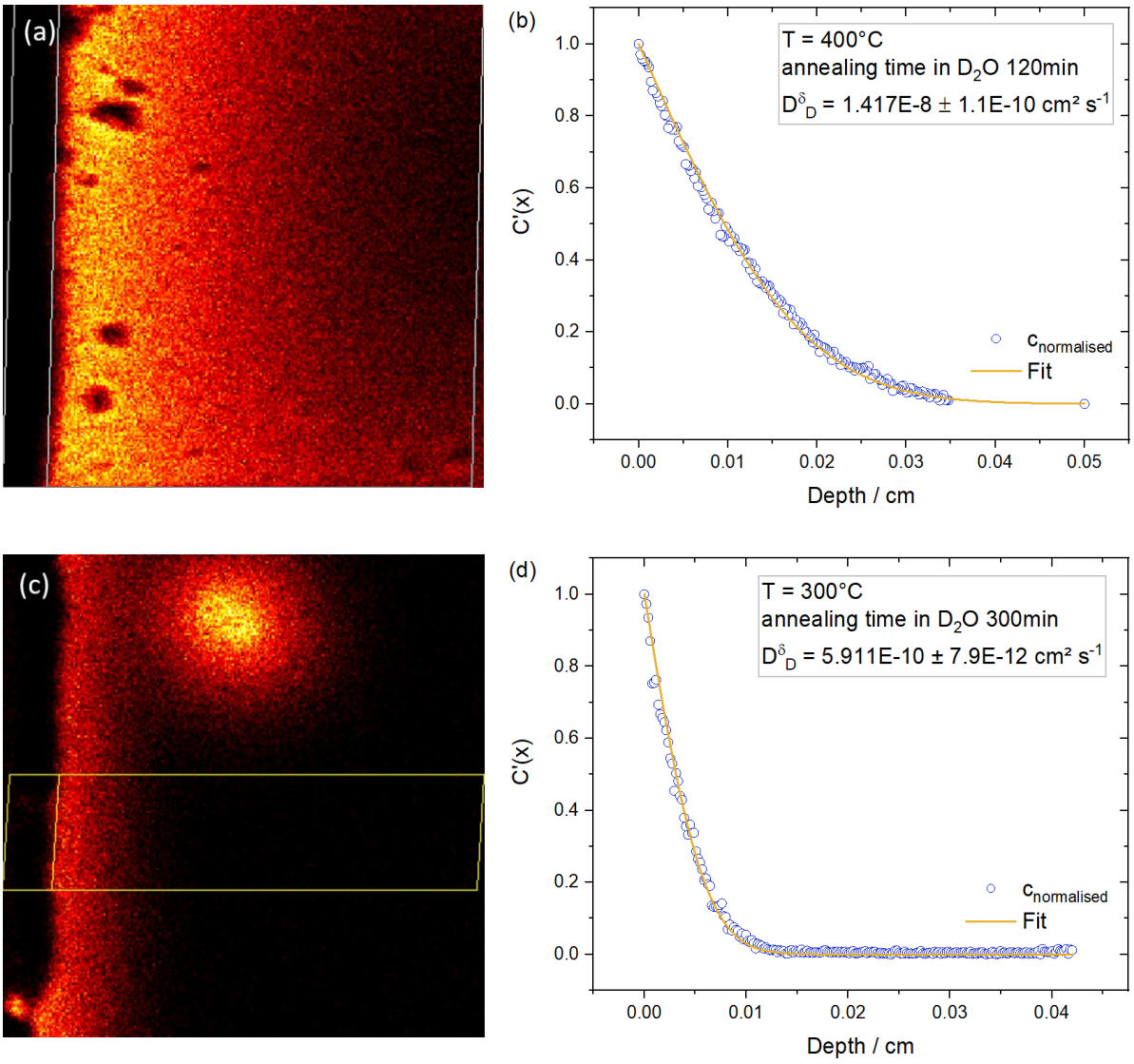

Fig. 4.28 (a) and **(c)** Secondary ion maps and **(b)** and **(d)** concentration profiles with fitting curves of selected experiments with $BaCe_{0.04}Fe_{0.76}Y_{0.20}O_{3-\delta}$ samples.

As described in section 3.6., the spatially resolved two-dimensional concentration plots from secondary ion mass spectrometry measurements are summed in a specified direction (Figure 4.28a) to obtain one-dimensional diffusion profiles. It should be noted that the recorded concentration plots are not always optimal and complete, as might be expected due to Figure 3.6 (refer to section 3.6. Isotope exchange diffusion profiling and secondary ion mass spectrometry). However, as these experiments are very complex and time-consuming, the aim was to generate knowledge also from suboptimal results, as it was not feasible to repeat those experiments without encountering significant effort. During the data evaluation process, areas that could potentially distort the results were excluded from the evaluation. Consequently, for certain measurements, only a part of the two-dimensional concentration plots was utilised, as shown in Figure 4.28c. Furthermore, the estimated annealing times were occasionally too long, resulting in the baseline being located outside the measurement area. In these cases, the baseline level was estimated in order to generate a suitable fit, as shown in Figure 4.28b. The resulting uncertainties are expected to be within the range of measurement uncertainty. Figures 4.28b and 4.28d show selected concentration profiles and the results from the non-linear fitting procedure for $BaCe_{0.04}Fe_{0.76}Y_{0.20}O_{3-\delta}$. The error function from Equation 3.3 (refer to section 3.6. Isotope exchange diffusion profiling and secondary ion mass spectrometry) was employed in the fitting process, yielding chemical diffusion coefficients of deuterium oxide $D^{\delta}_{D_2O}$. For further investigation, only measurement points with appropriate fitting results were included.

The chemical diffusion coefficient of deuterium oxide $D^{\delta}_{D_2O}$ as a function of inverse temperature, alongside the activation energies for proton diffusion for selected single phase materials is shown in Figure 4.29. As expected, the diffusion coefficient increases with increasing temperature, with the value for the Ce-rich phase (Figure 4.29a) being higher than that for the Fe-rich phase (Figure 4.29b). The results of the measurements in regimes with varying degrees of hydration (30 vs. 3 ml min^{-1}, refer to section 3.6. Isotope exchange diffusion profiling and secondary ion mass spectrometry) show no significant differences. Therefore, it was generally assumed that the experimental conditions were within the range of low hydration, and that the relation $D^{\delta}_{D_2O} \approx D_{OH^{\bullet}_O}$ is valid. Figure 4.29a shows $D^{\delta}_{D_2O}$ of the Ce-rich single phase $BaCe_{0.76}Fe_{0.04}Y_{0.20}O_{3-\delta}$ compared to the diffusion coefficient for protonic defects $D_{OH^{\bullet}_O}$ of BZY [8] und BCY [101]. The activation energy is consistent with the expected value of ~0.5 eV for the transport of protons in $BaCeO_3$ [71] or $BaZr_{0.8}Y_{0.2}O_{3-\delta}$ [102]. In comparison with the Fe-free samples, $D^{\delta}_{D_2O}$ of BCFY760420 is one order of magnitude lower. One possible explanation for this difference is that the Ce-rich phase has a high proton uptake capacity, suggesting that the condition of low hydration may not have been fully satisfied. This could result in an underestimation of $D^{\delta}_{D_2O}$. However, it may also be attributed to the 4% Fe on the B-site. In terms of the proton uptake capacity, it was already observed that even small amounts of Fe have a significant influence on the properties (refer to section 4.6. Proton uptake capacity, Figure 4.20). Figure 4.29b compares $D^{\delta}_{D_2O}$ of the Fe-rich single phase $BaCe_{0.04}Fe_{0.76}Y_{0.20}O_{3-\delta}$ with BL5F and BL5FY20 (to be published by C. Berger et al.). The activation energy of protonic transport of the Y-free BL5F is of a similar magnitude to that of

the materials shown in Figure 4.29a. BCFY047620 deviates from this trend. While $D^{\delta}_{D_2O}$ of BCFY047620 is within the same order of magnitude as that of BL5FY20, the activation energy of ~1 eV is higher than expected for the transport of protons. However, the Y-containing BL5FY20 has a similar activation energy, which indicates that the presence of Y plays a role in this phenomenon. The increased activation energy can be attributed to defect interactions, which however differ from typical trapping effects. The larger ionic radius of Y in the Fe-rich phase ($r(Y^{3+})$ = 0.900 Å, $r(Fe^{3+})$ = 0.645 Å and $r(Fe^{4+})$ = 0.585 Å for a coordination number of VI [86]) results in a longer distance between oxygen ions in the vicinity of Y. Proton conduction in these materials involves the movement of protons from one oxygen ion to another. A longer distance between the involved oxygen ions increases the proton transfer barrier, as the hydrogen bond is weakened, thereby inhibiting the proton mobility in the vicinity of Y.

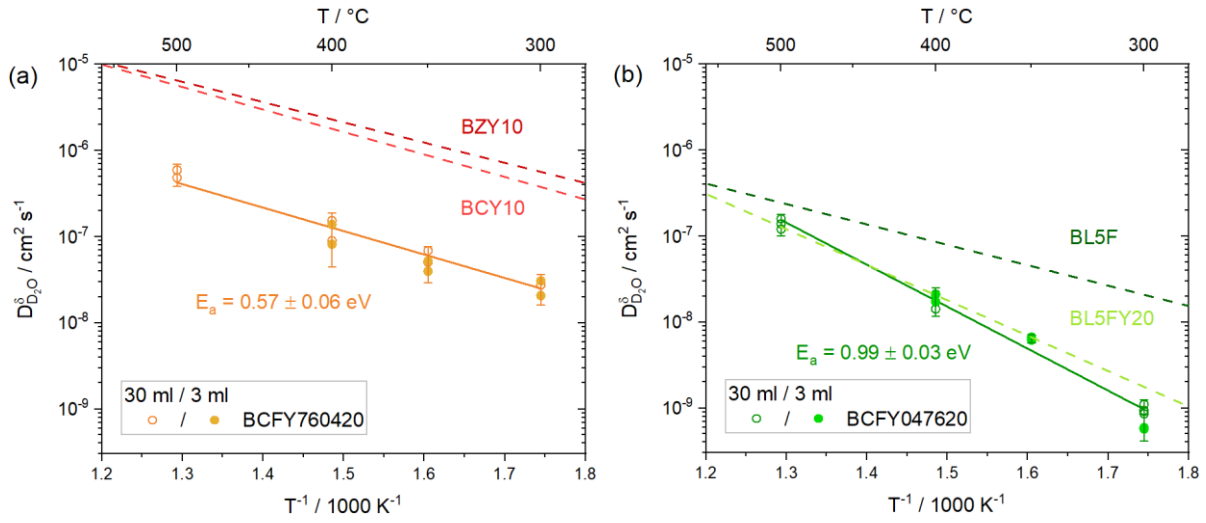

Fig. 4.29 Chemical diffusion coefficient of deuterium oxide $D^{\delta}_{D_2O}$ as a function of inverse temperature and activation energies for proton diffusion of **(a)** the single phase $BaCe_{0.76}Fe_{0.04}Y_{0.20}O_{3-\delta}$ compared to $D_{OH_O^{\bullet}}$ of $BaZr_{0.9}Y_{0.1}O_{3-\delta}$ [8] and $BaCe_{0.9}Y_{0.1}O_{3-\delta}$ [101] and **(b)** the single phase $BaCe_{0.04}Fe_{0.76}Y_{0.20}O_{3-\delta}$ compared to $Ba_{0.95}La_{0.05}FeO_{3-\delta}$ and $Ba_{0.95}La_{0.05}Fe_{0.80}Y_{0.20}O_{3-\delta}$ (to be published by C. Berger et al.). Activation energies are given in the plots. The lines are a guide to the eye.

Figure 4.30 shows the chemical diffusion coefficient of deuterium oxide as a function of inverse temperature, alongside the activation energies for proton diffusion for selected artificial composites compared to single phases. The activation energies for proton diffusion of the composites are also higher than expected for the transport of protons. $D^{\delta}_{D_2O}$ of the artificial composite BcBf8020, as shown in Figure 4.30a, is higher than that of BcBf6535 with a smaller amount of Ce-rich phase. This observation is consistent with the results obtained for single phase materials, where the Ce-rich phase also exhibited higher chemical diffusion coefficients compared to the Fe-rich phase. Given that both artificial composites are prepared by mixing these two single phases, it would be expected that their chemical diffusion coefficients will range somewhere between those of the single phases. As shown in

Figure 4.30a, this is not the case. $D^{\delta}_{D_2O}$ of the artificial composite BcBf8020, consisting of 80 vol.% Ce-rich phase, is located close to BCFY047620. The artificial composite BcBf6535 exhibits an even lower chemical diffusion coefficient. This suggests that the present composite materials have a lower chemical diffusion coefficient compared to single phases. One potential explanation for this may be the distribution of Y between the two phases (also interdiffusion of oversized Ce^{4+} during sintering of the composite may be detrimental for proton migration). As previously discussed, Y has a negative impact on the mobility of protons in the Fe-rich phase. Transmission electron microscopy analyses demonstrated that Y is enriched in the Fe-rich phase in both self-generated and artificial composites (refer to section 4.4. Microstructure and elemental distribution, Figure 4.11d), which may be the cause for the decreased mobility of protons in composites. Figure 4.30b compares $D^{\delta}_{D_2O}$ of an artificial composite, a self-generated composite and a single phase sample with the same overall stoichiometry of $BaCe_{0.48}Fe_{0.32}Y_{0.20}O_{3-\delta}$. The slightly lower chemical diffusion coefficient of the self-generated composite may be attributed to the pronounced enrichment of Y in the Fe-rich phase in comparison to the artificial composite (refer to section 4.4. Microstructure and elemental distribution, Figure 4.11d). The activation energy for proton diffusion of the self-generated composite is of a similar magnitude as that of the artificial composite. Compared to both composites, the single phase material has a significantly lower $D^{\delta}_{D_2O}$. However, the diffusion profiles for the single phase samples are relatively short, resulting in a high degree of uncertainty (also for the activation energy). Consequently, further measurements are planned for the future in order to confirm these results.

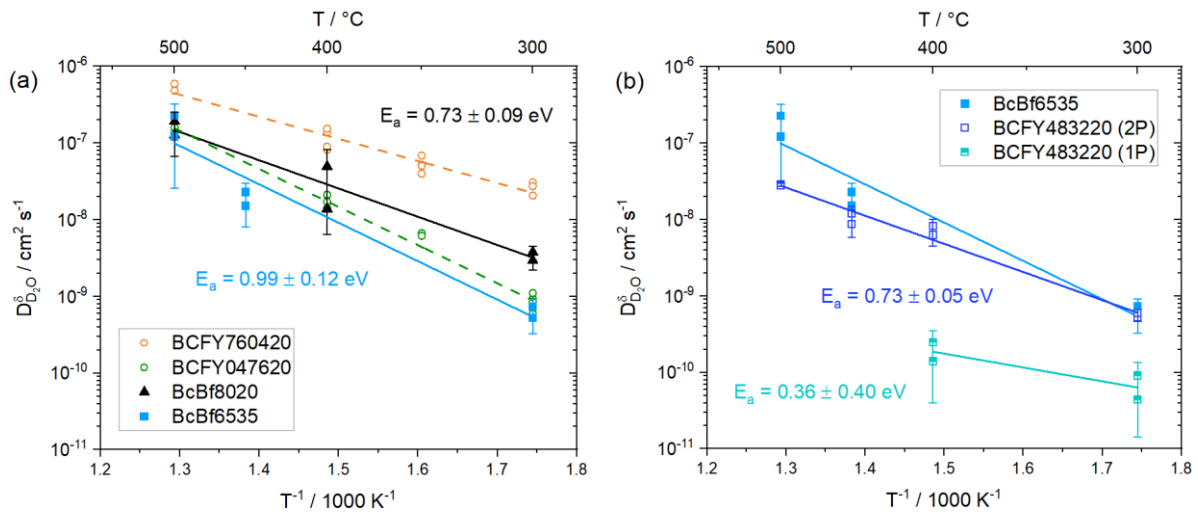

Fig. 4.30 Chemical diffusion coefficient of deuterium oxide $D^{\delta}_{D_2O}$ as a function of inverse temperature and activation energies for proton diffusion of **(a)** the artificial composites BcBf8020 and BcBf6535 compared to the single phases BCFY760420 and BCFY047620, and **(b)** the artificial composite BcBf6535 compared to a self-generated composite and a single phase with the same overall stoichiometry ($BaCe_{0.48}Fe_{0.32}Y_{0.20}O_{3-\delta}$). Activation energies are given in the plots. The lines are a guide to the eye.

4.8. Protonic conductivity

The proton conductivity can be calculated according to the Nernst-Einstein relation (refer to section 3.6. Isotope exchange diffusion profiling and secondary ion mass spectrometry, Equation 3.4) from the proton diffusion coefficients in Figure 4.29 ($D_{OH_O^\bullet} \approx D^{\delta}_{D_2O}$; refer to section 4.7. Chemical diffusion coefficient of D_2O) and the proton concentrations $[OH_O^\bullet]$ in Figure 4.25 (refer to section 4.6. Proton uptake capacity). Figure 4.31 shows the proton conductivities of BCFY760420 and BCFY047620, which exceed 10^{-6} S cm^{-1}. This order of magnitude is considered to be sufficient to activate the bulk path of ORR [22, 27].

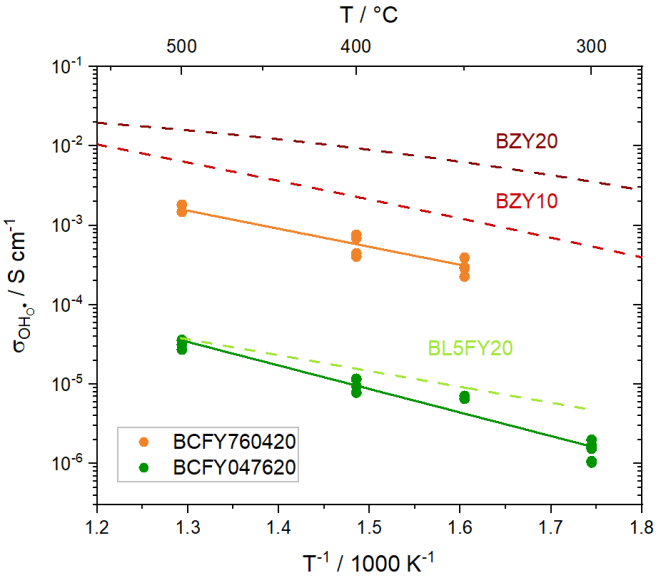

Fig. 4.31 Proton conductivities as a function of inverse temperature of the single phases $BaCe_{0.76}Fe_{0.04}Y_{0.20}O_{3-\delta}$ and $BaCe_{0.04}Fe_{0.76}Y_{0.20}O_{3-\delta}$ compared to BL5FY20 (to be published by C. Berger et al.), BZY20 and BZY10 [8]. The lines are a guide to the eye.

4.9. Electrical conductivity

In addition to their protonic conductivity, triple conducting oxides also transport oxygen ions and electrons (see Figure 4.32). The transport of oxygen is discussed in the following section. This section addresses the topic of electrical conductivity σ. Since the partial electronic conductivity σ_e can be assumed to be much higher than the partial ionic conductivities of both oxygen ions and protons, $\sigma \approx \sigma_e$ should apply. The transport of electronic charge carriers occurs by the small-polaron hopping mechanism, whereby p-type charge carriers (electron holes) are transferred between the B-site ions. This process is particularly sensitive to the amount of transition metals with mixed valence on the B-site (e.g. Fe^{3+}/Fe^{4+} or Fe^{2+}/Fe^{3+}). The percolation threshold is estimated to lie between 15% and 29% of the B-site occupied with transition metals [19]. In this range, there is a significant increase in conductivity. This limit should be achieved with all of the investigated compositions.

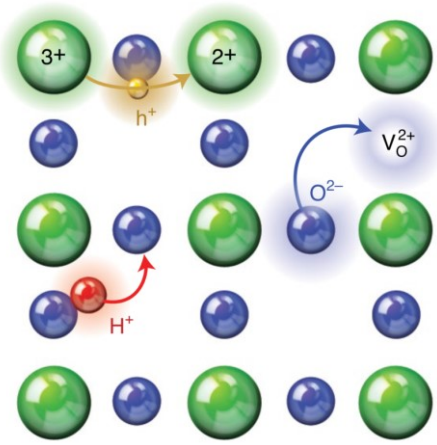

Fig. 4.32 Transport pathways of electron holes (h^+), oxygen ions (O^{2-}) and protons (H^+) in the B-O plane of perovskites. The large, green spheres represent B-site cations with different oxidation states and the smaller, blue spheres represent lattice oxygen. Image taken from [19].

The electrical conductivity of self-generated Y-substituted composites was investigated by dc-conductivity measurements in van der Pauw geometry. In consideration of the determining influence of the B-site composition, different Ce:Fe and Ce:Y ratios were investigated. The electrical conductivity of selected self-generated composites with varying amounts of Fe on the B-site in dry atmosphere as a function of inverse temperature is shown in Figure 4.33a. As expected, in accordance with the thermally activated nature of the electronic conductivity, an increase in temperature results in a corresponding rise in electrical conductivity. Furthermore, the electrical conductivity shows a positive correlation with increasing Fe content. Already small amounts of Fe on the B-site result in a considerable increase in electrical conductivity of several orders of magnitude from BCO to BCFY622. In comparison to the pure phases of BFO and BCO, the composites are situated between them, as expected. Figure 4.33b shows the electrical conductivity of selected self-generated composites with varying amounts of Y on the B-site. The addition of Y appears to have a detrimental effect on the electrical conductivity. In comparison with BCF55, the conductivity of BCFY541 is reduced by one order of magnitude with the addition of small amounts of Y. Despite the constant Fe content, the conductivity continues to decrease with increasing Y content. BCFY442 and BCFY343, which have different amounts of Y on the B-site, are at the same level, which differs from expectations. As BCFY442 was measured before an optimal surface preparation method was employed, additional measurements with a new sample are planned to verify this result. The electronic conductivity is not only affected by the composition and temperature, but also influenced by the atmosphere. For all investigated samples, measurements were conducted in both dry and humid atmospheres with two different oxygen partial pressures. Figure 4.34 gives an overview of the results of the self-generated composite BCFY343. The results of other investigated samples are summarised in the appendix (Figures A24–A27).

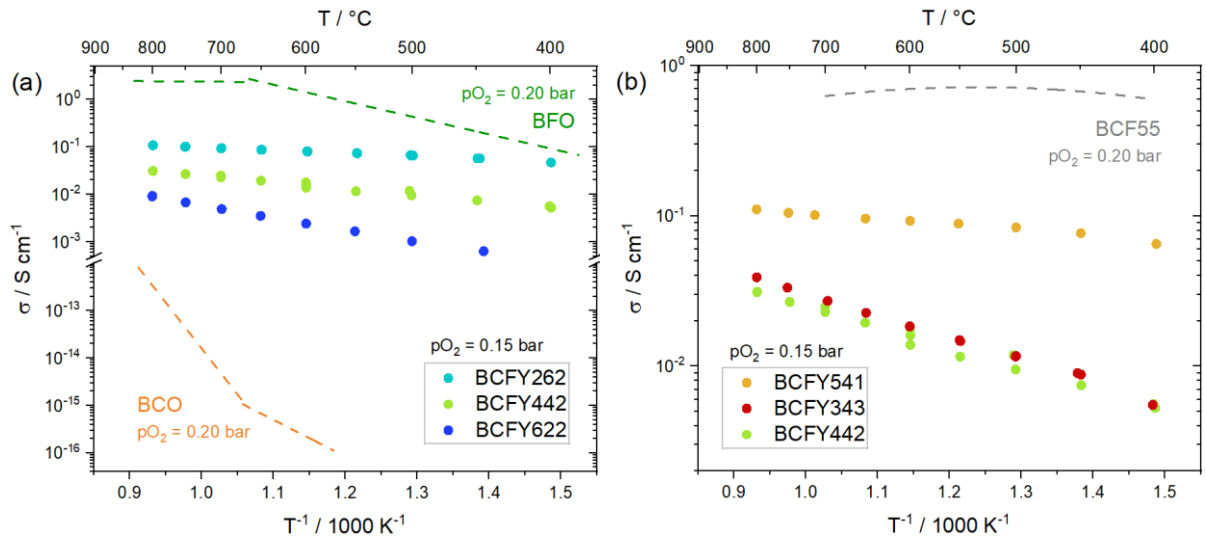

Fig. 4.33 Electrical conductivity in dry atmosphere with 0.15 bar pO_2 as a function of inverse temperature of **(a)** self-generated $BaCe_{0.8-x}Fe_xY_{0.2}O_{3-\delta}$ (x = 0.2, 0.4, 0.6) composites compared to the single phases $BaFeO_{3-\delta}$ [103] and $BaCeO_3$ [104] and **(b)** self-generated $BaCe_{0.6-x}Fe_{0.4}Y_xO_{3-\delta}$ (x = 0.1, 0.2, 0.3) composites compared to the self-generated composite $BaCe_{0.5}Fe_{0.5}O_{3-\delta}$ in humid atmosphere [105].

At the beginning, the electrical conductivity was determined in dry atmosphere with a pO_2 of 0.15 and 0.10 bar. A higher pO_2 favours the incorporation of oxygen according to Equation 2.8 (refer to section 2.4. Proton uptake in triple conducting oxides). This shifts the reaction to the right side, which leads to an increase in electronic charge carriers resulting in a higher electrical conductivity. As expected, the results show a higher conductivity at 0.15 bar than at 0.10 bar oxygen partial pressure. In humid atmosphere, the electrical conductivity decreases to a lower level (see Figure 4.34a). In accordance with Equation 2.7 (refer to section 2.4. Proton uptake in triple conducting oxides), this is as expected, as the incorporation of water occurs at the expense of electron holes, which leads to a decrease in electronic conductivity. The extent of the change resulting from the humidification process varies depending on the composition of the samples. As proton uptake occurs during humidification, it can be reasonably assumed that the proton uptake capacity is a contributing factor in the observed changes. Samples with a higher proton uptake capacity are considered to show the most pronounced differences in conductivity between the dry and humid atmosphere. However, the opposite was observed. The sample with the lowest proton concentration (BCFY262) showed the most pronounced change between dry and humid conditions. One potential explanation for this phenomenon is the small relative amount of Ce-rich phase in BCFY262 (Table A22). This implies that the proton uptake in this sample may have occurred to a large extent in the Fe-rich phase. It is essential to know the distribution of proton uptake between the two phases. This would enable a more meaningful investigation of the correlation between the change in electrical conductivity resulting from

humidification and the proton uptake in the Fe-rich phase, which is the phase mainly responsible for the electronic conductivity. Nevertheless, it should be noted that other factors may also contribute to the observed change by hydration. The proton concentration in comparison with the difference between the electrical conductivity in dry and humid atmosphere is summarised in Table A46 in the appendix. Figure 4.34b shows the electrical conductivity in dry atmosphere following the measurements in humid atmosphere. In general, after the drying process, the electrical conductivity returns to the same level as before the humidification. At elevated temperatures (measurements which have not been conducted directly after the drying process), a degradation can be observed, resulting in a slight decrease in conductivity over time.

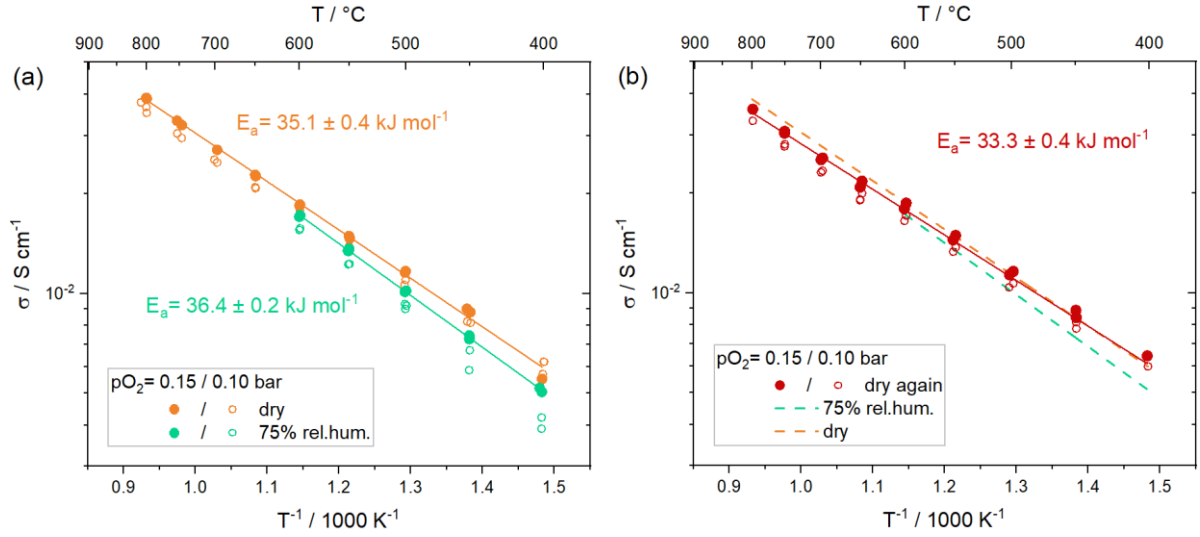

Fig. 4.34 Electrical conductivity as a function of inverse temperature of the self-generated composite $BaCe_{0.3}Fe_{0.4}Y_{0.3}O_{3-\delta}$ **(a)** in both dry and humid atmosphere and **(b)** in dry atmosphere following measurements in humid atmosphere. Activation energies are given in the plots. The lines are a guide to the eye.

This observation is also illustrated in Figure 4.35. However, not all samples showed the same behaviour following drying. The results in dry atmosphere following the measurements in humid atmosphere of other samples are summarised and discussed in the appendix (Figures A24–A27). Some of the samples underwent investigation over a period of approximately 10,000 hours, during which they were humidified and dried, which represents an additional stress on the sample. Figure 4.35 shows the data points for the electrical conductivity as a function of time. In humid atmosphere, the electrical conductivity decreases to a lower level and then returns to the level observed prior to humidification when dried. Following the drying process, the sample begins to degrade, a phenomenon that is not unexpected given the length of the measurement period. These figures are shown and discussed for two additional samples in the appendix (Figure A28).

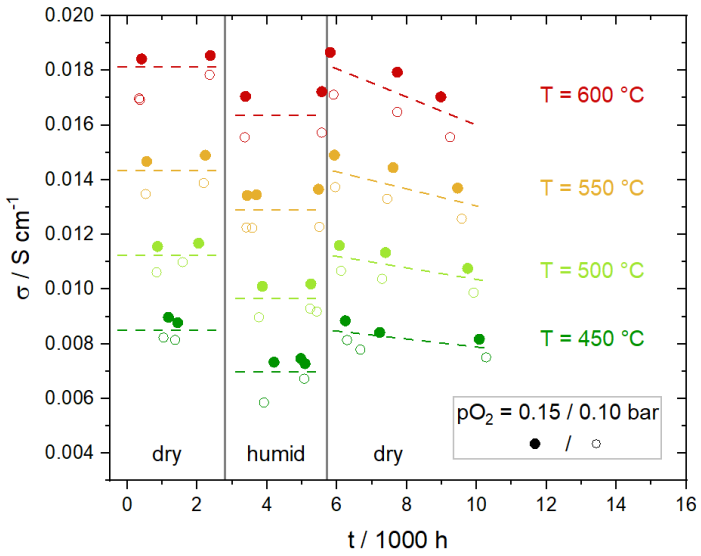

Fig. 4.35 Electrical conductivity of the self-generated composite $BaCe_{0.3}Fe_{0.4}Y_{0.3}O_{3-\delta}$ at selected temperatures (T = 450, 500, 550 and 600 °C) as a function of time. The lines are a guide to the eye.

4.10. Oxygen exchange kinetics

As illustrated in Figure 4.32 (refer to section 4.9. Electrical conductivity), oxygen ions migrate by vacancy diffusion. The oxygen ions are transferred from their original lattice position to a neighbouring oxygen vacancy [106, 107]. In perovskites, the transport of oxygen is primarily influenced by surface exchange and bulk diffusion. The bulk diffusion properties were investigated by conductivity relaxation measurements on selected composites. In most of the cases, the oxygen exchange kinetics were diffusion-controlled. However, some few measurements exhibited mixed controlled kinetics (refer to section 3.7.3. Dc-conductivity relaxation measurements). The migration of oxygen is influenced by the cations surrounding the oxygen path and the distance and configuration of the initial and final site of the vacancy [106]. Consequently, the oxygen exchange kinetics were investigated in relation to the B-site composition for different Ce:Fe and Ce:Y ratios. Figure 4.36 shows the chemical diffusion coefficients of oxygen for selected self-generated composites with varying B-site compositions in dry atmosphere, as a function of inverse temperature. It was observed that the diffusion coefficient of oxygen increased with increasing temperature and increasing Fe content in the precursor. As the Fe-rich phase is the phase with a higher oxygen vacancy concentration, this is consistent with expectations. A correlation was not found between the diffusion coefficient and the Y content. However, this phenomenon was also observed with the electrical conductivity (refer to section 4.9. Electrical conductivity, Figure 4.33), which leads to the assumption that there may be an issue with the

results of BCFY442. In comparison to typical SOFC cathode materials with a mixed oxygen ionic-electronic conducting character, such as $Ba_{0.5}Sr_{0.5}Co_{0.8}Fe_{0.2}O_{3-\delta}$ (BSCF) and $La_{0.6}Sr_{0.4}CoO_{3-\delta}$ (LSC64), the chemical diffusion coefficients of oxygen of the self-generated composites from this work are of a similar magnitude. As the oxygen exchange kinetics are also influenced by the atmosphere, conductivity relaxation measurements were conducted in both dry and humid atmospheres. In dry atmosphere, the concentration of protonic defects is sufficiently low for all samples and temperatures to be considered negligible in terms of their contribution to the diffusion coefficient. In humid atmosphere, however, this assumption may not be valid, as the concentration of protonic defects is significant, particularly at low temperatures and for samples with a high Ce content.

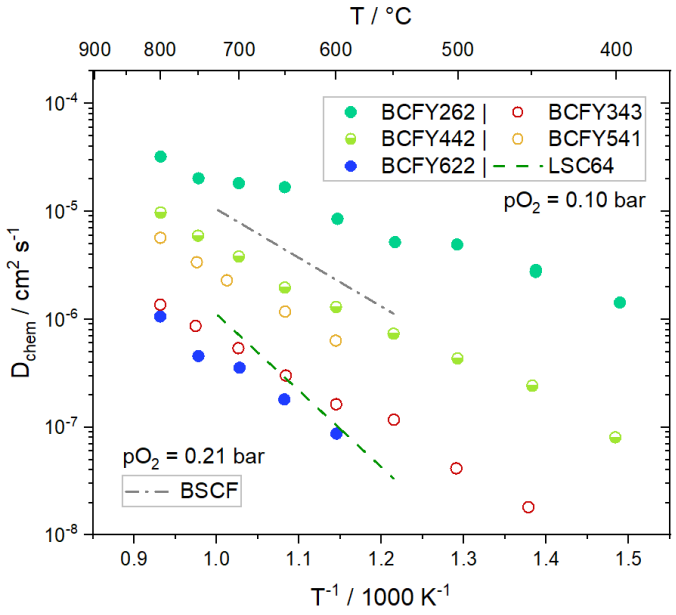

Fig. 4.36 Chemical diffusion coefficients of oxygen in dry atmosphere as a function of inverse temperature of self-generated $BaCe_{0.8-x}Fe_xY_{0.2}O_{3-\delta}$ (x = 0.2, 0.4, 0.6) and $BaCe_{0.6-x}Fe_{0.4}Y_xO_{3-\delta}$ (x = 0.1, 0.2, 0.3) composites compared to single phase $Ba_{0.5}Sr_{0.5}Co_{0.8}Fe_{0.2}O_{3-\delta}$ [108] and $La_{0.6}Sr_{0.4}CoO_{3-\delta}$ [109].

The chemical diffusion coefficients of the self-generated composite BCFY343 are shown Figure 4.37. At the beginning, the diffusion coefficients were determined in dry atmosphere, with a change in pO_2 from 0.15 to 0.10 bar and vice versa. The results of the oxidation and reduction process are in good agreement with each other. In humid atmosphere, the diffusion coefficients showed a slight increase (see Figure 4.37a), a phenomenon also observed in the BCFY442 sample (Figure A30 in the appendix). However, some of the fits do not match well with the relaxation curves, which raises questions about the reliability of the results in humid atmosphere. Figure 4.37b shows the chemical diffusion coefficients of oxygen in dry atmosphere following the measurements in humid atmosphere. After drying, the slope, which is related to the activation energy of oxygen migration, undergoes a change.

At elevated temperatures, the diffusion coefficients are lower than those observed prior to humidification. In contrast, at lower temperatures they are higher. This observation can be attributed to the degradation shown in Figure 4.35. For BCFY622 and BCFY541, the samples investigated with the highest Ce content, the data obtained from measurements in humid atmosphere could not be described using the diffusion models from section 3.7.3. Dc-conductivity relaxation measurements. However, the changes resulting in this phenomenon are reversible, as results were available for measurements after drying. The sample BCFY262 degraded irreversibly because of humidification, as previously discussed in relation to the results of the electrical conductivity (Figure A24 in the appendix). Consequently, the results for the chemical diffusion coefficients are only available in dry atmosphere prior to humidification. Similarly, irreversible changes were observed in the sample BCFY442, as the increase in chemical diffusion coefficients remains upon drying. A detailed summary of the results obtained for the additional samples can be found in Figures A29–A32 in the appendix.

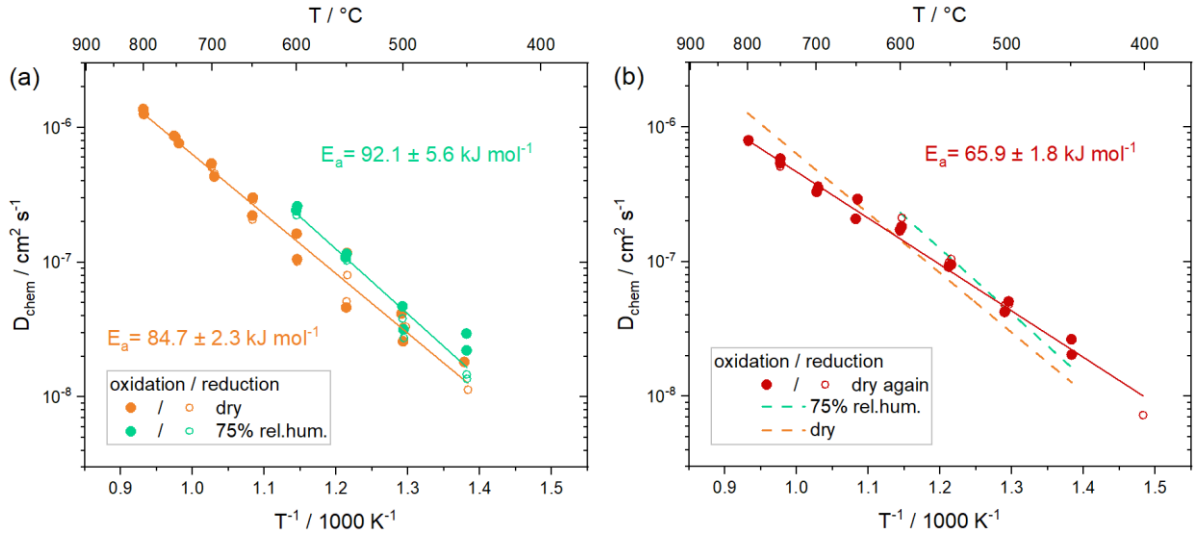

Fig. 4.37 Chemical diffusion coefficients as a function of inverse temperature of the self-generated composite $BaCe_{0.3}Fe_{0.4}Y_{0.3}O_{3-\delta}$ **(a)** in both dry and humid atmosphere and **(b)** in dry atmosphere following measurements in humid atmosphere. Activation energies are given in the plots. The lines are a guide to the eye.

5. Summary and conclusions

This thesis examined the impact of acceptor substitution in self-generated composites, focusing on the influence on the crystal structure, phase composition, and mass and charge transport properties of materials substituted with a variety of acceptors. More than 30 composites and over 30 single phases with varying acceptor dopants Acc^{3+} and compositions were prepared for investigating the complex structure-property relations in this system. Following the preparation of the calcined powders via "one-pot" synthesis, they were investigated by X-ray powder diffraction and Rietveld refinement, providing insights in crystal structure, lattice parameters and relative amounts of the respective phases. Subsequent to densification by SPS, the overall cation composition was examined for selected samples by ICP-OES, which demonstrated that no cations were lost during the processing. The composition of the B-site was determined using STEM, which revealed an enrichment of all acceptor dopants in the Fe-rich phase, even in the artificial composites (created by mixing two separately prepared powders). As anticipated, the proton uptake capacity was observed to increase with the addition of Acc^{3+} to the system, as determined by thermogravimetry. However, no significant differences were observed between the various acceptor substituents. Furthermore, the chemical diffusion coefficients of D_2O and oxygen, and the electrical conductivity were investigated by means of isotope exchange experiments, conductivity relaxation and conductivity measurements, respectively. At the outset of this thesis, four research questions were raised, which are answered in the following section.

I. Which properties of the acceptor substituent govern its distribution between the two phases of the composite?

The acceptor substituents show the most pronounced positive impact on the proton uptake capacity in the Ce-rich phase, given that this is the phase with the higher degree of hydration. However, it was observed that the acceptor substituents exhibit a strong tendency to accumulate in the Fe-rich phase. The initial approach to introduce the acceptor dopant specifically into the Ce-rich phase was to match the ionic radius of Acc^{3+} to that of the cerate phase. However, the use of trivalent ions with a similar ionic radius to Ce^{4+} did not yield the expected result. Furthermore, it was anticipated that the basicity of the oxides in terms of an acid-base reaction would result in the incorporation of a less basic acceptor substituent into the more basic $BaCeO_3$. However, this also did not demonstrate a clear correlation with the tendency to incorporate Acc^{3+} in one of the two phases. Based on the results of the present thesis, this aspect was further analysed by R. Merkle et al. using DFT calculations [91]. They discovered that the enrichment of oxygen vacancies $V_O^{\bullet\bullet}$ (i.e. positive-effective defects) in the Fe-rich phase is the primary driving force, which attracts the acceptor substituents (i.e. negative-effective defects) towards the ferrate phase. Consequently, despite different acidity and size mismatches, all the considered Acc^{3+} have a segregation tendency towards the Fe-rich phase, thereby strongly decreasing the capacity for hydration.

II. How can the protonic conductivity in materials with three charge carriers be meaningfully determined?

The direct measurement of the protonic conductivity in this system is challenging, as the separation of the protonic conductivity from the total electrical conductivity (which comprises electronic and ionic conductivity, including protons and oxygen ions) is difficult. This thesis presents a novel approach for determining the protonic conductivity in triple conducting oxides. The proton mobility is measured by evaluating the diffusion profiles resulting from isotope exchange experiments. From the diffusion profiles of D_2O, the chemical diffusion coefficient $D^{\delta}_{D_2O}$, which corresponds approximately to the diffusion coefficient of protonic defects $D_{OH^{\bullet}_O}$, can be derived. By employing the Nernst-Einstein equation in combination with the concentration of protonic defects, it is possible to obtain the proton conductivity. As there is currently only a limited amount of data available on this topic, the value of these results to the scientific community is particularly high.

III. What are the effects of acceptor substitution on the fundamental material properties?

The introduction of acceptor substituents results in a narrowing of the miscibility gap in comparison to the acceptor-free system. This phenomenon is more pronounced in composites containing acceptors with a larger ionic radius (Acc = Y, Gd, Sm) in comparison to composites containing acceptors with a smaller ionic radius (Acc = Sc, In, Yb). As the amount of Acc^{3+} increases, the miscibility gap narrows further. A smaller miscibility gap is unfavourable, as it complicates the processing procedure by requiring the avoidance of elevated temperatures. With regard to the proton uptake capacity, the incorporation of acceptor substituents results in a significant increase in comparison to the acceptor-free system. The thermodynamic parameters were determined for the Y- and In-substituted systems. With an increasing amount of acceptor substituent $\Delta G^{\circ}_{hydrat}$ becomes more negative, which leads to a stronger tendency for hydration. As anticipated, the proton uptake capacity also increases with increasing acceptor content. Conversely, the electronic conductivity decreases with increasing acceptor content.

IV. Which optimisation guidelines can be derived from the obtained comprehensive results?

In general, an increase in the overall concentration of Fe in the material results in an increased electrical conductivity. Conversely, an increase in the overall concentration of Ce in the material results in an increased proton uptake capacity. Accordingly, a compromise has to be found with regard to the Ce:Fe ratio, given that these properties show opposing trends. Additionally, the amount of acceptor substituent has to be chosen with care, as an increasing amount of acceptor not only enhances proton uptake but also narrows the miscibility gap and reduces the electrical conductivity. With the “one-pot” synthesis method, the distribution of the cations between the two phases cannot be influenced. This issue can be avoided through the preparation of artificial composites. However, as the two phases are similar in terms of their structures and defect chemistry, cation interdiffusion is likely to occur during processing and potentially also during operation, which could result in reduced stability. It can thus be

concluded that the present system, although highly interesting from a fundamental point of view, is not the optimal candidate for technical application in PCFC air electrodes.

An interesting approach for future studies would be to explore alternative material combinations consisting of two phases with differing structures and/or differing defect chemistry. For instance, such combinations may be composites consisting of a perovskite and a non-perovskite phase, the latter exhibiting a fluorite, Ruddlesden-Popper, spinel or brownmillerite structure. As demonstrated by the comprehensive results of the present thesis, special care must be taken to design the material system, in order to have a predominantly electronic and a predominantly protonic conducting phase, respectively, with a significant miscibility gap and weak attraction of acceptor ions into the electronic conducting phase.

6. References

[1] G. Notton, M.-L. Nivet, C. Voyant, C. Paoli, C. Darras, F. Motte, A. Fouilloy, Intermittent and stochastic character of renewable energy sources: Consequences, cost of intermittence and benefit of forecasting, *Renewable and Sustainable Energy Reviews* **87** (2018) 96, https://doi.org/10.1016/j.rser.2018.02.007.

[2] I.T. Bello, S. Zhai, Q. He, C. Cheng, Y. Dai, B. Chen, Y. Zhang, M. Ni, Materials development and prospective for protonic ceramic fuel cells, *International Journal of Energy Research* **46** (2022) (3) 2212, https://doi.org/10.1002/er.7371.

[3] M. Ni, Z. Shao, Fuel cells that operate at 300° to 500°C, *Science* **369** (2020) (6500) 138, https://doi:10.1126/science.abc9136.

[4] H. Iwahara, High temperature proton conducting oxides and their applications to solid electrolyte fuel cells and steam electrolyzer for hydrogen production, *Solid State Ionics* **28-30** (1988) 573, https://doi.org/10.1016/S0167-2738(88)80104-8.

[5] H. Iwahara, T. Esaka, H. Uchida, N. Maeda, Proton conduction in sintered oxides and its application to steam electrolysis for hydrogen production, *Solid State Ionics* **3-4** (1981) 359, https://doi.org/10.1016/0167-2738(81)90113-2.

[6] H. Iwahara, H. Uchida, K. Ono, K. Ogaki, Proton conduction in sintered oxides based on $BaCeO_3$, *Journal of The Electrochemical Society* **135** (1988) (2) 529, https://doi.org/10.1149/1.2095649.

[7] K. Katahira, Y. Kohchi, T. Shimura, H. Iwahara, Protonic conduction in Zr-substituted $BaCeO_3$, *Solid State Ionics* **138** (2000) 91, https://doi.org/10.1016/S0167-2738(00)00777-3.

[8] K.D. Kreuer, Proton-conducting oxides, *Annual Review of Materials Research* **33** (2003) (1) 333, https://doi.org/10.1146/annurev.matsci.33.022802.091825.

[9] N. Kochetova, I. Animitsa, D. Medvedev, A. Demin, P. Tsiakaras, Recent activity in the development of proton-conducting oxides for high-temperature applications, *RSC Advances* **6** (2016) (77) 73222, https://doi.org/10.1039/C6RA13347A.

[10] C. Duan, J. Tong, M. Shang, S. Nikodemski, M. Sanders, S. Ricote, A. Almansoori, R. O'Hayre, Readily processed protonic ceramic fuel cells with high performance at low temperatures, *Science* **349** (2015) (6254) 1321, https://doi.org/10.1126/science.aab3987.

[11] H.-I. Ji, J.-H. Lee, J.-W. Son, K.J. Yoon, S. Yang, B.-K. Kim, Protonic ceramic electrolysis cells for fuel production: A brief review, *Journal of the Korean Ceramic Society* **57** (2020) (5) 480, https://doi.org/10.1007/s43207-020-00059-4.

[12] S. Klinsrisuk, S. Tao, J.T.S. Irvine, In: A. Basile, L. Di Paola, F.l. Hai, V. Piemonte, Editors, *Membrane Reactors for Energy Applications and Basic Chemical Production*, Woodhead Publishing (2015), p.543-563. https://doi.org/10.1016/B978-1-78242-223-5.00018-2.

[13] S. Hamakawa, T. Hibino, H. Iwahara, Electrochemical hydrogen permeation in a proton-hole mixed conductor and its application to a membrane reactor, *Journal of The Electrochemical Society* **141** (1994) (7) 1720, https://doi.org/10.1149/1.2054993.

[14] S. Choi, C.J. Kucharczyk, Y. Liang, X. Zhang, I. Takeuchi, H.-I. Ji, S.M. Haile, Exceptional power density and stability at intermediate temperatures in protonic ceramic fuel cells, *Nature Energy* **3** (2018) (3) 202, https://doi.org/10.1038/s41560-017-0085-9.

[15] H. An, H.-W. Lee, B.-K. Kim, J.-W. Son, K.J. Yoon, H. Kim, D. Shin, H.-I. Ji, J.-H. Lee, A 5 × 5 cm^2 protonic ceramic fuel cell with a power density of 1.3 W cm^{-2} at 600 °C, *Nature Energy* **3** (2018) (10) 870, https://doi.org/10.1038/s41560-018-0230-0.

[16] F. He, Y. Zhou, T. Hu, Y. Xu, M. Hou, F. Zhu, D. Liu, H. Zhang, K. Xu, M. Liu, Y. Chen, An efficient high-entropy perovskite-type air electrode for reversible oxygen reduction and water splitting in protonic ceramic cells, *Advanced Materials* **35** (2023) (16) 2209469, https://doi.org/10.1002/adma.202209469.

[17] C. Duan, J. Huang, N. Sullivan, R. O'Hayre, Proton-conducting oxides for energy conversion and storage, *Applied Physics Reviews* **7** (2020) (1) 011314, https://doi.org/10.1063/1.5135319.

[18] E. Fabbri, D. Pergolesi, E. Traversa, Materials challenges toward proton-conducting oxide fuel cells: A critical review, *Chemical Society Reviews* **39** (2010) (11) 4355, https://doi.org/10.1039/B902343G.

[19] M. Papac, V. Stevanović, A. Zakutayev, R. O'Hayre, Triple ionic–electronic conducting oxides for next-generation electrochemical devices, *Nature Materials* **20** (2021) (3) 301, https://doi.org/10.1038/s41563-020-00854-8.

[20] R. Merkle, M.F. Hoedl, G. Raimondi, R. Zohourian, J. Maier, Oxides with mixed protonic and electronic conductivity, *Annual Review of Materials Research* **51** (2021) (1) 461, https://doi.org/10.1146/annurev-matsci-091819-010219.

[21] I.T. Bello, Y. Song, N. Yu, Z. Li, S. Zhao, A. Maradesa, T. Liu, Z. Shao, M. Ni, Evaluation of the electrocatalytic performance of a novel nanocomposite cathode material for ceramic fuel cells, *Journal of Power Sources* **560** (2023) 232722, https://doi.org/10.1016/j.jpowsour.2023.232722.

[22] R. Zohourian, R. Merkle, G. Raimondi, J. Maier, Mixed-conducting perovskites as cathode materials for protonic ceramic fuel cells: Understanding the trends in proton uptake, *Advanced Functional Materials* **28** (2018) 1801241, https://doi.org/10.1002/adfm.201801241.

[23] R. Peng, T. Wu, W. Liu, X. Liu, G. Meng, Cathode processes and materials for solid oxide fuel cells with proton conductors as electrolytes, *Journal of Materials Chemistry* **20** (2010) (30) 6218, https://doi.org/10.1039/C0JM00350F.

[24] Z. Wang, Y. Wang, J. Wang, Y. Song, M. Robson, A. Seong, M. Yang, Z. Zhang, A. Belotti, J. Liu, G. Kim, J. Lim, Z. Shao, F. Ciucci, Rational design of perovskite ferrites as high-performance proton-conducting fuel cell cathodes, *Nature Catalysis* **5** (2022), https://doi.org/10.1038/s41929-022-00829-9.

[25] R. Strandbakke, V.A. Cherepanov, A.Y. Zuev, D.S. Tsvetkov, C. Argirusis, G. Sourkouni, S. Prünte, T. Norby, Gd- and Pr-based double perovskite cobaltites as oxygen electrodes for proton ceramic fuel cells and electrolyser cells, *Solid State Ionics* **278** (2015) 120, https://doi.org/10.1016/j.ssi.2015.05.014.

[26] Z. Liu, Y. Chen, G. Yang, M. Yang, R. Ji, Y. Song, R. Ran, W. Zhou, Z. Shao, One-pot derived thermodynamically quasi-stable triple conducting nanocomposite as robust bifunctional air electrode for reversible protonic ceramic cells, *Applied Catalysis B: Environmental* **319** (2022) 121929, https://doi.org/10.1016/j.apcatb.2022.121929.

[27] R. Merkle, D. Poetzsch, J. Maier, Oxygen reduction reaction at cathodes on proton conducting oxide electrolytes: Contribution from three phase boundary compared to bulk path, *ECS Transactions* **66** (2015) (2) 95, https://doi.org/10.1149/06602.0095ecst.

[28] S. Cheng, Y. Wang, L. Zhuang, J. Xue, Y. Wei, A. Feldhoff, J. Caro, H. Wang, A dual-phase ceramic membrane with extremely high H_2 permeation flux prepared by autoseparation of a ceramic precursor, *Angewandte Chemie International Edition* **55** (2016) (36) 10895, https://doi.org/10.1002/anie.201604035.

[29] J. Cao, Y. Ji, Z. Shao, Perovskites for protonic ceramic fuel cells: A review, *Energy & Environmental Science* **15** (2022) (6) 2200, https://doi.org/10.1039/D2EE00132B.

[30] Z. Pan, C. Duan, T. Pritchard, A. Thatte, E. White, R. Braun, R. O'Hayre, N.P. Sullivan, High-yield electrochemical upgrading of CO_2 into CH_4 using large-area protonic ceramic electrolysis cells, *Applied Catalysis B: Environmental* **307** (2022) 121196, https://doi.org/10.1016/j.apcatb.2022.121196.

[31] C. Duan, R. Kee, H. Zhu, N. Sullivan, L. Zhu, L. Bian, D. Jennings, R. O'Hayre, Highly efficient reversible protonic ceramic electrochemical cells for power generation and fuel production, *Nature Energy* **4** (2019) (3) 230, https://doi.org/10.1038/s41560-019-0333-2.

[32] S. Choi, T.C. Davenport, S.M. Haile, Protonic ceramic electrochemical cells for hydrogen production and electricity generation: Exceptional reversibility, stability, and demonstrated faradaic efficiency, *Energy & Environmental Science* **12** (2019) (1) 206, https://doi.org/10.1039/C8EE02865F.

[33] D. Medvedev, Trends in research and development of protonic ceramic electrolysis cells, *International Journal of Hydrogen Energy* **44** (2019) (49) 26711, https://doi.org/10.1016/j.ijhydene.2019.08.130.

[34] R. O'Hayre, S.-W. Cha, W. Colella, F.B. Prinz, *Fuel cell fundamentals*, John Wiley & Sons, Inc., Hoboken, New Jersey (2016). https://doi.org/10.1002/9781119191766.

[35] Z. Shao, M.O. Tade, *Intermediate-temperature solid oxide fuel cells: Materials and applications*, Springer-Verlag, Berlin Heidelberg (2016). https://doi.org/10.1007/978-3-662-52936-2.

[36] K. Kendall, M. Kendall, Editors, *High-temperature solid oxide fuel cells for the 21st century*, Academic Press, Oxford, UK (2016), https://doi.org/10.1016/C2011-0-09278-5.

[37] A. Dubois, S. Ricote, R.J. Braun, Benchmarking the expected stack manufacturing cost of next generation, intermediate-temperature protonic ceramic fuel cells with solid oxide fuel cell technology, *Journal of Power Sources* **369** (2017) 65, https://doi.org/10.1016/j.jpowsour.2017.09.024.

[38] M. Oishi, S. Akoshima, K. Yashiro, K. Sato, J. Mizusaki, T. Kawada, Defect structure analysis of B-site doped perovskite-type proton conducting oxide $BaCeO_3$: Part 2: The electrical conductivity and diffusion coefficient of $BaCe_{0.9}Y_{0.1}O_{3-\delta}$, *Solid State Ionics* **179** (2008) (39) 2240, https://doi.org/10.1016/j.ssi.2008.08.005.

[39] T. Hibino, A. Hashimoto, M. Suzuki, M. Sano, Proton conduction at the surface of Y-doped $BaCeO_3$, *The Journal of Physical Chemistry B* **105** (2001) (46) 11399, https://doi.org/10.1021/jp0124342.

[40] N. Zakowsky, S. Williamson, J.T.S. Irvine, Elaboration of CO_2 tolerance limits of $BaCe_{0.9}Y_{0.1}O_{3-\delta}$ electrolytes for fuel cells and other applications, *Solid State Ionics* **176** (2005) (39) 3019, https://doi.org/10.1016/j.ssi.2005.09.040.

[41] S.M. Haile, G. Staneff, K.H. Ryu, Non-stoichiometry, grain boundary transport and chemical stability of proton conducting perovskites, *Journal of Materials Science* **36** (2001) (5) 1149, https://doi.org/10.1023/A:1004877708871.

[42] N. Taniguchi, C. Nishimura, J. Kato, Endurance against moisture for protonic conductors of perovskite-type ceramics and preparation of practical conductors, *Solid State Ionics* **145** (2001) (1) 349, https://doi.org/10.1016/S0167-2738(01)00930-4.

[43] E. Fabbri, A. D'Epifanio, E. Di Bartolomeo, S. Licoccia, E. Traversa, Tailoring the chemical stability of $Ba(Ce_{0.8-x}Zr_x)Y_{0.2}O_{3-\delta}$ protonic conductors for intermediate temperature solid oxide fuel cells (IT-SOFCs), *Solid State Ionics* **179** (2008) (15) 558, https://doi.org/10.1016/j.ssi.2008.04.002.

[44] A. D'Epifanio, E. Fabbri, E. Di Bartolomeo, S. Licoccia, E. Traversa, Design of $BaZr_{0.8}Y_{0.2}O_{3-\delta}$ protonic conductor to improve the electrochemical performance in intermediate temperature solid oxide fuel cells (IT-SOFCs), *Fuel Cells* **8** (2008) (1) 69, https://doi.org/10.1002/fuce.200700045.

[45] S. Luo, W.A. Daoud, Recent progress in organic–inorganic halide perovskite solar cells: Mechanisms and material design, *Journal of Materials Chemistry A* **3** (2015) (17) 8992, https://doi.org/10.1039/C4TA04953E

[46] P. Pers, V. Mao, M. Taillades, G. Taillades, Electrochemical behavior and performances of Ni-$BaZr_{0.1}Ce_{0.7}Y_{0.1}Yb_{0.1}O_{3-\delta}$ cermet anodes for protonic ceramic fuel cell, *International Journal of Hydrogen Energy* **43** (2018) (4) 2402, https://doi.org/10.1016/j.ijhydene.2017.12.024.

[47] X. Lv, H. Chen, W. Zhou, S.-D. Li, Z. Shao, A CO_2-tolerant $SrCo_{0.8}Fe_{0.15}Zr_{0.05}O_{3-\delta}$ cathode for proton-conducting solid oxide fuel cells, *Journal of Materials Chemistry A* **8** (2020) (22) 11292, https://doi.org/10.1039/D0TA02435J

[48] L. Bi, Z. Tao, W. Sun, S. Zhang, R. Peng, W. Liu, Proton-conducting solid oxide fuel cells prepared by a single step co-firing process, *Journal of Power Sources* **191** (2009) (2) 428, https://doi.org/10.1016/j.jpowsour.2009.02.049.

[49] Z. Shao, S.M. Haile, A high-performance cathode for the next generation of solid-oxide fuel cells, *Nature* **431** (2004) (7005) 170, https://doi.org/10.1038/nature02863.

[50] W.G. Wang, M. Mogensen, High-performance lanthanum-ferrite-based cathode for SOFC, *Solid State Ionics* **176** (2005) (5) 457, https://doi.org/10.1016/j.ssi.2004.09.007.

[51] L. Nie, M. Liu, Y. Zhang, M. Liu, $La_{0.6}Sr_{0.4}Co_{0.2}Fe_{0.8}O_{3-\delta}$ cathodes infiltrated with samarium-doped cerium oxide for solid oxide fuel cells, *Journal of Power Sources* **195** (2010) (15) 4704, https://doi.org/10.1016/j.jpowsour.2010.02.049.

[52] Y. Song, Y. Chen, W. Wang, C. Zhou, Y. Zhong, G. Yang, W. Zhou, M. Liu, Z. Shao, Self-assembled triple-conducting nanocomposite as a superior protonic ceramic fuel cell cathode, *Joule* **3** (2019) (11) 2842, https://doi.org/10.1016/j.joule.2019.07.004.

[53] M. Wang, C. Su, Z. Zhu, H. Wang, L. Ge, Composite cathodes for protonic ceramic fuel cells: Rationales and materials, *Composites Part B: Engineering* **238** (2022) 109881, https://doi.org/10.1016/j.compositesb.2022.109881.

[54] D. Neagu, J.T.S. Irvine, J. Wang, B. Yildiz, A.K. Opitz, J. Fleig, Y. Wang, J. Liu, L. Shen, F. Ciucci, B.A. Rosen, Y. Xiao, K. Xie, G. Yang, Z. Shao, Y. Zhang, J. Reinke, T.A. Schmauss, S.A. Barnett, R. Maring, V. Kyriakou, U. Mushtaq, M.N. Tsampas, Y. Kim, R. O'Hayre, A.J. Carrillo, T. Ruh, L. Lindenthal, F. Schrenk, C. Rameshan, E.I. Papaioannou, K. Kousi, I.S. Metcalfe, X. Xu, G. Liu, Roadmap on exsolution for energy applications, *Journal of Physics: Energy* **5** (2023) (3) 031501, https://doi.org/10.1088/2515-7655/acd146.

[55] C. Zhao, Y. Li, W. Zhang, Y. Zheng, X. Lou, B. Yu, J. Chen, Y. Chen, M. Liu, J. Wang, Heterointerface engineering for enhancing the electrochemical performance of solid oxide cells, *Energy & Environmental Science* **13** (2020) (1) 53, https://doi.org/10.1039/C9EE02230A.

[56] K. Pei, Y. Zhou, K. Xu, H. Zhang, Y. Ding, B. Zhao, W. Yuan, K. Sasaki, Y. Choi, Y. Chen, M. Liu, Surface restructuring of a perovskite-type air electrode for reversible protonic ceramic electrochemical cells, *Nature Communications* **13** (2022) (1) 2207, https://doi.org/10.1038/s41467-022-29866-5.

[57] W. Zhang, H. Muroyama, Y. Mikami, Q. Liu, X. Liu, T. Matsui, K. Eguchi, Effectively enhanced oxygen reduction activity and stability of triple-conducting composite cathodes by strongly interacting interfaces for protonic ceramic fuel cells, *Chemical Engineering Journal* **461** (2023) 142056, https://doi.org/10.1016/j.cej.2023.142056.

[58] F. Giannici, A. Longo, A. Balerna, K.-D. Kreuer, A. Martorana, Indium doping in barium cerate: The relation between local symmetry and the formation and mobility of protonic defects, *Chemistry of Materials* **19** (2007) (23) 5714, https://doi.org/10.1021/cm701902p.

[59] H. Iwahara, T. Yajima, H. Ushida, Effect of ionic radii of dopants on mixed ionic conduction (H^++O^{2-}) in $BaCeO_3$-based electrolytes, *Solid State Ionics* **70-71** (1994) 267, https://doi.org/10.1016/0167-2738(94)90321-2.

[60] W. Münch, G. Seifert, K.D. Kreuer, J. Maier, A quantum molecular dynamics study of proton conduction phenomena in $BaCeO_3$, *Solid State Ionics* **86-88** (1996) 647, https://doi.org/10.1016/0167-2738(96)00229-9.

[61] S. Patel, F. Liu, H. Ding, C. Duan, I. Ghamarian, On proton conduction mechanism for electrolyte materials in solid oxide fuel cells, *International Journal of Hydrogen Energy* (2023), https://doi.org/10.1016/j.ijhydene.2023.11.012.

[62] M.F. Hoedl, A. Chesnokov, D. Gryaznov, R. Merkle, E.A. Kotomin, J. Maier, Proton migration barriers in $BaFeO_{3-\delta}$ – insights from DFT calculations, *Journal of Materials Chemistry A* **11** (2023) (12) 6336, https://doi.org/10.1039/D2TA08664F

[63] K. Thabet, A. Le Gal La Salle, E. Quarez, O. Joubert, In: M. Lo Faro, Editor, *Solid oxide-based electrochemical devices*, Academic Press (2020), p.91-122. https://doi.org/10.1016/B978-0-12-818285-7.00004-6.

[64] F.J.A. Loureiro, N. Nasani, G.S. Reddy, N.R. Munirathnam, D.P. Fagg, A review on sintering technology of proton conducting $BaCeO_3$-$BaZrO_3$ perovskite oxide materials for protonic ceramic fuel cells, *Journal of Power Sources* **438** (2019) 226991, https://doi.org/10.1016/j.jpowsour.2019.226991.

[65] Z.A. Munir, U. Anselmi-Tamburini, M. Ohyanagi, The effect of electric field and pressure on the synthesis and consolidation of materials: A review of the spark plasma sintering method, *Journal of Materials Science* **41** (2006) (3) 763, https://doi.org/10.1007/s10853-006-6555-2.

[66] A. Coelho, TOPAS and TOPAS-Academic: An optimization program integrating computer algebra and crystallographic objects written in C++, *Journal of Applied Crystallography* **51** (2018) (1) 210, https://doi.org/10.1107/S1600576718000183.

[67] A. LeBail, Whole powder pattern decomposition methods and applications: A retrospection, *Powder Diffraction* **20** (2005) 316, https://doi.org/10.1154/1.2135315.

[68] D. Poetzsch, R. Merkle, J. Maier, Stoichiometry variation in materials with three mobile carriers - Thermodynamics and transport kinetics exemplified for protons, oxygen vacancies, and holes, *Advanced Functional Materials* **25** (2015) (10) 1542, https://doi.org/10.1002/adfm.201402212.

[69] C. Nader, J. Lammer, A. Egger, C. Berger, W. Sitte, W. Grogger, R. Merkle, J. Maier, E. Bucher, Phase composition and proton uptake of acceptor-doped self-generated $Ba(Ce,Fe)O_{3-\delta}$ – $Ba(Fe,Ce)O_{3-\delta}$ composites, *Solid State Ionics* **406** (2024) 116474, https://doi.org/10.1016/j.ssi.2024.116474.

[70] J.A. Kilner, S.J. Skinner, H.H. Brongersma, The isotope exchange depth profiling (IEDP) technique using SIMS and LEIS, *Journal of Solid State Electrochemistry* **15** (2011) (5) 861, https://doi.org/10.1007/s10008-010-1289-0.

[71] R.A. De Souza, J.A. Kilner, C. Jeynes, The application of secondary ion mass spectrometry (SIMS) to the study of high temperature proton conductors (HTPC), *Solid State Ionics* **97** (1997) (1) 409, https://doi.org/10.1016/S0167-2738(97)00038-6.

[72] R. Hancke, S. Fearn, J.A. Kilner, R. Haugsrud, Determination of proton- and oxide ion tracer diffusion in lanthanum tungstate (La/W = 5.6) by means of ToF-SIMS, *Physical Chemistry Chemical Physics* **14** (2012) (40) 13971, https://doi.org/10.1039/C2CP42278F.

[73] A. Seong, J. Kim, D. Jeong, S. Sengodan, M. Liu, S. Choi, G. Kim, Electrokinetic proton transport in triple ($H^+/O^{2-}/e^-$) conducting oxides as a key descriptor for highly efficient protonic ceramic fuel cells, *Advanced Science* **8** (2021) (11) 2004099, https://doi.org/10.1002/advs.202004099.

[74] H. Téllez Lozano, J. Druce, S.J. Cooper, J.A. Kilner, Double perovskite cathodes for proton-conducting ceramic fuel cells: Are they triple mixed ionic electronic conductors?, *Science and Technology of Advanced Materials* **18** (2017) (1) 977, https://doi.org/10.1080/14686996.2017.1402661.

[75] S. Carter, A. Selcuk, R.J. Chater, J. Kajda, J.A. Kilner, B.C.H. Steele, Oxygen transport in selected nonstoichiometric perovskite-structure oxides, *Solid State Ionics* **53-56** (1992) 597, https://doi.org/10.1016/0167-2738(92)90435-R.

[76] C. Cushman, J. Zakel, L. Fisher, J. Banerjee, B. Lunt, N. Smith, M. Linford, Sample charging in ToF-SIMS: How it affects the data that are collected and how to reduce it, Vacuum Technology & Coating (2018).

[77] In: H. Mehrer, Editor, *Diffusion in solids: Fundamentals, methods, materials, diffusion-controlled processes*, Springer Berlin Heidelberg, Berlin, Heidelberg (2007), p.179-190. https://doi.org/10.1007/978-3-540-71488-0_11.

[78] K.D. Kreuer, E. Schönherr, J. Maier, Proton and oxygen diffusion in $BaCeO_3$ based compounds: A combined thermal gravimetric analysis and conductivity study, *Solid State Ionics* **70-71** (1994) 278, https://doi.org/10.1016/0167-2738(94)90323-9.

[79] L.J. van der Pauw, A method of measuring specific resistivity and Hall effect of discs of arbitrary shape, Philips Research Reports **13** (1958).

[80] L.J. van der Pauw, A method of measuring the resistivity and hall coefficient on lamellae of arbitrary shape, Philips Technical Review **20** (1959).

[81] N. Schrödl, E. Bucher, A. Egger, P. Kreiml, C. Teichert, T. Höschen, W. Sitte, Long-term stability of the IT-SOFC cathode materials $La_{0.6}Sr_{0.4}CoO_{3-\delta}$ and $La_2NiO_{4+\delta}$ against combined chromium and silicon poisoning, *Solid State Ionics* **276** (2015) 62, https://doi.org/10.1016/j.ssi.2015.03.035.

[82] W. Preis, E. Bucher, W. Sitte, Oxygen exchange measurements on perovskites as cathode materials for solid oxide fuel cells, *Journal of Power Sources* **106** (2002) 116, https://doi.org/10.1016/S0378-7753(01)01036-9.

[83] J.A. Lane, J.A. Kilner, Measuring oxygen diffusion and oxygen surface exchange by conductivity relaxation, *Solid State Ionics* **136-137** (2000) 997, https://doi.org/10.1016/S0167-2738(00)00554-3.

[84] C. Berger, Development of new materials for solid oxide fuel cell cathodes with superior performance and improved long-term stability, PhD Thesis, *Chair of Physical Chemistry*, Montanuniversität Leoben (2019).

[85] C. Berger, E. Bucher, W. Sitte, Mass and charge transport properties of $La_{0.9}Ca_{0.1}FeO_{3-\delta}$, *Solid State Ionics* **299** (2017) 46, https://doi.org/10.1016/j.ssi.2016.09.015.

[86] R. Shannon, Revised effective ionic radii and systematic studies of interatomic distances in halides and chalcogenides, *Acta Crystallographica Section A* **32** (1976) (5) 751, https://doi.org/10.1107/S0567739476001551.

[87] C. Berger, E. Bucher, R. Merkle, C. Nader, J. Lammer, W. Grogger, J. Maier, W. Sitte, Influence of Y-substitution on phase composition and proton uptake of self-generated $Ba(Ce,Fe)O_{3-\delta}$–$Ba(Fe,Ce)O_{3-\delta}$ composites, *Journal of Materials Chemistry A* **10** (2022) (5) 2474, https://doi.org/10.1039/D1TA07208K.

[88] V.M. Goldschmidt, Die Gesetze der Krystallochemie, *Naturwissenschaften* **14** (1926) (21) 477, https://doi.org/10.1007/BF01507527.

[89] M. Erchak, Jr., I. Fankuchen, R. Ward, Reaction between ferric oxide and barium carbonate in the solid phase. Identification of phases by X-Ray diffraction, *Journal of the American Chemical Society* **68** (1946) (10) 2085, https://doi.org/10.1021/ja01214a063.

[90] L. Malavasi, H. Kim, T.E. Proffen, Local and average structures of the proton conducting Y-doped $BaCeO_3$ from neutron diffraction and neutron pair distribution function analysis, *Journal of Applied Physics* **105** (2009) 123519, https://doi.org/10.1063/1.3148864.

[91] R. Merkle, M.F. Hoedl, A. Chesnokov, D. Gryaznov, E. Bucher, E.A. Kotomin, W. Sitte, J. Maier, Electronic structure, phase formation, and defect distribution in the $Ba(Ce,Fe,Acc)O_{3-\delta}$ system, *Acta Materialia* (2024), under review.

[92] D.W. Smith, An acidity scale for binary oxides, *Journal of Chemical Education* **64** (1987) (6) 480, https://doi.org/10.1021/ed064p480.

[93] G. Raimondi, R. Merkle, A. Longo, F. Giannici, O. Mathon, C.J. Sahle, J. Maier, Interplay of chemical, electronic, and structural effects in the triple-conducting $BaFeO_3$–$Ba(Zr,Y)O_3$ solid solution, *Chemistry of Materials* **35** (2023) (21) 8945, https://doi.org/10.1021/acs.chemmater.3c01538.

[94] E.J. Little, Jr., M.M. Jones, A complete table of electronegativities, *Journal of Chemical Education* **37** (1960) (5) 231, https://doi.org/10.1021/ed037p231.

[95] A. Løken, T.S. Bjørheim, R. Haugsrud, The pivotal role of the dopant choice on the thermodynamics of hydration and associations in proton conducting $BaCe_{0.9}X_{0.1}O_{3-\delta}$ (X = Sc, Ga, Y, In, Gd and Er), *Journal of Materials Chemistry A* **3** (2015) (46) 23289, https://doi.org/10.1039/C5TA04932F.

[96] M. Oishi, S. Akoshima, K. Yashiro, K. Sato, T. Kawada, J. Mizusaki, Defect structure analysis of proton-oxide ion mixed conductor $BaCe_{0.9}Nd_{0.1}O_{3-\delta}$, *Solid State Ionics* **181** (2010) (29) 1336, https://doi.org/10.1016/j.ssi.2010.07.034.

[97] G. Raimondi, Defect chemistry of mixed conducting perovskites: Interplay of protonic defects, oxygen vacancies and electron holes, PhD Thesis, *Faculty of Chemistry*, University of Stuttgart (2022).

[98] D. Poetzsch, R. Merkle, J. Maier, Proton uptake in the H^+-SOFC cathode material $Ba_{0.5}Sr_{0.5}Fe_{0.8}Zn_{0.2}O_{3-\delta}$: transition from hydration to hydrogenation with increasing oxygen partial pressure, *Faraday Discussions* **182** (2015) (0) 129, https://doi.org/10.1039/C5FD00013K.

[99] M.F. Hoedl, D. Gryaznov, R. Merkle, E.A. Kotomin, J. Maier, Interdependence of oxygenation and hydration in mixed-conducting $(Ba,Sr)FeO_{3-\delta}$ perovskites studied by density functional theory, *The Journal of Physical Chemistry C* **124** (2020) (22) 11780, https://doi.org/10.1021/acs.jpcc.0c01924.

[100] R. Zohourian, R. Merkle, J. Maier, Proton uptake into the protonic cathode material $BaCo_{0.4}Fe_{0.4}Zr_{0.2}O_{3-\delta}$ and comparison to protonic electrolyte materials, *Solid State Ionics* **299** (2017) 64, https://doi.org/10.1016/j.ssi.2016.09.012.

[101] K.D. Kreuer, W. Munch, M. Ise, T. He, A. Fuchs, U. Traub, J. Maier, Defect interactions in proton conducting perovskite-type oxides, Berichte der Bunsengesellschaft/Physical Chemistry Chemical Physics **101** (1997).

[102] K.D. Kreuer, S. Adams, W. Münch, A. Fuchs, U. Klock, J. Maier, Proton conducting alkaline earth zirconates and titanates for high drain electrochemical applications, *Solid State Ionics* **145** (2001) (1) 295, https://doi.org/10.1016/S0167-2738(01)00953-5.

[103] J. Hombo, Y. Matsumoto, T. Kawano, Electrical conductivities of $SrFeO_{3-\delta}$ and $BaFeO_{3-\delta}$ perovskites, *Journal of Solid State Chemistry* **84** (1990) (1) 138, https://doi.org/10.1016/0022-4596(90)90192-Z.

[104] P. Pulphol, N. Vittayakorn, W. Vittayakorn, T. Kolodiazhnyi, Electrical conductivity, magnetism, and optical properties of reduced $BaCeO_3$, *Applied Physics A* **125** (2019) (3) 197, https://doi.org/10.1007/s00339-019-2497-9.

[105] Z. Zhao, M. Zou, H. Huang, X. Zhai, H. Wofford, J. Tong, Insight of $BaCe_{0.5}Fe_{0.5}O_{3-\delta}$ twin perovskite oxide composite for solid oxide electrochemical cells, *Journal of the American Ceramic Society* **106** (2023) (1) 186, https://doi.org/10.1111/jace.18643.

[106] A. Chroneos, B. Yildiz, A. Tarancón, D. Parfitt, J.A. Kilner, Oxygen diffusion in solid oxide fuel cell cathode and electrolyte materials: Mechanistic insights from atomistic simulations, *Energy & Environmental Science* **4** (2011) (8) 2774, https://doi.org/10.1039/C0EE00717J

[107] M. Cherry, M.S. Islam, C.R.A. Catlow, Oxygen ion migration in perovskite-type oxides, *Journal of Solid State Chemistry* **118** (1995) (1) 125, https://doi.org/10.1006/jssc.1995.1320.

[108] E. Bucher, A. Egger, P. Ried, W. Sitte, P. Holtappels, Oxygen nonstoichiometry and exchange kinetics of $Ba_{0.5}Sr_{0.5}Co_{0.8}Fe_{0.2}O_{3-\delta}$, *Solid State Ionics* **179** (2008) (21) 1032, https://doi.org/10.1016/j.ssi.2008.01.089.

[109] A. Egger, E. Bucher, M. Yang, W. Sitte, Comparison of oxygen exchange kinetics of the IT-SOFC cathode materials $La_{0.5}Sr_{0.5}CoO_{3-\delta}$ and $La_{0.6}Sr_{0.4}CoO_{3-\delta}$, *Solid State Ionics* **225** (2012) 55, https://doi.org/10.1016/j.ssi.2012.02.050.

[110] J. Schindelin, I. Arganda-Carreras, E. Frise, V. Kaynig, M. Longair, T. Pietzsch, S. Preibisch, C. Rueden, S. Saalfeld, B. Schmid, J.-Y. Tinevez, D.J. White, V. Hartenstein, K. Eliceiri, P. Tomancak, A. Cardona, Fiji: An open-source platform for biological-image analysis, *Nature Methods* **9** (2012) (7) 676, https://doi.org/10.1038/nmeth.2019.

[111] C. Nader, Preparation and characterisation of self-generated composites for protonic ceramic fuel cells, Master's Thesis, *Chair of Physical Chemistry*, Montanuniversitaet Leoben (2021).

7. Appendix

7.1. Declaration of usage of artificial intelligence

Topic	Usage in %	Tool / Version	Notes	Prompts
Improvement of translation and spellings	6	DeepL / Translator, Write	Translation, wording, phrasing, improving linguistic readability	Examples are available at the internal server of the Chair of Physical Chemistry

7.2. Publications

Parts of this thesis were published in the following peer-reviewed papers:

7.2.1. Paper 1

Title: Influence of Y-substitution on phase composition and proton uptake of self-generated $Ba(Ce,Fe)O_{3-\delta}$–$Ba(Fe,Ce)O_{3-\delta}$ composites

Authors: Christian Berger, Edith Bucher, Rotraut Merkle, Christina Nader, Judith Lammer, Werner Grogger, Joachim Maier, Werner Sitte

Journal: Journal of Materials Chemistry A

Year of publication: 2022

DOI: 10.1039/D1TA07208K

Contribution of the Authors:

Christian Berger: conceptualization, methodology, investigation, writing – original draft, writing – review & editing, visualization

Edith Bucher: conceptualization, writing – review & editing, supervision, project administration, funding acquisition

Rotraut Merkle: conceptualization, methodology, investigation, writing – review & editing, supervision

Christina Nader: investigation, writing – review & editing

Judith Lammer: investigation, writing – review & editing, visualization

Werner Grogger: writing – review & editing

Joachim Maier: conceptualization, writing – review & editing, supervision

Werner Sitte: conceptualization, writing – review & editing, supervision

7.2.2. Paper 2

Title: Phase composition and proton uptake of acceptor-doped self-generated $Ba(Ce,Fe)O_{3-\delta}$ – $Ba(Fe,Ce)O_{3-\delta}$ composites

Authors: Christina Nader, Judith Lammer, Andreas Egger, Christian Berger, Werner Sitte, Werner Grogger, Rotraut Merkle, Joachim Maier, Edith Bucher

Journal: Solid State Ionics

Year of publication: 2024

DOI: 10.1016/j.ssi.2024.116474

Contribution of the Authors:

Christina Nader: conceptualization, investigation, methodology, visualization, writing – original draft, writing – review & editing

Judith Lammer: investigation, methodology, visualization, writing – review & editing

Andreas Egger: writing – review & editing

Christian Berger: writing – review & editing

Werner Sitte: writing – review & editing

Werner Grogger: supervision, writing – review & editing

Rotraut Merkle: conceptualization, investigation, methodology, supervision, writing – review & editing

Joachim Maier: writing – review & editing

Edith Bucher: conceptualization, funding acquisition, project administration, supervision, writing – review & editing

7.3. Tables of materials synthesised

7.3.1. Self-generated composites

Tab. A1 Self-generated $BaCe_{0.3}Fe_{0.7-x}Y_xO_{3-\delta}$ ($0.20 \leq x \leq 0.40$) composites with fixed Ce content and varying Fe and Y contents.

Abbreviation	Precursor composition	[Ce]	[Fe]	[Acc] (Acc = Y)
BCFY334	$BaCe_{0.30}Fe_{0.30}Y_{0.40}O_{3-\delta}$	0.30	0.30	0.40
BCFY343	$BaCe_{0.30}Fe_{0.40}Y_{0.30}O_{3-\delta}$	0.30	0.40	0.30
BCFY352	$BaCe_{0.30}Fe_{0.50}Y_{0.20}O_{3-\delta}$	0.30	0.50	0.20

Tab. A2 Self-generated $BaCe_{0.6-x}Fe_{0.4}Y_xO_{3-\delta}$ ($0.10 \leq x \leq 0.30$) composites with fixed Fe content and varying Ce and Y contents.

Abbreviation	Precursor composition	[Ce]	[Fe]	[Acc] (Acc = Y)
BCFY343	$BaCe_{0.30}Fe_{0.40}Y_{0.30}O_{3-\delta}$	0.30	0.40	0.30
BCFY442	$BaCe_{0.40}Fe_{0.40}Y_{0.20}O_{3-\delta}$	0.40	0.40	0.20
BCFY541	$BaCe_{0.50}Fe_{0.40}Y_{0.10}O_{3-\delta}$	0.50	0.40	0.10

Tab. A3 Self-generated $BaCe_{0.8-x}Fe_xY_{0.2}O_{3-\delta}$ ($0.10 \leq x \leq 0.60$) composites with fixed Y content and varying Ce and Fe contents.

Abbreviation	Precursor composition	[Ce]	[Fe]	[Acc] (Acc = Y)
BCFY262	$BaCe_{0.20}Fe_{0.60}Y_{0.20}O_{3-\delta}$	0.20	0.60	0.20
BCFY352	$BaCe_{0.30}Fe_{0.50}Y_{0.20}O_{3-\delta}$	0.30	0.50	0.20
BCFY442	$BaCe_{0.40}Fe_{0.40}Y_{0.20}O_{3-\delta}$	0.40	0.40	0.20
BCFY483220	$BaCe_{0.48}Fe_{0.32}Y_{0.20}O_{3-\delta}$	0.48	0.32	0.20
BCFY532	$BaCe_{0.50}Fe_{0.30}Y_{0.20}O_{3-\delta}$	0.50	0.30	0.20
BCFY622	$BaCe_{0.60}Fe_{0.20}Y_{0.20}O_{3-\delta}$	0.60	0.20	0.20
BCFY712	$BaCe_{0.70}Fe_{0.10}Y_{0.20}O_{3-\delta}$	0.70	0.10	0.20

Tab. A4 Self-generated $BaCe_{0.6-x}Fe_{0.4}In_xO_{3-\delta}$ ($0.20 \leq x \leq 0.30$) composites with fixed Fe content and varying Ce and In contents.

Abbreviation	Precursor composition	[Ce]	[Fe]	[Acc] (Acc = In)
BCFI343	$BaCe_{0.30}Fe_{0.40}In_{0.30}O_{3-\delta}$	0.30	0.40	0.30
BCFI354025	$BaCe_{0.35}Fe_{0.40}In_{0.25}O_{3-\delta}$	0.35	0.40	0.25
BCFI442	$BaCe_{0.40}Fe_{0.40}In_{0.20}O_{3-\delta}$	0.40	0.40	0.20

Tab. A5 Self-generated $BaCe_{0.8-x}Fe_xIn_{0.2}O_{3-\delta}$ ($0.10 \leq x \leq 0.60$) composites with fixed In content and varying Ce and Fe contents.

Abbreviation	Precursor composition	[Ce]	[Fe]	[Acc] (Acc = In)
BCFI262	$BaCe_{0.20}Fe_{0.60}In_{0.20}O_{3-\delta}$	0.20	0.60	0.20
BCFI352	$BaCe_{0.30}Fe_{0.50}In_{0.20}O_{3-\delta}$	0.30	0.50	0.20
BCFI442	$BaCe_{0.40}Fe_{0.40}In_{0.20}O_{3-\delta}$	0.40	0.40	0.20
BCFI532	$BaCe_{0.50}Fe_{0.30}In_{0.20}O_{3-\delta}$	0.50	0.30	0.20
BCFI622	$BaCe_{0.60}Fe_{0.20}In_{0.20}O_{3-\delta}$	0.60	0.20	0.20
BCFI651520	$BaCe_{0.65}Fe_{0.15}In_{0.20}O_{3-\delta}$	0.65	0.15	0.20
BCFI712	$BaCe_{0.70}Fe_{0.10}In_{0.20}O_{3-\delta}$	0.70	0.10	0.20

Tab. A6 Self-generated $BaCe_{0.4}Fe_{0.4}Acc_{0.2}O_{3-\delta}$ (Acc = Gd, Nd, Sc, Sm, Yb) composites with different acceptor substituents.

Abbreviation	Precursor composition	[Ce]	[Fe]	[Acc]
BCFGd442	$BaCe_{0.40}Fe_{0.40}Gd_{0.20}O_{3-\delta}$	0.40	0.40	0.20
BCFNd442	$BaCe_{0.40}Fe_{0.40}Nd_{0.20}O_{3-\delta}$	0.40	0.40	0.20
BCFSc442	$BaCe_{0.40}Fe_{0.40}Sc_{0.20}O_{3-\delta}$	0.40	0.40	0.20
BCFSm442	$BaCe_{0.40}Fe_{0.40}Sm_{0.20}O_{3-\delta}$	0.40	0.40	0.20
BCFYb442	$BaCe_{0.40}Fe_{0.40}Yb_{0.20}O_{3-\delta}$	0.40	0.40	0.20

Tab. A7 Self-generated $BaCe_{1-x}Fe_xO_{3-\delta}$ ($0.30 \leq x \leq 0.70$) composites with varying Ce and Fe contents.

Abbreviation	Precursor composition	[Ce]	[Fe]	[Acc]
BCF37	$BaCe_{0.30}Fe_{0.70}O_{3-\delta}$	0.30	0.70	-
BCF55	$BaCe_{0.50}Fe_{0.50}O_{3-\delta}$	0.50	0.50	-
BCF73	$BaCe_{0.70}Fe_{0.30}O_{3-\delta}$	0.70	0.30	-

7.3.2. Single phase materials

Tab. A8 $BaCe_{0.92-x}Fe_{0.08}Y_xO_{3-\delta}$ ($0.05 \leq x \leq 0.20$) single phases with fixed Fe content and varying Ce and Y contents.

Abbreviation	Precursor composition	[Ce]	[Fe]	[Acc] (Acc = Y)
BCFY870805	$BaCe_{0.87}Fe_{0.08}Y_{0.05}O_{3-\delta}$	0.87	0.08	0.05
BCFY820810	$BaCe_{0.82}Fe_{0.08}Y_{0.10}O_{3-\delta}$	0.82	0.08	0.10
BCFY770815	$BaCe_{0.77}Fe_{0.08}Y_{0.15}O_{3-\delta}$	0.77	0.08	0.15
BCFY720820	$BaCe_{0.72}Fe_{0.08}Y_{0.20}O_{3-\delta}$	0.72	0.08	0.20

Tab. A9 $BaCe_{0.8-x}Fe_xY_{0.2}O_{3-\delta}$ ($0.04 \leq x \leq 0.76$) single phases with fixed Y content and varying Ce and Fe contents.

Abbreviation	Precursor composition	[Ce]	[Fe]	[Acc] (Acc = Y)
BCFY047620	$BaCe_{0.04}Fe_{0.76}Y_{0.20}O_{3-\delta}$	0.04	0.76	0.20
BCFY087220	$BaCe_{0.08}Fe_{0.72}Y_{0.20}O_{3-\delta}$	0.08	0.72	0.20
BCFY126820	$BaCe_{0.12}Fe_{0.68}Y_{0.20}O_{3-\delta}$	0.12	0.68	0.20
BCFY166420	$BaCe_{0.16}Fe_{0.64}Y_{0.20}O_{3-\delta}$	0.16	0.64	0.20
BCFY186220	$BaCe_{0.18}Fe_{0.62}Y_{0.20}O_{3-\delta}$	0.18	0.62	0.20
BCFY681220	$BaCe_{0.68}Fe_{0.12}Y_{0.20}O_{3-\delta}$	0.68	0.12	0.20
BCFY720820	$BaCe_{0.72}Fe_{0.08}Y_{0.20}O_{3-\delta}$	0.72	0.08	0.20
BCFY760420	$BaCe_{0.76}Fe_{0.04}Y_{0.20}O_{3-\delta}$	0.76	0.04	0.20

Tab. A10 $BaFe_{1-x}Y_xO_{3-\delta}$ ($0.05 \leq x \leq 0.20$) single phases with varying Fe and Y contents.

Abbreviation	Precursor composition	[Ce]	[Fe]	[Acc] (Acc = Y)
BFY05	$BaFe_{0.95}Y_{0.05}O_{3-\delta}$	-	0.95	0.05
BFY10	$BaFe_{0.90}Y_{0.10}O_{3-\delta}$	-	0.90	0.10
BFY15	$BaFe_{0.85}Y_{0.15}O_{3-\delta}$	-	0.85	0.15
BFY20	$BaFe_{0.80}Y_{0.20}O_{3-\delta}$	-	0.80	0.20

Tab. A11 $BaCe_{0.9-x}Fe_{0.1}In_xO_{3-\delta}$ ($0.05 \leq x \leq 0.20$) single phases with fixed Fe content and varying Ce and In contents.

Abbreviation	Precursor composition	[Ce]	[Fe]	[Acc] (Acc = In)
BCFI712	$BaCe_{0.70}Fe_{0.10}In_{0.20}O_{3-\delta}$	0.70	0.10	0.20
BCFI751015	$BaCe_{0.75}Fe_{0.10}In_{0.15}O_{3-\delta}$	0.75	0.10	0.15
BCFI801010	$BaCe_{0.80}Fe_{0.10}In_{0.10}O_{3-\delta}$	0.80	0.10	0.10
BCFI851005	$BaCe_{0.85}Fe_{0.10}In_{0.05}O_{3-\delta}$	0.85	0.10	0.05

Tab. A12 $BaCe_{0.8-x}Fe_xIn_{0.2}O_{3-\delta}$ ($0.04 \leq x \leq 0.68$) single phases with fixed In content and varying Ce and Fe contents.

Abbreviation	Precursor composition	[Ce]	[Fe]	[Acc] (Acc = In)
BCFI126820	$BaCe_{0.12}Fe_{0.68}In_{0.20}O_{3-\delta}$	0.12	0.68	0.20
BCFI166420	$BaCe_{0.16}Fe_{0.64}In_{0.20}O_{3-\delta}$	0.16	0.64	0.20
BCFI720820	$BaCe_{0.72}Fe_{0.08}In_{0.20}O_{3-\delta}$	0.72	0.08	0.20
BCFI760420	$BaCe_{0.76}Fe_{0.04}In_{0.20}O_{3-\delta}$	0.76	0.04	0.20

Tab. A13 $BaFe_{1-x}In_xO_{3-\delta}$ ($0.05 \leq x \leq 0.40$) single phases with varying Fe and In contents.

Abbreviation	Precursor composition	[Ce]	[Fe]	[Acc] (Acc = In)
BFI05	$BaFe_{0.95}In_{0.05}O_{3-\delta}$	-	0.95	0.05
BFI10	$BaFe_{0.90}In_{0.10}O_{3-\delta}$	-	0.90	0.10
BFI15	$BaFe_{0.85}In_{0.15}O_{3-\delta}$	-	0.85	0.15
BFI20	$BaFe_{0.80}In_{0.20}O_{3-\delta}$	-	0.80	0.20
BFI30	$BaFe_{0.70}In_{0.30}O_{3-\delta}$	-	0.70	0.30
BFI40	$BaFe_{0.60}In_{0.40}O_{3-\delta}$	-	0.60	0.40

Tab. A14 $BaCe_{1-x}Fe_xO_{3-\delta}$ ($0.80 \leq x \leq 0.95$) single phases with varying Ce and Fe contents.

Abbreviation	Precursor composition	[Ce]	[Fe]	[Acc]
BFC05	$BaCe_{0.05}Fe_{0.95}O_{3-\delta}$	0.05	0.95	-
BFC10	$BaCe_{0.10}Fe_{0.90}O_{3-\delta}$	0.10	0.90	-
BFC15	$BaCe_{0.15}Fe_{0.85}O_{3-\delta}$	0.15	0.85	-
BFC20	$BaCe_{0.20}Fe_{0.80}O_{3-\delta}$	0.20	0.80	-

7.3.3. Artificial composites

Tab. A15 Y-substituted artificial composites with fixed Y content and varying Ce and Fe contents.

Abbreviation	Precursor composition	[Ce]	[Fe]	[Acc] (Acc = Y)
BcBf8020	$BaCe_{0.60}Fe_{0.20}Y_{0.20}O_{3-\delta}$	0.60	0.20	0.20
BcBf6535	$BaCe_{0.48}Fe_{0.32}Y_{0.20}O_{3-\delta}$	0.48	0.32	0.20
BcBf5050	$BaCe_{0.37}Fe_{0.43}Y_{0.20}O_{3-\delta}$	0.37	0.43	0.20

7.4. Powder annealing

The original SEM images were edited with the software Fiji (ImageJ, Version: ImageJ 1.54f; Java 1.8.0_322 [32-bit]) [110] to obtain cropped images with uniform size bars.

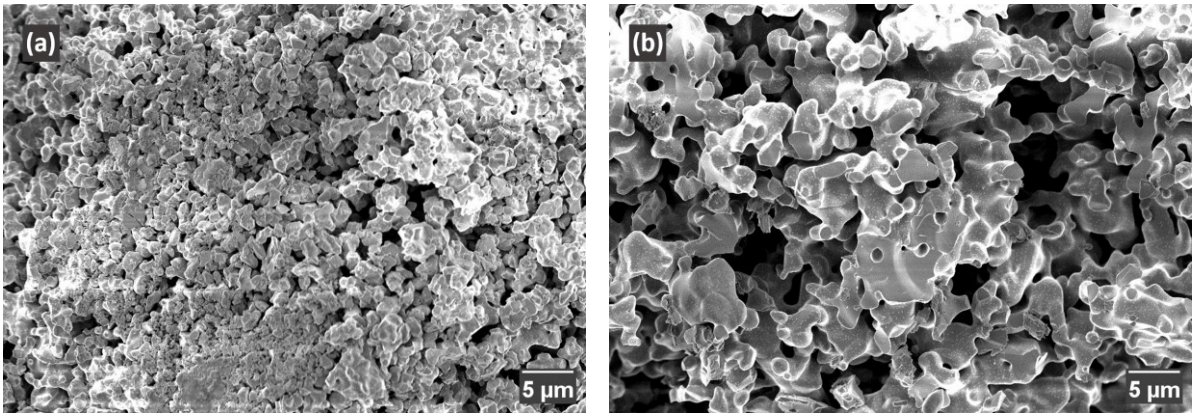

Fig. A1 SEM-SE images of $BaCe_{0.04}Fe_{0.76}Y_{0.20}O_{3-\delta}$ powders annealed for 24 hours at **(a)** 1100 °C and **(b)** 1200 °C.

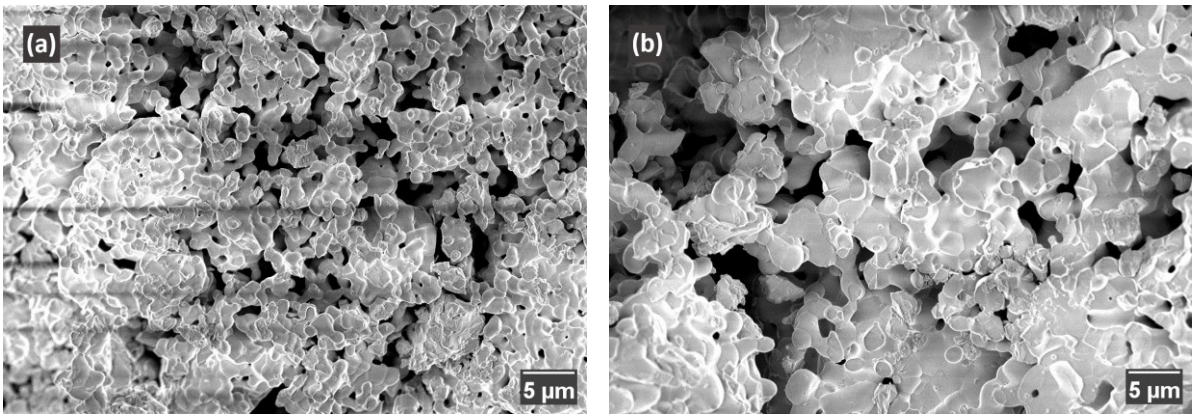

Fig. A2 SEM-SE images of $BaCe_{0.76}Fe_{0.04}Y_{0.20}O_{3-\delta}$ powders annealed for 24 hours at **(a)** 1300 °C and **(b)** 1400 °C.

7.5. Thermogravimetry

Tab. A16 Settings for the flow controllers and thermostat at different pH_2O levels.

pH_2O / mbar	Flow rate @ flow controller "dry" / ml min^{-1}	Flow rate @ flow controller "wet" / ml min^{-1}	Temperature of thermostat / °C
0	50	0	-
1.45	40	10	5
7.3	0	50	5
16.7	0	50	18

7.6. Isotope exchange experiments

7.6.1. Single phase materials

Tab. A17 Setup parameters and duration for isotope exchange experiments with single phase samples.

Sample	Temperature / °C	Duration / min	Flow rate through bubbler / ml min^{-1}	Bypass flow rate / ml min^{-1}
BCFY760420	300	60	30	-
BCFY760420	300	40	3	27
BCFY760420	350	30	30	-
BCFY760420	350	30	3	27
BCFY760420	400	20	30	-
BCFY760420	400	15	3	27
BCFY760420	500	10	30	-
BCFY047620	300	60 / 300	30	-
BCFY047620	300	300	3	27
BCFY047620	350	90	3	27
BCFY047620	400	120	30	-
BCFY047620	400	90	3	27
BCFY047620	500	60	30	-
BCFY483220	300	180	30	-
BCFY483220	400	40	30	-

7.6.2. Artificial composites

Tab. A18 Setup parameters and duration for isotope exchange experiments with self-generated and artificial composites.

Sample	Temperature / °C	Duration / min	Flow rate through bubbler / ml min^{-1}	Bypass flow rate / ml min^{-1}
BCFY483220	300	90	30	-
BCFY483220	400	20	30	-
BCFY483220	450	20	30	-
BCFY483220	500	10	30	-
BcBf8020	300	90	30	-
BcBf8020	350	50	30	-
BcBf8020	400	20	30	-
BcBf8020	500	10	30	-
BcBf6535	300	60	30	-
BcBf6535	400	20	30	-
BcBf6535	450	15	30	-
BcBf6535	500	10	30	-

7.7. Electrical conductivity and dc-conductivity relaxation measurements

Tab. A19 Temperature program for burning in the gold paste.

Steps	T / °C	Heating/cooling rate / K min^{-1}	Time / min
Heating	150	2	-
Isothermal step	150	-	10
Heating	850	2	-
Isothermal step	850	-	15
Cooling	20	2	-

7.8. Phase formation

7.8.1. Goldschmidt tolerance factors

In Tables A20 and A21, the precursor phases marked in green do not become single phase even at high temperatures. For those marked in blue, the temperature of single phase formation lies below the melting temperature.

Tab. A20 Goldschmidt tolerance factors of $BaCe_{0.8-x}Fe_xY_{0.2}O_{3-\delta}$, calculated for Ce- and Fe-rich phases in the composites, their mean values, as well as the precursor composition.

	Goldschmidt tolerance factor t			
Precursor	Ce-rich phase	Fe-rich phase	Mean value	Precursor phase
$BaCe_{0.2}Fe_{0.6}Y_{0.2}O_{3-\delta}$	0.9462	1.0121	1.0033	1.0111
$BaCe_{0.4}Fe_{0.4}Y_{0.2}O_{3-\delta}$	0.9447	1.0009	0.9744	0.9845
$BaCe_{0.6}Fe_{0.2}Y_{0.2}O_{3-\delta}$	0.9499	0.9819	0.9586	0.9592

Tab. A21 Goldschmidt tolerance factors of $BaCe_{0.6-x}Fe_{0.4}Y_xO_{3-\delta}$, calculated for Ce- and Fe-rich phases in the composites, their mean values, as well as the precursor composition.

	Goldschmidt tolerance factor t			
Precursor	Ce-rich phase	Fe-rich phase	Mean value	Precursor phase
$BaCe_{0.3}Fe_{0.4}Y_{0.3}O_{3-\delta}$	0.9571	1.0041	0.9941	0.9831
$BaCe_{0.4}Fe_{0.4}Y_{0.2}O_{3-\delta}$	0.9447	1.0009	0.9744	0.9845
$BaCe_{0.5}Fe_{0.4}Y_{0.1}O_{3-\delta}$	0.9546	1.0203	0.9807	0.9858

7.8.2. Phase fractions and molar masses

Tab. A22 Weight fractions, molar mass and molar fractions of the Ce-rich phases of self-generated Y-containing composites. The data is obtained from quantitative phase analysis of XRD patterns measured at room temperature on crushed sintered pellets.

	Ce-rich phase		
Precursor	Amount / wt.-%	M / g mol^{-1}	Amount / mol.-%
$BaCe_{0.2}Fe_{0.6}Y_{0.2}O_{3-\delta}$	15.7	302.7	14.1
$BaCe_{0.3}Fe_{0.5}Y_{0.2}O_{3-\delta}$	35.1	-	-
$BaCe_{0.4}Fe_{0.4}Y_{0.2}O_{3-\delta}$	51.1	313.8	47.3
$BaCe_{0.5}Fe_{0.3}Y_{0.2}O_{3-\delta}$	59.1	-	-
$BaCe_{0.6}Fe_{0.2}Y_{0.2}O_{3-\delta}$	75.0	307.1	73.0
$BaCe_{0.3}Fe_{0.4}Y_{0.3}O_{3-\delta}$	23.7	301.6	21.3
$BaCe_{0.5}Fe_{0.4}Y_{0.1}O_{3-\delta}$	64.0	308.6	60.2

Tab. A23 Weight fractions, molar mass and molar fractions of the Fe-rich phases of self-generated Y-containing composites. The data is obtained from quantitative phase analysis of XRD patterns measured at room temperature on crushed sintered pellets.

	Fe-rich phase		
Precursor	Amount / wt.-%	M / g mol^{-1}	Amount / mol.-%
$BaCe_{0.2}Fe_{0.6}Y_{0.2}O_{3-\delta}$	84.3	265.8	85.9
$BaCe_{0.3}Fe_{0.5}Y_{0.2}O_{3-\delta}$	64.9	-	-
$BaCe_{0.4}Fe_{0.4}Y_{0.2}O_{3-\delta}$	48.9	268.0	52.9
$BaCe_{0.5}Fe_{0.3}Y_{0.2}O_{3-\delta}$	40.9	-	-
$BaCe_{0.6}Fe_{0.2}Y_{0.2}O_{3-\delta}$	25.0	277.7	27.0
$BaCe_{0.3}Fe_{0.4}Y_{0.3}O_{3-\delta}$	76.3	262.4	78.7
$BaCe_{0.5}Fe_{0.4}Y_{0.1}O_{3-\delta}$	36.0	262.7	39.8

Tab. A24 Weight fractions, molar mass and molar fractions of the Ce-rich phases of self-generated acceptor-substituted (Acc = Gd, Sc, Sm, Yb) composites. The data is obtained from quantitative phase analysis of XRD patterns measured at room temperature on crushed sintered pellets.

	Ce-rich phase		
Precursor	Amount / wt.-%	M / g mol^{-1}	Amount / mol.-%
$BaCe_{0.4}Fe_{0.4}Gd_{0.2}O_{3-\delta}$	52.9	-	-
$BaCe_{0.4}Fe_{0.4}Sc_{0.2}O_{3-\delta}$	47.3	314.1	43.2
$BaCe_{0.4}Fe_{0.4}Sm_{0.2}O_{3-\delta}$	57.9	-	-
$BaCe_{0.4}Fe_{0.4}Yb_{0.2}O_{3-\delta}$	42.3	-	-

Tab. A25 Weight fractions, molar mass and molar fractions of the Fe-rich phases of self-generated acceptor-substituted (Acc = Gd, Sc, Sm, Yb) composites. The data is obtained from quantitative phase analysis of XRD patterns measured at room temperature on crushed sintered pellets.

	Fe-rich phase		
Precursor	Amount / wt.-%	M / g mol^{-1}	Amount / mol.-%
$BaCe_{0.4}Fe_{0.4}Gd_{0.2}O_{3-\delta}$	47.1	-	-
$BaCe_{0.4}Fe_{0.4}Sc_{0.2}O_{3-\delta}$	52.7	266.8	56.8
$BaCe_{0.4}Fe_{0.4}Sm_{0.2}O_{3-\delta}$	42.1	-	-
$BaCe_{0.4}Fe_{0.4}Yb_{0.2}O_{3-\delta}$	57.7	-	-

7.9. Cation composition

Tab. A26 Nominal composition of the precursors compared to the cation composition of SPS sintered composites determined by ICP-OES [87].

Nominal composition	Compositions from ICP-OES
$BaCe_{0.5}Fe_{0.5}O_{3-\delta}$	$BaCe_{0.503}Fe_{0.495}O_{3-\delta}$
$BaCe_{0.2}Fe_{0.6}Y_{0.2}O_{3-\delta}$	$BaCe_{0.201}Fe_{0.593}Y_{0.199}O_{3-\delta}$
$BaCe_{0.4}Fe_{0.4}Y_{0.2}O_{3-\delta}$	$BaCe_{0.398}Fe_{0.389}Y_{0.198}O_{3-\delta}$

Tab. A27 Nominal composition of the precursors compared to the cation composition of calcined powders of composites determined by ICP-OES [87].

Nominal composition	Compositions from ICP-OES
$BaCe_{0.5}Fe_{0.5}O_{3-\delta}$	$BaCe_{0.503}Fe_{0.489}O_{3-\delta}$
$BaCe_{0.2}Fe_{0.6}Y_{0.2}O_{3-\delta}$	$BaCe_{0.207}Fe_{0.581}Y_{0.201}O_{3-\delta}$
$BaCe_{0.4}Fe_{0.4}Y_{0.2}O_{3-\delta}$	$BaCe_{0.388}Fe_{0.390}Y_{0.199}O_{3-\delta}$
$BaCe_{0.6}Fe_{0.2}Y_{0.2}O_{3-\delta}$	$BaCe_{0.588}Fe_{0.197}Y_{0.203}O_{3-\delta}$

7.10. Lattice parameters

7.10.1. Self-generated composites

Tab. A28 Lattice parameters, unit cell volume and space group of the Fe-rich phase of In-containing composites obtained by LeBail fitting of XRD patterns of crushed sintered pellets.

Precursor	Lattice parameter a / Å	Unit cell volume / Å³	Space group
$BaFe_{0.8}In_{0.2}O_3$	4.08875	-	$Pm\bar{3}m$
$BaCe_{0.2}Fe_{0.6}In_{0.2}O_{3-\delta}$	4.15281(6)	71.619(3)	$Pm\bar{3}m$
$BaCe_{0.3}Fe_{0.5}In_{0.2}O_{3-\delta}$	4.18040(17)	73.056(9)	$Pm\bar{3}m$
$BaCe_{0.4}Fe_{0.4}In_{0.2}O_{3-\delta}$	4.18025(11)	73.048(6)	$Pm\bar{3}m$
$BaCe_{0.5}Fe_{0.3}In_{0.2}O_{3-\delta}$	4.1673(4)	72.369(18)	$Pm\bar{3}m$
$BaCe_{0.6}Fe_{0.2}In_{0.2}O_{3-\delta}$	4.22439(18)	75.386(10)	$Pm\bar{3}m$
$BaCe_{0.7}Fe_{0.1}In_{0.2}O_{3-\delta}$	4.2335(11)	75.87(6)	$Pm\bar{3}m$
$BaCe_{0.3}Fe_{0.4}In_{0.3}O_{3-\delta}$	4.22157(9)	75.235(5)	$Pm\bar{3}m$
$BaCe_{0.35}Fe_{0.40}In_{0.25}O_{3-\delta}$	4.1799(3)	73.027(13)	$Pm\bar{3}m$

Tab. A29 Lattice parameters, unit cell volume and space group of the Ce-rich phase of In-containing composites obtained by LeBail fitting of XRD patterns of crushed sintered pellets.

	Lattice parameter			
Precursor	a / Å	c / Å	Unit cell vol. / Å³	Space group
$BaCe_{0.2}Fe_{0.6}In_{0.2}O_{3-\delta}$	6.200(2)	15.218(11)	506.6(5)	$R\bar{3}c$
$BaCe_{0.3}Fe_{0.5}In_{0.2}O_{3-\delta}$	6.2081(8)	15.282(4)	510.07(19)	$R\bar{3}c$
$BaCe_{0.4}Fe_{0.4}In_{0.2}O_{3-\delta}$	6.1947(5)	15.126(2)	502.67(11)	$R\bar{3}c$
$BaCe_{0.5}Fe_{0.3}In_{0.2}O_{3-\delta}$	6.2361(7)	15.163(3)	510.69(15)	$R\bar{3}c$
$BaCe_{0.6}Fe_{0.2}In_{0.2}O_{3-\delta}$	6.1894(4)	15.128(2)	501.88(10)	$R\bar{3}c$
$BaCe_{0.7}Fe_{0.1}In_{0.2}O_{3-\delta}$	6.1620(4)	15.1842(17)	499.31(8)	$R\bar{3}c$
$BaCe_{0.3}Fe_{0.4}In_{0.3}O_{3-\delta}$	6.1964(12)	15.111(6)	502.5(3)	$R\bar{3}c$
$BaCe_{0.35}Fe_{0.40}In_{0.25}O_{3-\delta}$	6.2256(10)	15.134(5)	508.1(2)	$R\bar{3}c$

Tab. A30 Pseudo-cubic lattice parameters of the Ce-rich phase of In-containing composites.

Precursor	Pseudo-cubic lattice parameter a_{pseudo} / Å
$BaCe_{0.2}Fe_{0.6}In_{0.2}O_{3-\delta}$	4.387
$BaCe_{0.3}Fe_{0.5}In_{0.2}O_{3-\delta}$	4.397
$BaCe_{0.4}Fe_{0.4}In_{0.2}O_{3-\delta}$	4.376
$BaCe_{0.5}Fe_{0.3}In_{0.2}O_{3-\delta}$	4.399
$BaCe_{0.6}Fe_{0.2}In_{0.2}O_{3-\delta}$	4.373
$BaCe_{0.7}Fe_{0.1}In_{0.2}O_{3-\delta}$	4.366
$BaCe_{0.8}In_{0.2}O_3$	4.365
$BaCe_{0.3}Fe_{0.4}In_{0.3}O_{3-\delta}$	4.375
$BaCe_{0.35}Fe_{0.40}In_{0.25}O_{3-\delta}$	4.391

Tab. A31 Lattice parameters, unit cell volume and space group of the Fe-rich phase of Y-containing composites obtained by LeBail fitting of XRD patterns of crushed sintered pellets.

Precursor	Lattice parameter a / Å	Unit cell volume / Å³	Space group
$BaFe_{0.8}Y_{0.2}O_3$	4.12	-	$Pm\bar{3}m$
$BaCe_{0.2}Fe_{0.6}Y_{0.2}O_{3-\delta}$	4.1852(2)	73.308(12)	$Pm\bar{3}m$
$BaCe_{0.3}Fe_{0.5}Y_{0.2}O_{3-\delta}$	4.18909(16)	73.512(8)	$Pm\bar{3}m$
$BaCe_{0.4}Fe_{0.4}Y_{0.2}O_{3-\delta}$	4.2196(3)	75.132(15)	$Pm\bar{3}m$
$BaCe_{0.5}Fe_{0.3}Y_{0.2}O_{3-\delta}$	4.2396(3)	76.204(14)	$Pm\bar{3}m$
$BaCe_{0.6}Fe_{0.2}Y_{0.2}O_{3-\delta}$	4.2501(6)	76.77(3)	$Pm\bar{3}m$
$BaCe_{0.7}Fe_{0.1}Y_{0.2}O_{3-\delta}$	4.316(2)	80.41(11)	$Pm\bar{3}m$
$BaCe_{0.3}Fe_{0.4}Y_{0.3}O_{3-\delta}$	4.2269(3)	75.521(18)	$Pm\bar{3}m$
$BaCe_{0.5}Fe_{0.4}Y_{0.1}O_{3-\delta}$	4.14558(16)	71.245(8)	$Pm\bar{3}m$

Tab. A32 Lattice parameters, unit cell volume and space group of the Ce-rich phase of Y-containing composites obtained by LeBail fitting of XRD patterns of crushed sintered pellets.

	Lattice parameter			
Precursor	a / Å	c / Å	Unit cell vol. / Å³	Space group
$BaCe_{0.2}Fe_{0.6}Y_{0.2}O_{3-\delta}$	6.207(5)	15.11(2)	504.0(11)	$R\bar{3}c$
$BaCe_{0.3}Fe_{0.5}Y_{0.2}O_{3-\delta}$	6.2112(15)	15.125(8)	505.3(4)	$R\bar{3}c$
$BaCe_{0.4}Fe_{0.4}Y_{0.2}O_{3-\delta}$	6.2086(13)	15.125(6)	504.9(3)	$R\bar{3}c$
$BaCe_{0.5}Fe_{0.3}Y_{0.2}O_{3-\delta}$	6.1834(4)	15.079(2)	499.30(9)	$R\bar{3}c$
$BaCe_{0.6}Fe_{0.2}Y_{0.2}O_{3-\delta}$	6.2071(4)	15.1275(19)	504.76(9)	$R\bar{3}c$
$BaCe_{0.7}Fe_{0.1}Y_{0.2}O_{3-\delta}$	6.2003(5)	15.184(2)	505.52(11)	$R\bar{3}c$
$BaCe_{0.8}Y_{0.2}O_3$	-	-	341.37(4)	*Pnma*
$BaCe_{0.3}Fe_{0.4}Y_{0.3}O_{3-\delta}$	6.1788(13)	15.034(7)	497.1(3)	$R\bar{3}c$
$BaCe_{0.5}Fe_{0.4}Y_{0.1}O_{3-\delta}$	6.2125(3)	15.1276(16)	505.64(8)	$R\bar{3}c$

Tab. A33 Pseudo-cubic lattice parameters of the Ce-rich phase of Y-containing composites.

Precursor	Pseudo-cubic lattice parameter a_{pseudo} / Å
$BaCe_{0.2}Fe_{0.6}Y_{0.2}O_{3-\delta}$	4.380
$BaCe_{0.3}Fe_{0.5}Y_{0.2}O_{3-\delta}$	4.383
$BaCe_{0.4}Fe_{0.4}Y_{0.2}O_{3-\delta}$	4.382
$BaCe_{0.5}Fe_{0.3}Y_{0.2}O_{3-\delta}$	4.366
$BaCe_{0.6}Fe_{0.2}Y_{0.2}O_{3-\delta}$	4.382
$BaCe_{0.7}Fe_{0.1}Y_{0.2}O_{3-\delta}$	4.384
$BaCe_{0.8}Y_{0.2}O_3$	4.403
$BaCe_{0.3}Fe_{0.4}Y_{0.3}O_{3-\delta}$	4.359
$BaCe_{0.5}Fe_{0.4}Y_{0.1}O_{3-\delta}$	4.384

Tab. A34 Lattice parameters, unit cell volume and space group of the Fe-rich phase of $BaCe_{0.4}Fe_{0.4}Acc_{0.2}O_{3-\delta}$ composites (Acc = Gd, Sc, Sm, Yb) obtained by LeBail fitting of XRD patterns of crushed sintered pellets.

Precursor	Lattice parameter a / Å	Unit cell volume / Å³	Space group
$BaCe_{0.4}Fe_{0.4}Gd_{0.2}O_{3-\delta}$	4.2205(2)	75.179(12)	$Pm\bar{3}m$
$BaCe_{0.4}Fe_{0.4}Sc_{0.2}O_{3-\delta}$	4.1333(2)	70.616(10)	$Pm\bar{3}m$
$BaCe_{0.4}Fe_{0.4}Sm_{0.2}O_{3-\delta}$	4.2224(3)	75.279(14)	$Pm\bar{3}m$
$BaCe_{0.4}Fe_{0.4}Yb_{0.2}O_{3-\delta}$	4.2063(3)	74.424(14)	$Pm\bar{3}m$

Tab. A35 Lattice parameters, unit cell volume and space group of the Ce-rich phase of $BaCe_{0.4}Fe_{0.4}Acc_{0.2}O_{3-\delta}$ composites (Acc = Gd, Sc, Sm, Yb) obtained by LeBail fitting of XRD patterns of crushed sintered pellets.

	Lattice parameter			
Precursor	a / Å	c / Å	Unit cell vol. / Å³	Space group
$BaCe_{0.4}Fe_{0.4}Gd_{0.2}O_{3-\delta}$	6.2245(11)	15.169(6)	509.0(3)	$R\bar{3}c$
$BaCe_{0.4}Fe_{0.4}Sc_{0.2}O_{3-\delta}$	6.1909(6)	15.081(3)	500.59(13)	$R\bar{3}c$
$BaCe_{0.4}Fe_{0.4}Sm_{0.2}O_{3-\delta}$	6.2407(8)	15.166(4)	511.51(19)	$R\bar{3}c$
$BaCe_{0.4}Fe_{0.4}Yb_{0.2}O_{3-\delta}$	6.2044(8)	15.121(4)	504.10(18)	$R\bar{3}c$

Tab. A36 Pseudo-cubic lattice parameters of the Ce-rich phase of $BaCe_{0.4}Fe_{0.4}Acc_{0.2}O_{3-\delta}$ composites (Acc = Gd, Sc, Sm, Yb).

Abbreviation	Pseudo-cubic lattice parameter a_{pseudo} / Å
$BaCe_{0.4}Fe_{0.4}Gd_{0.2}O_{3-\delta}$	4.394
$BaCe_{0.4}Fe_{0.4}Sc_{0.2}O_{3-\delta}$	4.370
$BaCe_{0.4}Fe_{0.4}Sm_{0.2}O_{3-\delta}$	4.401
$BaCe_{0.4}Fe_{0.4}Yb_{0.2}O_{3-\delta}$	4.380

7.10.2. Artificial composites

Tab. A37 Lattice parameters, unit cell volume and space group of the Fe-rich phase of artificial composites obtained by LeBail fitting of XRD patterns of crushed sintered pellets.

Abbreviation	Lattice parameter a / Å	Unit cell volume / Å³	Space group
BcBf8020	4.2499(5)	76.76(3)	$Pm\bar{3}m$
BcBf6535	4.2146(4)	74.86(2)	$Pm\bar{3}m$
BcBf5050	4.1642(3)	72.211(16)	$Pm\bar{3}m$
BcBf5050s	4.1984(3)	74.004(17)	$Pm\bar{3}m$

Tab. A38 Lattice parameters, unit cell volume and space group of the Ce-rich phase of artificial composites obtained by LeBail fitting of XRD patterns of crushed sintered pellets.

	Lattice parameter			
Precursor	a / Å	c / Å	Unit cell vol. / Å³	Space group
BcBf8020	6.1924(5)	15.115(2)	501.93(11)	$R\bar{3}c$
BcBf6535	6.1734(5)	15.033(3)	496.15(12)	$R\bar{3}c$
BcBf5050	6.2214(7)	15.145(3)	507.66(16)	$R\bar{3}c$
BcBf5050s	6.1954(9)	15.093(5)	501.7(2)	$R\bar{3}c$

7.10.3. Single phase materials

Tab. A39 Lattice parameters, unit cell volume and space group of Fe-rich single phases obtained by LeBail fitting of XRD patterns of calcined powders.

Precursor	Lattice parameter a / Å	Cell volume / Å³	Space group
$BaCe_{0.12}Fe_{0.68}In_{0.20}O_{3-\delta}$	4.0944(2)	68.640(11)	$Pm\bar{3}m$
$BaCe_{0.16}Fe_{0.64}In_{0.20}O_{3-\delta}$	4.15034(14)	71.491(7)	$Pm\bar{3}m$
$BaCe_{0.04}Fe_{0.76}Y_{0.20}O_{3-\delta}$	4.12228(5)	70.051(2)	$Pm\bar{3}m$
$BaCe_{0.08}Fe_{0.72}Y_{0.20}O_{3-\delta}$	4.14465(4)	71.197(2)	$Pm\bar{3}m$
$BaCe_{0.12}Fe_{0.68}Y_{0.20}O_{3-\delta}$	4.15828(8)	71.902(4)	$Pm\bar{3}m$
$BaCe_{0.16}Fe_{0.64}Y_{0.20}O_{3-\delta}$	4.15952(11)	71.966(6)	$Pm\bar{3}m$
$BaCe_{0.18}Fe_{0.62}Y_{0.20}O_{3-\delta}$	4.18928(18)	73.522(10)	$Pm\bar{3}m$

Tab. A40 Lattice parameters, unit cell volume and space group of Ce-rich single phases obtained by LeBail fitting of XRD patterns of calcined powders.

	Lattice parameter			
Precursor	a / Å	c / Å	Unit cell vol. / Å³	Space group
$BaCe_{0.72}Fe_{0.08}In_{0.20}O_{3-\delta}$	6.2003(2)	15.1078(11)	502.99(5)	$R\bar{3}c$
$BaCe_{0.75}Fe_{0.10}In_{0.15}O_{3-\delta}$	6.21032(15)	15.1482(7)	505.97(3)	$R\bar{3}c$
$BaCe_{0.76}Fe_{0.04}In_{0.20}O_{3-\delta}$	6.2019(2)	15.1013(9)	503.04(5)	$R\bar{3}c$
$BaCe_{0.80}Fe_{0.10}In_{0.10}O_{3-\delta}$	6.1497(2)	15.1310(9)	495.58(5)	$R\bar{3}c$
$BaCe_{0.85}Fe_{0.10}In_{0.05}O_{3-\delta}$	6.2033(2)	15.1253(9)	504.06(4)	$R\bar{3}c$
$BaCe_{0.68}Fe_{0.12}Y_{0.20}O_{3-\delta}$	6.2103(3)	15.1420(12)	505.76(6)	$R\bar{3}c$
$BaCe_{0.72}Fe_{0.08}Y_{0.20}O_{3-\delta}$	6.2059(2)	15.2597(9)	508.96(4)	$R\bar{3}c$
$BaCe_{0.76}Fe_{0.04}Y_{0.20}O_{3-\delta}$	6.21395(18)	15.1607(9)	506.97(4)	$R\bar{3}c$
$BaCe_{0.77}Fe_{0.08}Y_{0.15}O_{3-\delta}$	6.17516(13)	15.1621(6)	500.71(3)	$R\bar{3}c$
$BaCe_{0.82}Fe_{0.08}Y_{0.10}O_{3-\delta}$	6.21342(13)	15.1706(6)	507.22(3)	$R\bar{3}c$
$BaCe_{0.87}Fe_{0.08}Y_{0.05}O_{3-\delta}$	6.21487(14)	15.1492(6)	506.74(3)	$R\bar{3}c$

7.10.4. Annealing experiments

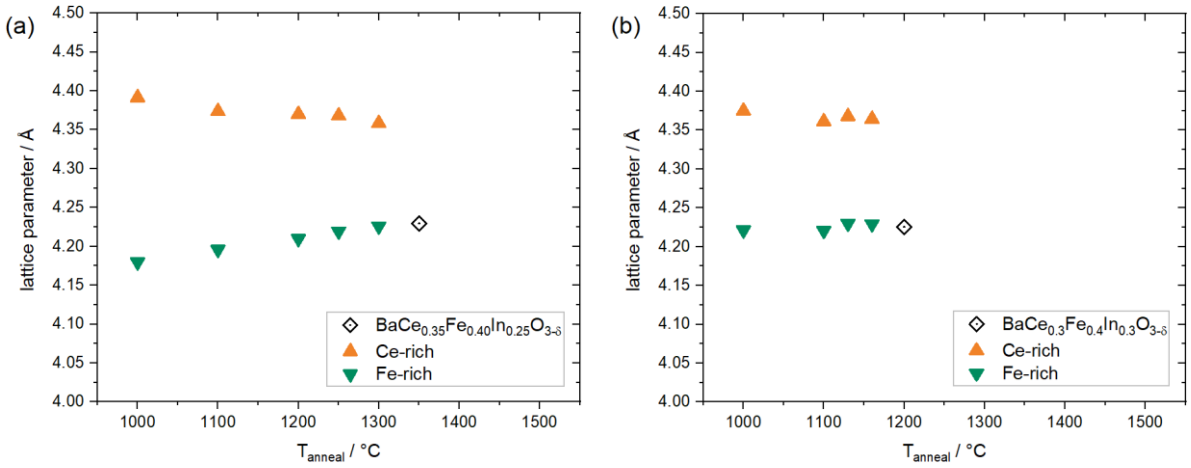

Fig. A3 (a) – (b) Lattice parameters of $BaCe_{0.6-x}Fe_{0.4}In_xO_{3-\delta}$ composites as a function of annealing temperature. The open symbols represent the temperature of single phase formation and the lattice parameter of the resulting Ce- or Fe-rich single phase [69].

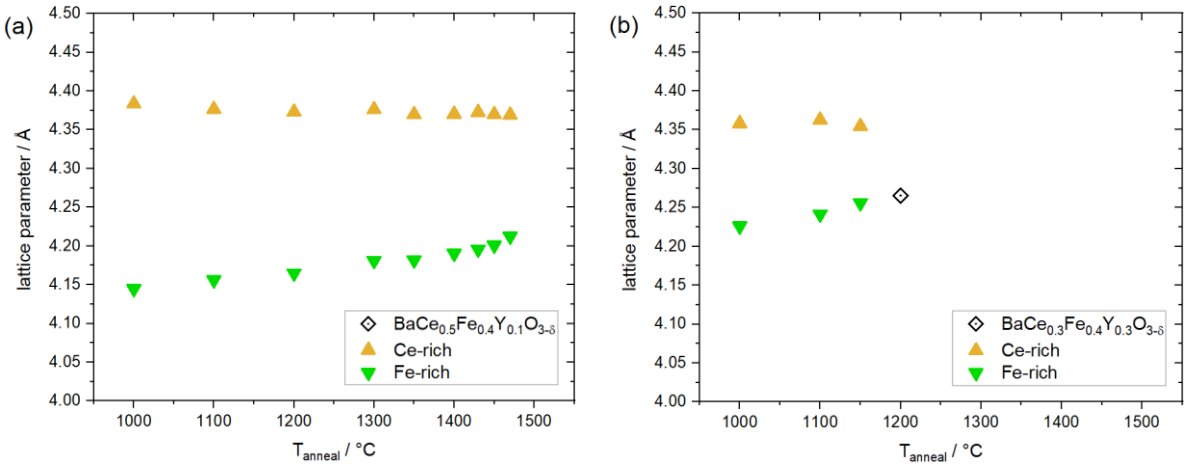

Fig. A4 (a) – (b) Lattice parameters of $BaCe_{0.6-x}Fe_{0.4}Y_xO_{3-\delta}$ composites as a function of annealing temperature. The open symbols represent the temperature of single phase formation and the lattice parameter of the resulting Ce- or Fe-rich single phase [69].

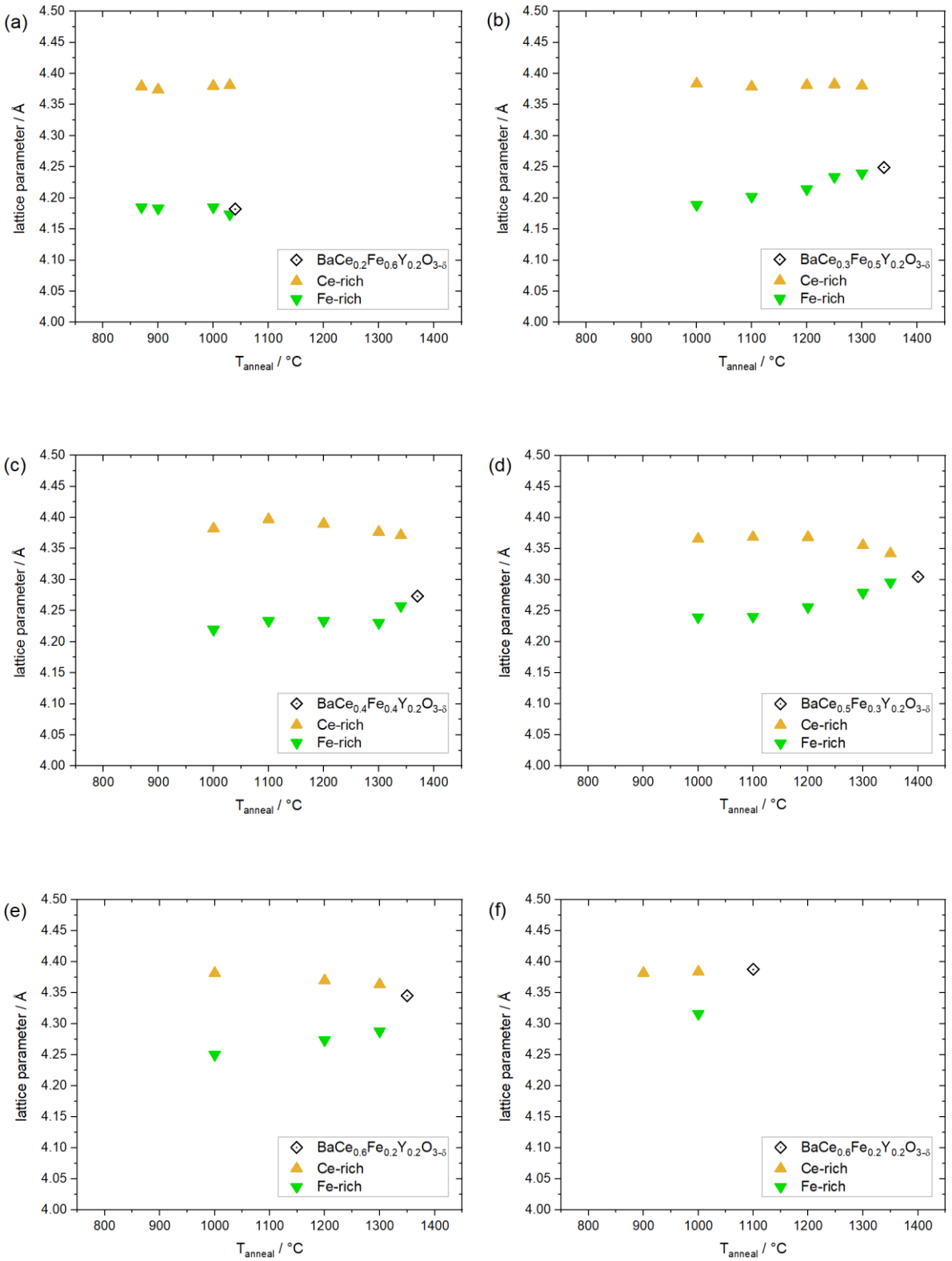

Fig. A5 (a) – (f) Lattice parameters of $BaCe_{0.8-x}Fe_xY_{0.2}O_{3-\delta}$ composites as a function of annealing temperature. The open symbols represent the temperature of single phase formation and the lattice parameter of the resulting Ce- or Fe-rich single phase [87].

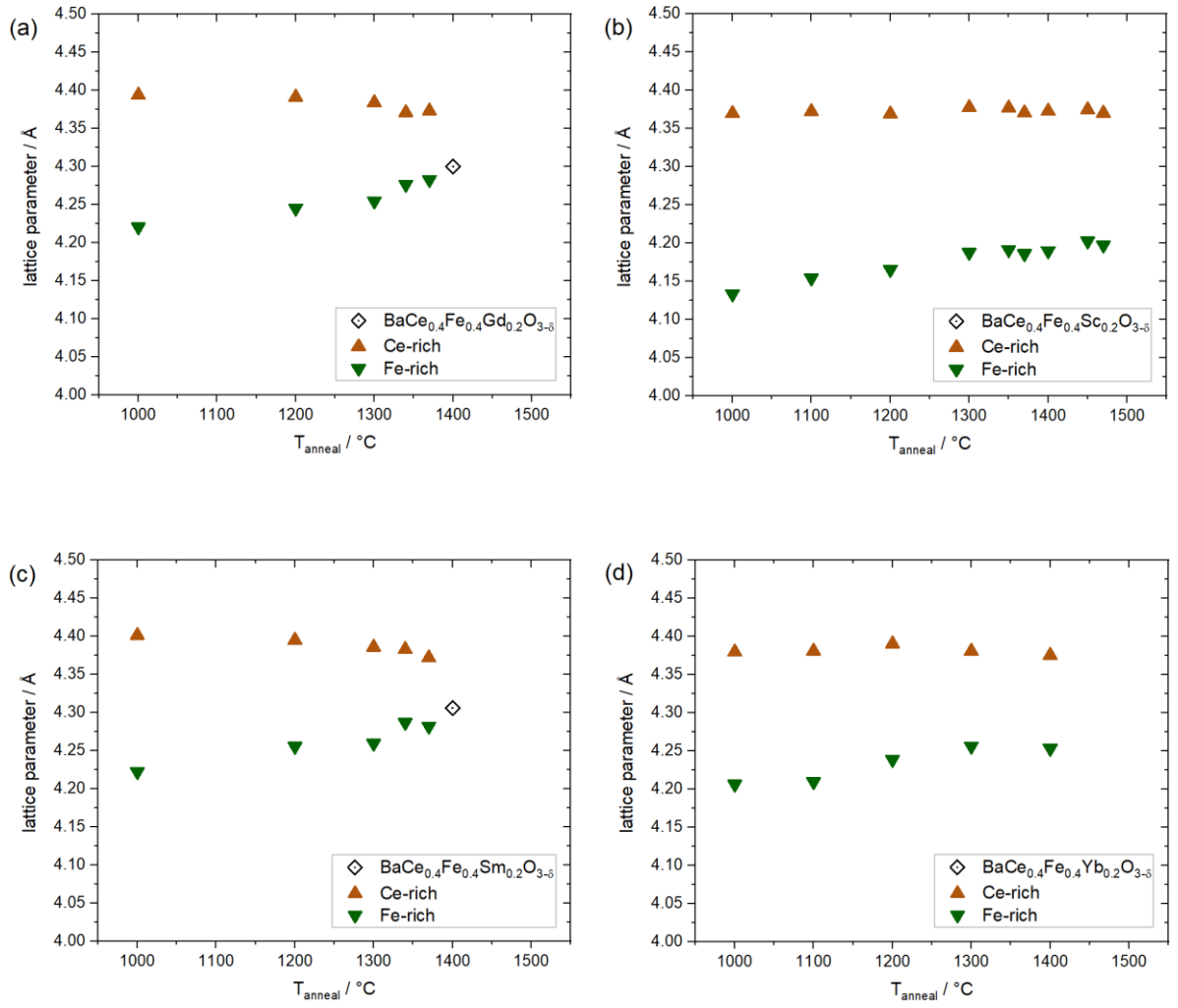

Fig. A6 (a) – (d) Lattice parameters of $BaCe_{0.4}Fe_{0.4}Acc_{0.2}O_{3-\delta}$ composites (Acc = Gd, Sc, Sm, Yb) as a function of annealing temperature. The open symbols represent the temperature of single phase formation and the lattice parameter of the resulting Ce- or Fe-rich single phase.

7.11. Microstructure and elemental distribution

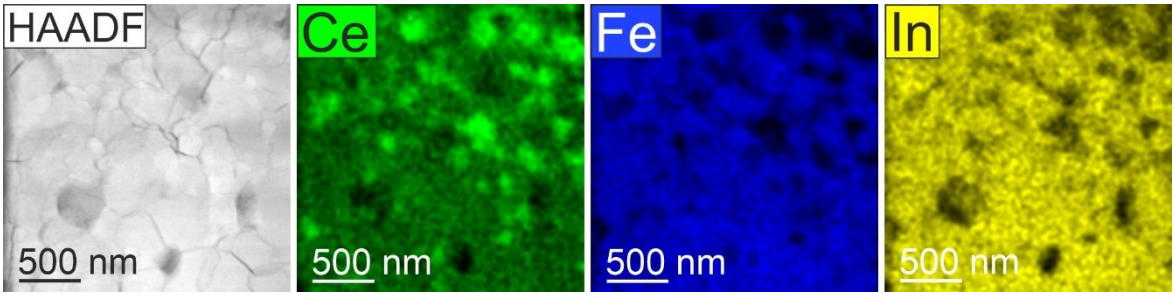

Fig. A7 STEM-HAADF image and EDX elemental maps of selected cations of a SPS sintered self-generated $BaCe_{0.3}Fe_{0.4}In_{0.3}O_{3-\delta}$ composite. The EDX point spectra used for quantification (results in Table A41) are obtained from this area [69].

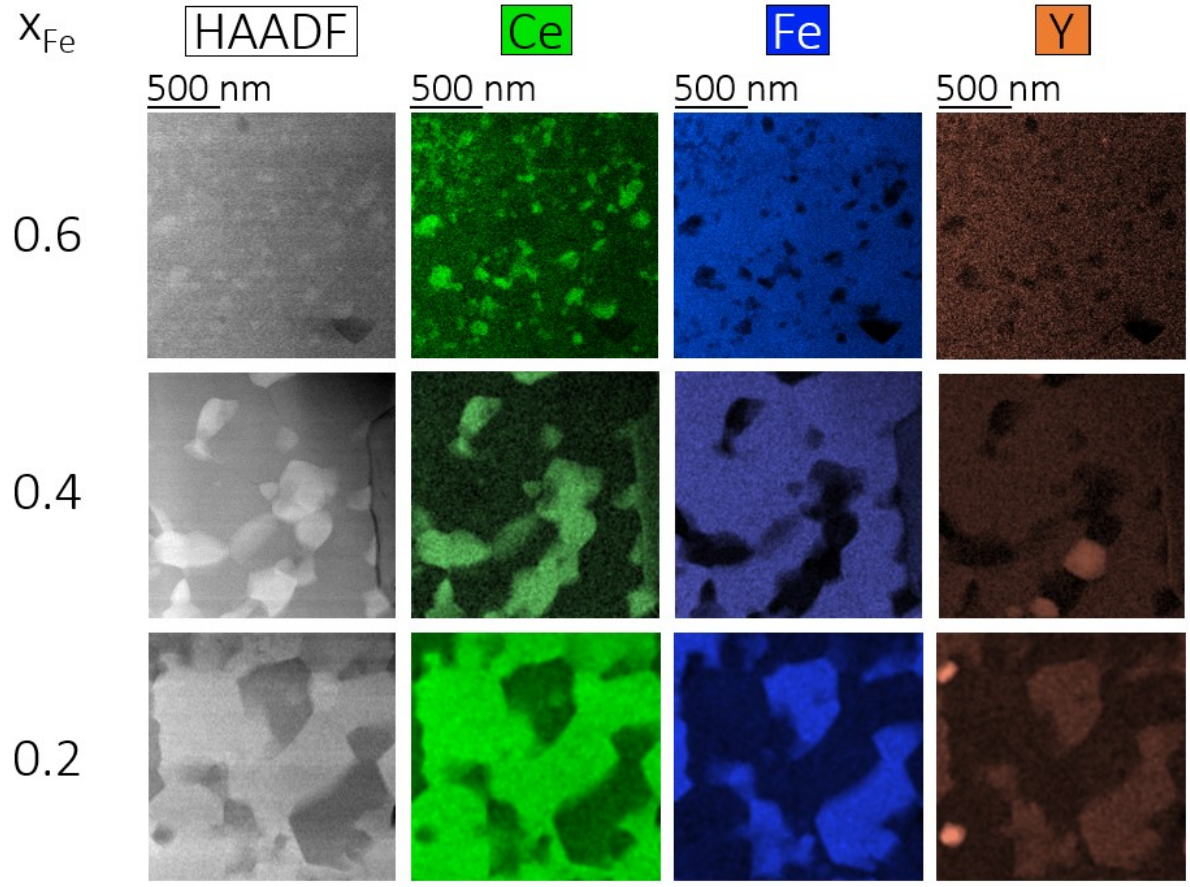

Fig. A8 STEM-HAADF images and EDX elemental maps of selected cations of SPS sintered self-generated $BaCe_{0.8-x}Fe_xY_{0.2}O_{3-\delta}$ composites. The EDX point spectra used for quantification (results in Table A42) are obtained from these areas [69].

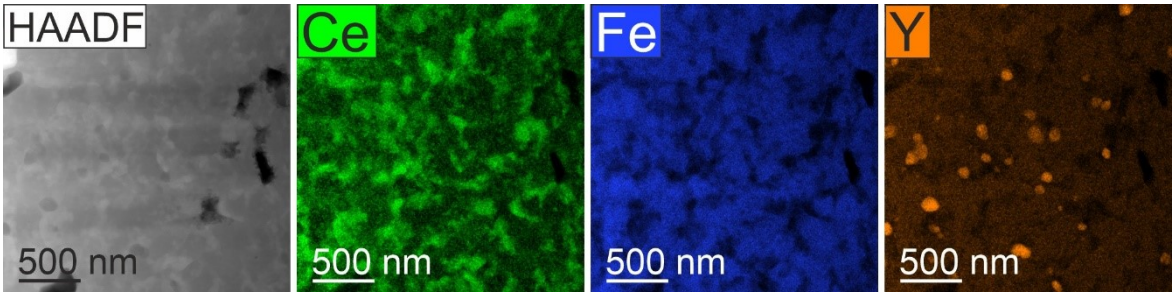

Fig. A9 STEM-HAADF image and EDX elemental maps of selected cations of a SPS sintered self-generated $BaCe_{0.3}Fe_{0.4}Y_{0.3}O_{3-\delta}$ composite. The EDX point spectra used for quantification (results in Table A42) are obtained from this area [69].

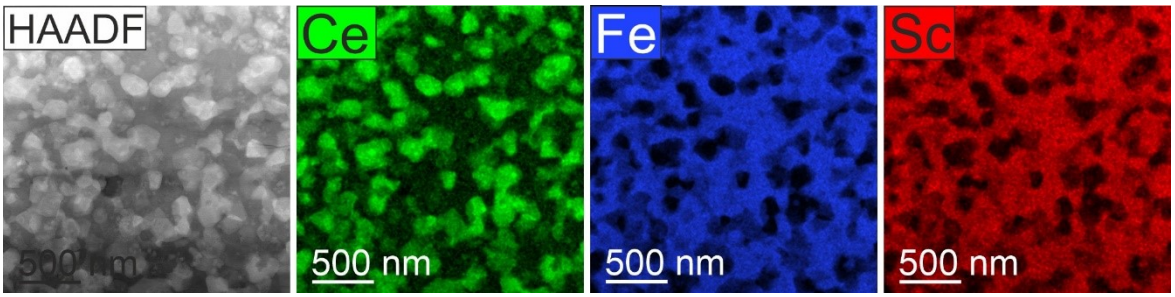

Fig. A10 STEM-HAADF image and EDX elemental maps of selected cations of a SPS sintered self-generated $BaCe_{0.4}Fe_{0.4}Sc_{0.2}O_{3-\delta}$ composite. The EDX point spectra used for quantification (results in Table A44) are obtained from this area [69].

Tab. A41 Local cation composition of the B-site of Ce- and Fe-rich phases of self-generated SPS sintered $BaCe_{0.8-x}Fe_xIn_{0.2}O_{3-\delta}$ and $BaCe_{0.3}Fe_{0.4}In_{0.3}O_{3-\delta}$ composites obtained from STEM-EDX point spectra [69].

Precursor	Ce-rich phase	Fe-rich phase
$BaCe_{0.2}Fe_{0.6}In_{0.2}O_{3-\delta}$	$BaCe_{0.50}Fe_{0.37}In_{0.13}O_{3-\delta}$	$BaCe_{0.26}Fe_{0.57}In_{0.17}O_{3-\delta}$
	$BaCe_{0.70}Fe_{0.20}In_{0.10}O_{3-\delta}$	
	$BaCe_{0.85}Fe_{0.07}In_{0.08}O_{3-\delta}$	
$BaCe_{0.3}Fe_{0.5}In_{0.2}O_{3-\delta}$	$BaCe_{0.49}Fe_{0.38}In_{0.13}O_{3-\delta}$	$BaCe_{0.21}Fe_{0.64}In_{0.15}O_{3-\delta}$
	$BaCe_{0.69}Fe_{0.21}In_{0.10}O_{3-\delta}$	
	$BaCe_{0.86}Fe_{0.08}In_{0.06}O_{3-\delta}$	
$BaCe_{0.4}Fe_{0.4}In_{0.2}O_{3-\delta}$	$BaCe_{0.70}Fe_{0.15}In_{0.15}O_{3-\delta}$	$BaCe_{0.29}Fe_{0.46}In_{0.25}O_{3-\delta}$
	$BaCe_{0.83}Fe_{0.06}In_{0.11}O_{3-\delta}$	
$BaCe_{0.5}Fe_{0.3}In_{0.2}O_{3-\delta}$	$BaCe_{0.49}Fe_{0.43}In_{0.08}O_{3-\delta}$	$BaCe_{0.22}Fe_{0.67}In_{0.11}O_{3-\delta}$
	$BaCe_{0.86}Fe_{0.10}In_{0.04}O_{3-\delta}$	$BaCe_{0.34}Fe_{0.56}In_{0.10}O_{3-\delta}$
$BaCe_{0.6}Fe_{0.2}In_{0.2}O_{3-\delta}$	$BaCe_{0.83}Fe_{0.06}In_{0.11}O_{3-\delta}$	$BaCe_{0.34}Fe_{0.35}In_{0.31}O_{3-\delta}$
$BaCe_{0.3}Fe_{0.4}In_{0.3}O_{3-\delta}$	$BaCe_{0.58}Fe_{0.27}In_{0.15}O_{3-\delta}$	$BaCe_{0.30}Fe_{0.48}In_{0.22}O_{3-\delta}$
	$BaCe_{0.75}Fe_{0.15}In_{0.10}O_{3-\delta}$	
	$BaCe_{0.87}Fe_{0.07}In_{0.06}O_{3-\delta}$	

Tab. A42 Local cation composition of the B-site of Ce- and Fe-rich phases of self-generated SPS sintered $BaCe_{0.8-x}Fe_xY_{0.2}O_{3-\delta}$, as well as $BaCe_{0.3}Fe_{0.4}In_{0.3}O_{3-\delta}$ and $BaCe_{0.5}Fe_{0.4}Y_{0.1}O_{3-\delta}$ composites obtained from STEM-EDX point spectra [87].

Precursor	Ce-rich phase	Fe-rich phase
$BaCe_{0.2}Fe_{0.6}Y_{0.2}O_{3-\delta}$	$BaCe_{0.52}Fe_{0.33}Y_{0.15}O_{3-\delta}$	$BaCe_{0.15}Fe_{0.64}Y_{0.22}O_{3-\delta}$
	$BaCe_{0.63}Fe_{0.25}Y_{0.12}O_{3-\delta}$	
	$BaCe_{0.75}Fe_{0.15}Y_{0.10}O_{3-\delta}$	$BaCe_{0.37}Fe_{0.45}Y_{0.18}O_{3-\delta}$
	$BaCe_{0.85}Fe_{0.08}Y_{0.07}O_{3-\delta}$	
$BaCe_{0.4}Fe_{0.4}Y_{0.2}O_{3-\delta}$	$BaCe_{0.82}Fe_{0.10}Y_{0.09}O_{3-\delta}$	$BaCe_{0.22}Fe_{0.53}Y_{0.25}O_{3-\delta}$
$BaCe_{0.6}Fe_{0.2}Y_{0.2}O_{3-\delta}$	$BaCe_{0.72}Fe_{0.12}Y_{0.16}O_{3-\delta}$	$BaCe_{0.32}Fe_{0.39}Y_{0.29}O_{3-\delta}$
$BaCe_{0.3}Fe_{0.4}Y_{0.3}O_{3-\delta}$	$BaCe_{0.65}Fe_{0.18}Y_{0.17}O_{3-\delta}$	$BaCe_{0.13}Fe_{0.56}Y_{0.31}O_{3-\delta}$
$BaCe_{0.5}Fe_{0.4}Y_{0.1}O_{3-\delta}$	$BaCe_{0.67}Fe_{0.23}Y_{0.09}O_{3-\delta}$	$BaCe_{0.20}Fe_{0.66}Y_{0.14}O_{3-\delta}$
	$BaCe_{0.79}Fe_{0.15}Y_{0.07}O_{3-\delta}$	
	$BaCe_{0.85}Fe_{0.08}Y_{0.07}O_{3-\delta}$	

Tab. A43 Averaged local cation composition of the B-site of Ce- and Fe-rich phases of Y-containing composites calculated from Table A42 [87].

Precursor	Ce-rich phase	Fe-rich phase
$BaCe_{0.2}Fe_{0.6}Y_{0.2}O_{3-\delta}$	$BaCe_{0.69}Fe_{0.20}Y_{0.11}O_{3-\delta}$	$BaCe_{0.21}Fe_{0.59}Y_{0.21}O_{3-\delta}$
$BaCe_{0.4}Fe_{0.4}Y_{0.2}O_{3-\delta}$	$BaCe_{0.82}Fe_{0.10}Y_{0.09}O_{3-\delta}$	$BaCe_{0.22}Fe_{0.53}Y_{0.25}O_{3-\delta}$
$BaCe_{0.6}Fe_{0.2}Y_{0.2}O_{3-\delta}$	$BaCe_{0.72}Fe_{0.12}Y_{0.16}O_{3-\delta}$	$BaCe_{0.32}Fe_{0.39}Y_{0.29}O_{3-\delta}$
$BaCe_{0.3}Fe_{0.4}Y_{0.3}O_{3-\delta}$	$BaCe_{0.65}Fe_{0.18}Y_{0.17}O_{3-\delta}$	$BaCe_{0.13}Fe_{0.56}Y_{0.31}O_{3-\delta}$
$BaCe_{0.5}Fe_{0.4}Y_{0.1}O_{3-\delta}$	$BaCe_{0.77}Fe_{0.15}Y_{0.08}O_{3-\delta}$	$BaCe_{0.20}Fe_{0.66}Y_{0.14}O_{3-\delta}$

Tab. A44 Local cation composition of the B-site of the Ce- and Fe-rich phase of self-generated SPS sintered $BaCe_{0.4}Fe_{0.4}Sc_{0.2}O_{3-\delta}$ obtained from STEM-EDX point spectra [69].

Precursor	Ce-rich phase	Fe-rich phase
$BaCe_{0.4}Fe_{0.4}Sc_{0.2}O_{3-\delta}$	$BaCe_{0.82}Fe_{0.09}Sc_{0.10}O_{3-\delta}$	$BaCe_{0.17}Fe_{0.57}Sc_{0.29}O_{3-\delta}$

Tab. A45 Local cation composition of the B-site of the Ce- and Fe-rich phase of artificial SPS sintered composites obtained from STEM-EDX point spectra. BcBf8020 and BcBf6535 have the precursor compositions $BaCe_{0.60}Fe_{0.20}Y_{0.20}O_{3-\delta}$ and $BaCe_{0.48}Fe_{0.32}Y_{0.20}O_{3-\delta}$.

Precursor	Ce-rich phase	Fe-rich phase
BcBf8020	$BaCe_{0.68}Fe_{0.13}Y_{0.19}O_{3-\delta}$	$BaCe_{0.20}Fe_{0.50}Y_{0.30}O_{3-\delta}$
BcBf6535	$BaCe_{0.71}Fe_{0.11}Y_{0.18}O_{3-\delta}$	$BaCe_{0.13}Fe_{0.63}Y_{0.24}O_{3-\delta}$

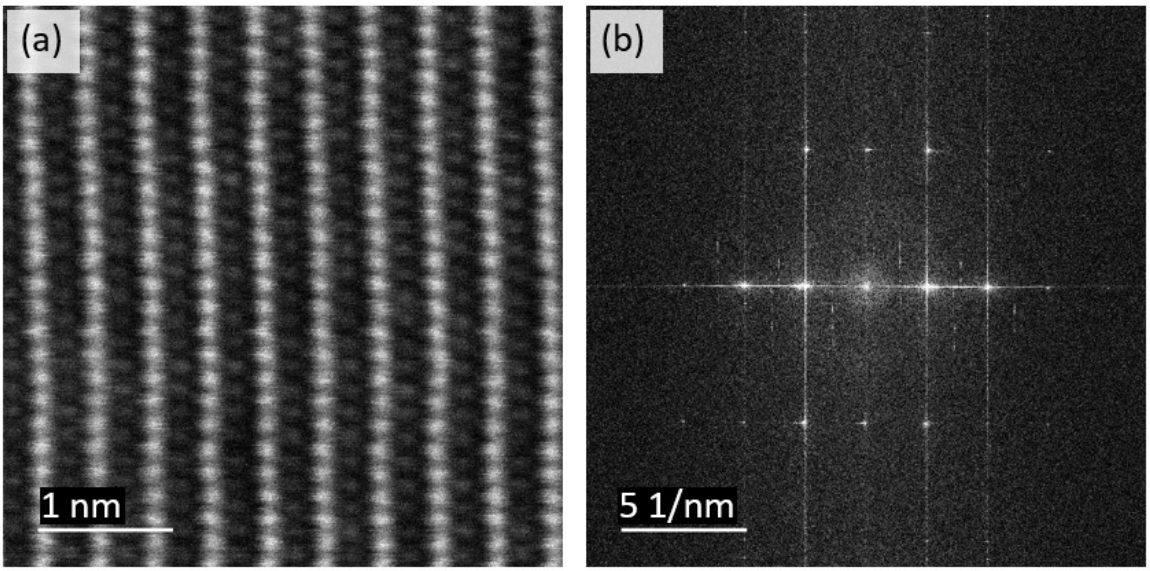

Fig. A11 (a) High resolution STEM-HAADF image with **(b)** the corresponding FFT image in [102] zone axis of $BaCe_{0.04}Fe_{0.76}Y_{0.20}O_{3-\delta}$.

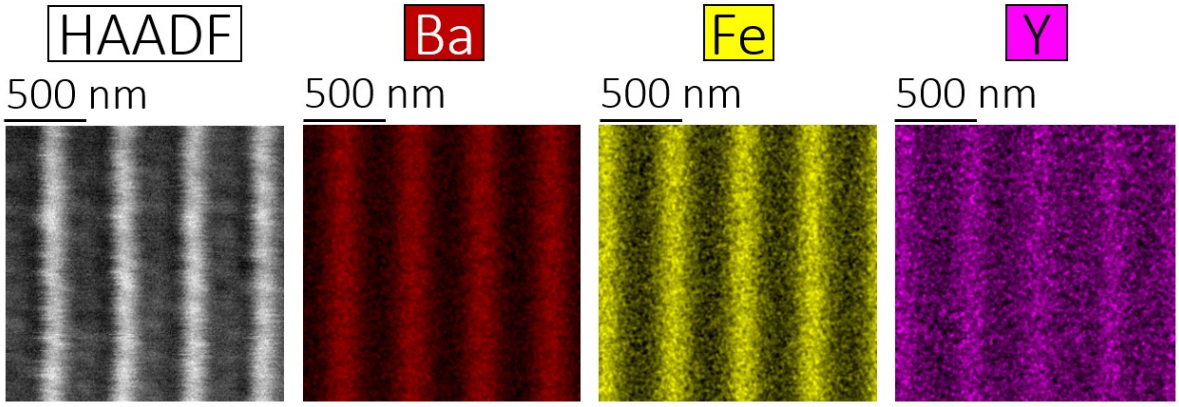

Fig. A12 High resolution STEM-HAADF image and EDX elemental maps for selected cations of $BaCe_{0.04}Fe_{0.76}Y_{0.20}O_{3-\delta}$, showing Ba on the A-site and Fe and Y on the B-site. The signal of Ce was not strong enough to be depicted due to the low concentration.

7.12. Proton uptake capacity

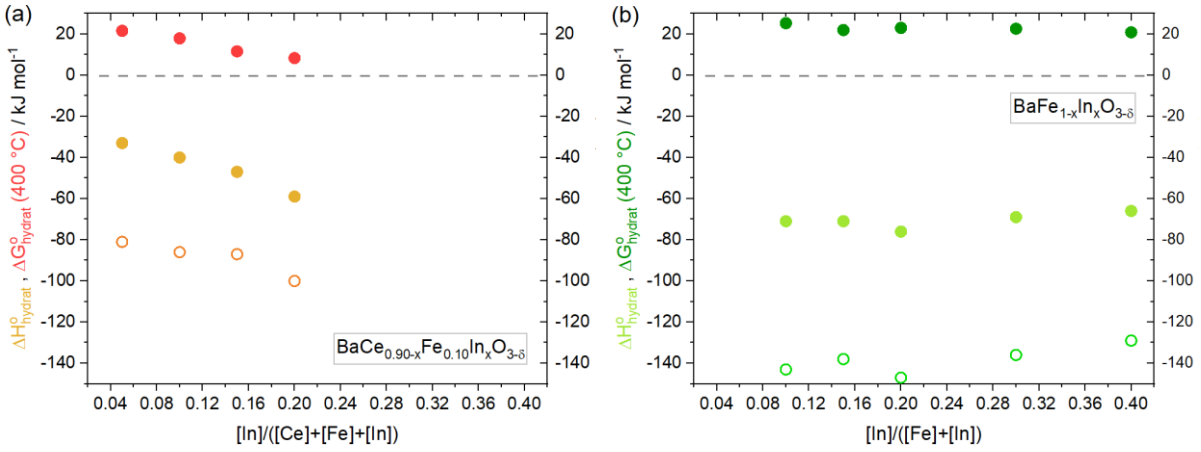

Fig. A13 $\Delta H^{\circ}_{hydrat}$, $\Delta S^{\circ}_{hydrat}$ and $\Delta G^{\circ}_{hydrat}$ as a function of In content of **(a)** $BaCe_{0.90-x}Fe_{0.10}In_xO_{3-\delta}$ single phases and **(b)** In-substituted ferrates at 400 °C.

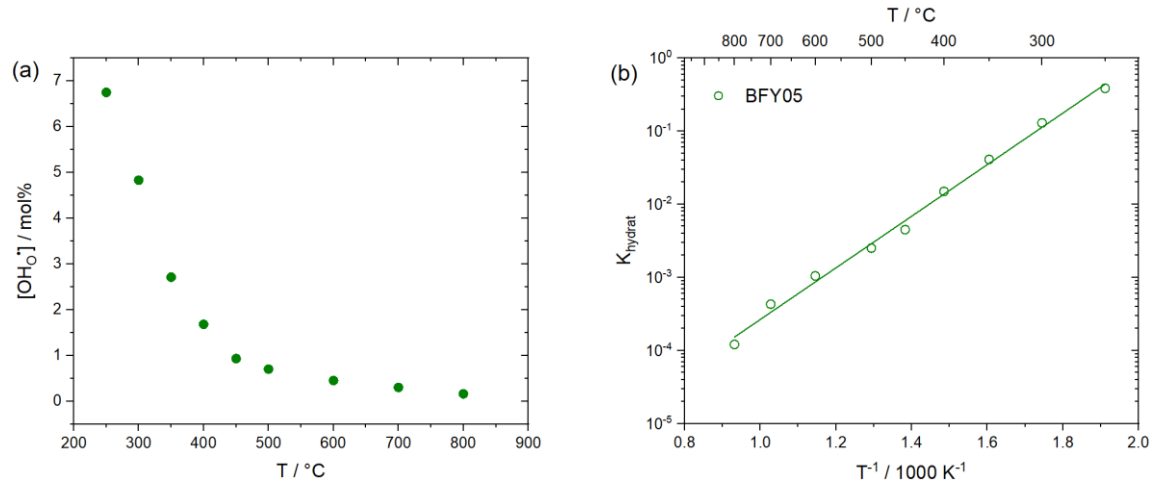

Fig. A14 Proton concentration as a function of temperature and van't Hoff plot of **(a)–(b)** BFY05.

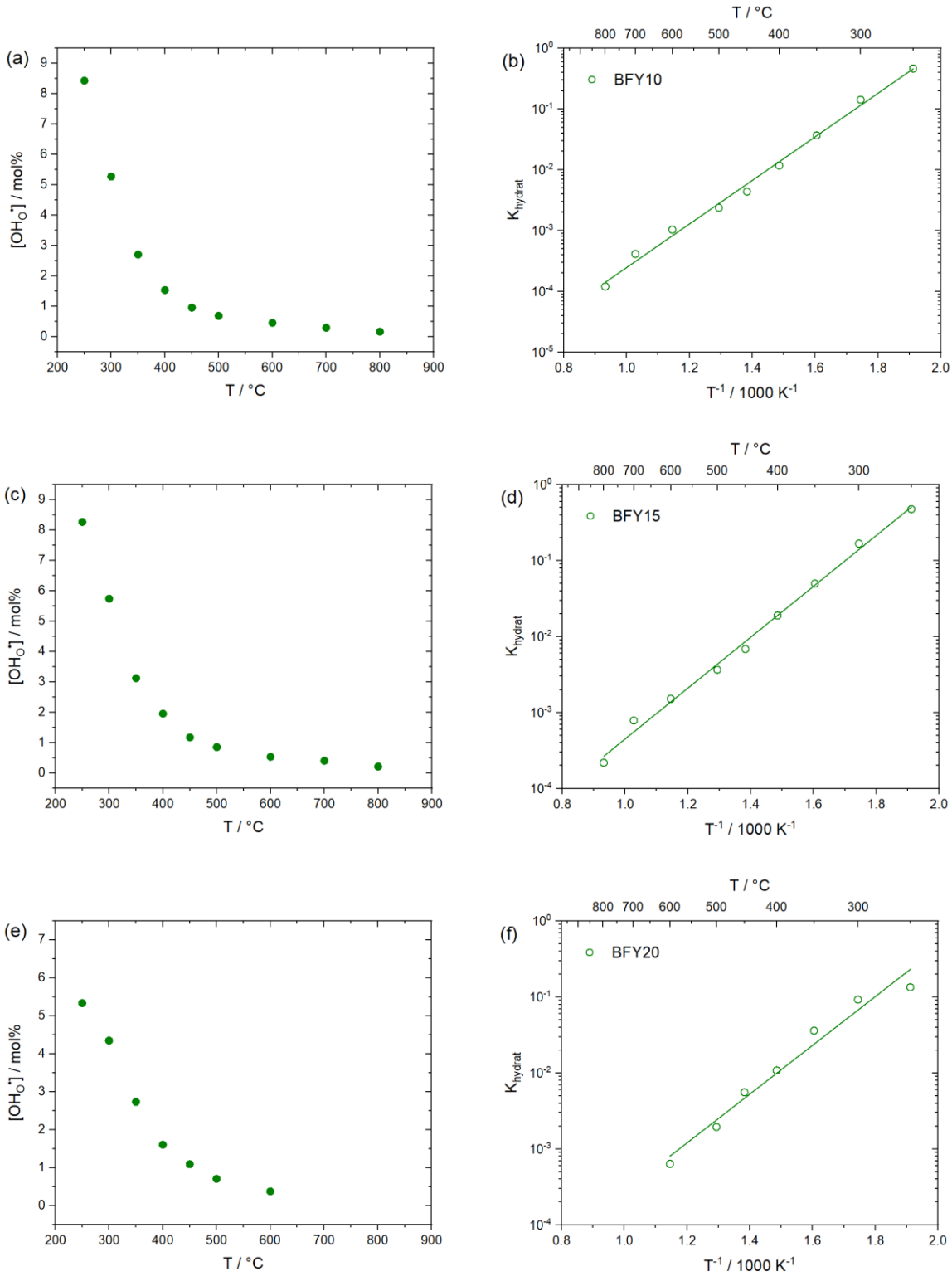

Fig. A15 Proton concentration as a function of temperature and van't Hoff plots of **(a)–(b)** BFY10, **(c)–(d)** BFY15 and **(e)–(f)** BFY20 (data taken from [97]).

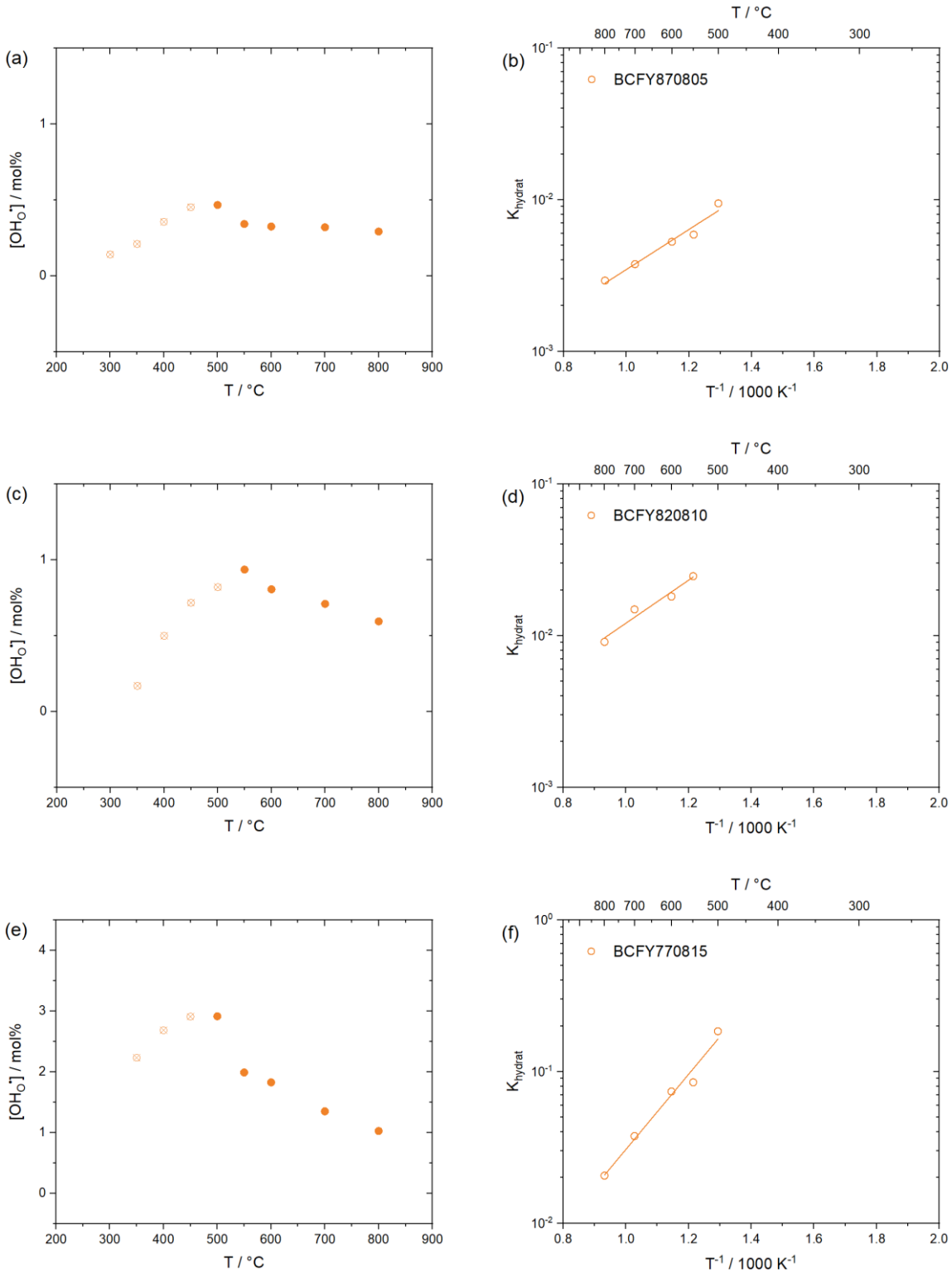

Fig. A16 Proton concentration as a function of temperature and van't Hoff plots of **(a)–(b)** BCFY870805, **(c)–(d)** BCFY820810 and **(e)–(f)** BCFY770815. The results of the calculations are based solely on the symbols filled.

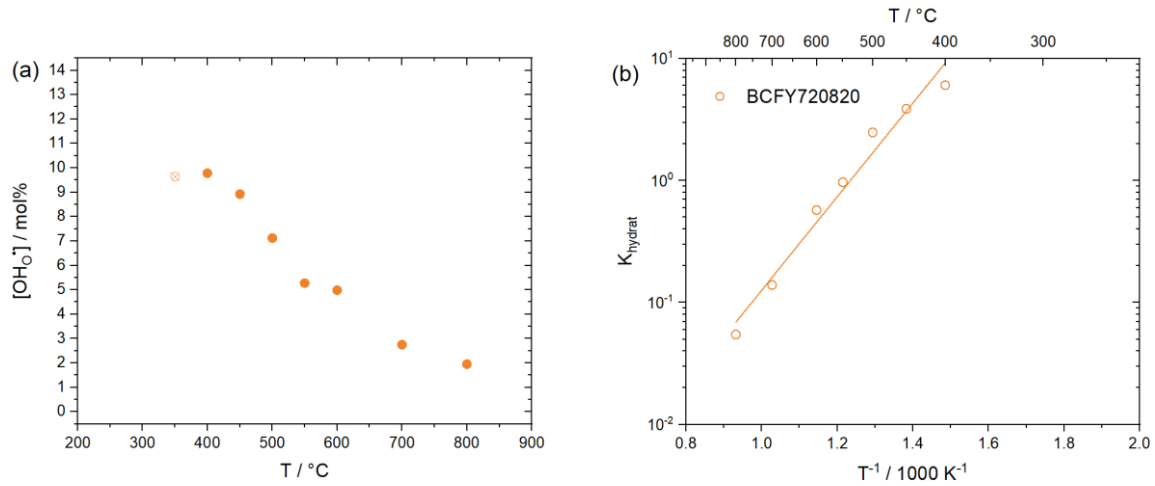

Fig. A17 Proton concentration as a function of temperature and van't Hoff plot of **(a)–(b)** BCFY720820. The results of the calculations are based solely on the symbols filled.

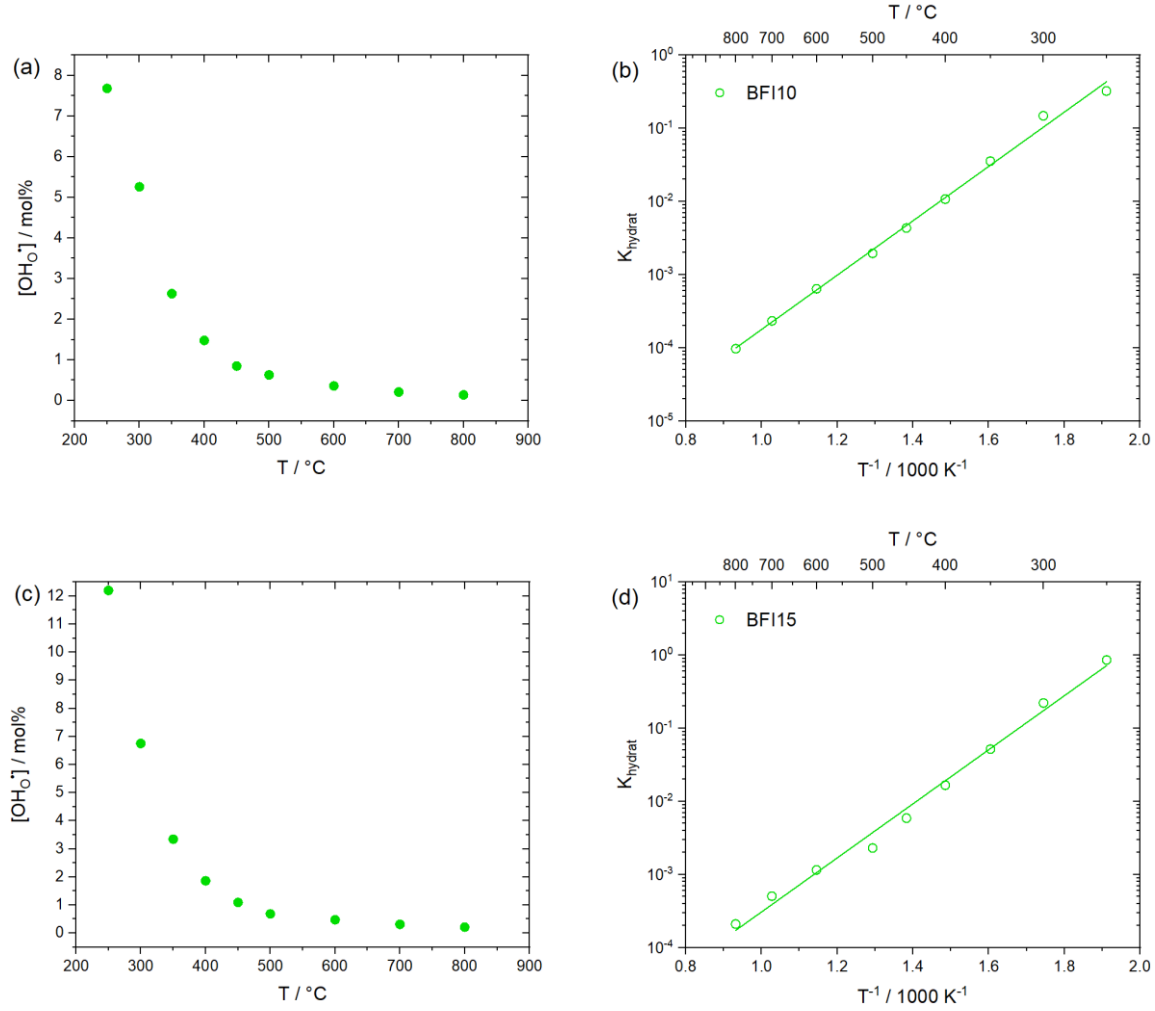

Fig. A18 Proton concentration as a function of temperature and van't Hoff plots of **(a)–(b)** BFI10 and **(c)–(d)** BFI15.

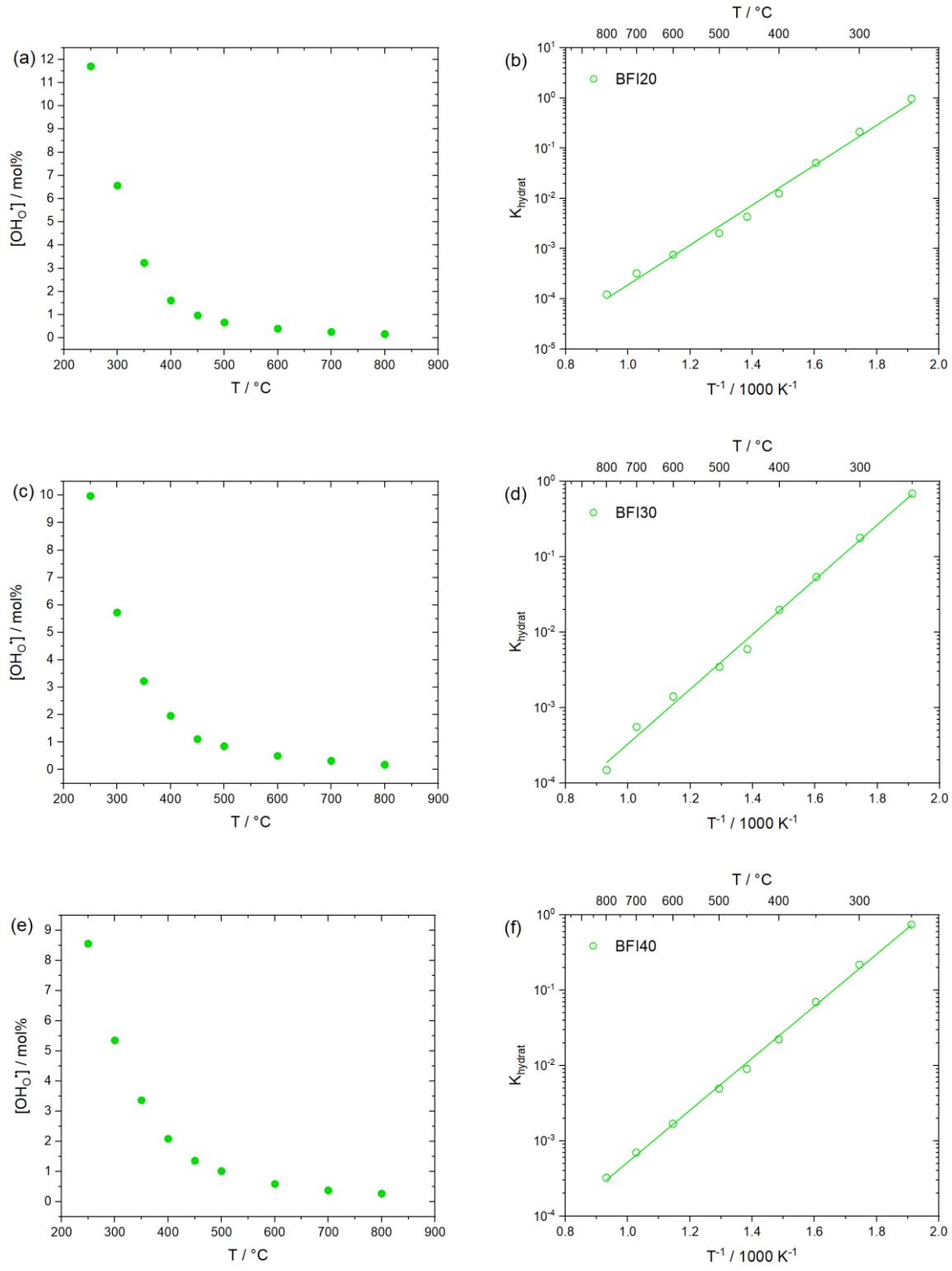

Fig. A19 Proton concentration as a function of temperature and van't Hoff plots of **(a)–(b)** BFI20, **(c)–(d)** BFI30 and **(e)–(f)** BFI40.

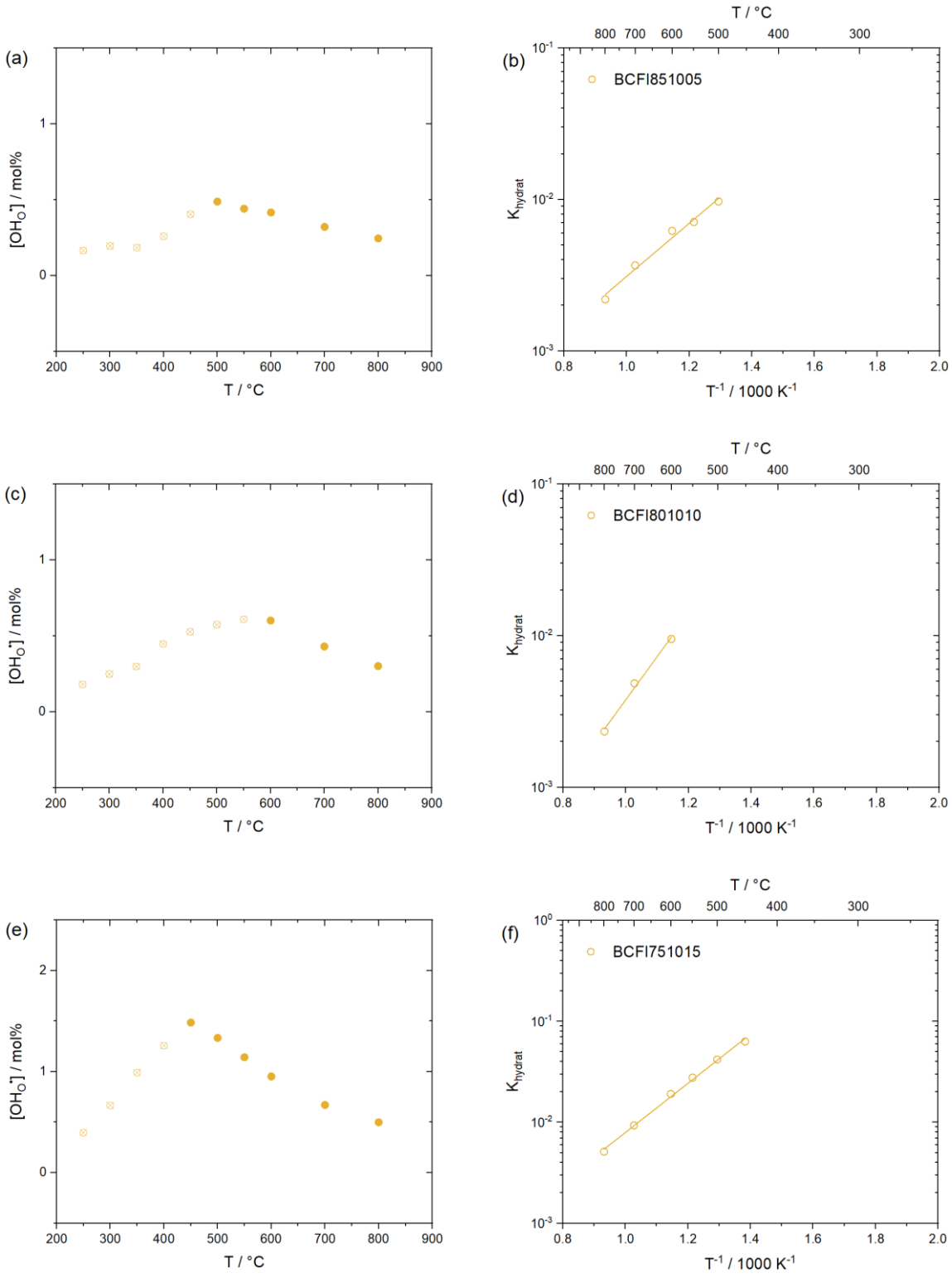

Fig. A20 Proton concentration as a function of temperature and van't Hoff plots of **(a)–(b)** BCFI851005, **(c)–(d)** BCFI801010 and **(e)–(f)** BCFI751015. The results of the calculations are based solely on the symbols filled.

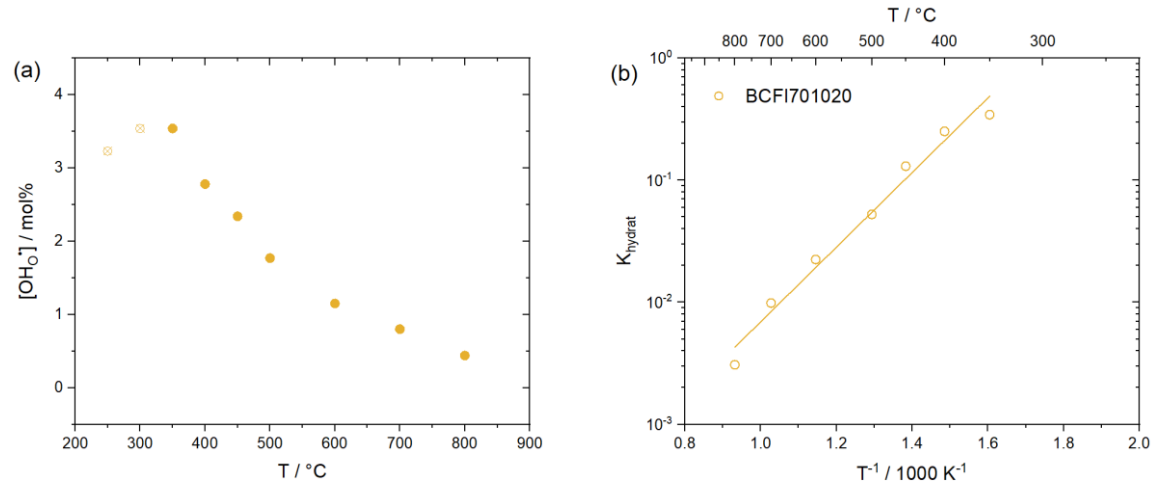

Fig. A21 Proton concentration as a function of temperature and van't Hoff plot of **(a)–(b)** BCFI701020. The results of the calculations are based solely on the symbols filled.

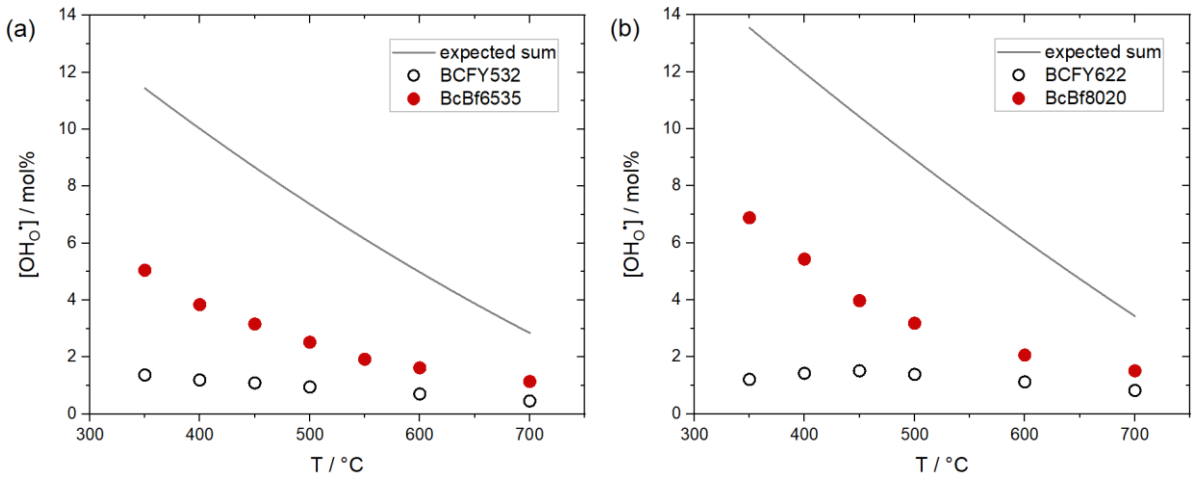

Fig. A22 Proton concentration as a function of temperature in 17 mbar pH_2O with frozen-in oxygen stoichiometry of **(a)** the artificial composite BcBf6535, which corresponds to a precursor composition of $BaCe_{0.48}Fe_{0.32}Y_{0.20}O_{3-\delta}$ and is thus compared to the self-generated composite BCFY532, and **(b)** BcBf8020, which corresponds to a precursor composition of $BaCe_{0.60}Fe_{0.20}Y_{0.20}O_{3-\delta}$ and is thus compared to the self-generated composite BCFY622. In addition, the obtained results are compared to the respective calculated expected averages.

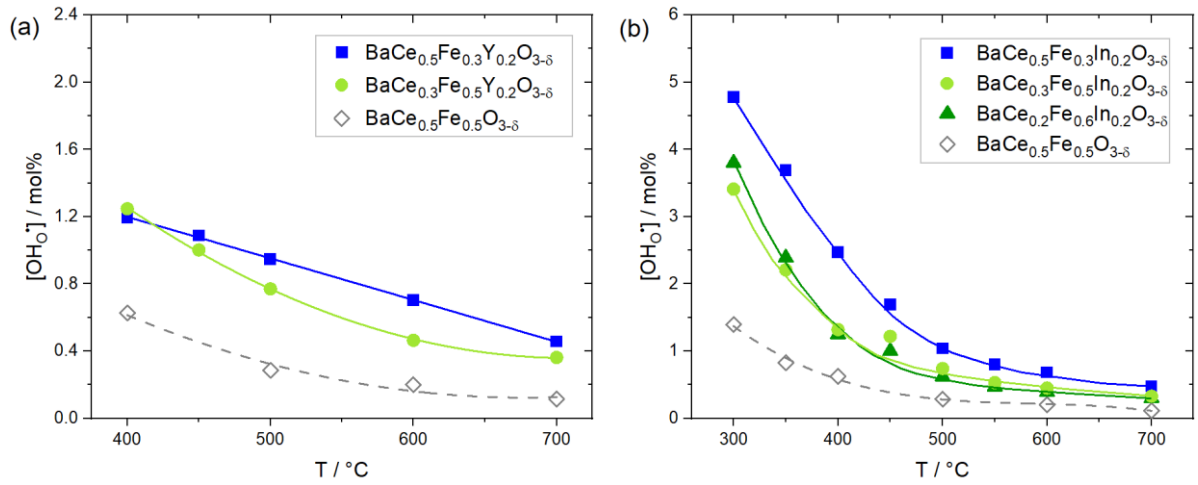

Fig. A23 Proton concentration as a function of temperature in 17 mbar pH_2O with frozen-in oxygen stoichiometry of self-generated **(a)** $BaCe_{0.8-x}Fe_xY_{0.2}O_{3-\delta}$ composites and **(b)** $BaCe_{0.8-x}Fe_xIn_{0.2}O_{3-\delta}$ composites compared to unsubstituted $BaCe_{0.5}Fe_{0.5}O_{3-\delta}$. Taken from [69]. The lines are a guide to the eye.

7.13. Electrical conductivity

Figures A24–A27 show the conductivity of selected self-generated composites in dry atmosphere following measurements in humid atmosphere. As previously discussed, not all samples return to the same level of electrical conductivity after drying. Figure A24 shows a slight increase in electrical conductivity of BCFY262 after drying, although it does not reach the same level as at the beginning in dry atmosphere. At temperatures between 650 and 700 °C, the conductivity decreased to a lower level, indicating degradation, such as cracks caused by humidification, as described elsewhere [111]. In Figure A25b, it is possible that the drying process of BCFY442 was not complete until the measurements in “dry” atmosphere started. The initial results are comparable to those obtained in humid atmosphere, increasing over time until they reach the same level as at the beginning in dry atmosphere.

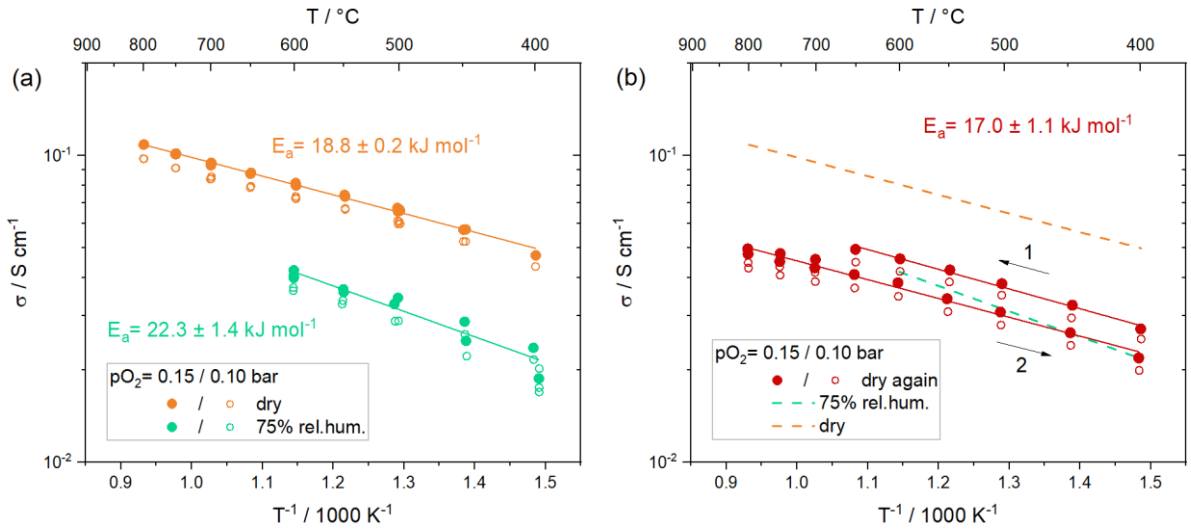

Fig. A24 Electrical conductivity as a function of inverse temperature of the self-generated composite $BaCe_{0.2}Fe_{0.6}Y_{0.2}O_{3-\delta}$ **(a)** in both dry and humid atmosphere and **(b)** in dry atmosphere following measurements in humid atmosphere. Activation energies are given in the plots. The lines are a guide to the eye.

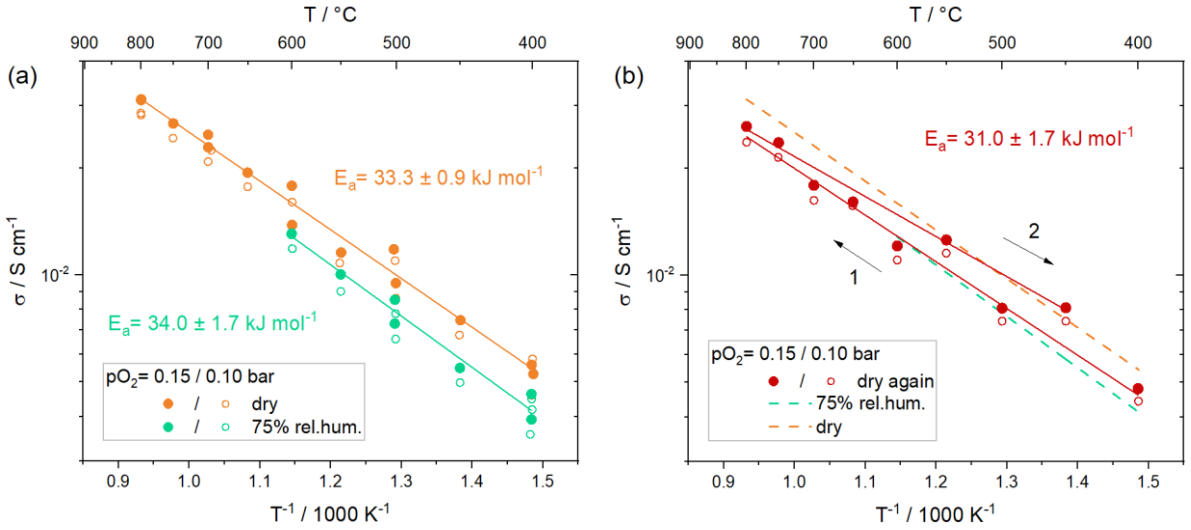

Fig. A25 Electrical conductivity as a function of inverse temperature of the self-generated composite $BaCe_{0.4}Fe_{0.4}Y_{0.2}O_{3-\delta}$ **(a)** in both dry and humid atmosphere and **(b)** in dry atmosphere following measurements in humid atmosphere. Activation energies are given in the plots. The lines are a guide to the eye.

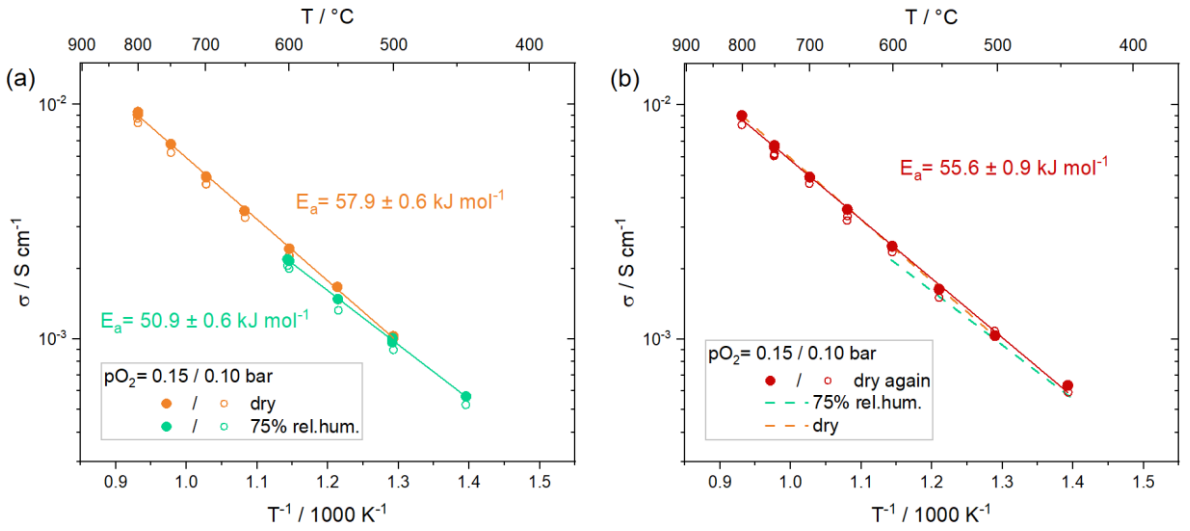

Fig. A26 Electrical conductivity as a function of inverse temperature of the self-generated composite $BaCe_{0.6}Fe_{0.2}Y_{0.2}O_{3-\delta}$ **(a)** in both dry and humid atmosphere and **(b)** in dry atmosphere following humid measurements. Activation energies are indicated. The lines are a guide to the eye.

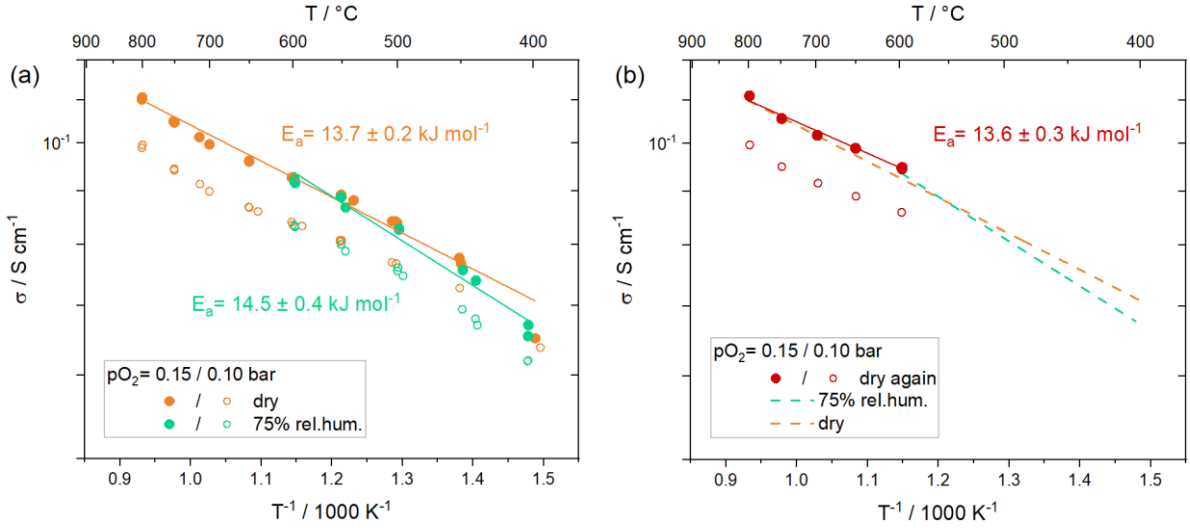

Fig. A27 Electrical conductivity as a function of inverse temperature of the self-generated composite $BaCe_{0.5}Fe_{0.4}Y_{0.1}O_{3-\delta}$ **(a)** in both dry and humid atmosphere and **(b)** in dry atmosphere following measurements in humid atmosphere. Activation energies are given in the plots. The lines are a guide to the eye.

Tab. A46 Proton uptake capacity compared to the factors by which the electrical conductivity of selected samples changes when the atmosphere changes from dry to humidified.

Abbreviation	$[OH_O^{\bullet}]$ / mol % (T = 600°C)	Factor / dry to humid
BCFY622	1.12	0.92
BCFY343	1.02	0.88
BCFY442	0.65	0.80
BCFY541	0.51	0.98
BCFY262	0.35	0.47

Figure A28 shows the electrical conductivity as a function of time for two additional samples. The sample BCFY262 in Figure A28a shows a decreased electrical conductivity in humid atmosphere. By drying it does not return to the same level as at the beginning in dry atmosphere, which was already discussed in connection with Figure A24. Figure A28b shows the results of BCFY541 remaining at the same level in dry and humid atmosphere.

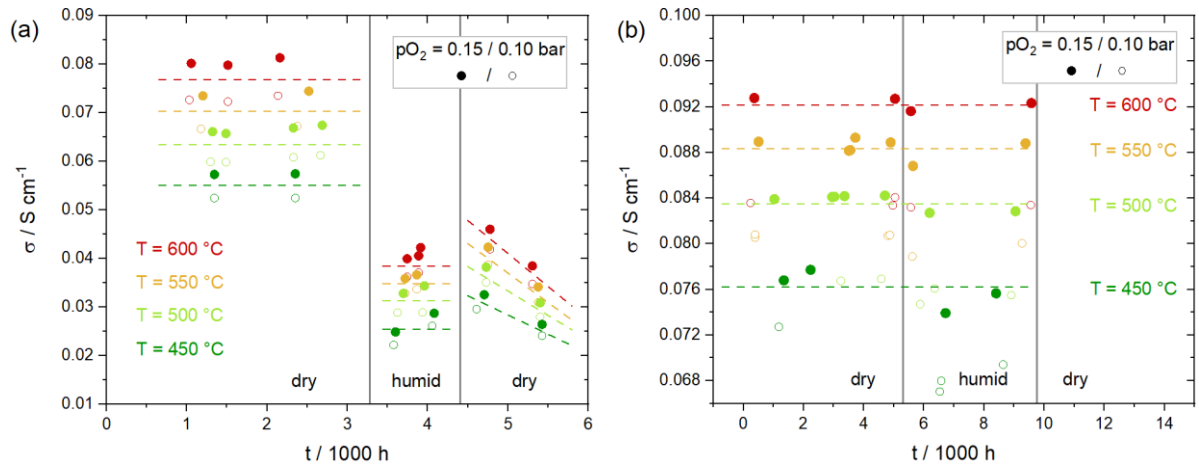

Fig. A28 Electrical conductivity of the self-generated composites **(a)** $BaCe_{0.2}Fe_{0.6}Y_{0.2}O_{3-\delta}$ and **(b)** $BaCe_{0.5}Fe_{0.4}Y_{0.1}O_{3-\delta}$ at selected temperatures (T = 450, 500, 550 and 600 °C) as a function of time. The lines are a guide to the eye.

7.14. Oxygen exchange kinetics

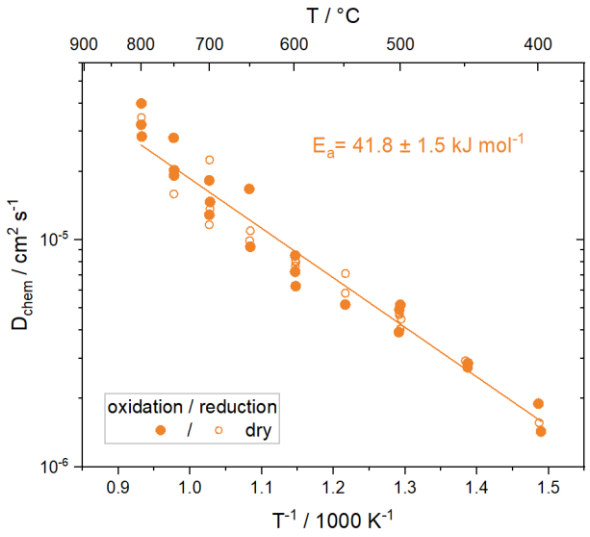

Fig. A29 Chemical diffusion coefficients as a function of inverse temperature of the self-generated composite $BaCe_{0.2}Fe_{0.6}Y_{0.2}O_{3-\delta}$ in dry atmosphere. The activation energy is given in the plot. The line is a guide to the eye.

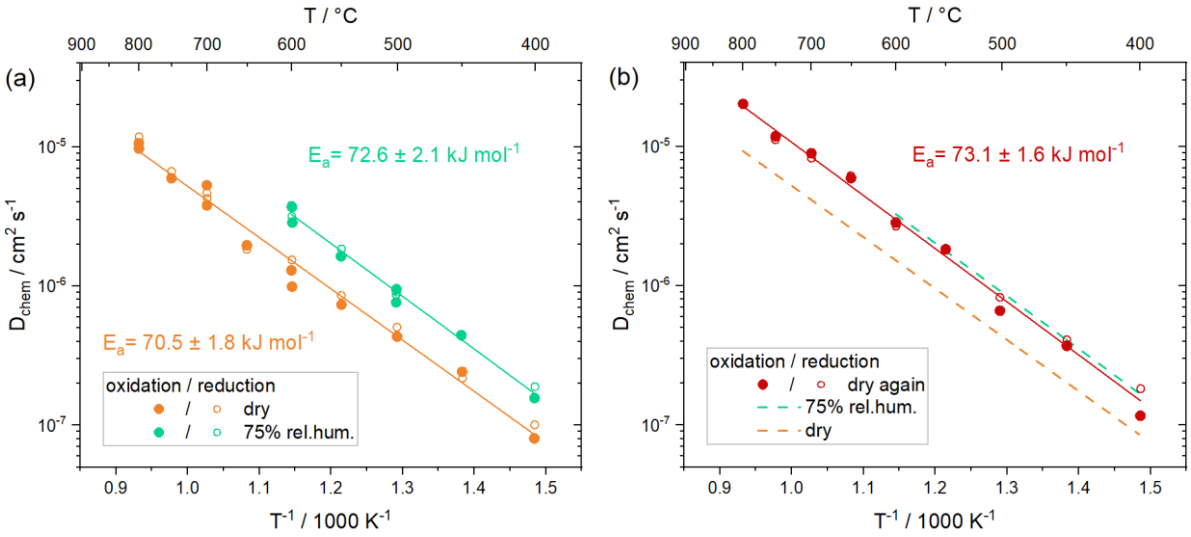

Fig. A30 Chemical diffusion coefficients as a function of inverse temperature of the self-generated composite $BaCe_{0.4}Fe_{0.4}Y_{0.2}O_{3-\delta}$ **(a)** in both dry and humid atmosphere and **(b)** in dry atmosphere following measurements in humid atmosphere. Activation energies are given in the plots. The lines are a guide to the eye.

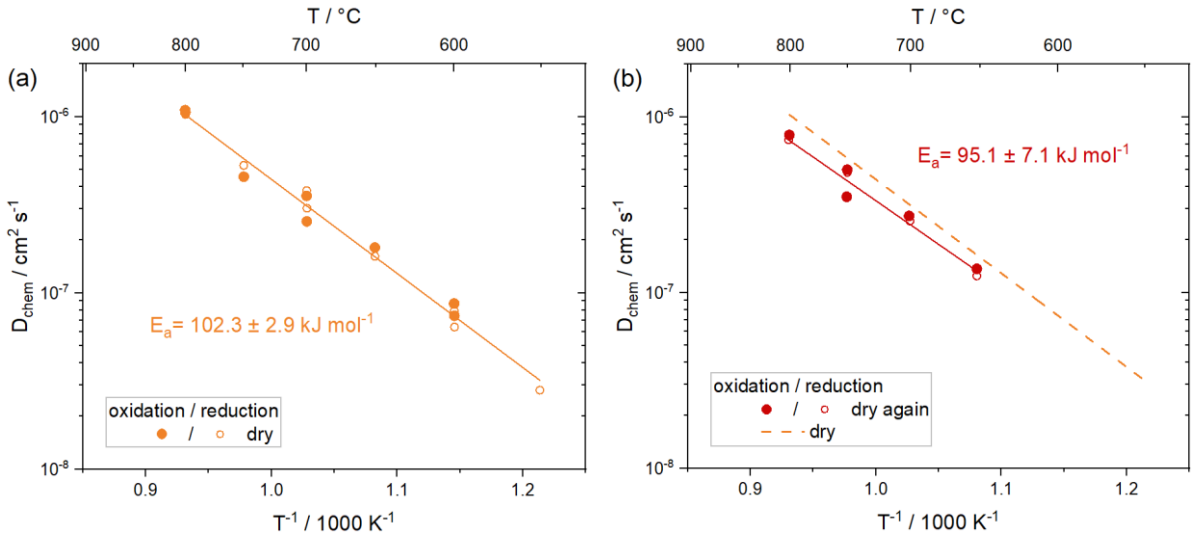

Fig. A31 Chemical diffusion coefficients as a function of inverse temperature of the self-generated composite $BaCe_{0.6}Fe_{0.2}Y_{0.2}O_{3-\delta}$ **(a)** in both dry and humid atmosphere and **(b)** in dry atmosphere following measurements in humid atmosphere. Activation energies are given in the plots. The lines are a guide to the eye.

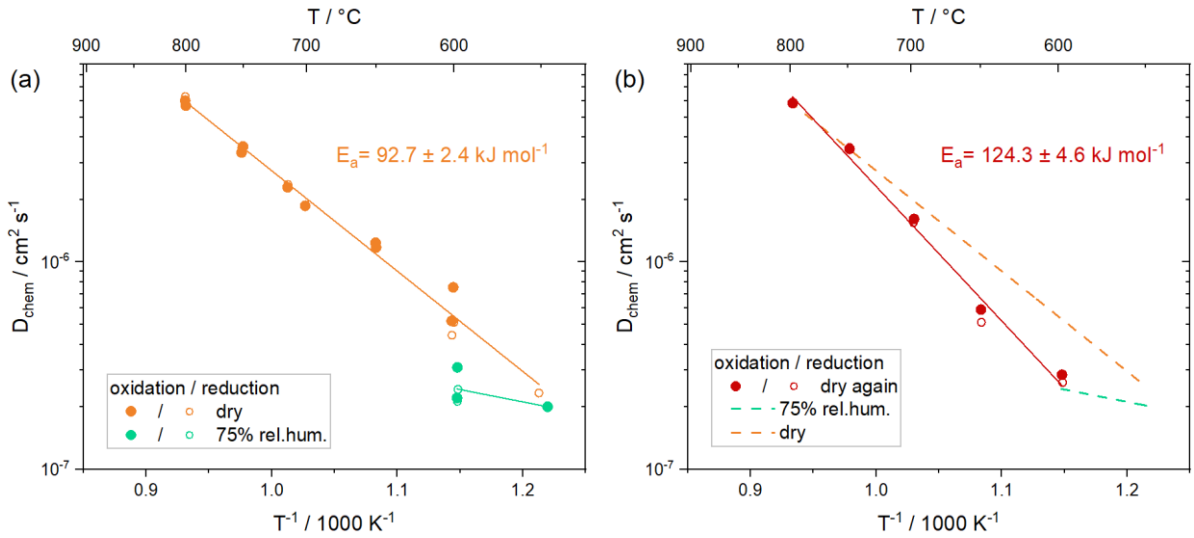

Fig. A32 Chemical diffusion coefficients as a function of inverse temperature of the self-generated composite $BaCe_{0.5}Fe_{0.4}Y_{0.1}O_{3-\delta}$ **(a)** in both dry and humid atmosphere and **(b)** in dry atmosphere following measurements in humid atmosphere. Activation energies are given in the plots. The lines are a guide to the eye.